Titre: Title:	Development of Polylactide (PLA) and PLA Nanocomposite Foams in Injection Molding for Automotive Applications
Auteur: Author:	Naqi Najafi Chaloupli
Date:	2015
Type:	Mémoire ou thèse / Dissertation or Thesis
Référence: Citation:	Najafi Chaloupli, N. (2015). Development of Polylactide (PLA) and PLA Nanocomposite Foams in Injection Molding for Automotive Applications [Thèse de doctorat, École Polytechnique de Montréal]. PolyPublie. https://publications.polymtl.ca/1863/

UNIVERSITÉ DE MONTRÉAL

DEVELOPMENT OF POLYLACTIDE (PLA) AND PLA NANOCOMPOSITE FOAMS IN INJECTION MOLDING FOR AUTOMOTIVE APPLICATIONS

NAQI NAJAFI CHALOUPLI

DÉPARTEMENT DE GÉNIE MÉCANIQUE

ÉCOLE POLYTECHNIQUE DE MONTRÉAL

THÈSE PRÉSENTÉE EN VUE DE L'OBTENTION

DU DIPLÔME DE PHILOSOPHIAE DOCTOR

(GÉNIE MÉCANIQUE)

AOÛT 2015

UNIVERSITÉ DE MONTRÉAL

ÉCOLE POLYTECHNIQUE DE MONTRÉAL

Cette thèse intitulée :

DEVELOPMENT OF POLYLACTIDE (PLA) AND PLA NANOCOMPOSITE FOAMS IN INJECTION MOLDING FOR AUTOMOTIVE APPLICATIONS

présentée par : NAJAFI CHALOUPLI Naqi

en vue de l'obtention du diplôme de : Philosophiae Doctor

a été dûment acceptée par le jury d'examen constitué de :

M. AJJI Abdellah, Ph. D., président

M. THERRIAULT Daniel, Ph. D., membre et directeur de recherche

Mme HEUZEY Marie-Claude, Ph. D., membre et codirectrice de recherche

M. CARREAU Pierre, Ph. D., membre et codirecteur de recherche

M. BATAILLY Alain, Ph. D., membre

M. RODRIGUE Denis, Ph. D., membre externe

DEDICATION

To my lovely wife, cheerful daughter, and beloved parent.

ACKNOWLEDGEMENTS

I wish to express my deep gratitude to my advisors, *professor Marie-Claude Heuzey*, *professor Pierre Carreau*, and *professor Daniel Therriault* for the trust they placed in me and for all their supports throughout the period of this research. My sincere appreciation goes to *prof. Heuzey* for her availability, patience, enthusiasm toward scientific research, and productive discussions. I owe my sincere gratitude to *prof. Carreau* for the thing I learnt from him; not only the scientific matters, but also lots of knowledge which are helpful in all aspects of my life. I also acknowledge all the efforts made by *prof. Therriault* for the improvement of the quality of the articles and eventually this thesis. I appreciate all his precious comments as well as his warm encouragements. I truly feel lucky to have had the opportunity to do my PhD under their supervision.

I am so thankful to *professor Chul Park* for his helpful discussions and valuable contribution in the first and third articles.

I am grateful of the financial support and scholarships from Canada's automotive R&D program (Auto 21), Networks of Centres of Excellence of Canada and Pierre Arbour Foundation.

Many Thanks to all technical and administrative staff of Chemical and Mechanical Engineering Departments, particularly *Mr. Guillaume Lessard*, *Mr. Jean Huard*, *Mr. Robert Delisle*, *Ms. Martine Lamarche*, *Mr. Gino Robin*, *Ms. Valérie Baudart*, and *Ms. Martine Bénard* for their kind cooperation during my work. Especial thank to *Ms. Melina Hamdine*, and *Dr. Amir Hossein Maani*, our brilliant ex-research associates, for all their technical assistance and revitalizing friendly discussions we had together.

I am also thankful to *Mr. Mohamed Aymen Ghoulia*, the research assistant at Cerestech Inc., who trained and helped me on injection molding process.

I would like to deeply thank *Mounia Arkoun* for her warm and quick response to my request for translating parts of this thesis to French.

I owe gratitude to the members of the rheology group who have organized the group meetings and generously shared their knowledge and experiences with me and who made the working place a fascinating area. My special word of thanks is owed to our helpful research associate, *Dr. Amir Saffar*.

I warmly thank all my friends and my colleagues for their supports and their willing to help me with my research. I have spent memorable times with them during these years and I never forget their kind regards to me.

Finally, with all my heart, I would like to express my undying gratitude to my beloved parents and my lovely wife for the overwhelming support they provided and for scarifies they made; there will never be a right word to express my feeling of appreciation for their unconditional love.

RÉSUMÉ

Les matériaux plastiques sont largement utilisés dans l'automobile, car ils permettent la fabrication de véhicules qui consomment moins d'énergie. Actuellement, l'industrie automobile cherche des solutions de rechange à base de matières bio-ressourcées et renouvelables comme alternative aux plastiques issus du pétrole et ce, afin de réduire la dépendance aux combustibles fossiles. Parmi les polymères issus de sources renouvelables, le polylactide (PLA) a suscité un vif intérêt en tant que polymère vert très prometteur. Aussi, l'utilisation de ce polymère dans les industries durables est-elle en plein essor.

Par ailleurs, les automobiles économiques en carburant sont aujourd'hui très demandées en raison de l'inquiétude croissante sur les questions environnementales. La consommation de carburant peut être améliorée en réduisant le poids de l'automobile et en utilisant un matériau léger. Une méthode potentielle pour atteindre cet objectif est l'utilisation de la technologie des mousses. La mousse est un matériau où une phase gazeuse est encapsulée par une phase solide. Le processus de moussage consiste en l'incorporation de gaz, la formation d'une solution uniforme polymère-gaz, la nucléation cellulaire, la croissance cellulaire et enfin la stabilisation des cellules. La technologie de moussage permet de fabriquer des pièces allégées avec des propriétés supérieures en comparaison avec leurs homologues solides.

Cependant, le moussage du PLA s'est révélé être une tâche difficile principalement en raison des faibles propriétés rhéologiques, d'une fenêtre de mise en forme restreinte et d'une cinétique de cristallisation lente. Le but ultime de ce projet est de réduire de 30 % le poids des nanocomposites de polylactide (PLA)-argile par la fabrication de pièces en mousse moulées par injection. Afin d'utiliser un équipement de mise en forme standard, un agent de soufflage chimique (ASC) a été employé dans le cadre de cette étude. La technique de moulage par injection a été employée, car c'est le procédé de fabrication le plus largement utilisé dans l'industrie et qui peut produire des pièces de formes complexes. Cependant, ce procédé est plus difficile que d'autres procédés de moussage car il possède de nombreux paramètres supplémentaires à contrôler.

Dans la première partie de ce projet, nous avons illustré la façon dont la ramification à longues chaînes (RLC) et la structure moléculaire influencent la rhéologie à l'état fondu, la cristallisation et le comportement moussant en discontinu du PLA. À cet effet, des PLA à longues chaines ramifiées (PLA-LCR) ont été préparés en présence d'un agent d'allongement de chaînes (AAC)

multifonctionnel en utilisant deux stratégies de préparation différentes. Dans la première stratégie, le PLA séché a été directement mélangé à l'état fondu à diverses quantités d'AAC. Pour examiner plus en détail l'impact de l'AAC sur la topologie moléculaire, un PLA-LCR a également été préparé en utilisant une deuxième approche, la stratégie S2. Dans cette approche, un PLA hautement ramifié a été d'abord préparé, puis mélangé avec un PLA pur dans un rapport en poids de 50:50. Les propriétés rhéologiques en régime permanent et transitoire du PLA-LCR ont révélé que ce dernier présentait une viscosité accrue, une sensibilité au cisaillement, ainsi qu'un temps de relaxation plus long en comparaison avec le PLA linéaire. De plus, l'incorporation d'un AAC dans le PLA et le PLA-LCR qui en résulte, a conduit à un comportement de durcissement important de la contrainte dans un écoulement élongationnel uniaxial. En revanche, aucun durcissement n'a été observé dans le cas du PLA linéaire. Le moussage en discontinu de différentes compositions a été réalisé en utilisant du CO_2 à différentes températures de moussage allant de 130 à 155 °C. L'impact de la structure moléculaire et de la température de moussage sur la morphologie cellulaire, la fraction de vide, la densité cellulaire et la taille des cellules a été examiné. Il a été constaté que l'augmentation de l'élasticité et de la résistance à l'état fondu, résultant de la ramification a fortement favorisé l'uniformité des cellules, la densité cellulaire et la fraction de vide. Parmi les compositions étudiées, le PLA-LCR préparé par la stratégie S2 a donné lieu à des cellules de taille plus petite et à une densité cellulaire plus élevée que celles des autres formulations.

Dans la plupart des procédés de mise en forme des polymères tels que l'extrusion et le moulage par injection, les chaînes de polymère sont soumises à des champs d'écoulement complexes (élongation, cisaillement et écoulement mixtes). Le cisaillement du polymère fondu pendant la mise en forme joue un rôle essentiel dans la cristallisation et, par conséquent, a un effet direct sur les propriétés finales du produit obtenu. L'impact de la structure moléculaire ramifiée et du cisaillement sur les cinétiques de cristallisation isotherme induite par le cisaillement ainsi que la morphologie du PLA ont été étudiés dans la deuxième partie de ce travail. Le comportement de cristallisation au repos a été étudié et les résultats ont ensuite été utilisés comme point de référence pour l'étude de la cristallisation induite par le cisaillement. Pour déterminer l'effet de la contrainte de cisaillement, un traitement de pré-cisaillement a été appliqué sur la masse fondue à deux taux de cisaillement constant pour une période de 1, 5 et 10 min. Les résultats ont démontré que le temps d'initiation de la cristallisation diminuait avec l'augmentation de la contrainte de cisaillement totale. En outre, l'impact de la contrainte de cisaillement est plus prononcé lorsque le degré de

ramification et le poids moléculaire sont accrus. Pour évaluer le rôle du taux de cisaillement sur la cristallisation induite, un pré-cisaillement a été appliqué à trois différents taux de cisaillement, tout en gardant la contrainte totale constante. Il a été constaté que le temps d'induction de la cristallisation du PLA linéaire et du PLA-LCR diminue à mesure que le taux de cisaillement augmente et ce, pour la même contrainte de cisaillement totale. La morphologie cristalline du PLA linéaire et à LCR dans des conditions de repos et d'écoulement en cisaillement a été observée. Les photographies ont fourni des informations sur la densité des sphérolites et leur taux de croissance. L'augmentation de la densité des sphérolites a été réalisée dans la masse fondue sous déformation et au repos et ce, dans le cas du PLA linéaire et du PLA à LCR. Une comparaison de la structure cristalline du PLA linéaire avec celle du PLA-LCR a révélé que les ramifications à longues chaînes favorisaient significativement la densité de nucléation, même si elles diminuaient le taux de croissance des cristaux.

Dans l'étape suivante, le moulage par injection de mousse de PLA linéaire et PLA-LCR pour différentes formulations a été réalisé en utilisant un agent de moussage chimique (AMC) dans une machine de moulage par injection conventionnelle. Plusieurs facteurs incluant la teneur en AMC, le degré de ramification ainsi que les paramètres en lien avec le moulage par injection tels que le volume de remplisage (short-shot), la vitesse d'injection, la contre-pression, le temps de refroidissement, ainsi que la température de la buse et du moule ont été variés afin d'optimiser les conditions de formulation et de mise en forme, sélectionnées pour la dernière étape du projet.

Dans la troisième et dernière partie de ce travail, l'impact de la RLC et de l'incorporation de nanoargiles sur le comportement du moussage par injection à basse pression du PLA ont été examinés. Les nanocomposites de PLA linéaire et de PLA-LCR ont été préparés mélange en utilisant une extrudeuse à double vis. Une argile organo-modifiée, Cloisite 30B, à une concentration de 0,25, 0,5 et 1% en poids a été utilisée dans cette étape. Les compositions résultantes ont ensuite été préparées par moulage par injection conventionnel en utilisant un AMC. Le degré de cristallinité, la dispersion de l'argile, la morphologie cellulaire et les propriétés mécaniques ont été étudiés. L'ajout d'argile a augmenté la cristallinité du PLA linéaire tandis que l'effet inverse a été observé pour le PLA-LCR. Les observations et quantifications morphologiques ont révélé qu'une structure cellulaire plus uniforme, plus fine et plus dense a été obtenue dans le cas du PLA-LCR renforcé par les nanoargiles. De plus, il a été constaté que la teneur optimale en argile nécessaire pour obtenir une morphologie uniforme avec une densité cellulaire élevée et une

densité relative de mousse de 0,7 est de 0,5 % en poids, dans le cas du PLA-LCR. Les propriétés mécaniques des échantillons de mousse ont été affectées de manière significative par la structure cellulaire et une amélioration significative de ces propriétés a été observée pour une charge pondérale en argile de 0,5 %.

Enfin, il est important de noter que l'ajout de seulement 0,4 % en poids d'AMC et de 0,5% en poids de nanoargile a conduit à la formation d'une structure cellulaire uniforme avec une densité relative de 0.7, avec une augmentation de 10 fois la densité cellulaire. Les propriétés mécaniques ont également été améliorées lorsque l'AMC et l'argile sont judicieusement ajoutés au PLA.

ABSTRACT

Plastic materials are extensively used in automotive structures since they make cars more energy efficient. Recently, the automotive industry is searching for bio-based and renewable alternatives to petroleum-based plastics to reduce the dependence on fossil fuels. Among polymers originating from renewable sources, polylactide (PLA) has attracted significant interest. The use of this polymer in durable industries is promising.

Fuel-efficient automobiles are nowadays demanded due to the increasing concerns about environmental and fuel issues. The automobile fuel efficiency can be improved by using a lightweight material and, thereby, reducing the automobile weight. A potential method to achieve this objective is the use of the foaming technology. Foam is a material where a gas phase is encapsulated by a solid phase. Foaming technology helps to manufacture lightweight parts with superior properties in comparison with their solid counterparts. The basic mechanisms of foaming process normally consists of gas implementation, formation of uniform polymer-gas solution, cell nucleation, cell growth and, finally, cell stabilization.

PLA foaming has, however, proved to be difficult mainly due to poor rheological properties, small processing window, and slow crystallization kinetics. The ultimate purpose of this work is to reduce by 30 % the weight of polylactide (PLA)-clay based nanocomposites by manufacturing injection-molded foamed parts. To use standard processing equipment, a chemical blowing agent (CBA) was employed. The injection molding technique was utilized in this project because it is the most widely used fabrication process in industry that can produce complex shaped articles. This process, however, is more challenging than other foaming processes since it deals with many additional controlling parameters.

In the first part of this project, we illustrated how long chain branching (LCB) and molecular structure impact the melt rheology, crystallization and batch foaming behavior of PLA. To this end, LCB-PLAs were prepared in the presence of a multifunctional chain extender (CE) using two different processing strategies. In the first strategy, the dried PLA was directly mixed in the molten state with various quantities of CE (the formation of LCB structure). To further examine the impact of CE and molecular topology, a LCB-PLA was also prepared using a second approach, strategy S2. In this approach, a highly branched PLA was first prepared and then mixed with the neat PLA at a weight ratio of 50:50 (the introduction of LCB structure). The steady and transient rheological

properties of the linear and LCB-PLAs revealed that the LCB-PLAs exhibited an increased viscosity, shear sensitivity and longer relaxation time in comparison with the linear PLA. The presence of the LCB structure, moreover, led to a strong strain-hardening behavior in uniaxial elongational flow whereas no strain hardening was observed for the linear PLA. The batch foaming of the samples was conducted using CO_2 at different foaming temperatures ranging from 130 to 155 ^oC. The impact of molecular structure and foaming temperature on the void fraction, cell density, and cell size were examined. It was found that the increased melt strength and elasticity, resulting from branching, strongly affected the cell uniformity, cell density and void fraction. Among the investigated compositions, LCB-PLA prepared by strategy S2 provided smaller cell size and higher cell density than the other compositions.

In most polymer processing operations such as extrusion and injection molding the polymeric chains are subjected to complex flow fields (elongation, shear, and mixed flows). Shearing the molten polymer during processing plays an essential role on crystallization and, thus, on the final properties of the product. The impact of the LCB structure and shear on the isothermal shear-induced crystallization kinetics, and the crystal morphology of PLA were studied in the second part of this work. The quiescent crystallization behavior was investigated and the results were, then, used as the reference point for the study of the shear-induced crystallization. To determine the effect of shear strain, a pre-shear treatment was applied on the melt at two constant shear rates for a period of 1, 5, and 10 min. The onset time of crystallization was decreased with increasing total shear strain. Meanwhile, the impact of shear strain was more pronounced as the degree of LCB and molecular weight increased. To investigate the effect of shear rate on the induced crystallization, pre-shear was applied at three different shear rates while keeping the total strain constant. The induction time of the linear PLA and LCB-PLAs was found to reduce as the shear rate increased, even though the total strain was the same. The crystal morphology of the linear PLA and LCB-PLAs under quiescent and shear flow conditions was observed. These micrographs provided information about the spherulite density and growth rate. An increase in the spherulite density was achieved in the strained melt of both linear and LCB-PLAs, as compared with those of unstrained counterparts. A comparison of the crystal structure of linear PLA with that of LCB-PLA revealed that long chain branching significantly promoted the nucleation density, although it diminished the crystal growth rate.

In the next step, the injection foam molding of the linear PLA and LCB-PLAs with different formulations was performed using a chemical blowing agent (CBA) in a conventional injection molding machine. Several factors including CBA content, degree of LCB, and injection molding processing parameters such as shot size, injection speed, back pressure, cooling time, and nozzle temperature were varied to optimize the formulation and processing conditions. The optimized formulation and processing conditions were selected for the last step of the project.

In the third and last part of this work, the impact of LCB and nanoclay inclusion on the low pressure injection foaming behavior of PLA were examined. The linear PLA and LCB-PLA nanocomposites were prepared via melt compounding using a twin-screw extruder. An organo-modified clay, Cloisite 30B, at concentrations of 0.25, 0.5, and 1 wt% was used in this step. The resulting compositions were then foamed in a conventional injection molding using a CBA. The degree of crystallinity, clay dispersion, cellular morphology and mechanical properties were studied. The addition of clay increased the linear PLA crystallinity while a reverse effect was observed for the LCB-PLA. The morphological observations and quantifications revealed that a more uniform, finer, and denser cellular structure was achieved in the LCB-PLA reinforced by nanoclay. In addition, 0.5 wt % clay was found to be the optimum content for achieving a uniform morphology with high cell density and relative foam density of 0.7 in the LCB-PLA. The mechanical properties of the foamed specimens were significantly influenced by the cellular structure. A significant improvement of the mechanical properties was observed at 0.5 wt% clay loading. Finally, it is worth noting that the addition of just 0.4 wt% CE and 0.5 wt% nanoclay led to the formation of a uniform cellular structure with relative density of 0.7, 10 times increase of the cell density and improved mechanical properties if they are judiciously added to the PLA.

TABLE OF CONTENTS

LIST OF TABLES

LIST OF FIGURES

NOMENCLATURES

English letters

A	Area of the micrographs
a_T	Shift factor
G'	Elastic modulus
G''	Loss modulus
M_w	Molecular weight
R_{cr}	Critical radius
t	Time
T	Temperature
T_0	Reference temperature
t_{in}	Induction time
V_f	Void fraction
We	Weber number
X_c	The degree of crystallinity

Greek Letters

γ	Strain
$\dot{\gamma}$	Shear rate
δ	Loss angle
η	Steady-shear viscosity
η_0	Zero-shear viscosity
η'	Dynamic viscosity
η''	Dynamic rigidity

η^+	Transient viscosity
η_B^+	Transient biaxial elongational viscosity
η_E^+	Transient uniaxial elongational viscosity
η^+ / η	Normalized shear stress growth coefficient
η^*	Complex viscosity
η_r^*	Reduced complex viscosity
θ	Normalized induction time
λ	Relaxation time
ρ_f	Density of foamed sample
ρ_S	Density of unfoamed sample
ω	Frequency

LIST OF SYMBOLS AND ABBREVIATIONS

ADC	Azodicarbonamide
BA	Blowing agents
CBA	Chemical blowing agent
CE	Chain extender
CNT	Classical nucleation theory
DSC	Differential scanning calorimetry
IM	Injection molding
LA	Lactic acid
LCB	Long chain branched
MFR	Melt flow rate
MIM	Microcellular injection molding
MWD	Molecular weight distribution
PBA	Physical blowing agent
PDLA	Poly (D-lactic) acid
PLA	Polylactide
PLLA	Poly (L-lactic) acid
ROP	Ring opening polymerization
SAOS	Small amplitude oscillatory shear
SCF	Supercritical fluid
SEM	Scanning electron microscopy
TEM	Transmission electron microscopy
VER	Volume expansion ratio
XRD	X-ray diffraction

LIST OF APPENDICES

CHAPTER 1

INTRODUCTION

1.1 Introduction

Plastic materials are extensively used in automotive structures for their light weight and high strength. A look at any model of cars indicates that polymers are now used in the exterior and interior parts such as bumpers, doors, safety components, headlight and side view mirror housing, trunk lids, hoods, and wheel covers [1]. Major polymers used in automotive manufacturing are polypropylene (PP), polyurethanes (PU), Nylon (PA), polyvinyl chloride (PVC), acrylonitrile-butadiene-styrene (ABS), polycarbonate (PC), polystyrene (PS), polymethyl methacrylate (PMMA), polybutylene terephthalate (PBT), and polyethylene (PE) [1, 2] among which PP and PU are most used [1]. Recently, the automotive industry searched for bio-based and renewable alternatives to petroleum-based plastics to reduce the dependence on fossil fuels [3, 4]. Among green polymeric materials, polylactide (PLA) has attracted significant interest due to its promising features. Polylactide (PLA) is a rigid thermoplastic polyester with a semi-crystalline or completely amorphous structure, depending on the stereopurity of the polymer backbone [5].

PLA bioplastics are increasingly becoming the material of choice for the automotive sector. Flexural properties, impact strength, long term durability and formability during the molding process are the main performance requirements for automobile interior parts to be considered. The overall mechanical performances of semi-crystalline polymers is remarkably influenced by the microstructure and crystallization [6]. Neat PLA, however, does not possess high enough performances to meet automobile specifications [7]. To enhance the thermo-mechanical properties, different techniques such as copolymerization, blending, and filling can be used [8]. Toyota has used these techniques and developed polypropylene (PP)/PLA blends [4] and PLA/kenaf fiber composites [3] for automotive interior applications such as door trim, roof trim, and spare tire cover skin.

Increasing concerns about environmental and fuel issues motivates the automobile industry to design and manufacture fuel-efficient cars [9]. The automobile fuel efficiency can be improved by using lightweight materials and, consequently, reducing the automobile weight. A potential method

to achieve this objective is the use of the foaming technology. Foaming helps to manufacture lightweight parts with superior properties in comparison with their unfoamed counterparts.

Foam is a material where a gas phase is encapsulated by a solid phase [10]. The morphology of foams can be categorized based on foam density, average cell diameter, cell density and, finally, cell structure [10, 11]. Different discontinuous and continuous foaming technologies have been developed to manufacture thermoplastic foams such as batch foaming, extrusion foaming, and injection foam molding [11-13]. The continuous processing technologies are currently being used for thermoplastic foam manufacturing in industries.

The basic mechanisms of the foaming process, normally, consists of gas implementation, formation of uniform polymer-gas solution, cell nucleation, cell growth and cell stabilization. The gas phase may be physically introduced into the molten polymer, hence called physical blowing agent (PBA), or released from a chemical reaction, called chemical blowing agent (CBA) [11]. Rheological properties of the resin were found to play a significant role at every stage of the foaming process. Melt strength, melt viscosity, particularly extensional viscosity and strain-hardening behavior are rheological factors that significantly impact foaming. The specific methods that have been used to improve the melt strength and strain-hardening properties are the creation of long chain branches (LCB), controlled cross-linking, grafting, blending and introduction of an inorganic filler like nano-particles into the resin [14].

To control the thermal degradation of PLA nanocomposites, three different chain extenders, tris (nonyl-phenyl) phosphite (TNPP), polycarbodiimide (PCDI) and Joncryl were employed in our previous study [15]. The results revealed that chain extension was the mechanism of stabilization. The chain extension resulted in the formation of longer linear chains in the PCDI and TNPP based nanocomposites, and long chain branched (LCB) structure in Joncryl-based nanocomposites. Considering that the produced LCB structure is expected to strongly influence the melt strength and extensional viscosity of the neat PLA, this chain extender was chosen for this investigation.

The introduction of nano-particle to the polymeric matrix yields a so-called nanocomposite material. Depending on the nanoparticle-polymeric matrix interactions, thermodynamic properties and mixing conditions, three broad classes of nanocomposites are obtained: intercalated, flocculated, or exfoliated structure [16]. Clay is a type of commonly used filler in composite manufacturing. Among different clays, Cloisite® 30B has considerable affinity with PLA due to

chemical interactions between the hydroxyl groups of the organo-modifier clay and the carboxyl groups of the PLA [17]. Hence, Cloisite 30B was chosen as the nanofiller for this study.

PLA crystallinity was found to play a significant role in durability and mechanical performances in structural applications [18]. An increase of the overall degree of crystallinity results in an improvement of the chemical resistance, heat deflection temperature, strength and stiffness [6]. The degree and rate of crystallization also markedly affected cell nucleation phenomenon. The nucleated crystals, indeed, act as heterogeneous nucleating sites and accelerate the bubble nucleation. To enhance the crystallization different approaches have been used such as adding nucleants or plasticizers. Nucleants are, generally, used to promote the nucleation density while plasticizers are added to promote the polymer chain mobility [19].

Processing conditions are other factors affecting foaming process. Applied shear rate, injection speed, pressure drop, pressure drop rate, shot size, back pressure, nozzle temperature, melt and mold temperatures are the main parameters that control the morphology of the cellular structure in the injection foam molding process [20].

PLA foaming has proved to be difficult mainly due to poor rheological properties, small processing window and slow crystallization kinetics. Considering that polymer foams with closed-cell structure and relative density (ρ_r) greater than 0.6 are generally used for structural purposes [21], the ultimate purpose of this work is to reduce by 30 % the weight of polylactide (PLA)-clay based nanocomposites by manufacturing injection-molded foamed parts. To use standard processing equipment, a chemical blowing agent (CBA) was employed in this study.

To achieve that goal, the first part of this thesis is dedicated to provide a clear understanding about the impact of long chain branching (LCB) and molecular structure on the melt rheology, and the batch foaming behavior of PLA. Subsequently, the effect of the branched molecular structure and shear flow on the isothermal shear-induced crystallization kinetics and the crystal morphology of PLA are studied. In the next step, the degree of long chain branching, CBA content, and injection molding processing conditions are optimized to fabricate PLA microcellular foams having high cell density, small cell size, and uniform cellular structure. Then, the impact of LCB and nanoclay incorporation on the low pressure injection foaming behavior of PLA are investigated.

1.2 Organization of the thesis

This thesis is based on three articles that have been published or submitted to scientific journals and is organized in 8 chapters:

Chapter 2 provides a critical literature survey of nanocomposites, foams, foaming mechanisms, foaming technologies, material properties and processing conditions affecting foaming, relation between the cellular structure and mechanical properties and PLA foaming. Research objectives and the coherence between the specific objectives and the three articles are described in Chapter 3. The three peer reviewed scientific papers, describing the main achievements of this study, are given in Chapters 4, 5, and 6. Finally, Chapter 7 is dedicated to a general discussion of the main results of this study, while conclusions and recommendations are presented in Chapter 8.

CHAPTER 2 LITERATURE REVIEW

Originally, polymers were synthesized since they offered good mechanical properties, excellent physical and chemical stability to serve as durable materials [1]. Polymeric components are rapidly replacing traditional materials such as metals and metal alloys that have been used in automotive industry [2]. The contribution of plastics to the average weight of vehicle is presented in Figure 2.1. For instance, a 9 % reduction was observed in the use of iron and steel in gross average weight of automotive vehicle since 1980. Plastics comprised 13% of the total average vehicle weight in 1990. This share increased to 14% in 2000 and will further increase to 18% in 2020 [22].

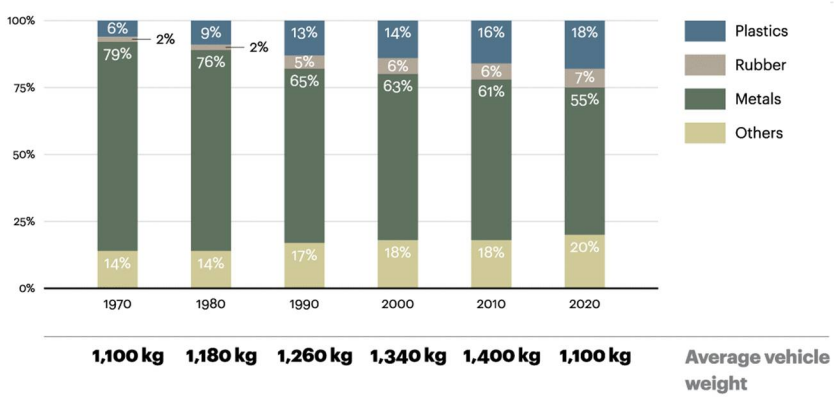

Figure 2.1: The contribution of different materials on total weight of vehicles [22].

The plastic materials are used to make cars more energy efficient by reducing weight, providing durability, corrosion resistance, toughness, design flexibility, and high performance at low cost [1]. Recently, the automotive industry is focusing on the use of bio-based and renewable alternatives to petroleum-based plastics to reduce the dependence on fossil fuels and decrease its ecological footprints.

2.1 Biodegradable and bio-based polymers

Biodegradable polymers are plastic materials that can be broken down and lose their initial integrity [23]. They can be produced from both natural sources such as corn, wood and cellulose and petroleum sources like aliphatic polyester [24]. Biodegradable polymers are globally used in mass-production applications such as packaging, paper coating, fibers, films, and for other disposable

materials [25]. Additionally, biocompatibility of such biopolymers makes them appropriate for biomedical applications such as resorbable surgical sutures, implants, and controlled drug delivery devices [25, 26].

In addition to such versatile and valuable applications, the use of bio-based polymers is becoming more important in durable industries, particularly the automotive industry [27]. Although bio-polymers can be ideally utilized for both exterior and interior components, their applications are, however, currently limited to interior parts due to the material property constraints [28]. The bio-polymer industry is still immature in comparison with the well-established petroleum polymer industry. However, future technology and process improvements could lead to the use of bio-polymers for exterior applications, as well [28]. Figure 2.2 shows the interior parts of a vehicle that can be made from bio-polymers.

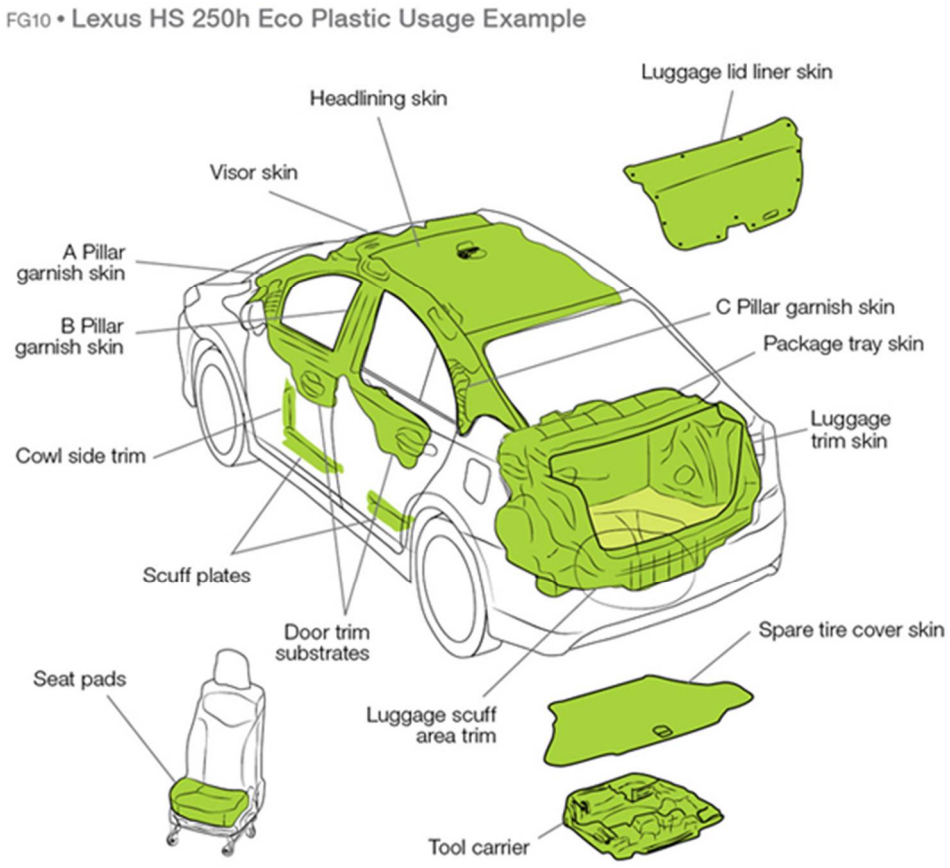

Figure 2.2: The interior parts of a vehicle that can be made from bio-based polymers [4].

Among polymers originating from renewable sources, polylactide (PLA) has recently attracted increasing interest because of its promising features. It is thermoplastic, biocompatible, bioresorbable, biodegradable, while having good processability and transparency after processing [16, 17, 29]. Significant studies have been currently directed to develop polylactide (PLA) as a substitute for commodity plastics such as polypropylene (PP) and polyethylene (PE), and/or as a bio-polyol to produce bio-based polyurethane (PU) foam [28, 30-33].

Polylactic acid/polylactide (PLA)

Polylactic acid and/or polylactide (PLA) is a linear, aliphatic thermoplastic polyester. Depending on the stereopurity of the polymer backbone, it can be semi-crystalline or totally amorphous [5]. Stereochemically, PLAs are categorized into L-lactic acid (PLLA) and D-lactic acid (PDLA), among which the former is the natural and most common form of the acid [34]. PDLA, however, is usually incorporated into PLLA for the sake of optimizing the crystallization kinetics. A synthesized PLA from a monomer feedstock comprising less than 7 % DLA (and more than 93% LLA) will be semi-crystalline, while the degree of crystallinity is enhanced with increasing LLA monomer purity [35].

To synthesize PLA, two different methods, direct polycondensation [36-38] and ring opening polymerization (ROP) [39, 40], were developed which are briefly described in the following section.

Direct polycondensation (DP) polymerization

Direct polycondensation (DP) is an economic approach of PLA polymerization, where the reactive end groups of lactic acid (LA) monomer linked to each other and forms a larger molecule [36-38]. This mechanism is schematically depicted in Figure 2.3. DP polymerization can be conducted in the absence of catalyst, solvent, and initiator to reduce the financial cost [36].

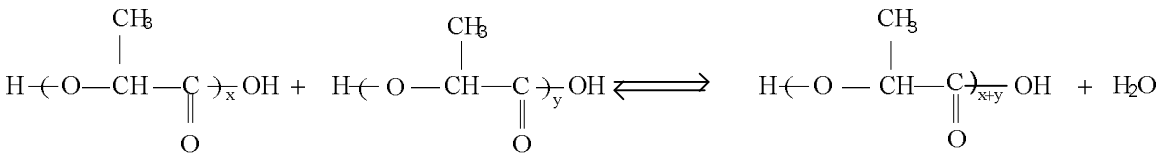

Figure 2.3: Polycondensation polymerization process of polylactic acid [34].

DP process has been accomplished by distilling-out water from 90 percent aqueous solution of lactic acids at high temperatures and a reduced pressure. The reactor temperature is gradually increased to the target point. When water ceases to distill off, the system pressure is continuously decreased, leading to an accelerated distillation of the water from the reactor. Considering that DP is an equilibrium reaction, it is difficult to eliminate water traces, particularly in the last step of polymerization, causing the formation of low molecular weight (M_w) polymer chains [34]. The synthesized polymer using this method is called polylactic acid and possesses *Mw* in the range of 2-10 kg/mol [41].

Ring-Opening Polymerization (ROP)

Ring-opening polymerization (ROP) is a successful method for synthesizing high *M*w PLA (*M*w >100 kg/mol [41]). Since the molecular weight of produced PLA by direct polycondensation is often low, ROP has gained an immense interest. It is a chain-growth polymerization process, where the terminal ends of polymer chains act as a reactive site. In ROP, a cyclic lactide (dimer) is synthesized from lactic acid. The cyclic monomers are, then, linked together by ionic propagation to create longer polymer chains. The treatment of some cyclic compounds with catalyst leads to cleavage of the ring, followed by polymerization to yield oligomers or pre-polymers [34, 42, 43]. The polymerization process of lactide with the aid of a catalyst is shown in Figure 2.4.

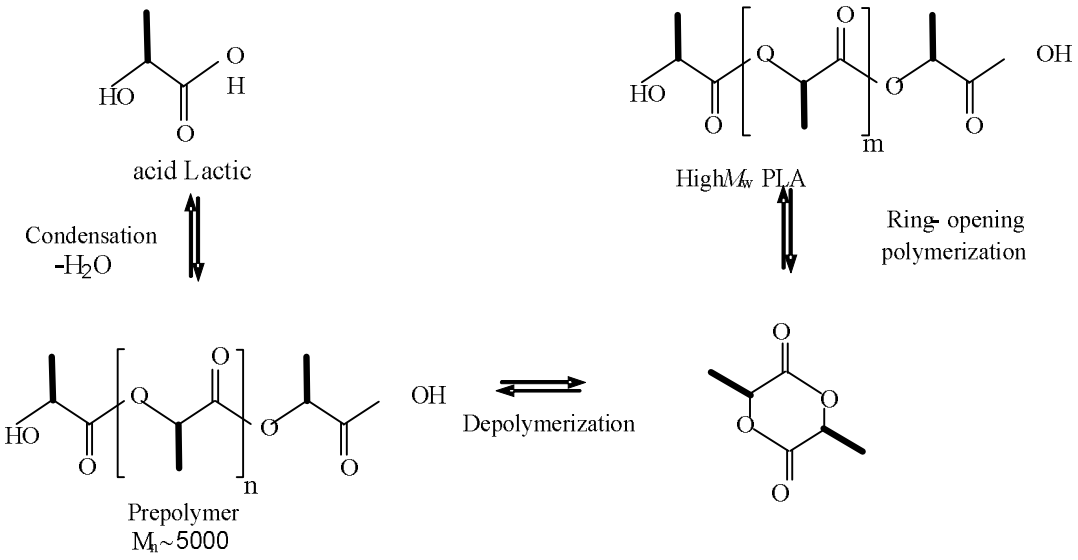

Figure 2.4: PLA production via pre-polymer and lactide [34].

Ring-opening polymerization is conducted in the presence of a catalyst. Different catalyst systems have been so far used for the ROP such as complexes of aluminum, zinc, tin, and lanthanide. Tin compounds, particularly tin (II) bis-2-ethylhexanoic acid (tin-octoate), is usually incorporated for the lactide polymerization since it is soluble in molten lactide. Meanwhile, it has high catalytic activity, low rate of racemization as well as high reaction rate that facilitate the synthesis of a high molecular weight polymer under relatively mild polymerization conditions [34, 43]. The high *Mw* PLA produced using this approach is called polylactide [39, 40].

2.2 Nanocomposites

A nanocomposite is a hybrid material consisting of a polymer matrix filled with a reinforcing component having at least one dimension in the nanometric scale (10^{-9} m) [44]. In spite of the existence of various nano-reinforcements, clay minerals have attracted considerable interest due to their wide availability, low cost as well as low environmental impact. Clay is one of the used filler in composite manufacturing. It is found naturally in a layered silicate structure with nanoscale dimensions thereby providing an increased surface area of about 750 $m^2.g^{-1}$ [8, 45].

Clay

The most commonly used layered silicates in filled-polymer nanocomposites belong to the structural family known as phyllosilicates which is illustrated in Figure 2.5. The crystal lattice is made of two dimensional layers where a central octahedral sheet of either alumina or magnesia is fused to two external tetrahedron silicon atoms so that the oxygen ions of the octahedral sheet do also belong to the tetrahedral sheets.

The layer thickness is around 1 nm while the lateral dimensions may vary from 30 nm to several microns, depending on the particular type of layered silicate. They are organized in stacked layers with a regular van der Waals gap between them, called gallery or interlayer spacing. The alkali or alkaline earth cations are present inside these galleries to counterbalance the generated negative charges arising from isomorphic substitution within the layers (for instance, Al^{3+} replaced by Mg^{2+} or Fe^{2+}) [24, 46].

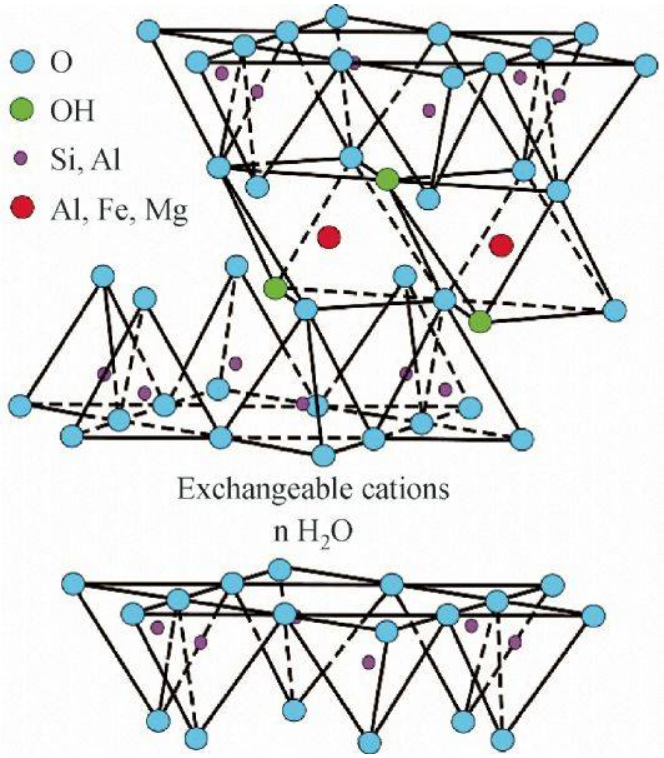

Figure 2.5: Structure of phyllosilicates [46].

Montmorillonite is one of the most commonly used layered silicates and is characterized by a moderate negative surface charge, called cation exchange capacity (CEC) and expressed in meq/100 g. Considering that this charge is not locally constant and varies from layer to layer, an average value over the whole crystal must rather be considered [47].

The hydrophilic nature of montmorillonite limits its compatibility with organophilic polymers and, therefore, the stacked silicate layers of the clay mineral remains intact after the intercalation. To enhance the affinity between these layers and the polymer matrix, the surface chemistry should be modified through ion-exchange reactions with organic and inorganic cations [46]. Nowadays, several organo-modified clays have been commercially produced at a rather low cost that not only impart an affinity to the polymer resin but also yield a larger interlayer spacing [24, 46]. The chemical structure of some organic modifiers used in the clay organophilization procedure are presented in Table 2.1.

Table 2.1: Structural formula and characteristics of some organo-modifiers used in clays (produced by Southern Clay product Co.) [48].

<table>
<tr>
<td colspan="2"> 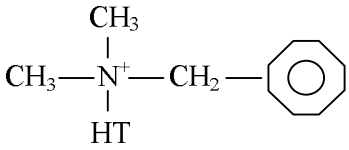
Cloisite 10A</td>
<td colspan="3"> 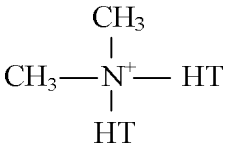
Cloisite 15A, 20A</td>
</tr>
<tr>
<td colspan="2"></td>
<td></td>
<td>15A</td>
<td>20A</td>
</tr>
<tr>
<td>CEC *(meq/100 mg)</td>
<td>125</td>
<td>CEC (meq/100 mg)</td>
<td>125</td>
<td>95</td>
</tr>
<tr>
<td>d-spacing (nm)</td>
<td>1.92</td>
<td>d-spacing (nm)</td>
<td>3.15</td>
<td>2.42</td>
</tr>
<tr>
<td colspan="2"> 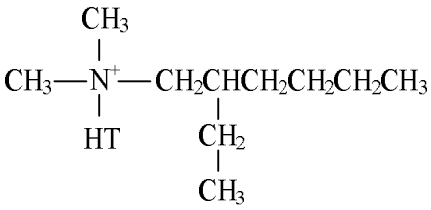
Cloisite 25A</td>
<td colspan="3"> 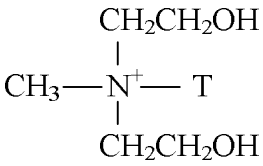
Cloisite 30B</td>
</tr>
<tr>
<td>CEC (meq/100 mg)</td>
<td>95</td>
<td>CEC (meq/100 mg)</td>
<td colspan="2">90</td>
</tr>
<tr>
<td>d-spacing (nm)</td>
<td>1.86</td>
<td>d-spacing (nm)</td>
<td colspan="2">1.85</td>
</tr>
</table>

* Cation exchange capacity

2.2.1 Polymer-clay nanocomposite structures

Depending on the clay-polymeric matrix interaction, thermodynamic properties and mixing conditions, three broad classes of nanocomposites can be achieved [16, 17, 49].

1- Intercalated nanocomposites, where the polymer chains diffuse into the gallery and are sandwiched in between silicate layers. This structure is schematically illustrated in Figure 2.6a. As shown, the galley spacing of the clay is increased while the clay still maintain their overall ordered structure.

2- Flocculated nanocomposites (Figure 2.6b) which conceptually are same as the intercalated nanocomposites. However, the intercalated silicate layers occasionally flocculate because of hydroxylated edge-edge interactions of the silicate layers.

3- Exfoliated nanocomposites (Figure 2.6c), where the individual silicate layers are totally delaminated and homogeneously dispersed and distributed in the polymer matrix.

Figure 2.6: Schematic structure of three broad classes achievable polymer-clay nanocomposites; a) Intercalated, b) Intercalated and flocculated, c) Exfoliated structures [46].

The enthalpic interaction of the clay organic modifier with the polymer chains is an imperative parameter, significantly affecting the dispersion of clay. The large driving force resulting from a high miscibility between the matrix and the modified clay causes further exfoliation of the silicate layers. Among the various clays presented in Table 2.1, Cloisite 30B is more compatible with PLA due to a chemical interaction occurring between the carboxyl groups of PLA and the hydroxyl groups of the organo-modifier [17].

2.2.2 Nanocomposites preparation

Based on the initially used materials and processing techniques, three main methods have been proposed to prepare nanocomposites; *in-situ* intercalative polymerization, solution intercalation, and melt intercalation [24, 46].

In-situ intercalative polymerization

In this method, a liquid monomer or a monomer solution is intercalated into the interlayer space of layered silicates and, subsequently, in-situ polymerized. To initiate the polymerization process, the clay-monomer mixture is exposed to either heat or radiation. An organic initiator or catalyst could be attached to the clay surface through cation exchange before the swelling step. This causes polymerization reaction inside the galleries and further delamination of clay particle platelets [50, 51]. Urbanczyk *et al.* [51] in-situ polymerized PLA/ 35 wt% cloisite 30B in supercritical carbon dioxide medium. The masterbatch was, then, diluted with the commercial PLA by melt compounding to reach a final clay content of 3 wt%. The TEM micrograph of the resulting nanocomposite, presented in Figure 2.7, indicated that an exfoliated structure was achieved using this technique.

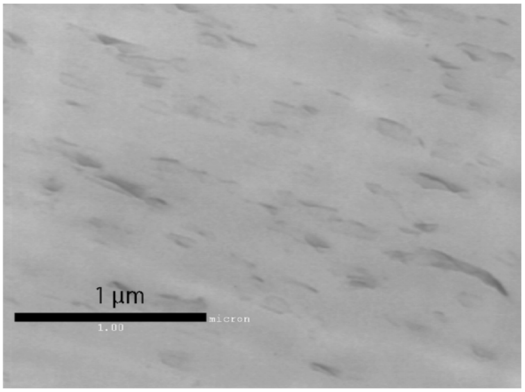

Figure 2.7: TEM images of PLA/3 wt% cloisite 30B obtained using in-situ polymerization technique [51].

Although the in-situ intercalation method is the most efficient technique to obtain an exfoliated structure, it is not the most viable and practical option for the industry [24, 46, 50].

Solution intercalation technique

This method is based on a solvent system in which the polymer is soluble while the silicate layers are swellable. The silicate layers are first swollen in a polar solvent suitable for the matrix. Then, the polymer will be added and mixed until a completely uniform solution is obtained. The dissolved polymer chains diffuse into the interlayer space during mixing. Once the mixing is completed, either the solvent is evaporated or the mixture is precipitated, leading to the formation of an intercalated-type nanocomposite [17, 52]. This technique is usually used to intercalate apolar or slightly polar water-soluble polymers into the silicate layers [24, 46].

The solution intercalation approach was used by Li *et al.* [53] to prepare PLA nanocomposites. They prepared PLA/organo-montmorillonite (OMMT) nanocomposite containing 1, 3, 5 and 7 wt% of clay using dichloromethane as solvent. The TEM results of the nanocomposites are shown in Figure 2.8. They believed that a majority of the OMMT was uniformly dispersed and fully delaminated in the matrix as a low content of clay was loaded. However, more intercalated structure and aggregates were formed at high clay loading.

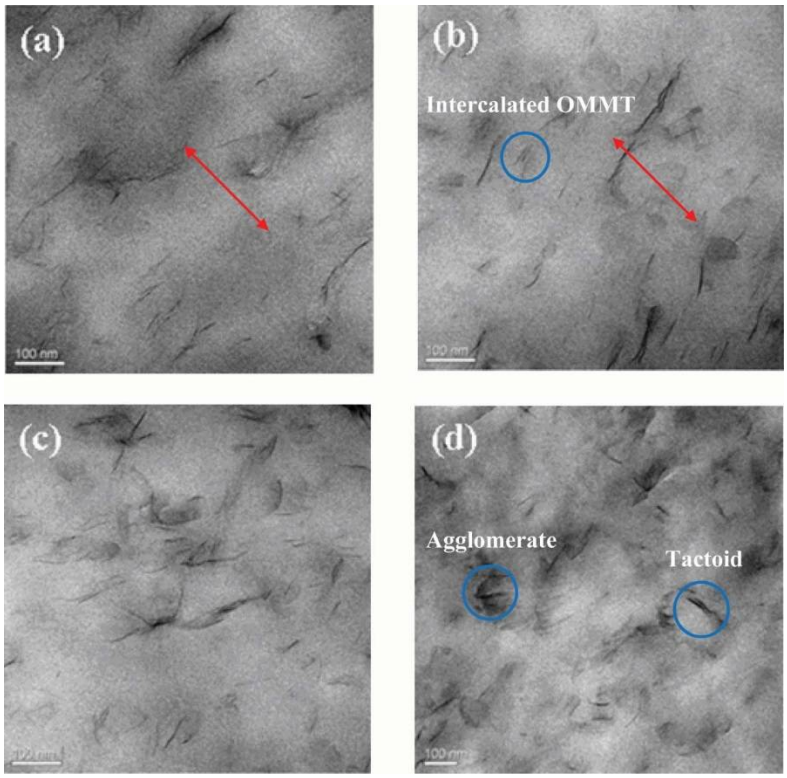

Figure 2.8: TEM of the PLA nanocomposite containing (a) 1 wt%, (b) 3 wt%, (c) 5 wt%, and (d) 7 wt% of organo-montmorillonite [53].

Melt-intercalation technique

The melt intercalation technique is a method that involves annealing a polymer-layered silicates mixture either statically or under shear at a temperature above the polymer melting point. While annealing, the polymer chains may diffuse from the bulk polymer melt into the interlayer gallery of the clay [46]. Nowadays, this technique is more versatile and, environmentally, benign approach and has been used as the most practical method for the preparation of polymer nanocomposites. It has some advantages in comparison with other approaches such as the presence of shear force and the absence of solvent. The applied shearing force during mixing promotes the diffusion of the polymer chains from the bulk to the gallery spacing, resulting in further clay delamination. Furthermore, the absence of solvent and compatibility with current industrial processing techniques make this method environmentally friendly and economical [24].

Depending on the degree of polymer diffusion into the galleries, different types of nanocomposites with structure, ranging from intercalated to exfoliated, can be achieved [49, 54]. The degree of

polymer diffusion is significantly affected by the silicate functionalization and constituent interactions. In addition to processing conditions such as temperature, applied shearing force, and the processing residence time, two other parameters were found to strongly impact the structure of the resulting nanocomposites. These parameters are: an optimal interlayer structure on the organo-modified clay (number of surfactant chains per unit area and their size), and the presence of polar interactions between the silicate layers and the polymeric matrix [24, 46].

Chen *et al.* [49, 54] attempted to achieve an exfoliated structure in PLA-clay nanocomposites through melt compounding by creating a chemical reaction between the polymer matrix and a functional group of the modified clay. They functionalized cloisite 25A with the epoxy group using a silane coupling agent, glycidoxypropyl trimethoxysilane (GPS). TEM micrographs of PLA nanocomposites containing 5 wt% cloisite 25A and modified cloisite 25A are respectively illustrated in Figures 2.9a and b. A large extent of exfoliation was observed for PLA/modified clay nanocomposites as the number of epoxy groups on the clay increased.

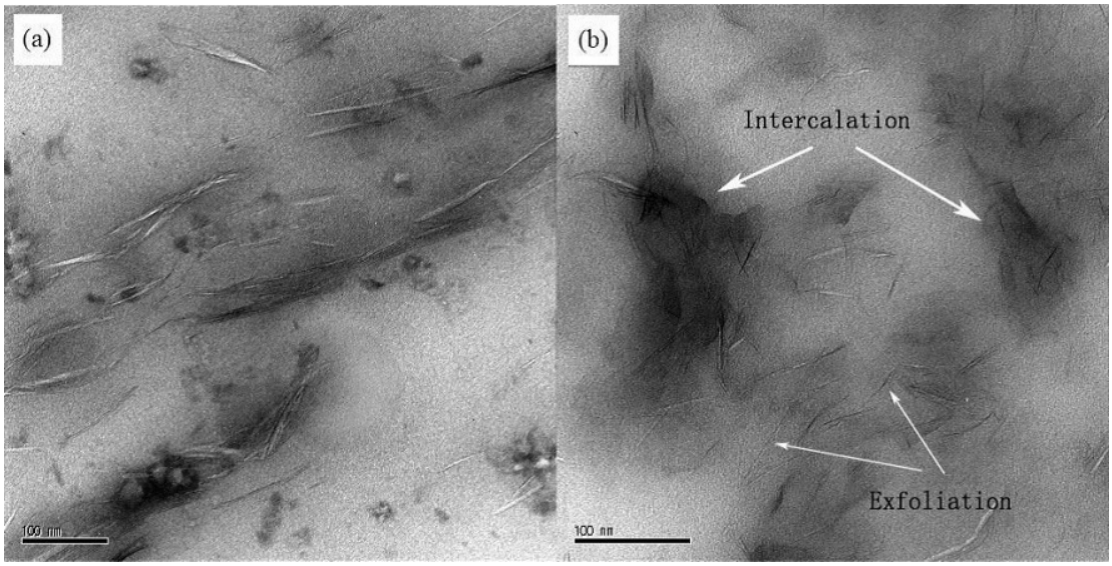

Figure 2.9: TEM images of PLA nanocomposites containing 5 wt% of : (a) cloisite 25A and (b) modified cloisite 25A [54].

Najafi *et al.* [55] investigated the impact of chain extender, Joncryl, and processing conditions on clay dispersion. The TEM results of PLA/2 wt% cloisite 30B with and without chain extender are

shown in Figures 2.10a and b, respectively. They found that the introduction of the chain extender enhanced the degree of clay dispersion provided that it was prepared using a masterbatch approach.

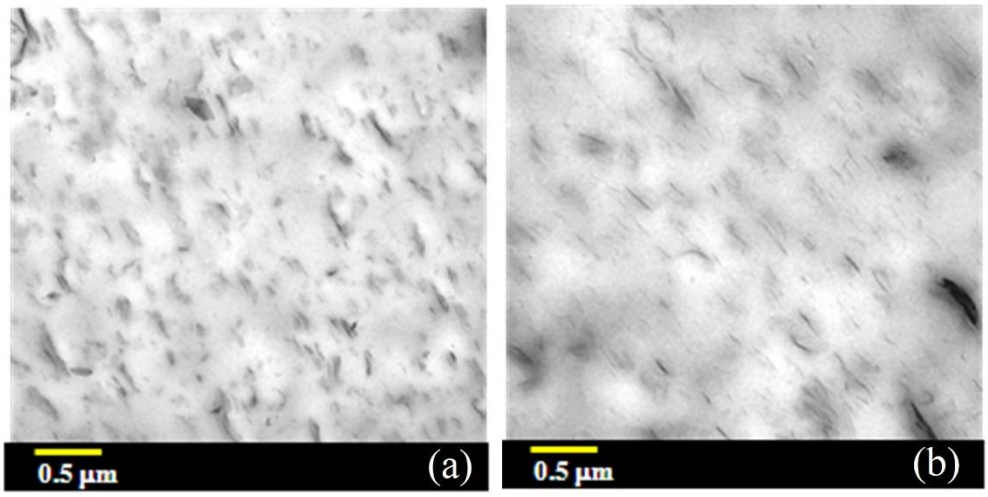

Figure 2.10: TEM images of PLA/2 wt% cloisite 30B nanocomposites containing: (a) 0 wt% and (b) 1 wt% chain extender [55].

2.3 Foams

Foam is a material where a gas phase is encapsulated by a denser liquid or solid phase [10]. The trapping of a gas within a polymer matrix results in forming a porous structure. Considering that the nature of gas and solid is drastically different, its dispersion in a polymeric matrix significantly alters the polymer structure and properties such as thermal insulation properties, dielectric properties, corrosion resistance, and mechanical properties [11]. Foamed materials exhibit outstanding cost-to-performance and favorable strength-to-weight ratio in comparison with the unfoamed counterparts due to a weight reduction [13]. Polymeric foams have been widely used in various applications such as packaging, biomedical, insulation, absorbency, cushioning, construction, and automotive industry [10, 11, 13, 56, 57].

2.3.1 Foam classifications

The morphology of foams can be categorized based on foam density, average cell diameter, cell density and, finally, cell structure [10, 11]. Foam density is generally determined by the volume expansion ratio (VER), indicating the volumetric ratio of the foamed plastic to the unfoamed plastic

material [58]. Accordingly, thermoplastic foams have been categorized in high, medium, low and very low density foams [10, 11]. The relevant VER of each category is presented in Table 2.2.

Table 2.2: Classification of the foamed thermoplastics based on volume expansion ratio (VER) [11].

Foam density	Volume expansion ratio (VER)
High-density foam	VER < 4
Medium-density foam	VER = 4 – 10
Low-density foam	VER = 10 – 40
Very low-density foam	VER > 40

Based on average cell size and cell density, thermoplastic foams can be classified into conventional, fine-cell and microcellular plastic foams [10, 11]. The details of these categories are summarized in Table 2.3.

Table 2.3: Classification of the foamed thermoplastics based on cell size and density [11].

Foam	Average cell diameter (μm)	Cell density (number/cm^3)
Conventional foam	< 300	$<10^6$
Fine-cell foam	10-300	10^6-10^9
Microcellular foam	0.1-10	10^9-10^{15}

Structurally, thermoplastic foams can be divided into two major types: closed-cell foams and open cell foams. In closed-cell structures, the gas phase forms individual cells that are completely separated. However, in open cell foams, adjacent cells are interconnected by pores existing on the cell walls. Among them, closed-cell foams are usually employed as structural materials since they generally have higher mechanical properties in comparison with open-cell foams [10, 11].

2.3.2 Plastic foaming mechanisms

The basic mechanisms of foaming process normally consists of gas implementation, formation of an homogeneous polymer-gas solution, cell nucleation, cell growth, and cell stabilization [12, 59]. The gas phase may be physically introduced into the molten polymer, hence called physical

blowing agent (PBA), or released from a chemical reaction, called chemical blowing agent (CBA) [60, 61]; the details on blowing agents will be described later. To achieve a uniform cellular structure and low density foam, the incorporated gas should be completely dissolved and uniformly dispersed in the matrix. In fact, generating a uniform cell structure would be very difficult if a uniform single phase gas-polymer solution is not obtained before foaming [62]. Cell nucleation results from a thermodynamic instability [59]. Such instability can be induced by either an increment of the processing temperature or a rapid reduction of the processing pressure, leading to diminished solubility of the gas and nucleation of bubbles [59]. Once cells are nucleated, the bubbles keep growing as the blowing agent diffuse into them [61]. Their growth will then continue till they stabilize or rupture [61]. All these steps are schematically illustrated in Figure 2.11 and discussed in the following sections.

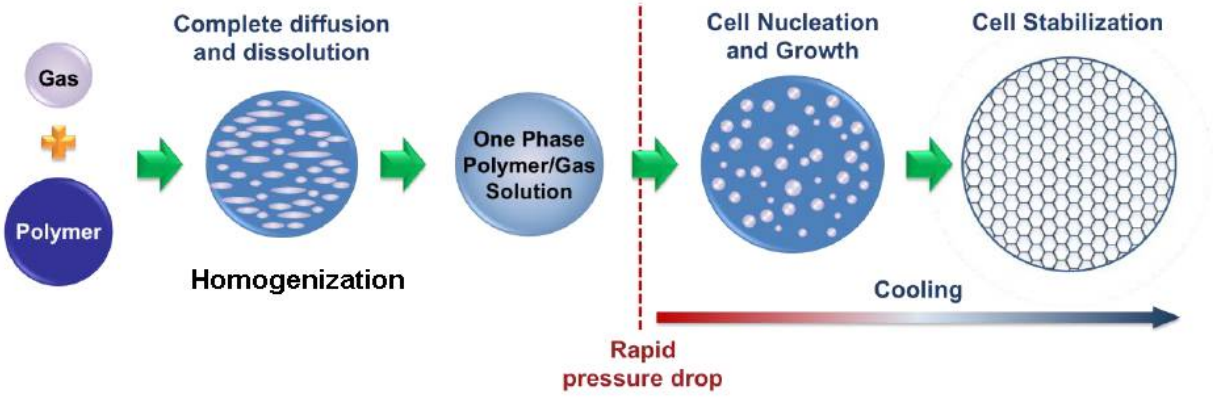

Figure 2.11: Schematic of typical plastic foaming steps [11].

Blowing agent (BA)

Blowing agents (BA) are a vital ingredients used in manufacturing of thermoplastic foams. They are generally divided into two major groups: physical blowing agents (PBA) and chemical blowing agents (CBA) [11, 63]. PBA is material directly injected during the foaming process as either low boiling volatile liquids or gases [11, 14, 63]. Chlorofluorocarbons (CFC) were commonly used as PBAs for foaming in the past. The high solubility, low toxicity, thermal conductivity, non-flammability, good thermal and chemical stability, as well as low cost made CFC excellent

candidates for PBA [64]. However, these compounds diminished the ozone layer in the atmosphere, leading to a significant increase in UV radiation reaching the Earth surface. This radiation is harmful to humans and other biological systems [64, 65]. Consequently, a United Nations agreement, known as the Montreal Protocol, was signed in 1987, banning the use of CFC, as well as other substances that can damage the ozone layer [66]. This protocol has markedly influenced the polymeric foam industry, as it looks for alternative PBA and encounters various technical challenges. Inert gases such as carbon dioxide (CO_2) and nitrogen (N_2) have been recently employed as PBA due to their low cost and minor impact on the environment.

CBA is a class of solid or liquid compounds that generate gases, typically CO_2 or N_2, when they are heated above their decomposition temperature upon processing [11, 14, 63]. CBA can be dry-blended with polymeric resins in solid state, or compounded with molten polymers in an extruder at a temperature below the decomposition temperature before the polymer-CBA blend is fed into the foam processing equipment [11]. To choose an appropriate CBA, there are some requirements that should be met such as adequate decomposition temperature, residue products, rate of gas liberation and rate of gas diffusion [11, 63]. CBA is generally categorized into two major classes; exothermic and endothermic [11, 14]. Exothermic CBA mainly generates gases in the form of N_2 and thermal energy (heat) during their decomposition. However, endothermic CBA liberates CO_2, while consuming thermal energy (heat) upon decomposition [11, 14]. The most common commercial CBAs are listed in Table 2.4.

CBA offers some advantages in comparison with PBA. Contrary to PBA, it can be uniformly distributed into the resin prior to a foaming process, facilitating the dispersion and dissolution of the liberated gas. Furthermore, the existing processing equipments such as extruder and injection molding systems can be directly used, without any modification, to manufacture thermoplastic foams [11, 63].

Table 2.4: Commercially used CBAs and their processing conditions [14].

Grade	Chemical Compound	Endo/Exo	Main evolved gas	Gas evolution (cc/g)	Decomposition temperature (°C)
	Citric acid/Sodium bicarbonate	Endo	CO_2	120	160-210
ADC	Azodicarbonamide	Exo	N_2	220	205-212
OBSH	*p, p'*-Oxybis (benzenesulfonyl hydrazide)	Exo	N_2	125	158-160
TSH	*p*-toluene solfonyl hydrazide	Exo	N_2	115	110-120
TSS	*p*-toluene solfonyl semicarbazide	Exo	N_2	140	228-235

Generation of uniform polymer gas mixture

The injected or generated gas should be completely dissolved into the molten polymer to generate a uniform polymer-gas mixture. This is a vital step in manufacturing a high quality thermoplastic foam with high cell density and uniform cellular structure. The existence of undissolved gas pockets leads to diffusion of the gas molecules into such pockets, undermining the polymer-gas solution capability to generate new cells in the foaming process [11, 67]. Furthermore, the small nucleated cells around them can collapse due to cell coarsening. In fact, the gas tends to diffuse from high pressure (small cells) to low pressure (large gas pockets) environment, causing the formation of non-uniform structure with reduced cell density [11, 67]. This phenomenon significantly impair the mechanical properties of the foamed product. To avoid forming undissolved gas pockets, the processing pressure should be at least equal to the solubility pressure of the BA at the processing temperature. In practice, however, the processing pressure is set significantly higher than the solubility pressure to expedite the dissolution of the gas [11, 67]. The gas diffusion rate is another critical parameter affecting the polymer-gas mixture uniformity. Three main factors impact the diffusion rate in a polymer-gas system: state of the gas, temperature, and shear rate. The gas diffusion rate at higher temperature and super critical state is three to four orders of magnitude higher than that at room temperature [68]. An adequate shearing force should be applied to the melt to create the appropriate bubble striation and, thus, accelerate the gas diffusion rate [68]. Consequently, a good distributive and dispersive mixing technique is required to achieve a uniform single phase polymer-gas system [11].

Cell nucleation

Cell nucleation is the formation of tiny gas bubbles from the liquid phase in polymeric system [63]. It is a thermodynamic process, which is caused by a rapid drop in solubility of the dissolved gas in polymers [10, 11, 69]. As a consequence of sudden solubility reduction and subsequent supersaturation, the polymer-gas system tend to achieve a lower energy and stable state by forming bubbles in the solution [10, 11, 69]. To predict the cell nucleation process, the classical nucleation theory (CNT) and the concept of critical radius (R_{cr}) has been developed based on thermodynamics [70]. According to CNT, the critical radius (R_{cr}) governs bubble growth and collapse [71]. This concept was experimentally verified by Tucker *et al.*[72] in a water-oxygen solution, as well. Bubbles with radius smaller than R_{cr} collapse, while those bubbles having a radius greater that R_{cr} grow, spontaneously [10, 11, 69-72]. The cell nucleation is classified into two categories:

homogeneous and heterogeneous nucleation. In homogeneous nucleation, the cells are generated within a continuous single homogeneous phase having no impurity or dirt. In heterogeneous nucleation, however, particles present in the molten polymer assist in forming cells [10, 11, 69]. The free energy change (ΔF_{hom}) of both mechanisms of nucleation are plotted as a function of bubble radius and shown in Figure 2.12 [11, 63, 71].

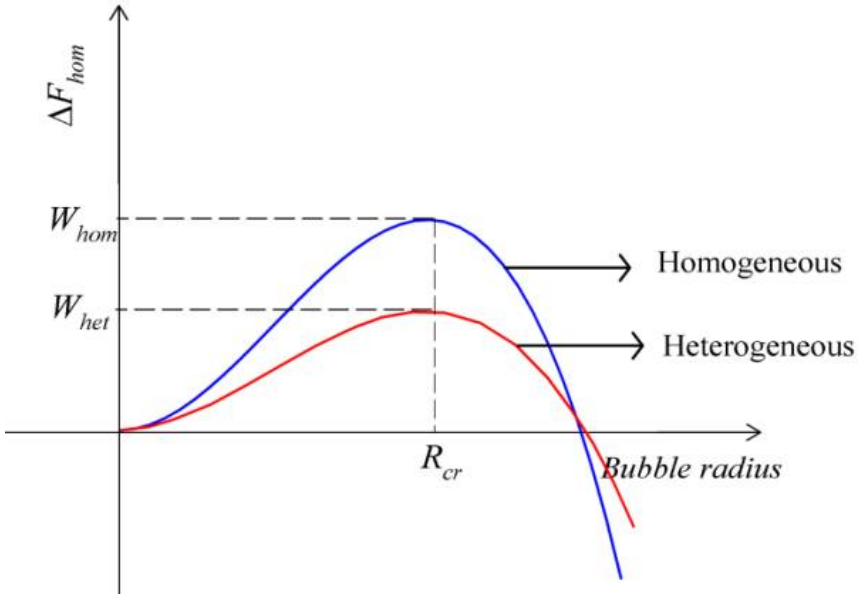

Figure 2.12: Change in free energy of homogeneous and heterogeneous nucleation as a function of bubble radius [63].

As demonstrated, there is a maximum value for ΔF_{hom}, representing the free energy barrier (W_{hom}) for nucleation. The bubble radius at which free energy reaches its maximum is called the critical radius and can be determined from Eq. 2.1 [10, 11, 63].

$$R_{cr} = \frac{2\gamma_{lg}}{P_{bub,cr} - P_{sys}} \qquad \text{Eq. 2.1}$$

where $P_{bub,cr}$, P_{sys} and γ_{lg} are the pressure inside a critical bubble, the system pressure and surface tension of bubble-liquid interface, respectively. Eq. 2.1 illustrates that R_{cr} depends on surface tension and degree of supersaturation [10, 11, 63]. In addition, the pressure drop rate ($-dP_{sys}/dt$) was found to impact the cell nucleation [10, 11]. As the pressure drop rate increases, the system pressure decreases more rapidly while the gas concentration in solution remains high; hence, W_{hom} and R_{cr} further drop, leading to a greater ease for the cell nucleation [10, 11, 63, 71].

For heterogeneous nucleation, Figure 2.8 and Eq. 2.2 indicate the energy barrier is, significantly, suppressed although its R_{cr} is the same as that of homogeneous nucleation. F is called a geometric factor and is a function of the solid-liquid phase contact angle (θ_c). To heterogeneously generate cell nuclei, different procedures have been used such as the incorporation of a nucleation agent into the polymer or crystallization of the polymer prior to the foaming process [10, 11, 35, 56, 73-75].

$$W_{\text{hom}} = \frac{16\,\pi\gamma_{lg}^{3}}{3\left(P_{bub,cr} - P_{sys}\right)^{2}} \qquad W_{het} = W_{\text{hom}} F \;,\quad F = \frac{2 + 3\cos\theta_c - \cos^{3}\theta_c}{4} \qquad \text{Eq. 2.2}$$

In addition to crystallization and nucleating agents, both shear stress and shear rate were found to significantly impact the cell nucleation phenomenon. The cell nucleation is promoted as the shear rate and shear stress increase. Such increment is attributed to the conversion of the mechanical energy from the shear flow to the interfacial energy required for bubble nucleation [11, 76]. The impact of these parameters on foaming will be discussed in details, later.

Cell growth

The bubble growth in the foaming process is generally controlled by bubble pressure and diffusion of the dissolved gas into the cells [77, 78]. At the onset of growth, the pressure inside the nucleated cells (P_{bub}) is quite high due to their small size. A large pressure difference thus exists between the gas and liquid phase causing the cell to grow. Meanwhile, the gradient of the gas concentration across the bubble-liquid interface results in gas diffusion from the melt to the bubble [77, 78]. As cell growth proceeds, the pressure inside the cell (P_{bub}) drops, and the cell growth is only controlled by the gas diffusion. Eventually, the cell growth stops when an equilibrium is established between the gas and liquid phases. Another mechanism governing the cell growth is gas loss [79]. This mechanism causes gas to escape from the polymer-gas solution to the surrounding, leading to reduced bubble growth rate [11, 62]. There are, additionally, a number of undesirable mechanisms, such as cell coalescence and cell coarsening, that may occur during cell growth and deteriorate the cellular structure [63, 67, 79]. Cell coalescence is a mechanism where two growing neighboring cells combine together due to cell wall rupture [11, 80]. To eliminate or decelerate this, the extensional properties of the polymer should be improved [11, 79]. Different methods have been used to enhance the melt strength of the resin such as the introduction of branched structure [61, 81, 82], a decrease of the melt temperature [79], and the incorporation of additives [83-85]. Cell

coarsening is another deterioration mechanism during which the large cells get larger while the small cells shrink [11]. This results from non-uniformity of cell size distribution. The concentration of gas in small cells is higher than that in adjacent large ones. The gas, therefore, tends to migrate from the small cells to adjacent large ones, leading to shrinkage and, eventually, collapse of the small sized cells [86]. This is the reason why the presence of undissolved gas pockets in the polymer-gas mixture significantly impairs the resulting foam cellular structure. This mechanism should, thus, be avoided in order to achieve a uniform cellular structure. It is worth to note that all the above-mentioned mechanisms controlling the cell growth are influenced by the polymer viscosity and elasticity, the foaming temperature, the applied pressure to the matrix, the nature and concentration of the nucleating agent [63, 67, 79].

Cell stabilization

To maintain the resultant cellular structure, the foam should be quickly stabilized [11]. To stabilize the structure, the melt strength of the polymer should be rapidly increased to suppress further changes in cell size [80]. Different methods such as decrease of the processing temperature, and an increase in the degree and rate of crystallization have been used to accelerate the cell stabilization step [14].

2.3.3 Plastic foaming technologies

Different discontinuous and continuous foaming technologies have been developed to manufacture thermoplastic foams such as batch foaming, extrusion foaming, and injection foam molding [11-13]. These technologies are briefly described in this section.

Batch Foaming

Batch foaming was the first developed foaming process that has been massively employed due to its ease of use and setup [13]. The batch foaming process can be classified as temperature-induced and pressure induced foaming [87]. In temperature induced foaming, the polymer is first saturated with the blowing agent at room temperature and an elevated pressure. The sample containing the dissolved gas is, then, submerged in an oil/water bath at the elevated temperature. A sudden drop of the gas solubility, resulting from heating, generates a thermodynamic instability for cell nucleation. The viscosity of the polymer is reduced with increasing temperature and heating; hence,

the cells are nucleated and grown. This procedure has been used by many investigators [87-91] to produce microcellular thermoplastic foams. For example, Di *et al.* [91] conducted the batch foaming process of the plain and chain extended/cross-linked PLA in a high pressure autoclave. The microstructure of the produced foam is presented in Figure 2.13. The higher viscosity and elasticity of the cross-linked PLA helped to produce a PLA foam with smaller cell size (24 μm) and higher cell density ($6.7x10^8$ cells/cm^3) in comparison with PLA (cell size: 230 μm and cell density $7.7x10^5$ cells/cm^3).

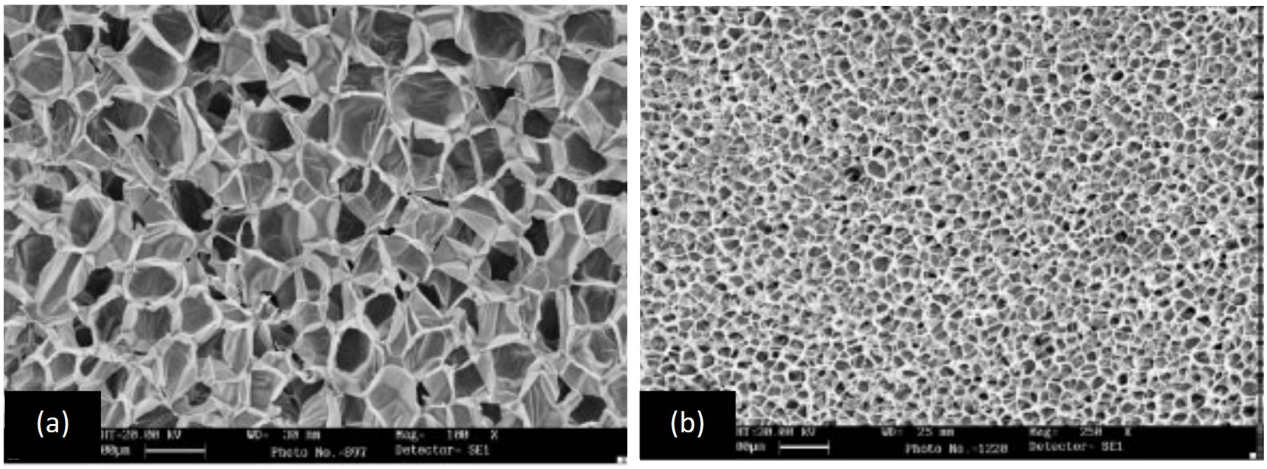

Figure 2.13: SEM micrographs for (a) foamed plain PLA and (b) cross-linked PLA at foaming temperature of 110 ºC [91].

The approach has a disadvantage of being time-consuming. Considering that the gas diffusion rate into the polymer is very low at ambient temperature [92], the saturation step typically takes a very long time (12 to 24 h).

Alternatively, the pressure induced foaming has been developed. In this approach, the thermoplastic resin is placed in a high pressure vessel where it is saturated with a PBA, such as N_2 or CO_2, under a high pressure at an elevated temperature [11, 13]. After the gas dissolution, a rapid depressurization leads to a sudden reduction of gas solubility and, consequently, cell nucleation. Finally, the foamed sample is cooled down to stabilize the resultant cellular structure [11]. An effective cooling strategy is, however, required in this methodology to stabilize the foam after depressurization. Although, this technique has been extensively employed to foam thermoplastic polymers [93-96], its application is vastly limited in industry due to its long production cycle and very low productivity [11, 12].

Extrusion foaming

Extrusion foaming is one of the most commercially important manufacturing processes [22, 24, 41]. In this process, the resin and additives are fed into a heated barrel containing two rotating screws. The materials, then, are melted and mixed, thoroughly. The gas phase, which is injected directly or produced from CBA decomposition, is subsequently introduced into the molten polymer.

The gas phase injection and dispersion make the extrusion foaming a complex process. Recently, Spitael *et al.*[97] designed an extrusion appropriate for foaming process using a twin-screw extruder, which is displayed in Figure 2.14.

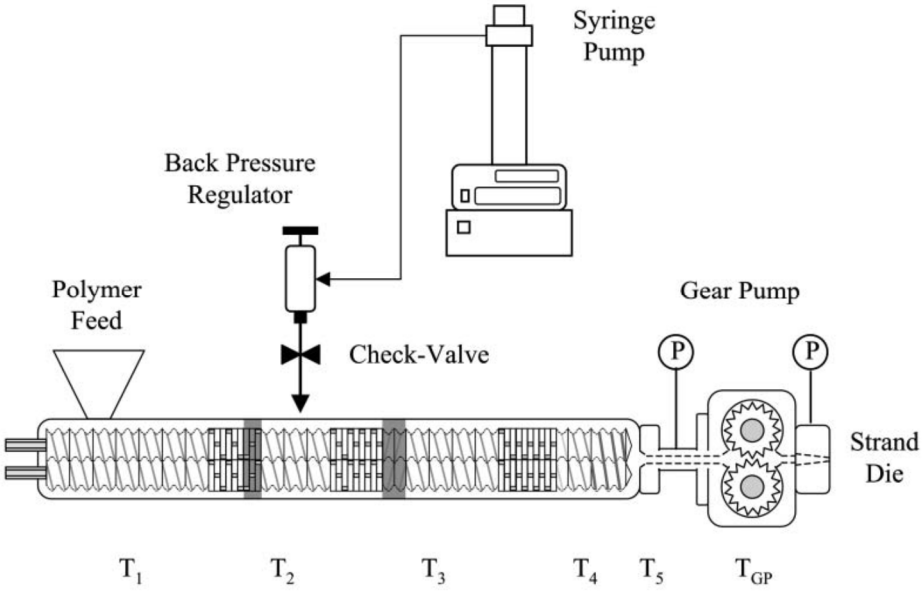

Figure 2.14: Schematic of the twin-screw foam extrusion setup designed by Spatiel *et al.* [97] with reverse flow elements (shaded). These are added to provide a melt seal and maintain a high pressure.

For the sake of minimizing the gas loss, they used a series of reverse kneading elements to create a melt seal before injection of the blowing agent in the barrel. A homogeneous polymer-gas mixture with uniform gas and temperature distribution can be achieved by carefully optimizing the processing conditions. The resultant homogenous mixture is, then, forced through a die. As the pressurized homogeneous mixture emerges from the die, foaming occurs due to a rapid depressurization. The stabilization of the resulting cellular structure is achieved by cooling at

ambient conditions or by immersing in a water bath [22, 24]. Extrusion foaming process has been, successfully, applied to many polymers such as polypropylene (PP) [83, 98], polyethylene (PE) [99, 100], polystyrene (PS) [101, 102], polycarbonate (PC) [103, 104], and polylactide (PLA) [35, 50, 58, 105-108]. The geometry of the foamed products is generally controlled by the shape of the die. The manufactured products, typically, are foamed rods, tubes, and sheets. Therefore, articles having a complex shape cannot be produced using this process.

Recently, the impact of adding an epoxy-based chain extender (Joncryl) to PLA on the PLA foamability was investigated by Julien *et al.* [108]. They varied the chain extender from 0 to 3 wt% to the PLA and foamed the samples in an extruder using a CBA (Hydrocerol CT3108). The foamed structure of the plain PLA and PLA containing 2 wt% chain extender are respectively illustrated in Figures 2.15a and b. The results revealed that, in the best case, the cell size decreased from 106 to 64 μm while the cell density increased from 7×10^5 to 2.7×10^6 cells/cm^3 after the addition of 2 wt% chain extender.

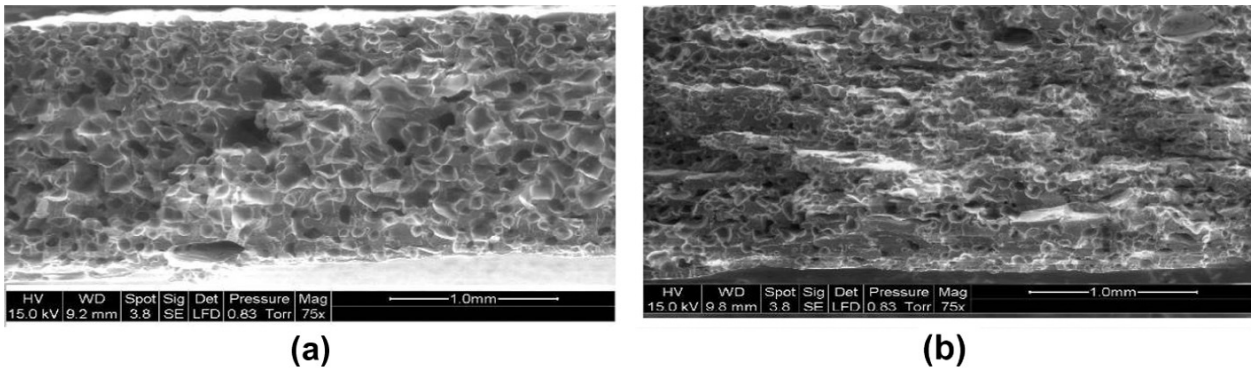

Figure 2.15: Morphological structure of the extrusion foamed (a) neat PLA and (b) chain extender-modified PLA [108].

The geometry of the foamed products extrusion foaming is generally controlled by the shape of the die. The manufactured products, typically, are foamed rods, tubes, and sheets. Therefore, articles having a complex shape cannot be produced using this process.

Injection foam molding

Injection foam molding is one of the most widely used fabrication processes to produce complex parts [13, 20]. This process appears more challenging than other foaming processes since it deals

with many additional controlling parameters such as injection speed, shot size, back pressure, mold temperature, etc. [11, 109]. In the case of injection foam molding using a CBA, a mixture of resin and CBA is fed into the barrel from the hopper and plasticated by the screw. The temperatures of different zones of the barrel are adjusted so that the CBA decomposition occurs, properly. The molten polymer-gas mixture, then, passes through a gate into a mold cavity. Depending on the mold and back pressure, foaming can occur at the gate or in the mold [109, 110]. To minimize the premature foaming, an accumulator can be used to store an appropriate shot size at high pressure. A shut-off valve can be also used in the nozzle to keep the pressure and prevent premature cell nucleation, while maintaining the shot size constant from one cycle to the other. Upon injection into the mold, the nucleated cells grow because of depressurization; hence, the thermoplastic foam expands to fill the mold geometry. The resultant cellular structure is stabilized as its temperature decreased by contact with the cold mold. Finally, the mold is opened and the foamed part is released [109, 110].

Considering that the surface of the molded part is quickly cooled by the mold surface, the produced foam is typically surrounded by an unfoamed skin layer [109, 111, 112]. The resulting foam structure is therefore composed of three layers; two unfoamed layers, called skin and a foamed layer, called core [111, 112]. This composite structure is shown in Figure 2.16 and called structural foam [109, 111, 112].

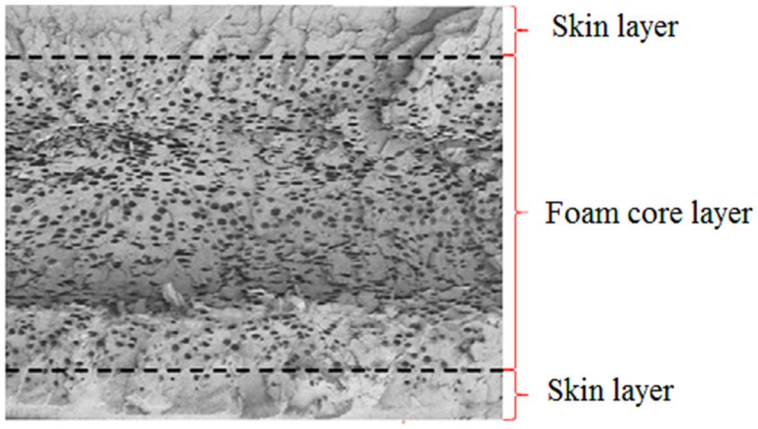

Figure 2.16: A typical cross-sectional view of a polystyrene (PS) structural foam [113].

The skin thickness of structural foams is influenced by different processing parameters such as temperature, pressure and injection speed [111, 112]. In comparison with conventional foams (integral foams), structural foams offers more advantages, mainly better surface quality and higher

mechanical resistance such as impact strength and flexural strength [111, 112]. The injection foam molding of different polymers such as high density polyethylene (HDPE) [111, 112], low density polyethylene (LDPE) [20], polypropylene (PP) [109], and PLA [110, 114] has been reported in the literature. The injection foam molding of PLA reinforced with 1 to 10 wt% needle-like sepiolite nanoclay was, recently, performed using an endothermic chemical blowing agent (Hydrocerol CF 40 E) by Peinado *et al.* [114]. The foam structure of the neat, PLA containing 1, 2, 5 and 10 wt% nanoclay are presented in Figure 2.17. It was found that the cellular morphology became finer and denser as the clay loading increased from 0 to 10 wt%.

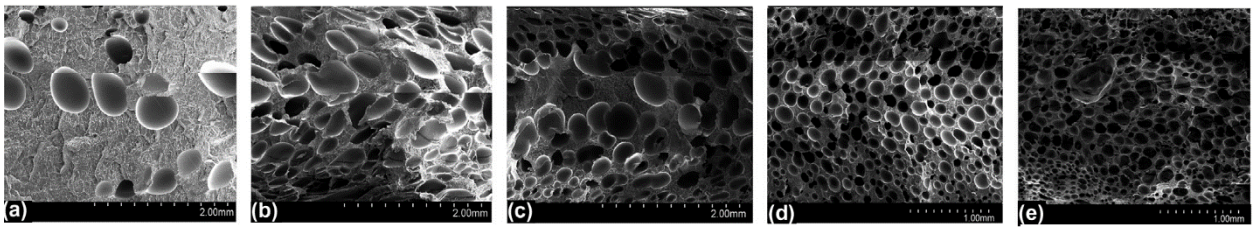

Figure 2.17: SEM micrographs of injection foamed PLA reinforced with (a) 0 wt%, (b) 1 wt%,, (c) 2 wt%,, (d) 5 wt%, and (e) 10 wt% of needle-like sepiolite nanoclay [114].

2.3.4 Material properties affecting foaming

As mentioned in section 2.3.2, thermoplastic foaming involves several key steps, where BA properties, resin properties, the interaction of the BA with resins, and filler incorporation play essential roles. The impact of these parameters is briefly explained in this section.

Solubility of the BA

Gas solubility and diffusivity is an important factor in foaming since they significantly affect the cell nucleation and growth phenomena. The solubility depends on the available free volume in polymeric matrix, and accordingly, temperature and pressure [63]. For instance, the solubility and diffusion coefficient of carbon dioxide (CO_2) and nitrogen (N_2) in PLA melt were reported by Li *et al.* [115] at a temperature of 180 and 200 ◦C as a function of pressure. It was found that the solubility of N_2 and CO_2 significantly increases with increasing the pressure, while the solubility of CO_2 in PLA was 10 times greater (20 %) than that of N_2 (2 %). As the temperature is raised, the free volume of a polymer increases; hence, the gas solubility, for example N_2, increases. However,

in some cases, like CO_2, the solubility significantly decreases with increasing temperature due to interaction between the polymer and gas [14, 115, 116].

In addition to these parameters, the solubility was found to be influenced by molecular structure, degree of cross-linking, degree of crystallinity, the presence of plasticizer, and filler [14]. Features in polymer molecular structure disrupt chain packing, leading to an increment of the free volume. Therefore, branched structures possess an increased solubility in comparison with linear structures [14]. Cross-linking of the polymer chains generally promotes gas solubility since it decreases the degree of densification [14]. The sorption and diffusion of the gas in a semi-crystalline polymer decreases as the degree of crystallization increases. Because the solubility and diffusivity occurs in the amorphous phase, while the crystal phase increases the tortuosity of gas diffusion path [14]. In the case of fillers, however, a reduction in the solubility and diffusivity is observed since they are impermeable [14].

Resin viscoelastic properties

Rheology was found to play a significant role at every stage during the foaming process [14]. Melt strength, melt viscosity, particularly extensional viscosity, and strain-hardening behavior are critical rheological parameters that significantly affect foaming [14, 63]. During the cell growth, the molten polymer is subjected to intense bi-axial elongational deformation and the evolving cell structure can, then, be stabilized by a rapid increase of the melt viscosity. The melt strength is defined as the tensile stress at the point where the extruded material from a die is ruptured [14]. A polymer having inadequate melt strength cannot sustain this deformation and provide a homogeneous cellular structure [63].

The occurrence of strain hardening (SH) in elongational viscosity is quite important, as well. SH is, generally, related to the inability of the macromolecules to disentangle quickly enough to follow the elongational deformation. SH helps to generate uniform and stable cell structure with high VER by preventing cell wall rupture [14, 117]. A typical transient elongational viscosity response, at a given strain rate, is illustrated in Figure 2.18. The critical stages occurring during foaming are also indicated.

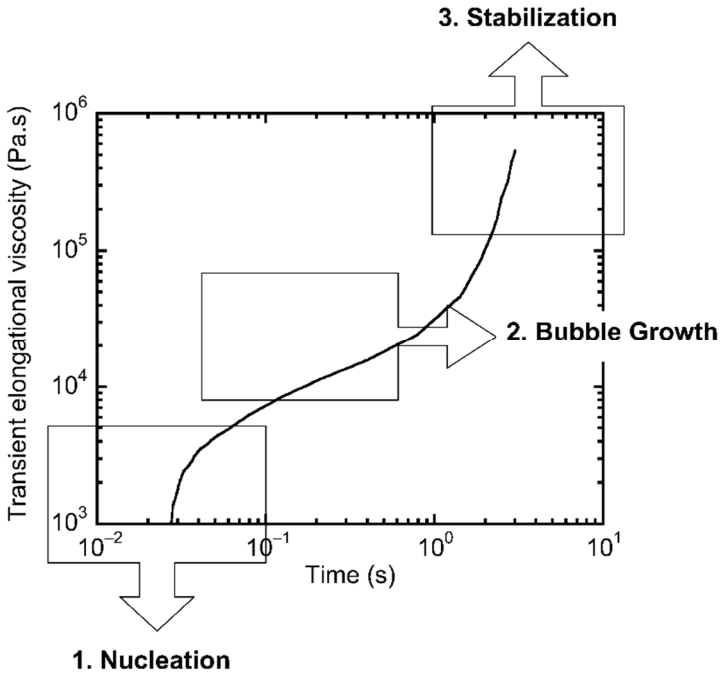

Figure 2.18: A typical transient elongational viscosity behavior; zone 1: initial slope of stress growth function; zone 2: linear viscoelastic behavior; and zone 3: non-linear viscoelastic behavior highlighted by the presence of strain hardening [14].

As shown, the cell growth and stabilization is, respectively, controlled by the steady state viscosity and elongational strain hardening behavior of the polymer. Accordingly, the foaming process of polymers with low melt elasticity and viscosity is characterized by unstable cell growth, nonuniform cell size and cell wall tearing [63]. These polymers usually have low molecular weight (M_w), narrow molecular weight distribution (MWD), low melt viscosity, particularly elongational viscosity, poor shear sensitivity in viscosity and low melt elasticity [63]. To enhance the foamability of rheologically inadequate resins, the melt viscosity, elasticity and SH behavior should be improved by incorporation of an additive or change in M_w and MWD [63]. The specific methods that have been used to improve the foamability are: the addition of long chain branching (LCB), controlled cross-linking, grafting, blending, and introduction of an inorganic filler such as nano-particles into the resin [14, 63, 117]. For example, Nam *et al.* [118] studied the impact of the addition of LCB structure on the rheological properties and foamability of a linear PP. The results are shown in Figure 2.19. They revealed that the degree of a LCB was the most significant factor, affecting the foam density.

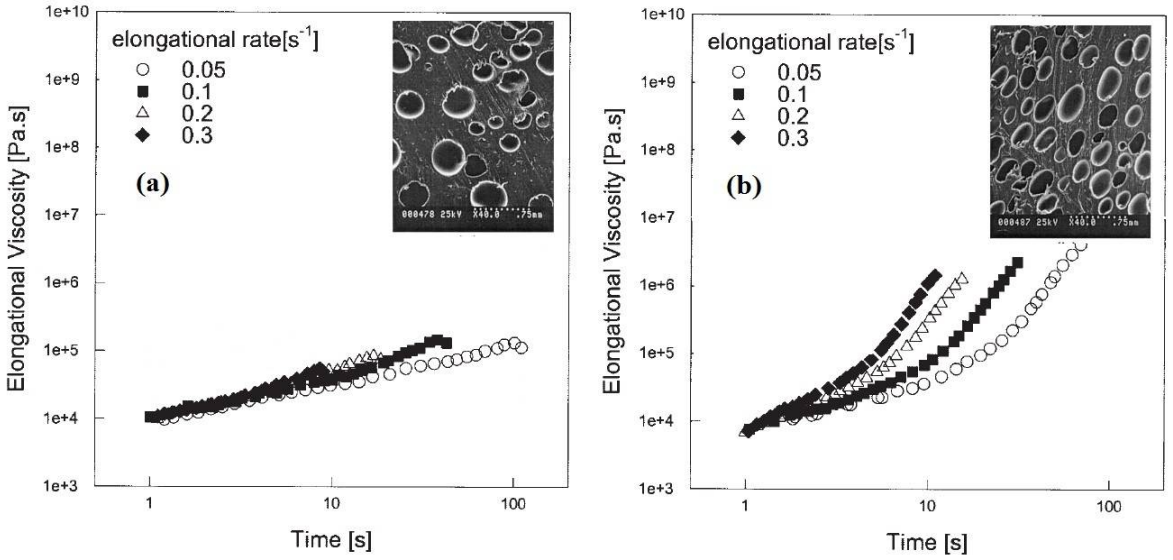

Figure 2.19: Elongational viscosity and SEM morphologies of (a) linear and (b) branched PP with 0.2 phr CBA at 190°C and a screw speed of 40 rpm [118].

Yamaguchi *et al.*[119] found that blending a small amount of a cross-linked linear low density polyethylene (cLLDPE) with linear low density polyethylene (LLDPE), drastically, enhanced the melt elasticity of a linear polymer (Figures 2.20a and b). Meanwhile, it had less or no influence on the steady-state shear viscosity (Figure 2.20c). The increased strain hardening led to the formation of a foam with a uniform cell size distribution.

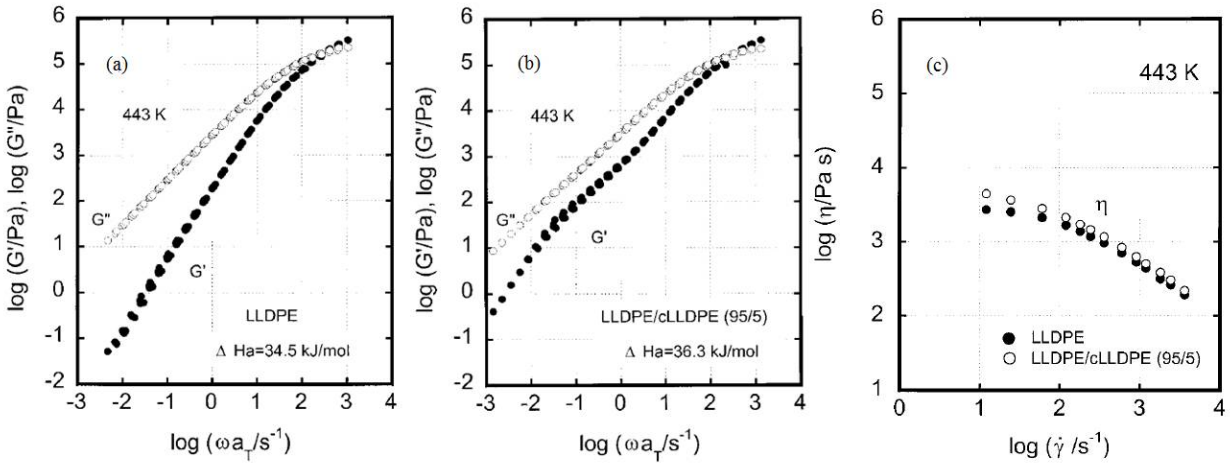

Figure 2.20: Rheological properties of LLDPE/cLLDPE blend: (a) storage and loss modulus of 100/0 LLDPE/cLLDPE, (b) storage and loss modulus of 95/5 LLDPE/cLLDPE and (c) steady state shear viscosity of 100/0 and 95/5 LLDPE/cLLDPE blends [119].

Li *et al.* [120] increased the melt strength of PP by melt grafting with specific unsaturated linear polyester (ULP) branches. Laguna-Gutierrez *et al.* [121] improved the melt strength of linear PP by blending with a high melt strength polypropylene (HMSPP). The linear PP did not exhibit a strain hardening behavior (Figure 2.21a). The absence of SH behavior caused cell rupture during cell growth, leading to an increment of open cell content. A cellular structure with more uniform structure was obtained using HMSPP as a result of strain hardening (Figure 2.21a). The transient extensional viscosity and foamed structure of the PP/HMSPP blend at a weight ratio of 50/50 are shown in Figure 2.21b. The PP/HMSPP blend shows a pronounced SH behavior and more uniform cellular structure in comparison with the linear PP.

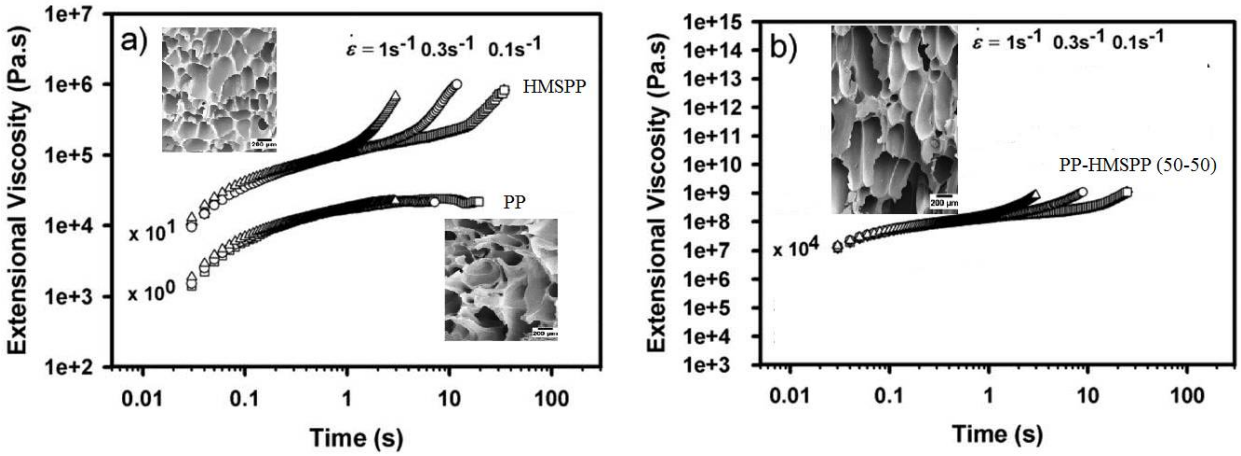

Figure 2.21: Extensional viscosity and SEM morphologies of (a) linear PP and HMSPP (b) PP/HMSPP blend at a weight ratio of 50/50 at 200°C [121].

The melt strength is believed to be significantly improved as additives with a high aspect ratio are incorporated into the resin [63]. Bhattacharya *et al.* [122] indicated that the extended strain hardening effect observed in the clay containing polymer plays an important role in stabilizing foam cell sizes (see Figure 2.22). The additives can, on the other hand, act as nucleating agents and barriers for gas diffusion. As a result, cell nucleation density would be increased while gas loss to the environment would be decelerated [11]. The modified resins, usually, exhibit a strain-hardening behavior that is responsible for the abrupt rise in the transient viscosity response, causing the cell structure to remain stable under elongational flow [14, 63, 117].

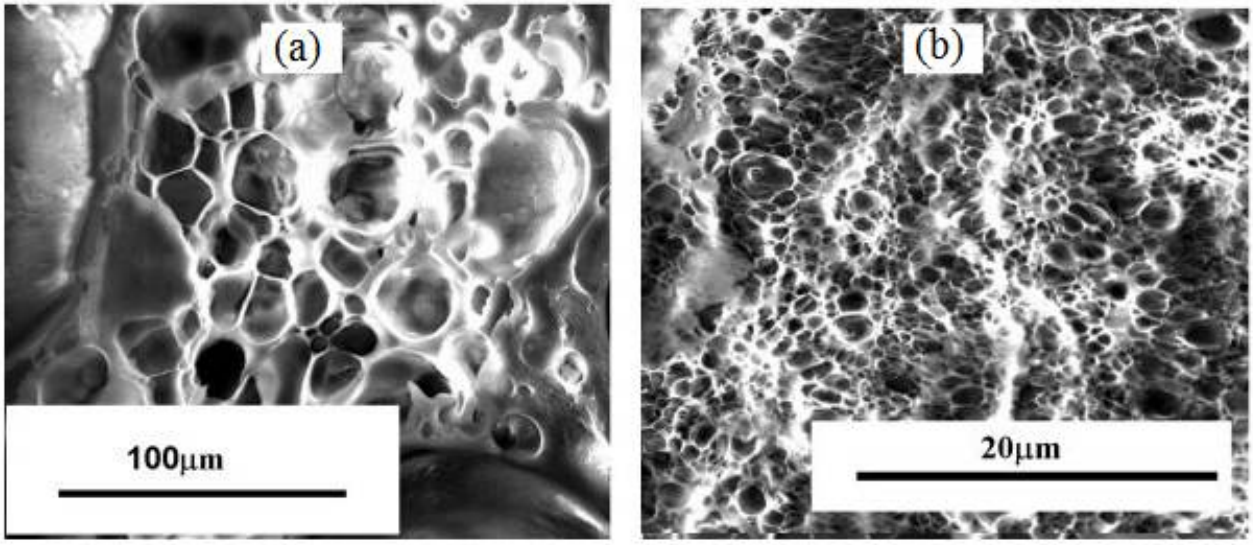

Figure 2.22: SEM micrographs of (a) HMSPP and (b) HMSPP containing 4 wt% clay (C20A) saturated at *T* of 50 °C and *P* of 17.7 MPa. The samples were then foamed at 170 °C [122].

Resin crystallinity

The degree and rate of the crystallization is another factor that significantly impact the cell nucleation density since the nucleation can be promoted at the interface of polymer and hard phase crystals [75, 123, 124]. According to the heterogeneous cell nucleation theory (CNT) [125], the nucleated crystals acted as heterogeneous nucleating sites, similar to fillers, and accelerate the bubble nucleation. This mechanism was demonstrated by Taki *et al.* [75] using in-situ observations of the foaming process of PLA-CO_2 system. An example of their findings is reported in Figure 2.23. They demonstrated that the majority of cells were nucleated around the crystal spherulites. The effect of crystal size on the foaming behavior was investigated by Liao *et al.* [126]. They compared the crystallization kinetics and foaming behavior of linear and LCB-PP and reported that a large density of crystals with small size are favorable for generating high cell density foams.

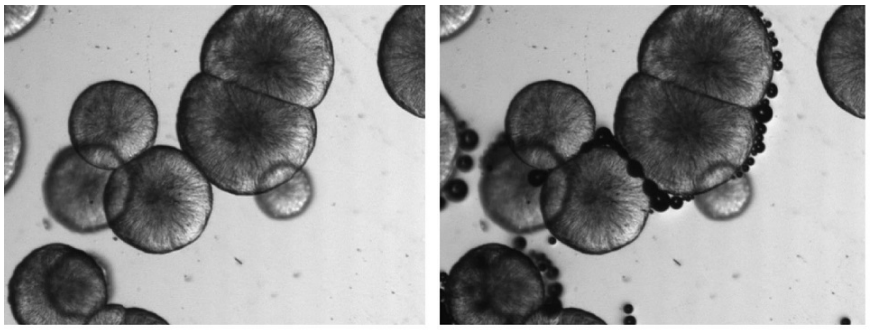

(a) 0 sec (11 MPa) (b) 5.1 sec (7.2 MPa)

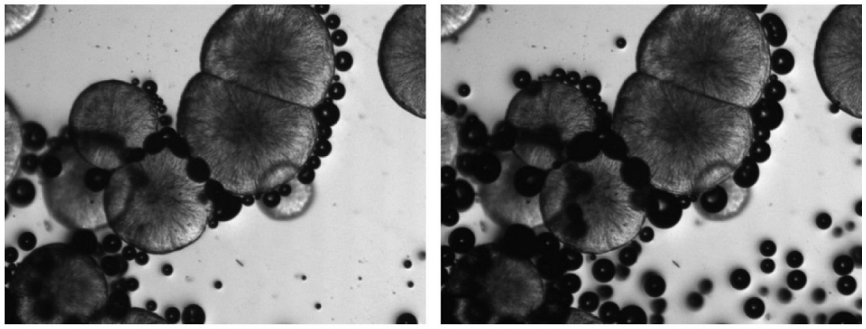

(c) 6.1 sec (6.8 MPa) (d) 7.1 sec (6.5 MPa)

Figure 2.23: Foam visualization of PLLA-CO_2 system under an optical microscope. The saturation temperature and pressure, respectively, were 180 ^oC and 11 MPa, while the foaming temperature was set at 110 ^oC. Cell nucleation at (a) 0, (b) 5.1, (c) 6.1, and (d) 7.1 s after depressurization [75].

On the other hand, crystallinity affects the VER and, consequently, the resultant cellular structure [79]. The melt stiffness of the resin is increased by the presence of crystal domains, leading to suppression of cell coalescence, reducing gas diffusion rate, and decreasing VER [79, 127].

The quality and level of crystallization, i.e. the nucleation density, size and shape of the crystallites, are affected by different factors including molecular weight, molecular structure, thermal history, cooling rate, presence of additives, and melt processing conditions [128]. The overall crystal nucleation and growth rate of PLA was found to be relatively low [19]. To enhance the PLA crystallization different approaches have been used such as adding nucleants or plasticizers [19]. Nucleants, including talc [129] and clay [52], are generally used to promote the nucleation density of PLA, while plasticizers are added to promote the polymer chain mobility.

Shearing the molten polymer during processing, indeed, plays a key role on crystallization kinetics and, therefore, on the final properties of the product [130, 131]. Nevertheless, very little work has been devote to the study of shear-induced crystallization behavior of PLA [132, 133].

2.3.5 Processing conditions affecting foaming

Applied shear rate, melt temperature, die temperature, pressure drop, and pressure drop rate are the main parameters that control the morphology of the cellular structure in extrusion foaming process [58-60, 67, 76]. The impact of shear stress and shear rate on the cell nucleation was investigated by Chen *et al.* [76]. They found that the cell density sharply increases with elevated shear stress and the level of shear rate. To create a cell, the gas nuclei in the polymer should overcome the energy barrier from the surface force. Indeed, the bubble formation process is the transformation of the potential energy of the pressurized gas in the nuclei into the surface energy. If the potential energy of the pressurized gas is not sufficient to overcome the surface force, the nucleated cells collapse.

As the flow is exposed to a shear stress, the nucleated cells are stretched depending on the cell diameter, level of shear rate, surface tension, and the polymer melt viscosity. The stretched cells can expand much easier than unstretched ones due to their non-spherical shape and larger surface area. As a result, some cells with an initial radius less than R_{cr} may grow under shear stress. The applied shear stress also plays a critical role in generating the single phase polymer gas solution [59]. The applied shear force stretches the gas droplets into long and thin forms and breaks them as soon as the critical Weber number is reached [134]. The Weber number indicates the ratio of shear force to surface force and is defined as Eq. 2.3 [135]:

$$We = \frac{\rho_g V^2 d_b}{\sigma} = \frac{\dot{\gamma}\, d_b \eta_p f(\lambda)}{2\sigma} \qquad f(\lambda) = \frac{(19\lambda + 16)}{(16\lambda + 16)} \qquad \lambda = \frac{\eta_g}{\eta_p} \qquad \text{Eq. 2.3}$$

where ρ_g, V, σ, d_b, $\dot{\gamma}$, λ, η_p and η_g is gas density, droplet velocity, surface tension, droplet size, applied shear rate, viscosity ratio of gas to polymer, polymer viscosity and gas viscosity, respectively.

The VER, crystallization behavior, gas solubility and diffusivity are sensitive functions of the melt temperature and die temperature [58, 79]. Pressure drop and pressure drop rate strongly impact the cell nucleation rate and density [12, 58, 67]. The increment of the pressure drop leads to a promoted cell nucleation rate since a greater thermodynamic instability is induced [67]. The impact of pressure drop rate on the cell density and cell size was comprehensively discussed by Park *et al.*

[67]. They reported that there is a competition between cell nucleation and cell growth which is controlled by the pressure drop rate.

It is worth noting that the pressure drop and cell nucleation time are not instantaneous and happen over a finite time period. During the course of the pressure drop, some stable cells are nucleated early. Then, the gas in solution in the polymer melt diffuses to the nucleated cells to decrease the free energy of the system. As a result of gas diffusion, a low gas concentration regions are generated adjacent to the stable nuclei, as depicted in Figure 2.24. New nuclei cannot be formed in the depleted regions since the gas concentration is lower than the critical level. As the pressure further drops, the system would either just expand the existing cells by gas diffusion or nucleating additional cells while expanding the existing cells. The nucleation of new cells are controlled by the depletion regions of the previously nucleated cells. Additional cells will nucleate between the existing cells as long as the depleted regions of the existing cells do not impinge upon each other.

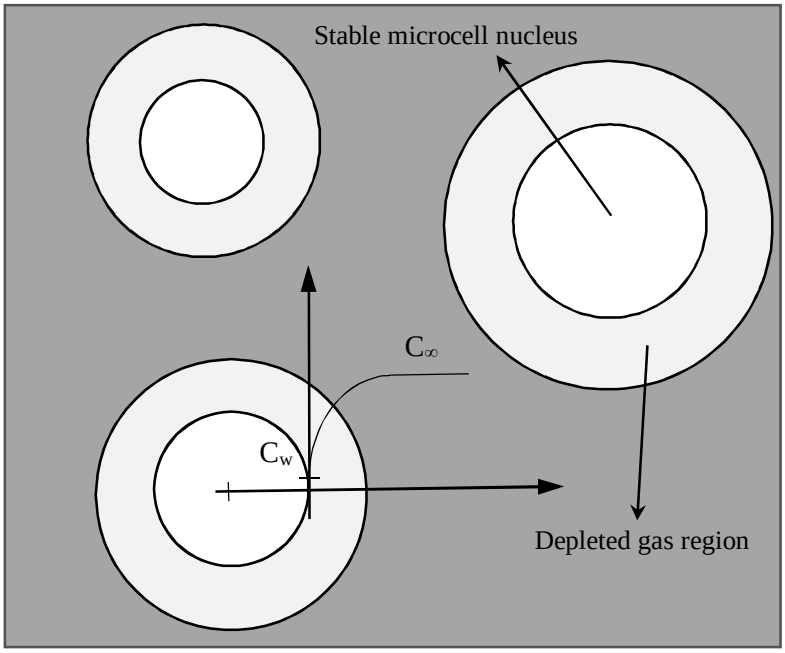

Figure 2.24: Competition between the growth of the existing cells and nucleation of new cells [67].

Based on this explanation, cell nucleation takes place over a longer time as the pressure drop rate decreases. Therefore, the depleted region of the previously nucleated cells has longer time to grow and impinge upon each other, leading to a reduction of additional cell nucleation. In contrast, major

part of the dissolved gas is used for cell nucleation as the pressure drop rate increases [67]. As a result, less gas is available for each nucleated cell to grow, causing a reduction in cell size.

Similar to extrusion foaming, in the batch foaming process, the melt temperature, and applied pressure are found to significantly affect the resulting cellular structure [12, 14].

Injection foam molding, however, has many additional controlling parameters. For this reason, it is more complicated than other foaming processes [20, 109]. To achieve improved mechanical properties, while having acceptable cellular structure, the resultant structural foam should possesses the following characteristics: thin skin layer, small cell size, narrow cell size distribution, high cell density and low foam density [20].

The effect of injection molding conditions were evaluated by Barzegari *et al.* [20] for a low density polyethylene (LDPE) system, by Chandra *et al.* [136] for a polyamide system, and by Guo *et al.* [109] for a polypropylene (PP) system to identify the most important processing variables affecting the morphology of structural foams. The impact of the most important parameters that controls the morphology of the foam in injection foam molding using a CBA is briefly discussed below.

Shear rate: Alike in batch and extrusion foaming, the shear rate affects the melt viscosity, melt elasticity, dissolution and diffusion of the gas into the molten polymer. Figure 2.25 shows the morphology of the injection foamed polystyrene (PS) where mixing of the gas and the resin was performed at two different shear rates of 52 and 161 s^{-1}. Increment of the shear rate accelerates the gas diffusion process and, hence, leads to the formation of a more homogenous polymer-gas solution [20, 134]. As a result, a uniform cellular structure, shown in Figure 2.23b, with an average cell size of 40 μm without voids is generated at high shear rate of 161 s^{-1}.

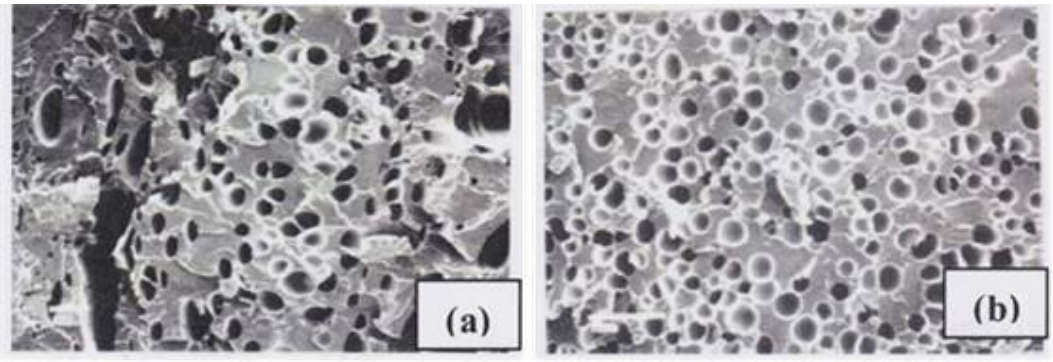

Figure 2.25: Cell structure of injection foamed polystyrene: (a) shearing rate 52 s^{-1} and (b) shearing rate 161 s^{-1} [134].

Shot size: The shot size is defined as the maximum amount of molten polymer injected into the mold in each cycle. Shot size was found to have a profound impact on cell size and cell density [109]. This parameter should be properly optimized in order to achieve small cell size, high cell density, and low foam density. Guo *et al.* [109] extensively investigated the effect of the shot size, ranging from 16 to 24 mm (64 % to 96 % full mold), on the morphology of the cellular structure. The variations of the cell density and cell size as functions of shot size is shown in Figure 2.26. The cell density gradually decreased with increasing the shot size due to suppression of cell nucleation. The dissolved gas in the polymer melt diffused into the fewer nucleated cells, leading to increased cell sizes [109].

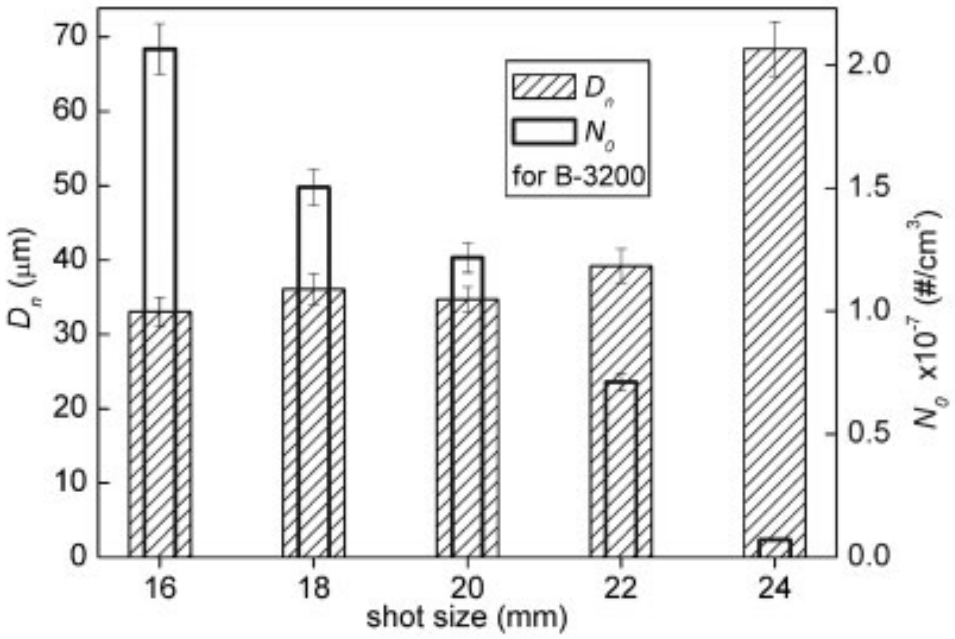

Figure 2.26: Variations of the cell size and cell density of injection foamed branched polypropylene as functions of shot size [109].

CBA concentration: The concentration of the CBA should be also optimized. Increment of the CBA concentration decreases the thickness of the skin layer, due to viscosity reduction resulting from the dissolution of larger gas fraction in the polymer [20]. The impact of CBA concentration on the cell density and cell size is illustrated in Figure 2.27. An increase of the CBA concentration

from 1 to 2 wt% led to an increased cell density from 2.3x 10^7 to 4.6x 10^7 cells/cm^3 and a reduction of cell size from 37 to 31 μm. Guo *et al.* [109] demonstrated that an incorporation of higher concentration of CBA (2.5 wt%), however, significantly impaired the cellular morphology. In fact, a dissolution of a larger fraction of the gas in the resin further reduced the melt viscosity. Therefore, cell coalescence favorably occurred causing a decreased cell density and highly heterogeneous cellular structure [20, 109].

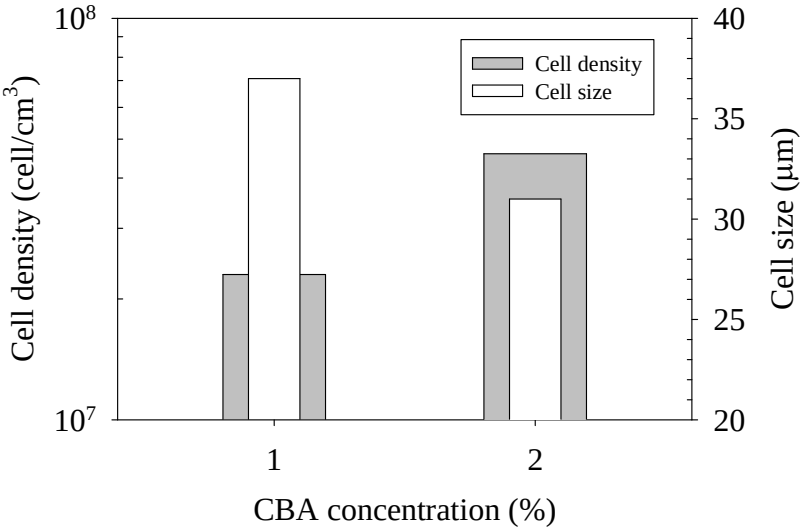

Figure 2.27: Variations of the cell size and cell density of injection foamed branched polypropylene as functions of CBA concentration [109].

Back pressure: It was found that the dissolution of the gas into a molten polymer is facilitated as the applied back pressure during the screw retraction phase increases [109]. Nevertheless, it detrimentally affects the skin thickness, cell size and cell density. Figure 2.28 shows the effect of back pressure on the cell density and cell size. The cell density decreased from 0.7x10^7 to 0.1x10^7 cells/cm^3 as the back pressure increased from 2 to 15 MPa. Due to constant contact of the injection nozzle with the mold during the retraction phase, the back pressure could not be completely released, leading to reduction of pressure drop, pressure drop rate, and consequently, cell density. As a consequence of a reduced cell density, more gas was available for creating cells to grow, causing an increase of the cell size.

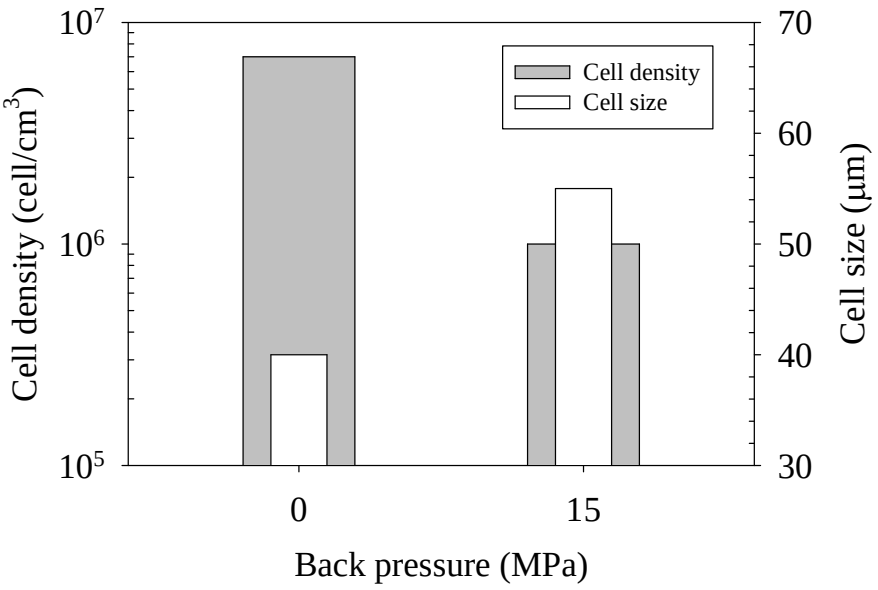

Figure 2.28: Variations of the cell size and cell density of injection foamed branched polypropylene as functions of back pressure [109].

The detrimental impacts of the back pressure on the cellular structure most likely result from the remaining effect of pressure on cell nucleation. To avoid this, the back pressure should consequently be kept as low as possible [20, 68, 109].

Injection speed: Figures 2.29a and b illustrate the morphology of acrylonitrile-butadiene-styrene (ABS) foamed at injection speeds of 13 and 100 mm/s, respectively. The results reveal that injection speed (pressure) has a significant impact on the morphology of the cellular structure. An increase of the injection speed leads to an increased cell density and a decreased cell size. The increased cell nucleation rate results from increasing the pressure drop rate as the injection pressure is raised [20, 109]. An increased injection pressure also decreases the possibility of premature cell nucleation in runners. The cell nucleation, therefore, starts in the mold cavity leading to smaller cell size and more uniform cell size distribution [20, 109]. Moreover, the shear rate applied to the gas-polymer solution increases as the injection speed is increased. As a result, the melt viscosity decreases further causing a reduced skin thickness [20].

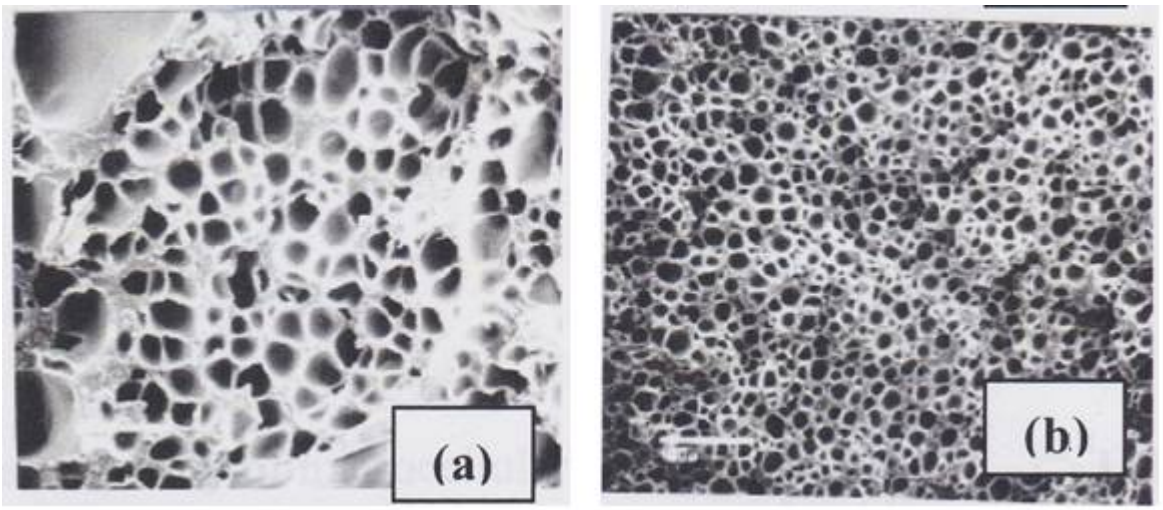

Figure 2.29: Cell structure of injection foamed acrylonitrile-butadiene-styrene (ABS) at injection speeds of: (a) 13 mm/s and (b) 100 mm/s [134].

Melt temperature: Melt temperature significantly affects the viscoelastic properties of the resin, and subsequently, the cellular structure. Increasing the melt temperature decreases the skin thickness since it reduces the melt viscosity [20]. In addition to melt viscosity, the increased melt temperature influences the surface tension, gas diffusion rate, and the gas generation from CBA, and as a result, positively impacts the cell size and cell density [20, 109].

Mold temperature: Temperature gradients between the melt and mold walls significantly affect heat transfer and solidification time. As the mold temperature decreases, heat transfer rate increases due to a higher temperature gradient. As a result, the material near the wall quickly solidifies, leading to formation of a thicker skin layer. Moreover, the melt viscosity increases more rapidly, and hence, cell size decreases since less time is available for cells to grow [20, 109, 111].

2.4 Cellular structure-mechanical properties relationship

In addition to the intrinsic properties of the base materials, the mechanical properties of a cellular structure depend on the microstructure and foam density [21]. As aforementioned, polymeric foams are classified into high, medium, low, and very low density foams. Among them, high density foams, with relative density (ρ_r) greater than 0.6, are generally used for structural purposes [21]. In

the case of tensile and impact properties, mechanical responses are mainly controlled by the relative density, skin thickness, uniformity, and open-cell content [21, 137]. The tensile modulus, tensile and impact strength diminish as the relative density decreases due to material reduction per unit volume [21, 137]. Nevertheless, the specific properties, for instance the specific tensile modulus, specific tensile and impact strength of cellular structures are improved in comparison with unfoamed counterparts [137]. The specific properties are defined as the ratio of the properties and density.

Skin thickness is another crucial factor that impacts the mechanical properties. Tovar-Cisneros *et al.* [112] and Wong *et al.* [137] studied the effect of the skin thickness on the mechanical properties of injection molded high density polyethylene (HDPE) and thermoplastic polyolefin (TPO) structural foam, respectively. It was found that increasing the skin thickness led to an increase of the impact and tensile strength, flexural and tensile modulus [111, 112, 137]. The increased tensile properties can correspond to an increase of the material per unit volume. The impact properties increase since more energy can be absorbed by a thicker skin layer, while it is harder to fracture than the core layer [21, 111, 112].

These mechanical responses are also significantly affected by the presence of open cells. In closed-cell structures, stresses are sustained by cell walls and cell struts. A cell strut is a polymeric domain where three or more cells meet. However, this effect is limited to cell struts as the open-cell content increases, leading to reductions of the mechanical performance [21]. In the case of thermo-mechanical properties, however, the uniformity of the cellular structure also plays a critical role on dynamic mechanical properties [109]. Damping characteristics (tan δ) of foams increase in comparison with that of unfoamed counterparts. To obtain a larger damping function, a uniform cellular structure is highly desirable [109].

2.5 PLA foaming

Recently, foaming of PLA has gained a great interest due to its potential applications in different areas such as biomedical, packaging and durable industries. Several research studies have been devoted to the development of PLA foams. The initial reports on PLA foaming deal mainly with a batch foaming process. For examples Fujimoto *et al.* [138] produced PLA and PLA-clay

nanocomposites foams through a batch foaming process using CO_2 as a PBA. They investigated the impact of different types of clays on the foam structure and found that clay acted as a nucleating agent. Depending on the type and the concentration of added clay, the density of PLA was reduced down to 50%, while the cell size varied from 0.3 to 3 μm. Di *et al.* [91] studied the batch foaming of chain-extended/branched PLA using a mixture of CO_2/N_2 (20/80) as PBA. To produce a chain extended PLA, they used butane diisocyanate (BDI) as a chain extender. Their findings revealed that the cell density of the modified PLA significantly increased (from 7.7×10^5 to 6.7×10^8 cells/cm^3) while its cell size was markedly reduced from 230 to 24 μm depending on the Mw of the chain-extended PLA. The impact of growing crystalline phase on cell nucleation in PLA-CO_2 batch foaming was considered by Taki *et al.* [75]. To this end, they measured the ratio of cells nucleated around the spherulites to the total number of nucleated cells (nc). It was found that nc was strongly dependent on the types of the spherulites formed, their surface area, and accordingly, the foaming temperature. At low foaming temperature (105 °C), most of the cells (90 %) were nucleated around the spherulites; however, this ratio reduced down to 50 % at a foaming temperature of 110 °C.

Several investigations have been published on the extrusion foaming of PLA. The extrusion foaming behavior of commercially available linear amorphous PLA was studied by Lee *et al.* [139] and Reignier *et al.* [140]. They foamed the samples with 9 wt% high pressure CO_2 as a PBA. A highly nonuniform cellular structure with the volume expansion ratio (VER) of 25 was achieved. However, the majority of the developed cells had coalesced, thereby undermining the mechanical properties. The extrusion foaming of PLA-thermoplastic starch (TPS) blends, amorphous and semi-crystalline linear and LCB-PLA was performed using CO_2 as a PBA by Mihai *et al.* [35, 107], Wang *et al.* [141] and Pilla *et al.* [58]. Mihai *et al.* aimed at producing a low density open-cell foam structure. They found that a critical CO_2 level of around 9 and 7 wt% is respectively required for an amorphous and semi-crystalline PLA to achieve low density foams. Below these concentrations, the foams significantly collapsed regardless of the processing temperature. The presence of crystal domains in the semi-crystalline PLA led to an increment of the cell density and a reduction of cell size. The role of branching on the foam structure was evident. An increase of the melt strength, as a result of branching, reduced the cell size from 120 μm to around 40 μm and increased the cell density up to 5 times, depending on the degree of branching [35, 58, 107, 141]. It is noteworthy to highlight that the reaction time and temperature for chain branching was limited in their case since

the chain branching and its foaming were conducted in one-step extrusion process at low processing temperature. The impact of different additives such as talc, nanoclay, and nano-silica on extrusion foaming of PLA was also examined [127, 142]. The findings demonstrated that fillers had an effective role on the PLA crystallization rate, and foamability due to more cell nucleation sites. Nucleated crystals, at the same time, acted as cell nucleation sites, leading to a further increment in the cell density [127, 142].

A tandem-line extrusion system was used by Wang *et al.* [143] to study the foaming behavior of PLA with various degrees of branching in the presence of different nano-particles. The tandem-line extrusion system was consisted of two single screw extruders connected to each other. The first one was designed to generate a uniform polymer-gas mixture while the second one provided an additional mixing and a uniform cooling profile. They achieved low density foams with VER of 40 and average cell size of 50 μm. Zhang *et al.* [94] examined the extrusion foaming behavior of PLA-starch blends using water as a blowing agent and talc as a nucleating agent. A very non-uniform cellular structure with cell size ranging from few microns to 2.5 mm was obtained. Yuan *et al.* [144] investigated the extrusion foaming of PLA-PBAT (polybutylene adipate-co-terephthalate) system using a chemical blowing agent (ADC). They blended PLA with PBAT to increase its melt properties. To improve the compatibility of PLA with PBAT, maleic anhydride (MAH) was added to the system. Their results demonstrated that a more uniform cellular structure with much larger size was achieved in PLA-PBAT blends as compared with the neat PLA. Matuana *et al.* [105] conducted extrusion foaming of PLA with different melt flow indices (MFI) in the presence of an endothermic CBA. The impact of melt viscosity, CBA content and screw speed on the morphology of the resulting foams were investigated. The VER was found to be strongly affected by the melt viscosity. The void fraction and cell density increased with an initial increase of the CBA concentration, reached to a maximum at CBA content of 1.5 wt%, and then dropped with further increase of CBA content. The cell density of the foamed samples was significantly influenced by the screw speed: the cell density was raised one order of magnitude as the screw speed increased from 40 to 120 rpm.

Grimes *et al.*[145] added an acrylic melt enhancer to a PLA matrix and investigated its effect on the foamability of PLA in extrusion using a CBA. They optimized the melt strength enhancer concentration in conjunction with various CBAs to achieve a low density foam with fine cellular

structure. Keshtkar *et al.* [127] considered the impact of nanoclay on the PLA foamability. Samples containing 0 to 5 wt % Cloisite 30B were prepared and foamed in an extruder using 5 and 9 wt% CO_2 as a PBA. The foamed results revealed that the cell density and VER were significantly promoted with increased clay content and the dissolved gas. Liu *et al.* [146] compounded a PLA with a soy protein concentrate (SPC) in the presence of a compatibilizer using a twin-screw extruder. The resulting blends were then extrusion foamed using a CBA. Their results indicated that the compatibilizer, CBA content, and processing temperature were the factors affecting the cell and foam density.

Although injection molding is a promising manufacturing technique; very little work has been, nevertheless, published on injection foam molding of PLA [74, 110, 114, 147-151]. Supercritical nitrogen is generally used as a blowing agent in the foam injection molding since it has a powerful cell nucleating force [152]. High-pressure foam injection molding (i.e., MuCell Technology–microcellular injection molding) has been used in the majority of these studies. In this technique, gas is blended in supercritical state with the polymeric melt, thereby facilitating the generation of homogeneous single phase polymer-gas solution [153]. Furthermore, a vigorous shearing and mixing of the materials under a high melt pressure, significantly, accelerates the gas dissolution in the polymer. The pressure level in high pressure injection molding is approximately 10 times higher than that in a conventional injection molding machine [153]. Pilla *et al.* [74] studied the influence of hyper-branched polyesters (HBP) and nanoclay on controlling the cellular morphology in a microcellular PLA. They used supercritical nitrogen fluid (SCF) as a PBA and foamed the samples in microcellular injection molding (MIM) machine equipped with the MuCell technology. Depending on the concentration of HBP and nanoclay added to PLA, the cell density increased up to 10 times, while the cell size and the weight of microcellular sample reduced down to 4 times and 16 %, respectively. In other studies, they investigated the injection foaming behavior of PLA-multi-walled carbon nanotube (MWCNT) nanocomposites [147] and PLA–flax fiber composites [148]. It was found that the addition of a high aspect ratio filler decreased the cell size, while increasing the cell density. The transmission electron microscopy (TEM) results of the PLA-MWCNT nanocomposites revealed that the degree of the filler dispersion was better in MIM equipped with the MuCell technology as compared with the conventional injection molding. Kramschuster *et al.* [149] studied the foaming behavior of PLA-recycled paper shopping bag fibers in MIM equipped with the MuCell technology. Silane was added to the PLA-fiber compounds as

a coupling agent. It was demonstrated that the fiber inclusion resulted in an increase of the cell density and a reduction of the average cell size. Li *et al.* [150] foamed PLA-PBAT blends containing various contents of nanoclay in MIM equipped with the MuCell technology. The impact of nanoclay inclusion on the cellular morphology as well as the mechanical properties were investigated. The obtained results revealed that most of the clay platelets located at the PLA-PBAT interface, leading to improved interfacial adhesion of the two phases. Furthermore, the addition of clay, significantly, affected the cellular morphology, leading to the formation of a finer and denser cellular structure.

The MIM equipped with the MuCell technology has recently been modified by introducing a mold opening as an additional step [137, 154]. In this technique, the mold cavity is first pressurized and thereafter fully filled with polymer-gas solution. Afterward, the mold is opened in the thickness direction while the mold cavity is depressurized. Recently, Ameli *et al.* [110] used this technique and foamed a PLA and PLA micro/nanocomposites using a PBA. They used talc and nanoclay (Cloisite 30B) as a filler in micro and nanocomposites, respectively. The injection foamed samples obtained using this technique showed a relatively uniform cellular structure with a high void fraction of 65 % and a minimum average cell size of 38 μm.

Low pressure injection foam molding is another technique that has been used to produce foamed products. A few investigations have been conducted to develop foamed PLA using this technique. The injection foam molding of PLA using a combined CBA and PBA (N_2) was performed by Seo *et al.* [151]. The morphology of the foamed structures are shown in Figure 2.30.

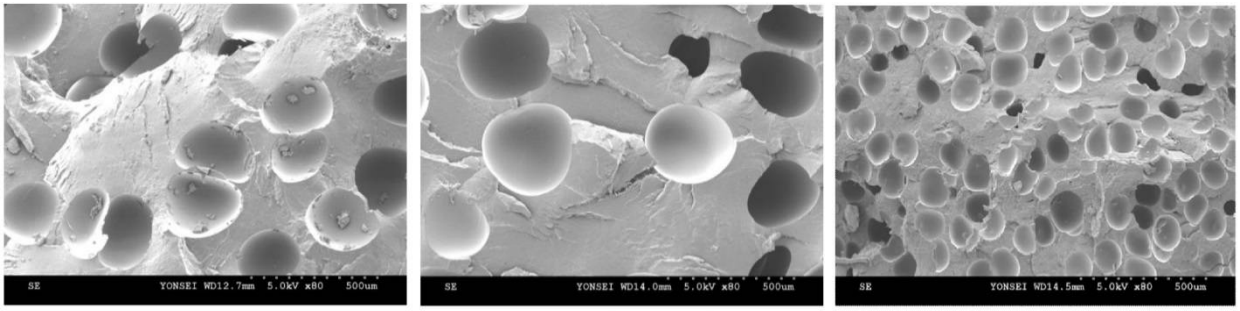

Figure 2.30: Cellular structure of injection foamed PLA using (a) CBA, (b) PBA and (c) a combined CBA and PBA [151].

Based on their findings, the average cell size of the generated foam using CBA and PBA was 100 μm (Figures 2.30a and b). However, as shown in Figure 2.30c, using the CBA and PBA at the same time increased the cell density and reduced the cell size and microcellular weight by a factor of 2 (from 100 to 50 μm), and down to 14%, respectively. Peinado *et al.* [114], recently, foamed PLA reinforced with 1 to 10 wt% needle-like sepiolite nanoclay in low pressure injection foam molding using a 2 wt% CBA. They achieved a relatively uniform cellular structure with a high void fraction of 30 %. Although they did not quantitatively analyze the morphology of the resulting foams, the results clearly showed that the cell density increased particularly after the addition of 5 and 10 wt% nano-filler.

Finally, it is worth to note that not only very few studies have been conducted on PLA foaming using a conventional injection molding; the obtained cellular structures (cell size of 50 μm and cell density of about 10^6 cell/cm^3) are far from the microcellular structure. Therefore, more investigations to optimize the polymer molecular structure and control the injection molding processing conditions are required to achieve a uniform microcellular structure with an average cell size of 10 μm and cell density of 10^9 cell/cm^3 using a conventional injection molding machine.

2.6 Summary

The use of a bio-based polymer, like polylactide (PLA), in durable industries is promising. A key parameter affecting the car fuel efficiency is the weight of automobiles. The weight reduction while maintaining the mechanical performance is one of the challenges in automotive industry. A potential method to accomplish this objective is the use of the foaming technology. This technology leads to manufacturing lightweight automotive parts with superior properties in comparison with their unfoamed counterparts.

In thermoplastic polymers, the main requirements for foamability are the rheological characteristics of the melt, solubility and diffusivity of the BA and the use of adequate processing conditions. The strain-hardening behavior in elongational viscosity is also found to be a fundamental characteristic since it sustains the elongational deformation at the latter stage of cell growth. Generally, PLA foaming has proved to be difficult mainly due to poor rheological properties, small processing window and slow crystallization kinetics. The rheological properties

of the melts are mostly impacted by M_w, MWD, and the presence of short and long chain branching (LCB). To improve the rheological properties, particularly elongational properties, different approaches have been used such as optimizing M_w and MWD, controlled cross-linking, grafting, blending, branching of the macromolecules and introduction of an inorganic filler like nano-particles into the resin.

The crystallinity is another factor significantly affecting the foaming behavior of thermoplastic polymer including PLA. The quality and level of crystallization, i.e. the nucleation density, size and shape of the crystallites, are affected by different factors including molecular weight, molecular structure, thermal history, cooling rate, presence of additives, and melt processing conditions. An increased crystallization kinetics was found to influence the melt stiffness, cell density, and cell size. The formed crystal nuclei, heterogeneously, increases the cell nucleation since they act as a cell nucleating agent, promoting the cell density. As a consequence of increased cell density, less gas is available for cell growth and, thereby, cell size is generally reduced.

The quality and level of crystallization are affected by different factors including molecular weight, molecular structure, thermal history, cooling rate, presence of additives, and melt processing conditions. The overall crystal nucleation and growth rate of PLA was found to be relatively low. To enhance PLA crystallization, different approaches have been used such as adding nucleants or plasticizer. Shearing the molten polymer during processing such as extrusion and injection molding plays a key role on crystallization kinetics, as well. Nevertheless, very little work has been done on the shear-induced crystallization behavior of PLA.

Molecular features are, therefore, of great importance since they directly affect the rheological properties, crystallization and, consequently, foaming behavior. Recently, a few attempts have been devoted to produce long chain branched PLA or increase the degree and rate of PLA crystallization to improve its foamability. However, little attention has been paid to develop a strategy in which these features would be combined and, indeed, produce high melt strength and crystallized PLA appropriate for foaming.

The incorporation of fillers, such as nanoclay, has been reported as another strategy to improve the foamability of thermoplastic polymers in literature. Nevertheless, no investigation has been carried out on the influence of low concentration nanoclay (less than 1 wt%) on the morphological and mechanical properties of PLA structural foams.

The results of many investigations have been published on the extrusion foaming of PLA, PLA blends and nanocomposites with various volume expansion ratios for different applications. However, only a few attempts have been made to manufacture PLA foams using a cost-effective conventional injection molding technique.

CHAPTER 3
RESEARCH OBJECTIVES AND COHERENCE OF ARTICLES

3.1 Project objectives

This study aims at developing lightweight microcellular PLA-clay based nanocomposites with superior properties for automotive applications. To this end, the impacts of the rheological properties, molecular structure and presence of clay on the performance of PLA foams are investigated. The role of molecular features and degree of long chain branching on the viscoelastic properties and cellular morphology of PLA foams is not well understood yet. Hence, further studies are required to better apprehend the impacts of the involved parameters on the high melt strength and crystallized PLA, appropriate for foaming. Moreover, the shear induced crystallization behavior of linear and branched PLAs needs to be clarified.

Although a few attempts have been devoted to develop injection molded foams of PLA, no systematic and extensive studies have been yet carried out on the conventional injection foam molding of PLAs and the technology remains immature. Furthermore, no study has been done to assess the effect of low concentration of nanoclay (less than 1 wt%) on the morphological and mechanical properties of PLA structural foams.

3.1.1 Main objective

The main objective of this project is to reduce by 30 % the weight of polylactide (PLA)-clay based nanocomposites by manufacturing low pressure injection-molded foamed parts using a chemical blowing agent (CBA). Meanwhile, the mechanical properties of the injected foamed parts should remain to a satisfactory level.

3.1.2 Specific objectives

To achieve the main objective of the project the following specific objectives will be pursued:

1- To produce high melt strength and crystallized PLAs appropriate for foaming.
2- To assess how the shear flow impacts the crystallization of linear and LCB-PLAs.

3- To optimize the injection molding processing parameters, chemical blowing agent (CBA) content and the degree of long chain branching (LCB) to fabricate PLA microcellular foams having high void fraction, low density and uniform cell size distribution.
4- To develop injection foamed PLA-clay-based nanocomposites with relative density around 0.7, with small and uniform cell size, as well as acceptable mechanical properties.

While investigating the shear induced crystallization behavior of linear and LCB-PLA systems and optimizing the processing conditions of the conventional injection mold foaming, this study also focuses on the impacts of the rheological properties, long chain branching (LCB), topology of the branched polymers, clay introduction into PLA and its dispersion on the morphology and mechanical properties of the resultant cellular structure of PLAs.

3.2 Article presentation and coherence with research objectives

The main scientific achievements of this research project are presented in the form of three scientific papers in the following three chapters:

Chapter 4 presents the results of the first paper *"Rheological and foaming behavior of polylactide with different molecular structures"* that has been published in *Rheologica Acta* (Vol. 53, 2014, Page 779-790).

Polylactide suffers from low melt strength and elasticity and does not exhibit an increase in resistance to stretching during elongation flows. Considering that the cell walls are exposed to biaxial stretching during cell growth, low viscosity and melt strength may lead to cell coalescence and coarsening and, hence, deterioration of the foam morphology. The first part of this study aims at improving the rheological properties of the PLA by using a chain extender in the scope of obtaining improved PLA foams. In this first article, a chain extender (CE) was added to polylactide (PLA) to improve its melt strength and, consequently, the foamability. The steady and transient rheological properties of a neat PLA and CE-modified PLAs prepared using different strategies were investigated. The introduction of the CE profoundly affected the melt viscosity and elasticity. The linear viscoelastic properties of CE-modified PLAs suggested that a long chain branching structure was formed from the reaction with the CE. The LCB-PLAs exhibited an increased viscosity and more shear sensitivity in comparison with the linear PLA. LCB-PLA exhibited a pronounced strain hardening, whereas no strain hardening was observed for the linear PLA. Batch

foaming of the linear and LCB-PLAs was also examined at various foaming temperatures. The batch foaming process was chosen for this step, because it is the simplest foaming technique to evaluate the impact of material composition and molecular structure on the cell morphology, nearly independent of processing conditions. The architecture of polymer chains was found to significantly affect the cellular structure of the resulting foams.

Chapter 5 presents the second article "*Quiescent and shear-induced crystallization of linear and branched polylactides"* that is now in production for publication in *Rheologica Acta*.
It is well known that the polymeric chains are subjected to complex flow fields in most polymer processing operations such as extrusion, injection molding, fiber spinning, and film blowing. Molten polymers, for example, are subjected to high shear rate for short times as they flow through dies and nozzles. The effect of applied shear on the crystallization kinetics and morphology of semi-crystalline PLA should be fundamentally investigated because crystals have remarkable impact on the cell nucleation and cell growth phenomena in foaming processes. In this chapter, we show how the use of the chain extender and, hence, the presence of long chain branches in PLA, affects the quiescent and shear-induced isothermal crystallization at a temperature of 130 ^{o}C. In quiescent crystallization the presence of the LCB structure was found to accelerate the nucleation process and reduce the induction time, depending on the level of branching. The shear-induced crystallization of the linear and LCB-PLAs was affected by both the total shear strain and shear rate. The crystallization kinetics of the LCB-PLAs was more affected by shear than that of the linear PLA. The crystalline morphology of the linear and LCB-PLAs under quiescent and step shear conditions was also observed. The spherulite density was greater in the strained melt of both linear and LCB-PLAs as compared with those of unstrained counterparts. Moreover, long chain branching significantly promoted the nucleation density although it reduced the crystal growth rate. This knowledge on shear-induced crystallization is useful in the scope of foaming applications.

Chapter 6 presents the third article "*Mechanical and morphological properties of injection molded linear and branched-polylactide (PLA) nanocomposite foams"* that has been submitted to *European Polymer Journal*.
After optimizing the molecular structure in the first part, and fundamentally investigating the effect of imposed shear during processing on the crystallization in the second part, we examined, in the last part of this thesis, injection molding processing conditions to develop foamed PLA

nanocomposites with relative density of 0.7 and uniform cellular structure were examined in the last part of this study. In this step, linear PLA and LCB-PLA nanocomposites were prepared via melt compounding using a twin-screw extruder. An organo-modified clay, Cloisite 30B, at a concentration of 0.25, 0.5, and 1 wt% was used. The resulting compositions were then foamed in a conventional injection molding using a chemical blowing agent (CBA).

Before conducting this investigation, several factors including CBA content, the degree of LCB, and injection molding processing parameters such as shot size, injection speed, back pressure, cooling time, nozzle and mold temperatures were initially varied to optimize the formulation and processing conditions. The detailed results are presented in Appendix E.

The PLA crystallinity, clay dispersion, and the cellular morphology were characterized in this study. The clay inclusion as well as the LCB structure led to a reduction of cell size and foam density, while increasing the cell density. The mechanical properties of the solid and foamed linear and LCB-PLA and their corresponding nanocomposites were also examined by tensile and Izod impact tests. The LCB-PLA nanocomposite with 0.5 wt% clay loading exhibited a uniform fine cellular structure with relative density of 0.7, hence a 30 wt% reduction with respect to its solid counterpart, 10 times increase of the cell density and improved mechanical properties in comparison with other foamed samples.

To summarize the three articles, the first is devoted to manipulate the molecular structure using the chain extender and produce a high melt strength and crystallized PLA. Then, the effect of imposed shear as well as LCB structure, resulting from the addition of the chain extender, on the crystallization kinetics and morphology is investigated in the second article. Based on the previous knowledge acquired, the injection molding processing conditions and nanoclay content are optimized in order to develop foamed PLA nanocomposites with relative density of 0.7 (weight reduction of 30%) and uniform cellular structure in the third article.

.

CHAPTER 4

ARTICLE 1

Rheological and foaming behavior of linear and branched polylactides

N. Najafi[1,2], M. C. Heuzey[1] *, P. J. Carreau[1], D. Therriault[2], C. B. Park[3]

1- Research Center for High Performance Polymer and Composite Systems, CREPEC, Department of Chemical Engineering, Ecole Polytechnique, Montreal, Quebec, Canada

2- Research Center for High Performance Polymer and Composite Systems, CREPEC, Department of Mechanical Engineering, Ecole Polytechnique, Montreal, Quebec, Canada

3- Microcellular Plastics Manufacturing Laboratory, Department of Mechanical and Industrial Engineering, University of Toronto, Toronto, Ontario, Canada

Parts of this work have been presented at the
84th annual meeting of the Society of Rheology (February 2013)
4th international conference on biofoams, BioFoams (August 2013)
86th annual meeting of the Society of Rheology (October 2014)

Published in *Rheologica Acta* (Volume 53, Issue 10-11 (2014), Pages 779-790).

4.1 Abstract

In this work, a chain extender (CE) was added to polylactide (PLA) to improve its foamability. The steady and transient rheological properties of neat PLA and CE-treated PLA revealed that the introduction of the CE profoundly affected the melt viscosity and elasticity. The linear viscoelastic properties of CE-enriched PLA suggested that a long chain branching (LCB) structure was formed from the reaction with the CE. LCB-PLA exhibited an increased viscosity, more shear sensitivity, and longer relaxation time in comparison with the linear PLA. The LCB structure was also found to affect the transient shear stress growth and elongational flow behavior. LCB-PLA exhibited a pronounced strain hardening, whereas no strain hardening was observed for the linear PLA. Batch foaming of the linear and LCB-PLAs was also examined at foaming temperatures of 130, 140, and 155 ^{o}C. The LCB structure significantly increased the integrity of the cells, cell density and void fraction.

Keywords: polylactide, long chain branching, rheological properties, foaming behavior

4.2 Introduction

Biodegradable polymers have been extensively studied in the recent decades due to their remarkable properties (Drumright *et al.* 2000; Eslami and Kamal 2013; Garlotta 2001; Lunt 1998). Among them, polylactic acid or polylactide (PLA) is one of the most promising choices from both economic and environmental perspectives for commodity applications (Drumright *et al.* 2000; Garlotta 2001). Polylactide is a biodegradable, thermoplastic, aliphatic polyester synthesized from renewable resources such as corn, starch, and sugarcane using ring opening polymerization (Drumright *et al.* 2000; Garlotta 2001). PLA is expected to be one of the most competitive and favorable candidates as a substitute to petroleum-based polymers such as polystyrene (PS), polyethylene terephthalate (PET), and polyurethane (PU), which are either non-biodegradable (PS) or non-recyclable (Eslami and Kamal 2013; Garlotta 2001; Wang *et al.* 2012c; Wang *et al.* 2012e). PLA has been increasingly used in biomedical applications such as resorbable surgical sutures, implants, controlled drug delivery devices (Garlotta 2001; Soppimath *et al.* 2001; Theinsathid *et al.* 2009) and mass-production applications such as industrial and food packaging (Drumright *et al.* 2000; Garlotta 2001; Theinsathid *et al.* 2009). In addition to such versatile and valuable applications, the use of bio-based polymers is becoming more common in durable industries,

particularly the automotive industry (So 2012). One of the key factors affecting the fuel consumption of automobiles is their weight, hence a reduction while maintaining the structural performance is one of the main challenges of the automotive industry (Airale *et al.* 2011). A potential approach to accomplish this objective is the use of the foaming technology. A microcellular foam is a polymeric foam with average cell size and cell density of 10 μm and 10^9 cells/cm^3, respectively (Pilla *et al.* 2009; Wang *et al.* 2012a). To achieve thermoplastic foaming, the polymer is first saturated with a gas under pressure and then subjected to thermodynamic instability, leading to a rapid liberation of the gas and, consequently, cell nucleation. The nucleated cells start to grow until they stabilize (Mahmoodi *et al.* 2009; Zhu *et al.* 2006). The thermodynamic instability can be induced by either sudden pressure release or temperature increase (Mahmoodi *et al.* 2009; Zhu *et al.* 2006). The manufacturing of PLA foams has recently drawn great attention since this technique reduces the weight and cost of the final products (Lee and Ramesh 2004; Matuana and Diaz 2013; Pilla *et al.* 2009). However PLA was found to exhibit poor foamability (Matuana and Diaz 2013; Pilla *et al.* 2009; Wang *et al.* 2012e; You *et al.* 2013). The major obstacles in stabilizing the foamed cell structure of PLA are its low melt strength and melt elasticity, slow crystallization rate, and narrow processing window (Eslami and Kamal 2013; Matuana and Diaz 2013; Pilla *et al.* 2009; Wang *et al.* 2012a). Low viscosity and melt strength may lead to cell coalescence and coarsening and, hence, reduction of the cell density (Spitael and Macosko 2004). Crystallinity is another factor profoundly affecting cell nucleation and growth phenomena in PLA foaming (Wang *et al.* 2012b). The crystal phase may induce heterogeneous cell nucleation, resulting in an increased cell density and a reduced cell size (Lee and Ramesh 2004; Matuana and Diaz 2013; Wang *et al.* 2012a; Wang *et al.* 2012b). The melt strength of the resin is also increased by the presence of crystal domains, leading to suppression of cell coalescence, and more uniform cellular structure (Matuana and Diaz 2013; Wang *et al.* 2012a; Wang *et al.* 2012b). Different methods have been so far used to improve the melt strength and, subsequently, foamability of polymers; these include broadening of the molecular weight distribution (MWD) (Minegishi *et al.* 2001), controlled cross-linking (Mitomo *et al.* 2005), blending (Eslami and Kamal 2013), introduction of a filler like nano-particles or wood flour (Matuana and Diaz 2013) and the formation of a long chain branching (LCB) structure (Pilla *et al.* 2009; Spitael and Macosko 2004; Wood-Adams *et al.* 2000). LCB is believed to increase the melt strength and elasticity, leading to an increased ability to form and maintain a good cellular structure (Pilla *et al.* 2009; Spitael and

Macosko 2004). Among the several research studies devoted to PLA foams (Di *et al.* 2005; Fujimoto *et al.* 2003; Mihai *et al.* 2010; Pilla *et al.* 2009; Pilla *et al.* 2010b; Seo *et al.* 2012; Taki *et al.* 2011; Wang *et al.* 2012a), the initial reports deal mainly with batch foaming (Di *et al.* 2005; Fujimoto *et al.* 2003; Taki *et al.* 2011), which is most useful to evaluate the impact of material composition and molecular structure on the cell morphology (Wang *et al.* 2012a). For example, Fujimoto *et al.* (2003) produced PLA and PLA-clay nanocomposite foams through a batch foaming process using CO_2 as a physical blowing agent (PBA). They investigated the impact of different types of clays on the foam structure and found that clay acted as a nucleating agent, decreasing foam density and cell size. Di *et al.* (2005) used butane diisocyanate (BDI) to achieve chain-extended PLAs. They studied the batch foaming of the modified PLAs using a mixture of CO_2/N_2 (20/80) as PBA. Their findings revealed that the cell density significantly increased (around 10 times), while its cell size was markedly reduced from 230 to 24 μm, depending on the molecular weight (M_W) of the chain-extended PLAs. The impact of the growing crystalline phase on cell nucleation in PLA-CO_2 batch foaming was considered by Taki *et al.* (2011). To this end, they measured the ratio of cells nucleated around the spherulites to the total number of nucleated cells (n_c). It was found that n_c was strongly dependent on the type of spherulites formed and their surface area. On the other hand, continuous microcellular processing studies have also been carried out, including extrusion foaming (Mihai *et al.* 2010; Pilla *et al.* 2009; Wang *et al.* 2012a) and foam injection molding (Pilla *et al.* 2010b; Seo *et al.* 2012).The impact of LCB (Mihai *et al.* 2010) and different additives such as talc, nanoclay and nanosilica (Keshtkar *et al.* 2011; Nofar *et al.* 2012) on extrusion foaming of PLA was examined. The findings demonstrated that an increased melt strength reduced the cell size while increasing the cell density. This improvement in continuous foaming processes cannot be only related to the molecular structure since the processing parameters such as applied shear, pressure drop and pressure drop rate would also be changed with the introduction of LCB. The incorporated fillers had an effective role on the PLA crystallization rate and on foamability, due to more cell nucleation sites. Nucleated crystals, conversely, acted as cell nucleation sites, leading to further increment of the cell density (Keshtkar *et al.* 2011; Nofar *et al.* 2012). The impact of hyper-branched polyesters (HBPs) and nanoclay on controlling the cellular morphology of microcellular PLA was investigated by Pilla *et al.* in foam injection molding (Pilla *et al.* 2010b). Depending on the concentration of HBPs and nanoclay added to PLA, they found

that the cell density increased up to 10 times, while the cell size and weight of microcellular samples was reduced by 4 times and 16 %, respectively.

This paper aims at illustrating how LCB and molecular structure impact the melt rheology and batch foaming behavior of PLA. To this end, LCB-PLAs were prepared in the presence of a multifunctional chain extender using two different processing strategies. Then, their rheological properties and foamability were investigated in details and correlated to their molecular architecture.

4.3 Experimental

4.3.1 Materials

The polylactide (PLA) used in this study, PLA 3001D, was purchased from NatureWorks LLC Co. (USA). The selected grade is a semi-crystalline linear polymer with an *L*-lactide to *D*-lactide ratio of 98.5:1.5 (Kramschuster and Turng 2009) and its melt flow rate (MFR) is 22 g/10 min under a load of 2.16 kg at 210 °C (ASTM D1238), as reported by the manufacturer. Joncryl® ADR-4368F, supplied by BASF (Germany), is a modified acrylic copolymer with epoxy functions that was used as a chain extender in this work. Our previous study showed that the incorporation of 1 wt% Joncryl into PLA was found to increase the weight average molecular weight from 95 to 668 kg/mol, while broadening the molecular weight distribution from 1.53 to 2.85 (Najafi *et al.* 2012a).

4.3.2 Material processing

Melt compounding of PLA with chain extender (CE) was performed using a counter-rotating Brabender Plasti-Corder® internal mixer. Before compounding, the PLA was dried at 70 °C in a vacuum oven for 24 h. The dried PLA was then directly mixed in the molten state with 0.4 and 0.7 wt% CE in the internal mixer at a set temperature of 185 °C, a procedure called strategy S1. The mixing was conducted under a nitrogen atmosphere at a rotation speed of 100 rpm for 10 min, after which a relatively steady state torque was established. The neat PLA, as received, was dried and used as a reference in this study. To further examine the impact of CE and molecular topology, a PLA containing 0.4 wt% of CE was prepared using a second approach, strategy S2, in which the PLA was first compounded with 0.8 wt% CE in the internal mixer for 10 min at conditions stated above. The resulting blend was dried in a vacuum oven (70 °C) for 24 h. Then, in the second run,

it was mixed with the neat PLA at a weight ratio of 50:50 using the same operating conditions. The processed materials were placed in a vacuum oven (70 ºC) for 24 h. To determine the uniaxial elongational and shear rheological properties, rectangular sheets of 18×10×1 mm^3 and disk-shaped samples of 25 mm diameter and 1.5 mm thickness, respectively, were prepared by compression molding under a nitrogen atmosphere at 185 ºC and 20 MPa for 8 min, followed by fast cooling to ambient temperature. The prepared samples were stored in a desiccator until use.

For batch foaming, disk-shaped samples of 20 mm diameter and 0.6 mm were prepared and placed in a high pressure vessel hosted in a MCR501 rheometer (Anton Paar, Austria). The samples were first heated up to 180 ºC and held at that temperature for 10 min. The molten polymers were then pressurized with CO_2 at a pressure of 9 MPa at the same temperature for 30 min. While keeping the pressure constant, the processing temperature was reduced to the foaming temperature (T_f), ranging from 130 to155 ºC and held for 90 min. Thereafter, the CO_2 pressure was rapidly reduced to supersaturate the specimen with gas, leading to the formation of foamed cells.

4.3.3 Characterization

Rheological measurements

The prepared disk-shaped samples were used to measure steady and dynamic shear rheological properties. Both steady-state viscosity (η) and small amplitude oscillatory shear (SAOS) data were measured at 180 °C under a nitrogen atmosphere using a MCR-301 rotational rheometer (Anton Paar, Austria) with a parallel flow plate geometry of 25 mm diameter. A 0.95 mm gap was used to measure the steady-state viscosity at various shear rates ($\dot{\gamma}$) ranging from 0.01 to 1 s^{-1}. A 1.1 mm gap was used for the SAOS measurements and the strain amplitude was set at 0.05, large enough to give a reliable signal while keeping the measurement in the linear viscoelastic regime. Time sweep tests were first performed at a frequency of 6.28 rad/s, indicating that maximum variation in dynamic data was less than 8 % over the time frame of the experiments (25 min). The rheological material functions such as complex viscosity (η*), elastic (G') and loss modulus (G'') were measured in the frequency range of 0.628 to 628 rad/s.

Nonlinear transient rheological measurements were also carried out using a strain controlled Rheometric Scientific ARES rheometer (TA Instruments, USA). Stress growth experiments were

conducted in a parallel plate geometry with a diameter of 25 mm and a gap of 1.1 mm under a nitrogen atmosphere at 180 °C and a range of shear rates ($\dot{\gamma}$) = 0.1, 1, and 2 s^{-1}). For each test, a fresh sample was used and preheated 10 min at the set temperature. Finally, the prepared rectangular sheet samples were used to measure the uniaxial elongational viscosity. This measurement was carried out using the ARES rheometer equipped with a SER universal testing platform (Xpansion Instruments, USA). Measurements were performed under a nitrogen atmosphere over a range of Hencky strain rates from 0.3 to 20 s^{-1} while the temperature was respectively kept at 170 and 180 °C for the neat PLA and CE-enriched PLAs. A lower temperature of 170 °C was selected for the neat PLA because its melt viscosity at 180 °C was too low and insufficient for extensional testing. A sufficient time (5 min) was elapsed prior to starting the test to ensure thermal equilibrium within the specimen.

Morphological characterization

The density of the foamed samples was measured using the water displacement method at ambient pressure and temperature based on the standard ASTM792-00. The void fraction was determined using Eq. 4.1 (Lee and Park 2006).

$$V_f = \left(1 - \frac{\rho_f}{\rho_s}\right) \times 100 \qquad \text{Eq. 4.1}$$

where ρ_f and ρ_s are the density of the foamed and solid sample (1.24 g/cm^3), respectively. Cell morphology of the foamed samples was observed using a JSM-840 scanning electron microscope (SEM) (JEOL, USA) operated at accelerating voltage of 10 kV. Prior to the SEM observations, the samples were freeze-fractured in liquid nitrogen and sputter-coated with a thin layer of gold. A quantitative analysis of the average cell size and cell density of 200 cells was carried out using an image analysis tool (ImageJ, NIH). The cell density, or the number of cells per unit volume (cm^3) of the original unfoamed polymer, was calculated using Eq. 4.2 (Naguib *et al.* 2002).

$$\text{Cell density} = \left(\frac{n}{A}\right)^{3/2} \times \left(\frac{\rho_p}{\rho_f}\right) \qquad \text{Eq. 4.2}$$

where n, and A are the number of the cells in the micrograph and area of the micrograph (cm^2), respectively.

4.4 Results and discussion

4.4.1 Rheological properties

Viscoelasticity is typically found to significantly influence the foamability of thermoplastic polymers (Gendron 2005; Lee and Ramesh 2004). The viscoelastic properties of molten polymers are markedly affected by molecular weight (M_w), molecular weight distribution (MWD), and the entanglement density (Gendron 2005; Lee and Ramesh 2004). Low M_W and narrow MWD resins exhibit inadequate rheological properties and narrow processing window for foaming (Lee and Ramesh 2004). The steady-shear viscosity (η), complex viscosity (η*) and elastic modulus of the neat PLA and PLA prepared with various concentrations of CE using the two different compounding strategies are plotted as functions of shear rate ($\dot{\gamma}$) and frequency (ω) in Figure 4.1.

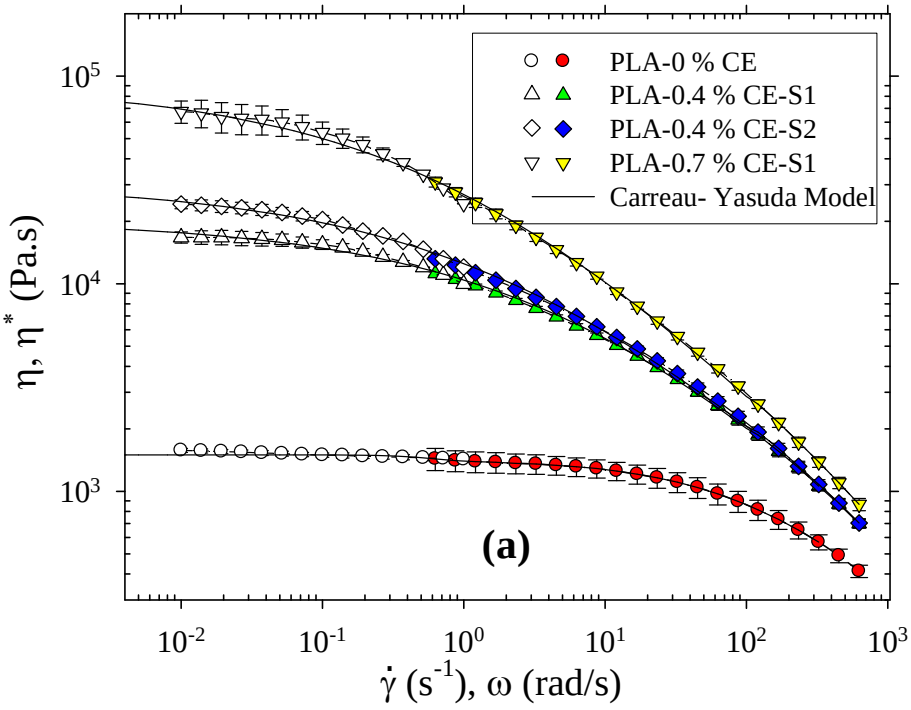

Figure 4.1: The linear viscoelastic properties (a) shear (open symbols) and complex viscosity (filled symbols) (b) storage modulus of the neat and CE-enriched PLAs at 180 °C.

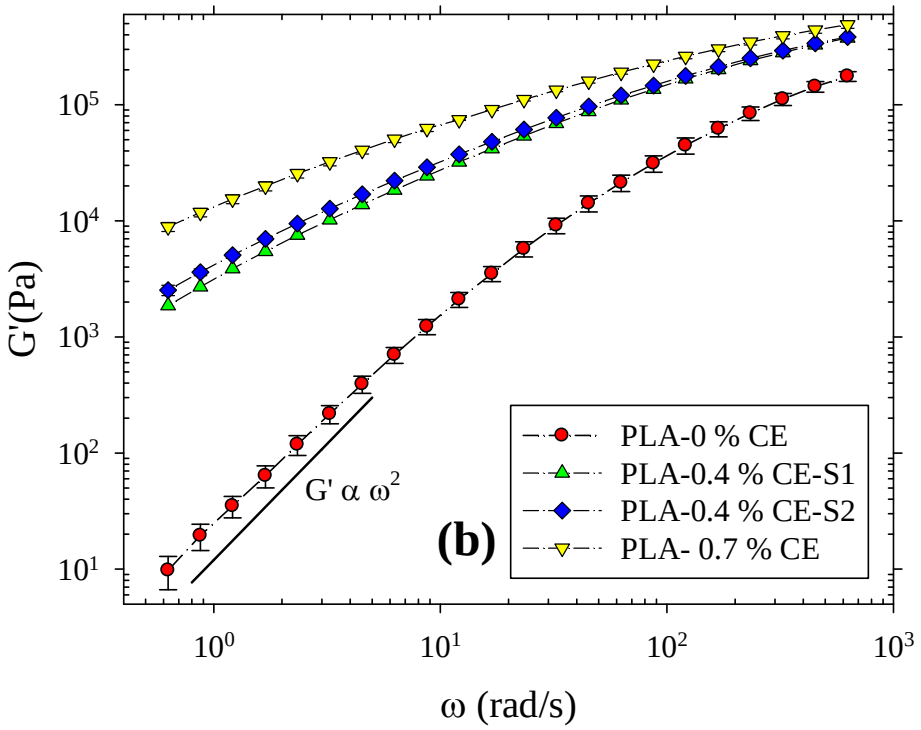

Figure 4.1 (continued): The linear viscoelastic properties (a) shear (open symbols) and complex viscosity (filled symbols) (b) storage modulus of the neat and CE-enriched PLAs at 180 °C.

The solid lines in Figure 4.1a represent the fits of the Carreau-Yasuda model (Carreau *et al.* 1997) used to extrapolate the zero-shear viscosity (η_0), reported in Table 4.1.

Table 4.1: The zero-shear viscosity of the neat and CE-enriched PLAs at 180 °C calculated using (a) the Carreau-Yasuda model and (b) the area under the relaxation time distribution.

Composition	η_0 (kPa.s)[a]	η_0 (kPa.s)[b]
PLA-0 wt% CE	1.4 ±0.1	1.3
PLA-0.4 wt% CE-S1	20.1 ±1.0	19.4
PLA-0.4 wt% CE-S2	30.1 ±1.4	30.5
PLA-0.7 wt% CE	89.8 ±2.8	84.3

We note the Cox-Merz rule is valid for all the samples. The Carreau-Yasuda model describes well all sets of data. Both η and η*, as shown in Figure 4.1a, gradually decrease with increasing $\dot{\gamma}$ and/or ω, exhibiting the typical shear-thinning behavior of polymer melts. The neat PLA is

characterized by a low complex viscosity, shear viscosity, shear sensitivity and a broad Newtonian plateau.

The incorporation of CE into the neat PLA, however, changes considerably its rheological response. The magnitude of the complex and steady shear viscosity is increased by two orders of magnitude at low frequencies or shear rates, depending on the CE content. Meanwhile, the transition from a Newtonian plateau to the so-called shear-thinning regime shifts to a lower frequency or shear rate, as the CE content is increased, suggesting the presence of a microstructure with a long relaxation time. The observed change in the viscosity behavior can be attributed to the macromolecular chain extension and branching, as discussed in a previous publication (Najafi *et al.* 2012b) and summarized below. In comparison with the PLA treated by 0.4 wt% CE and prepared by strategy S1, the sample prepared by strategy S2 exhibits a higher viscosity and elasticity at very low shear rates and frequencies. The reason of this increase is also explained below.

Structural changes in polymeric materials can be evaluated with the linear viscoelastic properties, considering that they are very sensitive to topological structure of macromolecular chains. The storage modulus (G') is even more sensitive to structural changes in viscoelastic materials (Coppola *et al.* 2006). G' data of the neat PLA and CE-enriched PLAs are presented in Figure 4.1b as a function of ω. G' of PLAs treated by CE is larger than that of the neat PLA in the entire range of ω and increases with increasing CE content. The storage modulus of polymeric materials with a linear macromolecular structure theoretically grows with the square of ω in the terminal zone (i.e. at low frequencies where $G' \sim \omega^2$), where only the longest relaxation time contributes to the viscoelastic behavior (Tian *et al.* 2006). The slope of G' versus ω of the neat PLA and CE-enriched PLAs were calculated in the terminal zone. The value for the neat PLA is 1.88, quite close to the theoretical value of 2, confirming the linear structure of the polymer. However, the slope for S1 and S2 compounded samples and the PLA containing 0.7 wt% of CE is reduced to 1.06, 1, and 0.80, respectively. The observed non-terminal behavior can be ascribed to a long chain branching structure. This evidence was used in (Eslami and Kamal 2013; Tian *et al.* 2006; Wood-Adams *et al.* 2000) to verify the formation of long chain branching structure.

To gain further understanding of the polymer molecular structure after the CE incorporation, the reduced complex viscosity and loss angle were considered as a function of shifted frequency using the zero-shear viscosity, as illustrated in Figure 4.2.

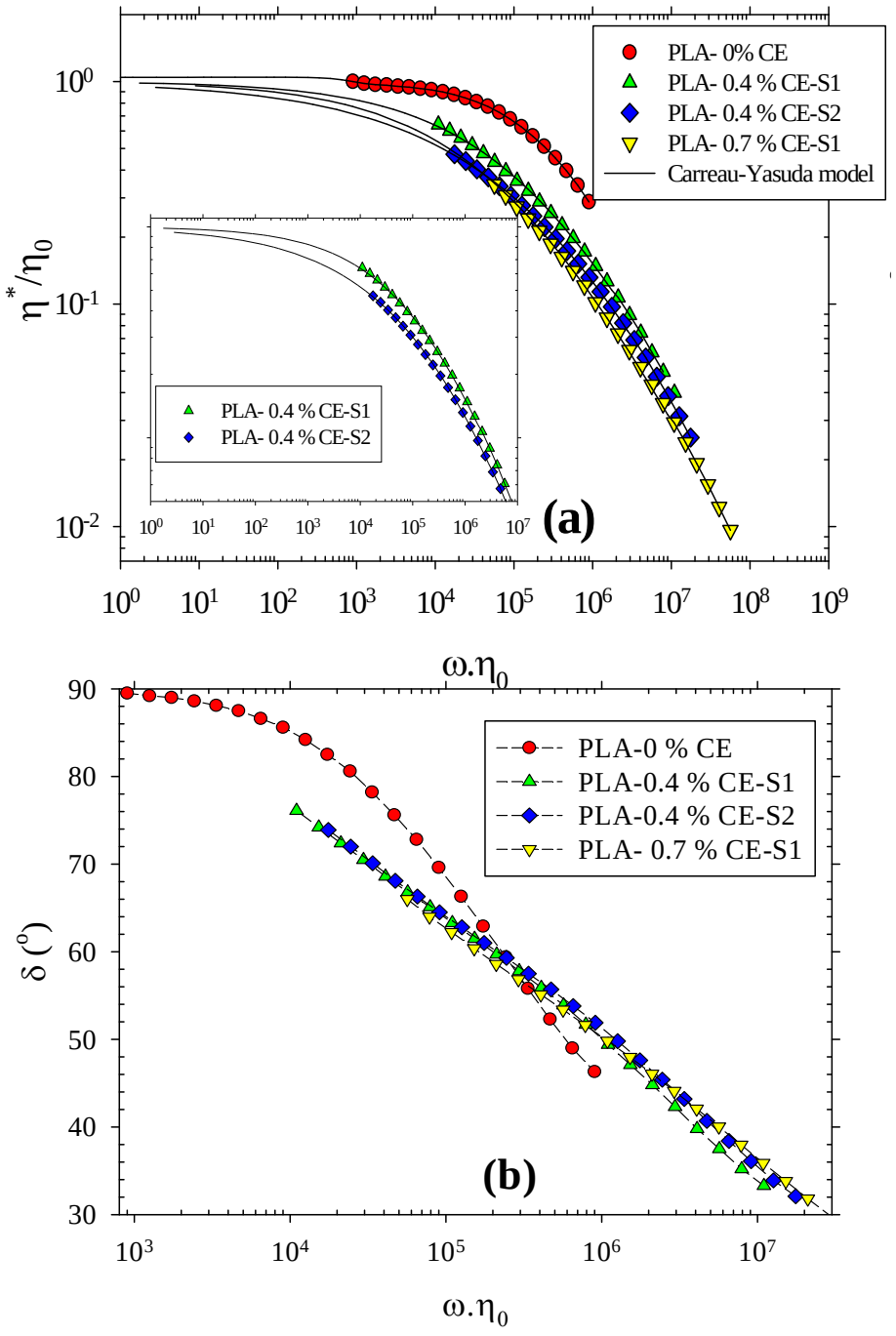

Figure 4.2: The shifted rheological properties (a) complex viscosity and (b) loss angle of neat and CE-enriched PLAs at 180 °C as a function of shifted frequency.

A narrower Newtonian plateau and a broad transition region between the Newtonian plateau and the power-law zone, as observed in Figure 4.2a for the CE-PLA samples, can be caused by the broadening of the MWD as discussed in (Najafi *et al.* 2012b; Wood-Adams *et al.* 2000).
Due to the presence of relaxation modes at long times related to branched chains in a LCB structure, the shape of the loss angle curve also prominently changes (Najafi *et al*. 2012b; Wood-Adams *et al.* 2000). The results in Figure 4.2b reveal that the molecular structure of CE-enriched systems significantly differ from that of the neat PLA and is consistent with the presence of a long chain branching (LCB) structure, as extensively discussed in our previous work (Najafi *et al*. 2012b). The formation of the LCB structure is responsible for the increased M_W and MWD, leading to increased melt strength, elasticity, shear sensitivity, and consequently, as we will see later, to improved foamability.
The CE-enriched PLA prepared by strategy S2 shows a slightly broader transition region (see inset of Figure 4.2a), and consequently, a broader MWD as compared with that prepared by strategy S1. In the S2 compounded sample, increased CE content (in the first run) favored the formation of a highly LCB structure in comparison with that prepared using S1. The longer residence time due to the second compounding step may also influence the extent of reaction of the chain extender.

To examine the impact of LCB on the compound's relaxation behavior, the time-weighted relaxation spectra, $\lambda H(\lambda)$ of the linear and LCB-PLAs were calculated using the SAOS data via the non-linear regularization (NLREG) method and are illustrated in Figure 4.3a. The dashed, vertical lines show the experimental window. The area under the relaxation time spectra represents the zero-shear viscosity (η_0) of the melt and the values are given in Table 4.1.

There is a good agreement between these values and those obtained using the Carreau-Yasuda model, implying that the calculated time-weighted relaxation spectra are self-consistent. As the results show, the formation of the LCB-structure dramatically changes the shape and peak location of the relaxation spectrum. This shift mainly results from the change of relaxation mechanisms (He *et al.* 2004). While reptation is the main relaxation mechanism for linear chains (Van Ruymbeke *et al*. 2005), branched chains relaxes by arm retraction, leading to a retardation of chain movement along their backbone (He *et al*. 2004) and, consequently, broadening of the relaxation spectrum.

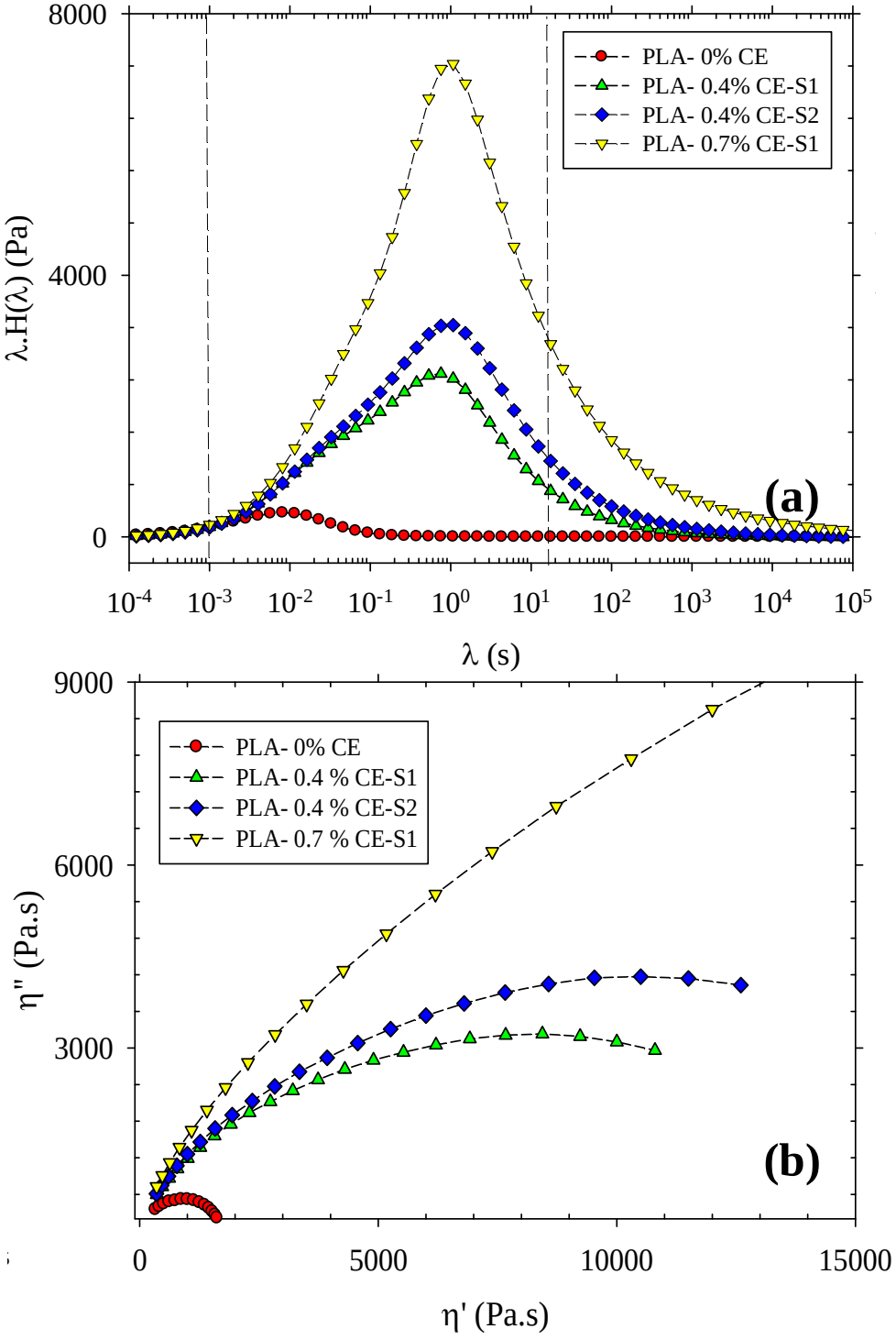

Figure 4.3: (a) Weighted relaxation spectra and (b) Cole-Cole plots of the neat and LCB-PLAs prepared using the two different strategies.

In comparison with the 0.4 wt% CE-PLA prepared using strategy S1, the S2 sample exhibits a slightly broader relaxation spectrum as shown in Figure 4.3a due to a more developed LCB structure. Increasing the CE content from 0.4 to 0.7 wt% further increases the fraction of branched macromolecules, leading to the broadening of the relaxation spectrum.

To further analyze the relaxation process, Cole-Cole plots (η" versus η') (He *et al*. 2004; Tian *et al*. 2006) are presented in Figure 4.3b. The Cole-Cole plot of the linear PLA is found to be semicircular. Depending on the degree of LCB, the plots for the CE-enriched PLAs deviate from the semicircular shape and exhibit more evident upturning at high viscosity values, implying the existence of LCB macromolecules. This behavior was also observed by others (He *et al*. 2004; Tian *et al*. 2006) for polymers with long chain branching.

The transient flow properties were also studied since they play an important role in the foaming phenomenon. The normalized shear stress growth coefficient ($\eta^+(t)/\eta$) of the linear and LCB-PLAs at different shear rates are illustrated in Figure 4.4. The viscosity at steady state was reported in Figure 4.1a.

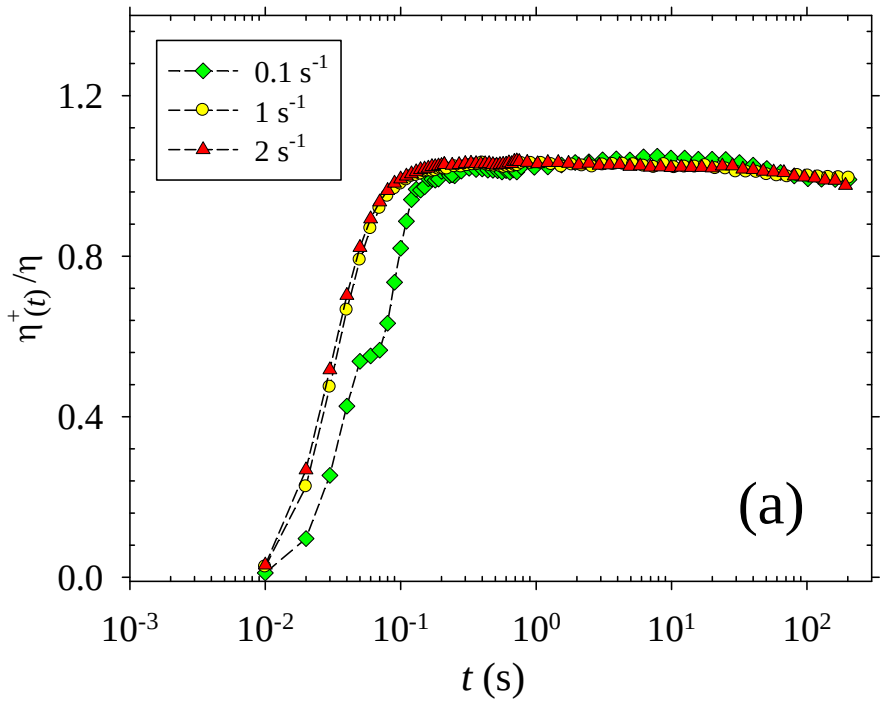

Figure 4.4: Normalized stress growth coefficient of (a) the neat PLA, (b) PLA containing 0.4 wt% CE prepared using strategy S1, (c) PLA containing 0.4 wt% CE prepared using strategy S2, and (d) PLA containing 0.7 wt% CE prepared by strategy S1 at 180 °C and three different shear rates.

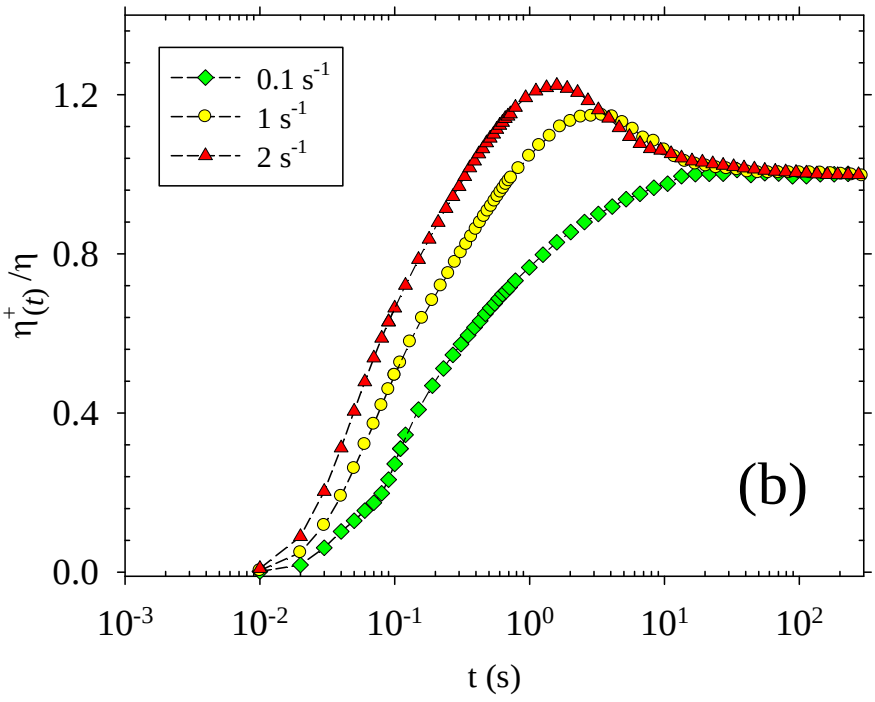

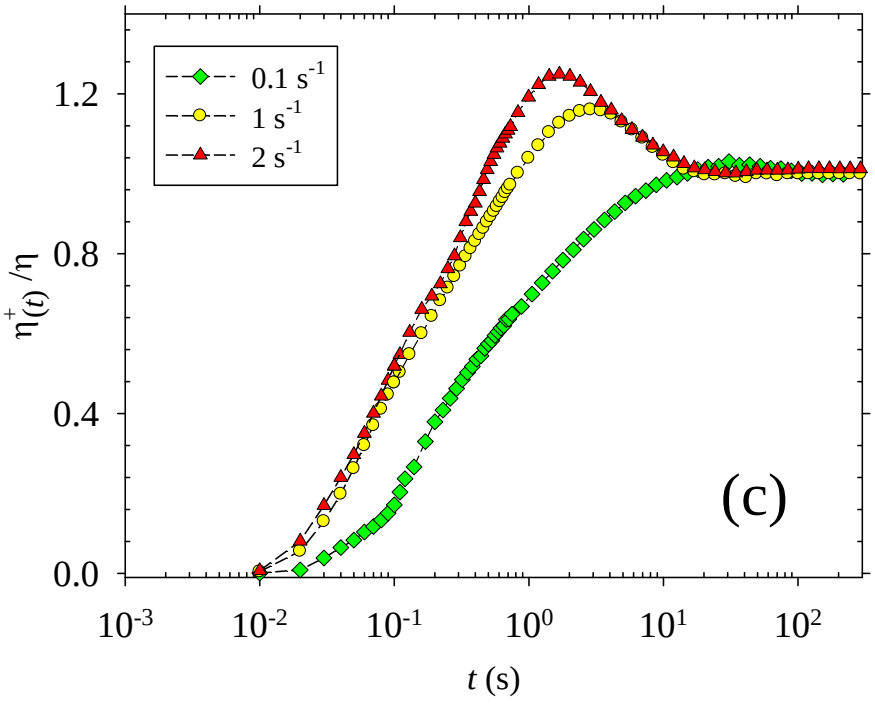

Figure 4.4 (continued): Normalized stress growth coefficient of (a) the neat PLA, (b) PLA containing 0.4 wt% CE prepared using strategy S1, (c) PLA containing 0.4 wt% CE prepared using strategy S2, and (d) PLA containing 0.7 wt% CE prepared by strategy S1 at 180 °C and three different shear rates.

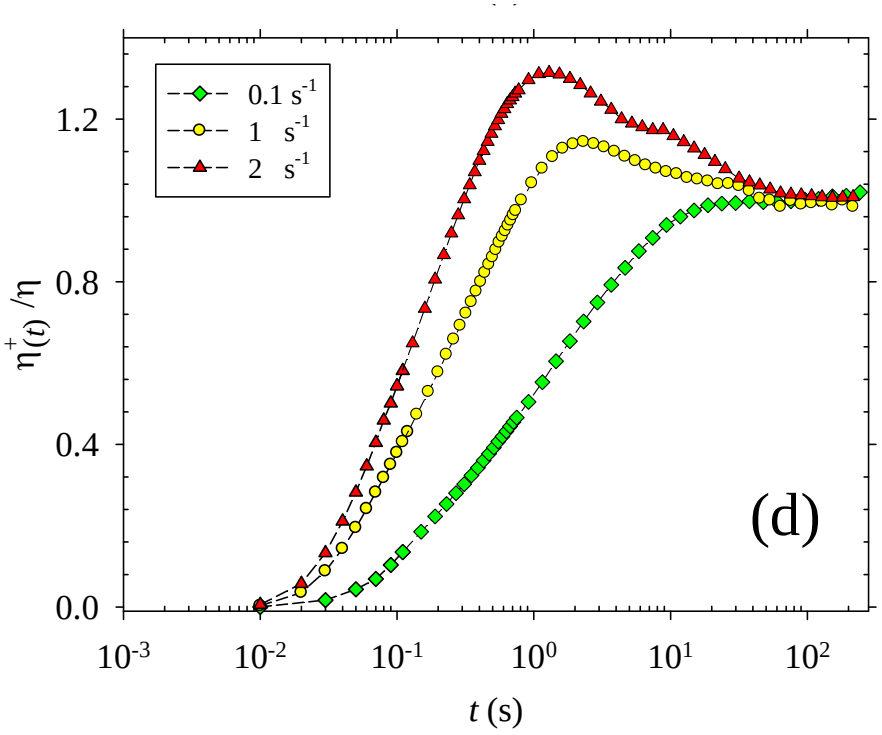

Figure 4.4 (continued): Normalized stress growth coefficient of (a) the neat PLA, (b) PLA containing 0.4 wt% CE prepared using strategy S1, (c) PLA containing 0.4 wt% CE prepared using strategy S2, and (d) PLA containing 0.7 wt% CE prepared by strategy S1 at 180 °C and three different shear rates.

The origin of the transient response is considered to be the orientation of the macromolecules and decreases in the entanglement density (Robertson *et al*. 2002). No significant overshoots are observed for the neat PLA, even at the larger shear rate as shown in Figure 4.4a, suggesting the low entanglement density of the polymer. Contrary to the neat PLA, the CE-enriched PLAs (Figure 4.4b-d), however, exhibit prominent overshoots in their transient shear response. For instance, an overshoot of roughly 25 and 35 % above the steady state value is observed at a shear rate of 2 s^{-1} for PLA containing 0.4 and 0.7 wt % CE, respectively. This is caused by the increased entanglement density as a consequence of long chain branching. The stress growth behavior of the PLA containing 0.4 wt% CE prepared using the two strategies is about the same at these shear rates. The stress overshoot becomes more pronounced and occurs at shorter time with increasing shear rate. The required shearing time to reach the steady state also increases from 0.3 s for the neat PLA to 30 and 70 s for the PLA containing 0.4 and 0.7 wt% CE, respectively. The enhanced

entanglement density in LCB-macromolecules (Wever *et al.* 2013) inhibits the motion of the polymer chains and delays their relaxation. Figure 4.5 presents the transient uniaxial elongational viscosity of the neat PLA, measured at 170 °C, and the LCB-PLAs, measured at 180 °C, at different strain rates. Even though cell expansion in foaming is controlled by biaxial elongational viscosity, the uniaxial behavior can provide useful information about melt strength.

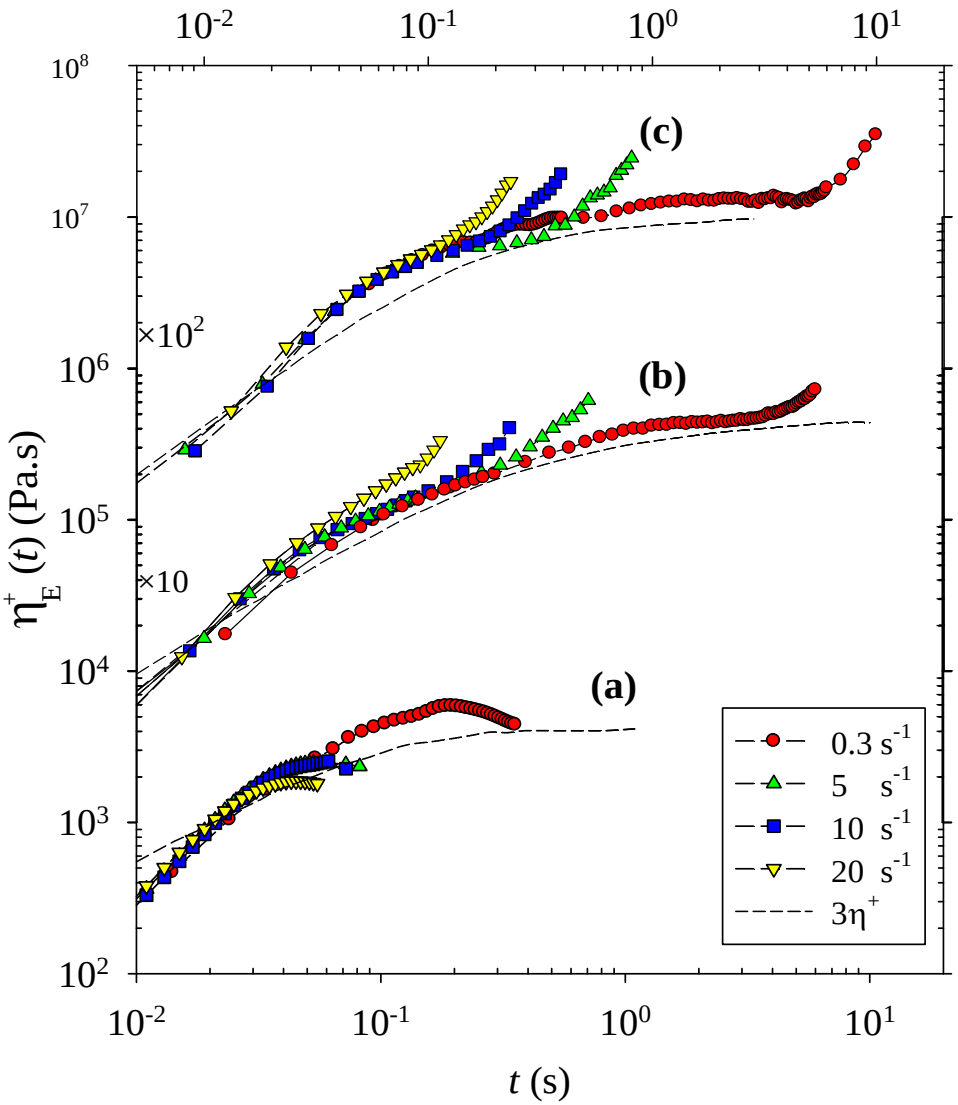

Figure 4.5: Transient elongational viscosities of (a) neat PLA at 170 °C and (b) LCB-PLA containing 0.4 wt% of CE prepared using strategy S2, and (c) LCB-PLA containing 0.7 wt% of CE at 180 °C and different strain rates. The transient elongational viscosity of LCB-PLAs containing 0.4 wt% CE prepared using strategy S1 showed a similar trend with those prepared using S2 and, hence, is not presented.

The dashed lines illustrate the transient shear viscosity predicted from the linear viscoelasticity data using the generalized Maxwell model and multiplied by three. Note that at very early stages of the test, i.e. at times less than 0.05 s, the measured extensional viscosity of all samples is less than that predicted by the time-dependent shear viscosity. This is most likely due to instrument limitations in reaching instantaneously the set strain rate. The elongational viscosity of the neat PLA increases until it reaches a steady value. As expected for a molten linear polymer, strain hardening (SH) is not observed for the neat PLA (Figure 4.5a) confirming the results of the literature (Eslami and Kamal 2013; Matuana and Diaz 2013; Wang et al. 2012c). In contrast, the elongational viscosity of the LCB-PLAs profoundly deviates from the linear viscoelasticity (Figure 4.5b and c) at all strain rates and shows an upturn behavior (SH) at longer times. This upturn behavior occurs faster as the strain rate is increased. In fact, increased entanglements associated with LCB hinder the chain contraction during extension, leading to a pronounced SH behavior (Lee and Ramesh 2004).

4.4.2 Foaming behavior

The foaming behavior of the linear and LCB-PLAs is investigated at temperatures of 130, 140, and 155 ^{o}C. Representative SEM images of the fractured surfaces of foamed samples are shown in Figure 4.6. Contrary to the linear PLA, LCB-PLAs are not foamed effectively at the foaming temperature of 130 ^{o}C (see the first column of Figure 4.6) due to too high stiffness and strength of the polymer molten phase. Moreover, isothermal and non-isothermal crystallization studies revealed that the crystallization rate and degree of LCB-PLAs were much larger than those of the linear counterpart (data are not presented here for brevity). These findings are consistent with the study of Wang *et al.* on PLA with controlled branch length (Wang *et al.* 2012d). Considering that the foaming temperature is below the melting point and close to the crystallization temperature, LCB polymer melts, hence, solidify too quickly before the nucleated cells could grow. However at higher foaming temperatures of 140 and 155 ^{o}C, the contribution of crystallization to the cellular structure cannot be assessed since they are above the melting point (the melting point of PLA is depressed from 160 to 135 ^{o}C at this pressure (9 MPa) (Nofar *et al.* 2013)). As shown in Figure 4.6b-d the LCB-PLAs exhibit more uniform cells with smaller size and larger cell density at 140 and 155 ^{o}C in comparison with the linear PLA.

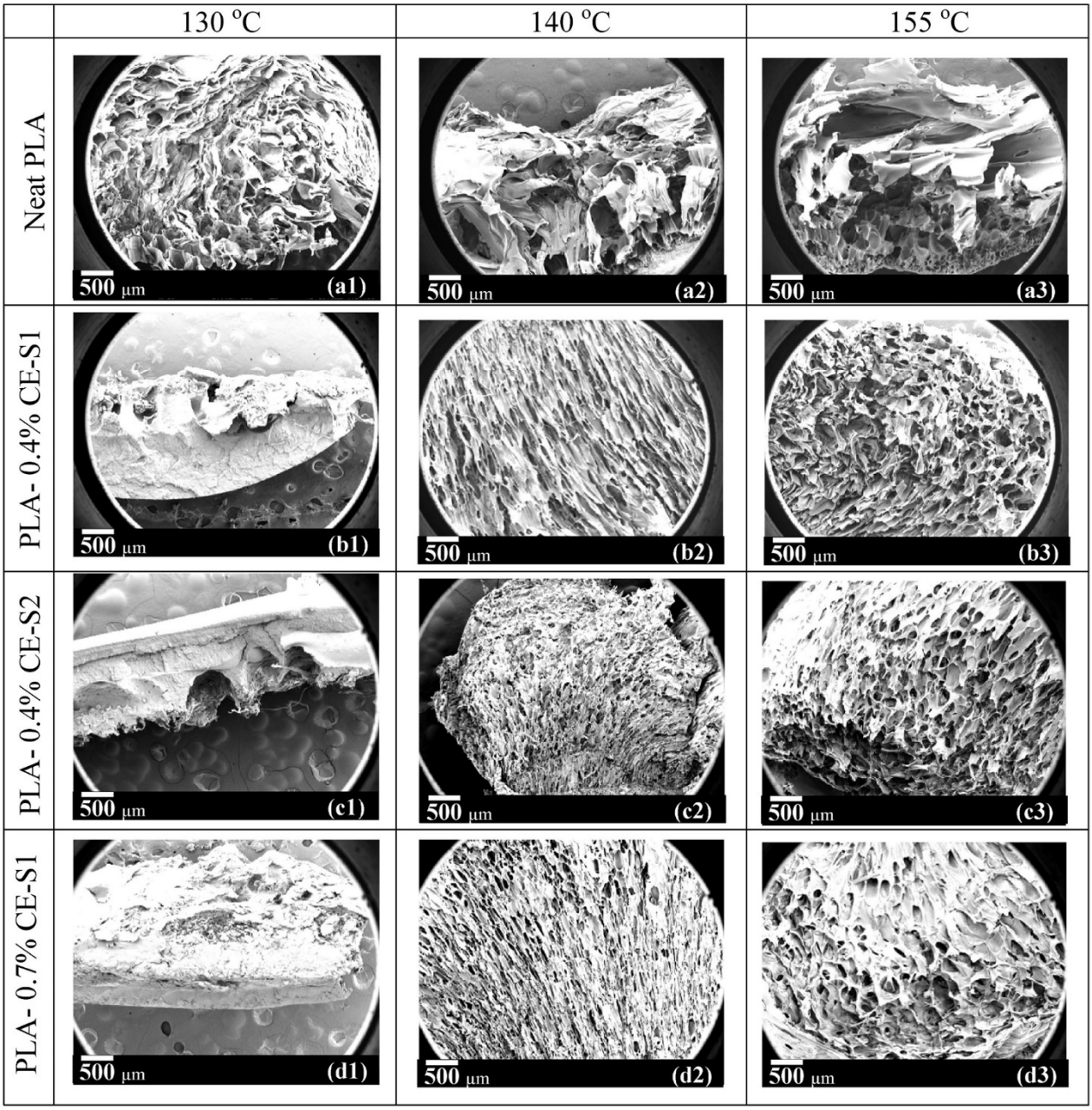

Figure 4.6: Representative SEM micrographs of cryo-fractured surfaces of (a) neat PLA, (b) PLA containing 0.4 wt% CE prepared using strategy S1, (c) PLA containing 0.4 wt% CE prepared using strategy S2, and (d) PLA containing 0.7 wt% CE prepared by strategy S1 at different foaming temperature.

As a result of long chain branching, the melt strength of PLA is improved and the cellular structure of the foams becomes well-developed and uniform. The volume expansion ratios of the linear and LCB-PLA foams, defined as the ratio of polymer density (1.24 g/cm^3) to foam density, was measured at different foaming temperatures and used to characterize the void fraction (Eq. 4.1).

Figure 4.7a depicts the void fraction of the resulting foams with respect to the foaming temperature. The obtained results indicate that the expansion ratio and, consequently, the void fraction is strongly dependent on the LCB content and processing conditions. The void fraction of the foamed neat PLA decreases from 0.75 to 0.17 with increasing foaming temperature from 130 to 155 °C. In contrast with the neat PLA, the void fraction of LCB-PLAs is enhanced with increasing foaming temperature. The void fraction of S1 (0.12 at 130 °C) and S2 (0.08 at 130 °C) compounded samples and the PLA containing 0.7 wt% CE (0.08 at 130 °C) increases to 0.90, 0.88, and 0.85, respectively, as the foaming temperature is raised to 155 °C.

Naguib *et al.* (2004) investigated the fundamental mechanisms governing the expansion behavior of polymeric foams. They found that the final expansion ratio was governed either by the gas loss that occurred through diffusion out of the foam or by the crystallization and melt stiffening of the polymeric matrix (Lee *et al.* 2005; Naguib *et al.* 2004). If the foaming temperature was too high, the solidification time became too long. Therefore, the gas that diffused out of the melt towards the nucleated cells had enough time to escape out of the foam. Under these conditions, the maximum expansion ratio was governed by gas loss and it decreased with increasing processing temperature. However, if the processing temperature was too low, the maximum expansion ratio was controlled by solidification and increased with temperature (Naguib *et al.* 2004). According to these investigations, the expansion ratio and void fraction of the samples, excluding the neat PLA, are governed by melt stiffening and crystallization, at least at 130 °C. As the foaming temperature increases, the degree of crystallization, melt viscosity and, thus, melt strength of the polymer decrease, allowing the created cells to be further expanded. A reverse trend in the case of the neat PLA is illustrated in Figure 4.7a. The SEM images presented in Figure 4.6a clearly reveal that increasing the foaming temperature from 130 to 155 °C promotes cell rupture due to a reduced melt viscosity and elasticity. As a result, most of the gas escapes from the foam during the expansion process. The amount of gas retained in the foam, thus, decreases, leading to a reduction of the gas pressure for expansion and a decreased void fraction. Although the effect of LCB on void fraction is striking when compared to linear PLA, the differences between the various LCB-PLAs are within the experimental uncertainty at all foaming temperatures.

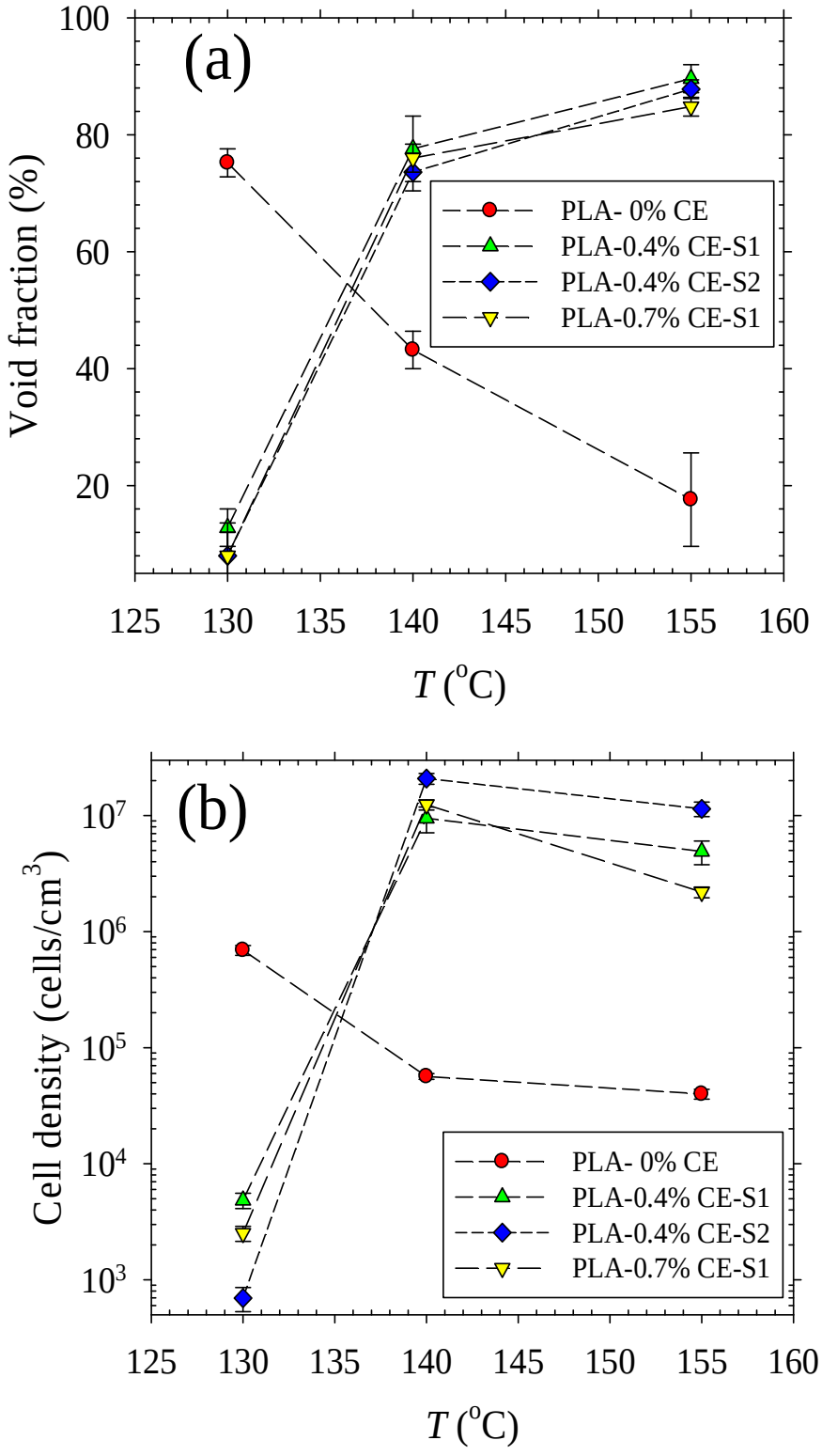

Figure 4.7: The effect of long chain branching and foaming temperature on (a) void fraction, (b) cell density, and (c) cell size of PLA foams.

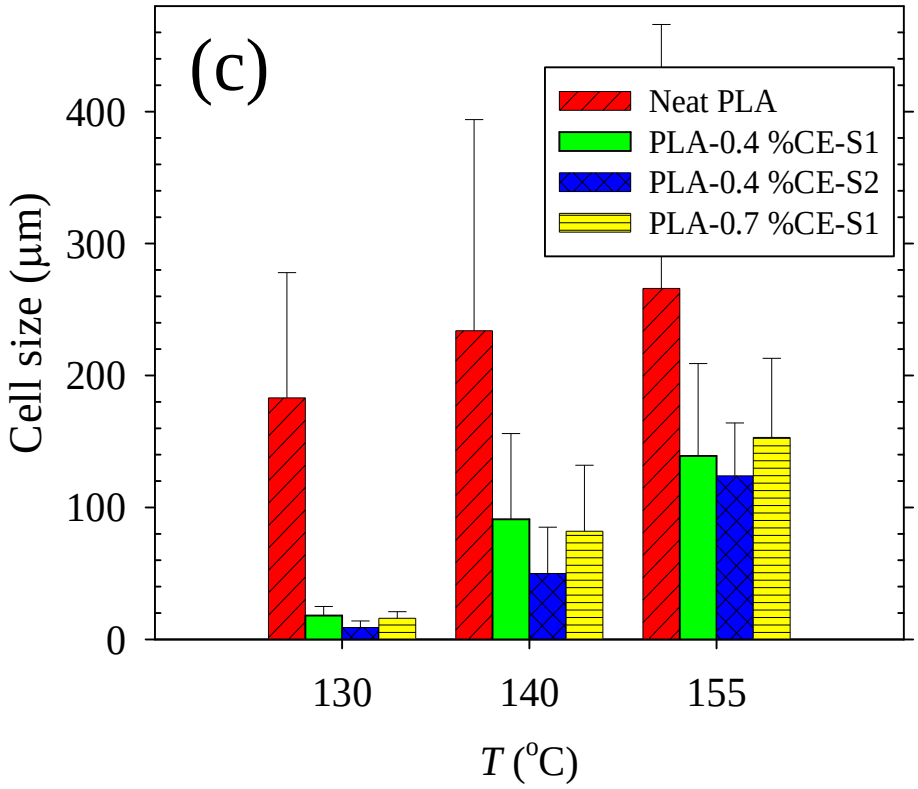

Figure 4.7 (continued): The effect of long chain branching and foaming temperature on (a) void fraction, (b) cell density, and (c) cell size of PLA foams.

The cell density (Eq. 4.2) and cell size are reported in Figure 4.7b and c, respectively. The cell density of the neat PLA continuously decreases from 7×10^5 to 4×10^4 cells/cm^3 (more than one order of magnitude) as the foaming temperature is raised from 130 to 155 °C. The increase of the foaming temperature decreases the melt strength of the polymer, leading to severe cell coalescence and cell rupture (Lee *et al.* 2005; Nofar and Park 2014). Consequently, most of the nucleated cells are broken during expansion, as shown in Figure 4.6a and the cell density of the foam is reduced by more than 17 times. Another possibility is the crystal-induced cell nucleation at a lower temperature due to the stress variations around the stiffened crystal nuclei (Garancher and Fernyhough 2012; Wong *et al.* 2013). The cell density of LCB PLAs is less than 4×10^3 cells/cm^3 at a foaming temperature of 130 °C. As mentioned earlier, too high stiffness and strength of the branched

polymer melts at 130 °C make it difficult for the cells to nucleate and grow. However, with increasing foaming temperature to 140 °C (see in Figure 4.6b-d), the cell density increases to 9.5×10^6, 2.1×10^7, and 1.2×10^7 cells/cm^3 in PLA containing 0.4 wt% CE with strategy S1, with strategy S2, and the PLA containing 0.7 wt% CE, respectively. The incorporation of the chain extender into the neat PLA enhances the cell density by two orders of magnitude.

The increased cell density of LCB-PLAs is attributed to higher melt strength and strain hardening behavior, resulting from long chain branching, that stabilize the nucleated cells by minimizing cell coalescence. A comparison of the cell density for PLA containing 0.4 wt% CE indicates that the S2 sample has a higher cell density (two times) than the S1 sample. The results presented in Figure 4.1a reveal that the melt viscosity of the LCB-PLA containing 0.4 wt% CE prepared using strategy S2 was higher than sample S1, particularly at low frequencies or shear rate. The increase in cell density can be explained by a decreased gas diffusion rate with increasing polymer melt viscosity (Wong *et al.* 2007). This is in agreement with results published by Di *et al.* (2005) in PLA treated with butane diisocyanate (BDI). As extensively discussed by Park *et al.* (1995), there is a competition between cell nucleation and cell growth. They reported that the real pressure drop and cell nucleation time were not instantaneous and happened over a finite time period. During the course of the pressure drop, some stable cells nucleated early and, then, the gas in solution in the polymer melt diffused to the nucleated cells. As the pressure further dropped, the system would either just expand the existing cells by gas diffusion or nucleate additional cells while expanding the existing cells. An increase of the melt viscosity makes difficult the gas diffusion and mass transfer into the nucleated cells. Thus, the gas in solution preferentially nucleates new microcells rather than diffusing to the existing cells, leading to an increase of the cell density. In comparison with the S2 compounded sample, PLA containing 0.7 wt% CE shows a lower cell density, even though it has a higher melt strength. The increase of the free volume resulting from branching (Gong *et al.* 2005) is most likely responsible for the observed decline in the cell density. A higher degree of branching, obtained after incorporation of 0.7 wt% CE further increases the free volume between the chains and, thus, increases the gas diffusion rate. As a result, more gas in solution in the melt migrates preferentially to the existing cells rather than nucleating new bubbles, causing a decreased cell density. Comparing the results in Figure 4.7b also show that the cell density of LCB-PLAs tends to decrease by more than 50 % as the foaming temperature is increased from 140 to 155 °C. The reduction of the cell density with respect to temperature can be related to many factors

such as a reduction in gas solubility (Mahmood *et al.* 2014), a decrease of the melt strength, an increase of the gas diffusion rate (Pilla *et al.* 2010a; Wong *et al.* 2007), and a decreased number of the crystal nuclei that can affect cell nucleation (Wong *et al.* 2013).

The average cell size of the foamed samples is determined by measuring the maximum diameter of 200 cells in SEM micrographs and reported in Figure 4.7c. The average cell size for the linear and LCB-PLAs increases with foaming temperature due to enhanced gas diffusivity and reduction of the melt strength. This, in turn, promotes the gas diffusion into the nucleated cells and decreases the resistance for cell growth (Wong *et al.* 2007). At the same foaming temperature, LCB-PLAs exhibit a smaller cell size than the linear PLA. For instance, at a foaming temperature of 140 ^{o}C the average cell size is reduced from 234 µm in neat PLA to 91, 50, and 82 µm in the PLA containing 0.4 wt% CE prepared using strategies S1 and S2, and the PLA containing 0.7 wt% CE, respectively. This reduction might be due to increased melt strength and viscosity of the LCB-PLAs as a result of branching. The cell wall stability is improved with increasing melt strength, thereby decreasing the cell coalescence and average cell size (Nofar and Park 2014). Among the investigated compositions, the PLA containing 0.4 wt% CE prepared using strategy S2 exhibits the smaller average cell size at all foaming temperatures. Considering that more cells are nucleated in this case (higher cell density), there is less gas available for each cell to grow (Pilla *et al.* 2010a), leading to the formation of cells with smaller size. Moreover, the increased viscosity may itself restrict the rate of cell growth, resulting in cells with smaller size.

4.5 Conclusion

In this study, long chain branched (LCB) PLAs were prepared by a melt grafting reaction in the presence of a multi-functional chain extender (CE). Two different concentrations, 0.4 and 0.7 wt%, CE were added to the neat PLA to achieve different degrees of branching. LCB-PLA containing 0.4 wt% CE were prepared using two strategies called S1 and S2. The rheological and foaming behavior of linear and resulting LCB-PLAs was investigated. The steady and transient rheological properties of the linear and LCB-PLAs revealed that the introduction of the CE profoundly affected the melt viscosity and elasticity. The LCB-PLAs exhibited an increased viscosity, shear sensitivity, and longer relaxation time in comparison with linear PLA. A prominent overshoot was found in the transient shear response of CE-enriched PLAs due to an increase of the entanglement density and, consequently, melt elasticity. The incorporation of CE into PLA and the resulting LCB,

moreover, led to a strong strain hardening behavior in uniaxial elongational flow whereas no strain hardening was observed for the linear PLA.

The batch foaming of the linear and LCB-PLAs was conducted using CO_2 at different foaming temperatures ranging from 130 to 155 ^oC. The impact of molecular structure and foaming temperature on the cell morphology, void fraction, cell density, and cell size were examined. It was found that increased melt strength and elasticity, resulting from branching, strongly promoted the cell uniformity, cell density and void fraction. In general, the cell growth was accelerated with increasing foaming temperature. The cell density of LCB-PLAs was enhanced as the foaming temperature increased up to 140 ^oC, beyond which the cell density decreased. Among the investigated compositions, PLA containing 0.4 wt% CE prepared by strategy S2 provided smaller cell size and higher cell density than the others. As a result, the foaming temperature of 140 ^oC and chain extender content of 0.4 wt%, added based on the strategy S2, were found the optimum conditions to achieve finer and denser cell morphology in PLA foams.

4.6 Acknowledgements

Financial support from AUTO21 (Canada's automotive R&D program) and NCE (Networks of Centres of Excellence of Canada) is gratefully acknowledged.

4.7 References

Airale A, Carello M, Scattina A (2011) Carbon fiber monocoque for a hydrogen prototype for low consumption challenge Material Wiss Werkst 42:386-392 doi:10.1002/mawe.201100793

Carreau PJ, De Kee DCR, Chhabra RP (1997) Rheology of Polymeric Systems Principles and Applications Hanser-Garner Publications

Coppola S, Acierno S, Grizzuti N, Vlassopoulos D (2006) Viscoelastic Behavior of Semicrystalline Thermoplastic Polymers during the Early Stages of Crystallization Macromolecules 39:1507-1514 doi:10.1021/ma0518510

Di Y, Iannace S, Di Maio E, Nicolais L (2005) Reactively Modified Poly(lactic acid): Properties and Foam Processing Macromol Mater Eng 290:1083-1090 doi:10.1002/mame.200500115

Drumright RE, Gruber PR, Henton DE (2000) Polylactic Acid Technology Adv Mater 12:1841-1846 doi:10.1002/1521-4095(200012)12:23<1841::aid-adma1841

Eslami H, Kamal MR (2013) Effect of a chain extender on the rheological and mechanical properties of biodegradable poly(lactic acid)/poly[(butylene succinate)-co-adipate] blends J Appl Polym Sci 129:2418-2428 doi:10.1002/app.38449

Fujimoto Y, Ray SS, Okamoto M, Ogami A, Yamada K, Ueda K (2003) Well-Controlled Biodegradable Nanocomposite Foams: From Microcellular to Nanocellular Macromol Rapid Comm 24:457-461 doi:10.1002/marc.200390068

Garancher J-P, Fernyhough A (2012) Crystallinity effects in polylactic acid-based foams J Cell Plast 48:387-397 doi:10.1177/0021955x12448804

Garlotta D (2001) A literature review of poly(lactic acid) J Polym Environ 9:63-84 doi:Unsp 1566-2543/01/0400-0063/0

Gendron R (ed) (2005) Thermoplastic foam processing, principles and development. CRC Press,

Gong W, Mai Y, Zhou Y, Qi N, Wang B, Yan D (2005) Effect of the Degree of Branching on Atomic-Scale Free Volume in Hyperbranched Poly[3-ethyl-3-(hydroxymethyl)oxetane]. A Positron Study Macromolecules 38:9644-9649 doi:10.1021/ma051026j

He C, Wood-Adams P, Dealy JM (2004) Broad frequency range characterization of molten polymers J Rheol 48:711-724 doi:doi:http://dx.doi.org/10.1122/1.1763943

Keshtkar M, Nofar M, Majithiya K, Park CB, Carreau P Foaming behavior of PLA/nanocolay nanocomposites in continious extrusion. In: BioFoams, Italy, 2011.

Kramschuster A, Turng L-S (2009) An injection molding process for manufacturing highly porous and interconnected biodegradable polymer matrices for use as tissue engineering scaffolds J Biomed Mater Res Part B: Appl Biomat 92B:366-376 doi:10.1002/jbm.b.31523

Lee JWS, Park CB (2006) Use of Nitrogen as a Blowing Agent for the Production of Fine-Celled High-Density Polyethylene Foams Macromol Mater Eng 291:1233-1244 doi:10.1002/mame.200600203

Lee JWS, Wang K, Park CB (2005) Challenge to Extrusion of Low-Density Microcellular Polycarbonate Foams Using Supercritical Carbon Dioxide Ind Eng Chem Res 44:92-99 doi:10.1021/ie0400402

Lee ST, Ramesh NS (eds) (2004) Polymeric Foams; Mechanisms and Materials. CRC Press LLC

Lunt J (1998) Large-scale production, properties and commercial applications of polylactic acid polymers Polym Degrad Stabil 59:145-152 doi:http://dx.doi.org/10.1016/S0141-3910(97)00148-1

Mahmood SH, Keshtkar M, Park CB (2014) Determination of carbon dioxide solubility in polylactide acid with accurate PVT properties J Chem Thermodyn 70:13-23 doi:http://dx.doi.org/10.1016/j.jct.2013.10.019

Mahmoodi M, Behravesh AH, Rezavand SAM, Golzar M (2009) Theoretical and visual study of bubble dynamics in foam injection molding Polym Eng Sci 50:561-569 doi:10.1002/pen.21565

Matuana LM, Diaz CA (2013) Strategy To Produce Microcellular Foamed Poly(lactic acid)/Wood-Flour Composites in a Continuous Extrusion Process Ind Eng Chem Res 52:12032-12040 doi:10.1021/ie4019462

Mihai M, Huneault MA, Favis BD (2010) Rheology and extrusion foaming of chain-branched poly(lactic acid) Polym Eng Sci 50:629-642 doi:10.1002/pen.21561

Minegishi A, Nishioka A, Takahashi T, Masubuchi Y, Takimoto J., Koyama K (2001) Uniaxial elongational viscosity of PS/a small amount of UHMW-PS blends Rheol Acta 40:329-338 doi:10.1007/s003970100165

Mitomo H, Kaneda A, Quynh TM, Nagasawa N, Yoshii F (2005) Improvement of heat stability of poly(l-lactic acid) by radiation-induced crosslinking Polymer 46:4695-4703 doi:http://dx.doi.org/10.1016/j.polymer.2005.03.088

Naguib HE, Park CB, Panzer U, Reichelt N (2002) Strategies for achieving ultra low-density polypropylene foams Polym Eng Sci 42:1481-1492 doi:10.1002/pen.11045

Naguib HE, Park CB, Reichelt N (2004) Fundamental foaming mechanisms governing the volume expansion of extruded polypropylene foams J Appl Polym Sci 91:2661-2668 doi:10.1002/app.13448

Najafi N, Heuzey MC, Carreau PJ, Wood-Adams PM (2012a) Control of thermal degradation of polylactide (PLA)-clay nanocomposites using chain extenders Polym Degrad Stab 97:554-565 doi:http://dx.doi.org/10.1016/j.polymdegradstab.2012.01.016

Najafi N, Heuzey MC, Carreau PJ, Wood-Adams PM (2012b) Control of thermal degradation of polylactide (PLA)-clay nanocomposites using chain extenders Polym Degrad Stab 97:554-565 doi:http://dx.doi.org/10.1016/j.polymdegradstab.2012.01.016

Nofar M, Barzegari MR, Tabatabaei A, Keshtkar M, Park CB (2012) Effect of various additives (talc, nanoclay, and nanosilica) on extrusion foaming of PLA through crystallization. Paper presented at the Annual Technical Conference - ANTEC,

Nofar M, Park CB (2014) Poly (lactic acid) Foaming: A Review Prog Polym Sci doi:http://dx.doi.org/10.1016/j.progpolymsci.2014.04.001

Nofar M, Tabatabaei A, Ameli A, Park CB (2013) Comparison of melting and crystallization behaviors of polylactide under high-pressure CO2, N2, and He Polymer 54:6471-6478 doi:http://dx.doi.org/10.1016/j.polymer.2013.09.044

Park CB, Baldwin DF, Suh NP (1995) Effect of the pressure drop rate on cell nucleation in continuous processing of microcellular polymers Polym Eng Sci 35:432-440 doi:10.1002/pen.760350509

Pilla S, Kim SG, Auer GK, Gong S, Park CB (2009) Microcellular extrusion-foaming of polylactide with chain-extender Polym Eng Sci 49:1653-1660 doi:10.1002/pen.21385

Pilla S, Kim SG, Auer GK, Gong S, Park CB (2010a) Microcellular extrusion foaming of poly(lactide)/poly(butylene adipate-co-terephthalate) blends Mater Sci Eng 30:255-262 doi:http://dx.doi.org/10.1016/j.msec.2009.10.010

Pilla S, Kramschuster A, Lee J, Clemons C, Gong S, Turng L-S (2010b) Microcellular processing of polylactide-hyperbranched polyester-nanoclay composites J Mater Sci 45:2732-2746 doi:10.1007/s10853-010-4261-6

Robertson CG, Roland CM, Puskas JE (2002) Nonlinear rheology of hyperbranched polyisobutylene J Rheol 46:307-320 doi:http://dx.doi.org/10.1122/1.1428318

Seo J-H, Han J, Lee KS, Cha SW (2012) Combined Effects of Chemical and Microcellular Foaming on Foaming Characteristics of PLA (Poly Lactic Acid) in Injection Molding Process Polym Plast Tech Eng 51:455-460 doi:10.1080/03602559.2011.651239

So K (2012) Automotive giants turn to bioplastics Eur Plast News 39:31-32

Soppimath KS, Aminabhavi TM, Kulkarni AR, Rudzinski WE (2001) Biodegradable polymeric nanoparticles as drug delivery devices J Control Release 70:1-20 doi:http://dx.doi.org/10.1016/S0168-3659(00)00339-4

Spitael P, Macosko CW (2004) Strain hardening in polypropylenes and its role in extrusion foaming Polym Eng Sci 44:2090-2100 doi:10.1002/pen.20214

Taki K, Kitano D, Ohshima M (2011) Effect of Growing Crystalline Phase on Bubble Nucleation in Poly(L-Lactide)/CO2 Batch Foaming Ind Eng Chem Res 50:3247-3252 doi:10.1021/ie101637f

Theinsathid P, Chandrachai A, Keeratipibul S (2009) Managing Bioplastics Business Innovation in Start Up Phase 2009 4 doi:82-93

Tian J, Yu W, Zhou C (2006) The preparation and rheology characterization of long chain branching polypropylene Polymer 47:7962-7969 doi: http://dx.doi.org/10.1016/j.polymer.2006.09.042

Van Ruymbeke E, Keunings R, Bailly C (2005) Prediction of linear viscoelastic properties for polydisperse mixtures of entangled star and linear polymers: Modified tube-based model and comparison with experimental results J Non-Newtonian Fluid Mech 128:7-22 doi:http://dx.doi.org/10.1016/j.jnnfm.2005.01.006

Wang J, Zhu W, Zhang H, Park CB (2012a) Continuous processing of low-density, microcellular poly(lactic acid) foams with controlled cell morphology and crystallinity Chem Eng Sci 75:390-399 doi:http://dx.doi.org/10.1016/j.ces.2012.02.051

Wang L, Jing X, Cheng H, Hu X, Yang L, Huang Y (2012b) Blends of Linear and Long-Chain Branched Poly(l-lactide)s with High Melt Strength and Fast Crystallization Rate Ind Eng Chem Res 51:10088-10099 doi:10.1021/ie300526u

Wang L, Jing X, Cheng H, Hu X, Yang L, Huang Y (2012c) Rheology and Crystallization of Long-Chain Branched Poly(l-lactide)s with Controlled Branch Length Ind Eng Chem Res 51:10731-10741 doi:10.1021/ie300524j

Wang L, Jing X, Cheng H, Hu X, Yang L, Huang Y (2012d) Rheology and Crystallization of Long-Chain Branched Poly(l-lactide)s with Controlled Branch Length Ind Eng Chem Res 51:10731-10741 doi:10.1021/ie300524j

Wang L, Wan D, Qiu J, Tang T (2012e) Effects of long chain branches on the crystallization and foaming behaviors of polypropylene-g-poly(ethylene-co-1-butene) graft copolymers with well-defined molecular structures Polymer 53:4737-4757 doi:http://dx.doi.org/10.1016/j.polymer.2012.08.036

Wever DAZ, Picchioni F, Broekhuis AA (2013) Branched polyacrylamides: Synthesis and effect of molecular architecture on solution rheology Eur Polym J 49:3289-3301 doi:http://dx.doi.org/10.1016/j.eurpolymj.2013.06.036

Wong A, Guo Y, Park CB (2013) Fundamental mechanisms of cell nucleation in polypropylene foaming with supercritical carbon dioxide Effects of extensional stresses and crystals J Supercrit Fluids 79:142-151 doi:http://dx.doi.org/10.1016/j.supflu.2013.02.013

Wong A, Leung SN, Li GYG, Park CB (2007) Role of Processing Temperature in Polystyrene and Polycarbonate Foaming with Carbon Dioxide Ind Eng Chem Res 46:7107-7116 doi:10.1021/ie070551z

Wood-Adams PM, Dealy JM, deGroot AW, Redwine OD (2000) Effect of Molecular Structure on the Linear Viscoelastic Behavior of Polyethylene Macromolecules 33:7489-7499 doi:10.1021/ma991533z

You J, Lou L, Yu W, Zhou C (2013) The preparation and crystallization of long chain branching polylactide made by melt radicals reaction J Appl Polym Sci 129:1959-1970 doi:10.1002/app.38912

Zhu W, Zhou N, Wu H (2006) Multiplex shear stress-induced nucleation in dynamic microcellular foaming process Polym Eng Sci 46:1728-1738 doi:10.1002/pen.20651

CHAPTER 5

ARTICLE 2

Quiescent and shear-induced crystallization of linear and branched polylactides

N. Najafi[1,2], M. C. Heuzey[1] *, P. J. Carreau[1], D. Therriault[2]

1- Research Center for High Performance Polymer and Composite Systems, CREPEC, Department of Chemical Engineering, Ecole Polytechnique, Montreal, Quebec, Canada

2- Research Center for High Performance Polymer and Composite Systems, CREPEC, Department of Mechanical Engineering, Ecole Polytechnique, Montreal, Quebec, Canada

Parts of this work have been presented at the
85th annual meeting of the Society of Rheology (October 2013)
30th International Conference of the Polymer Processing Society, PPS, (June 2014)

Accepted for publication in *Rheologica Acta*

5.1 Abstract

The quiescent and shear-induced isothermal crystallization behavior of linear and long chain branched (LCB) polylactides (PLAs) was investigated at a temperature of 130 ^{o}C. LCB-PLAs were produced by the reaction with a multi-functional chain extender, Joncryl©. In quiescent crystallization the presence of the LCB structure accelerated the nucleation process and reduced the induction time, depending on the level of branching. The impact of shear strain, and shear rate on crystallization was also examined. The shear-induced crystallization of the linear and LCB-PLAs was affected by both the total shear strain and shear rate. The crystallization kinetics of the LCB-PLAs was more affected by shear than that of the linear PLA. The crystalline morphology of the linear and LCB- PLAs under quiescent and step shear rate conditions was examined using a Linkam optical shearing system. An increase in the spherulite density was observed in the strained melt of both linear (33 %) and LCB-PLAs (15 %), in comparison with those of unstrained counterparts. Optical micrographs confirmed that the crystal nucleation was affected by the shear flow. Long chain branching significantly promoted the nucleation density (6.7 times), although it diminished the crystal growth rate from 4.4 to 2.0 µm/min.

Keywords: polylactide, chain extender, long chain branching, shear-induced crystallization, induction time

5.2 Introduction

Polymer crystallization is a process involving partial arrangement of molecular chains initiated from nucleation and followed by subsequent crystalline growth (Ryan *et al.* 1999; Li *et al.* 2000; Kausch *et al.* 2005). The crystal formation and spherulitic structure in bulk polymers have been observed by polarized optical microscopy (Wunderlich and Mielillo 1968; Norton and Keller 1985; Tsuji and Ikada 1996; Eder and Janeschitz-Kriegl 2006) and atomic force (Li *et al.* 2000; Kausch *et al.* 2005). Once the nucleation occurs, segments of a chain tend to fold on themselves and form an ordered structure called lamellae. The formed lamellae, then, arrange themselves into larger spheroidal entities named spherulites (Li *et al.* 2000; Kausch *et al.* 2005).

Polymeric materials generally form a semi-crystalline rather than fully crystalline structure (Binsbergen 1966) because of defects. The mechanical and physical properties of semi-crystalline polymers have been found to strongly depend on the crystallization degree and type of morphology

(Suryanegara *et al.* 2009; Han *et al.* 2013). The quality and level of crystallization, i.e. the nucleation density, size and shape of the crystallites, are affected by different factors including molecular weight, molecular structure, thermal history, cooling rate, presence of additives, and melt processing conditions (Hadinata *et al.* 2005; Yu *et al.* 2009; Jabbarzadeh and Tanner 2010; Najafi *et al.* 2013).

In most polymer processing operations such as extrusion, injection molding, fiber spinning, and film blowing, the polymeric chains are subjected to complex flow fields (elongation, shear, mixed flows) (Lellinger *et al.* 2003; Baert and Van Puyvelde 2006; Ma *et al.* 2013). Shearing the molten polymer during processing, indeed, plays a key role on crystallization and, therefore, on the final properties of the product (Lellinger *et al.* 2003; Yu *et al.* 2009; Jabbarzadeh and Tanner 2010; Ma *et al.* 2013). To provide a fundamental understanding of the crystallization phenomenon during processing, it is required to separate the thermal and flow contributions. The global effect of flow on crystallization is known as flow-induced crystallization (FIC). To investigate FIC of polymers, steady shear and step-shear flows can be applied to the molten polymer (Wereta and Gogos 1971; Lellinger *et al.* 2003; Ma *et al.* 2013).

In the initial studies on flow-induced crystallization of molten polymers, Haas and Maxwell (1969); Wereta and Gogos (1971) examined the structure evolution in continuous flow fields. Rheological parameters such as complex viscosity and dynamic moduli can also be monitored to study the kinetics of the crystallization process. For example, (Yuryev and Wood-Adams 2010) considered the sensitivity of rheological properties to crystallinity to accurately determine the onset of crystallization. Once the crystals are nucleated and start growing from the melt state, the linear viscoelastic properties such as the complex viscosity, η^*, storage modulus, G', and loss modulus, G'', are found to increase since they are very sensitive to the structural changes occurring in the polymer (Madbouly and Ougizawa 2003). This stresses the impact of flow on the crystallization under steady shear, giving rise to a self-accelerating mechanism (Ma *et al.* 2013). Step-shear experiments were carried out by Liedauer *et al.* (1993) where the sample was subjected to a step shear rate flow for a short time, and then, allowed to crystallize at rest. Two different strategies have been used in step shear rate flow studies: (i) applying shear in the molten state, followed by a quench to the final crystallization temperature (Madbouly and Ougizawa 2003; Jabbarzadeh and Tanner 2010), (ii) applying shear for short times at the crystallization temperature; then, after the

cessation of flow induced nucleation is followed by crystal growth (Baert and Van Puyvelde 2006; Favaro *et al.* 2009; Ma *et al.* 2013).

Shear-induced crystallization has been investigated on high density polyethylene (HDPE) by Chen *et al.* (2007), on polybutene (PB) by Acierno *et al.* (2003), on polypropylene (PP) by Ma *et al.* (2013), on polycaprolactone (PCL) by Lellinger *et al.* (2003); Madbouly *et al.* (2003); Acierno *et al.* (2006), on polytrimethylene terephthalate (PTT) by Favaro *et al.* (2009) and finally on polyethylene terephthalate (PET) by Ahn *et al.* (2002) at low and high shear rates. In the vast majority of cases, it was found that the shear flow mainly affected the crystal nucleation rate. Although shear-induced crystallization of linear polymers has been frequently investigated, only a few studies have examined the effect of long chain branching on flow-induced crystallization (Heeley *et al.* 2006; Yu *et al.* 2009). It was reported that the presence of a small fraction of high molecular weight macromolecules significantly influences the shear-induced crystallization kinetics (Kumaraswamy *et al.* 2002; Acierno *et al.* 2003; Eder and Janeschitz-Kriegl 2006).

Polylactic acid or polylactide (PLA) is a biodegradable, thermoplastic, aliphatic polyester synthesized from renewable resources such as corn, starch, and sugarcane (Drumright et al. 2000; Garlotta 2001; Najafi *et al.* 2012; Eslami and Kamal 2013). PLA can be synthesized either by direct condensation polymerization of lactic acid (Nagahata *et al.* 2007; Achmad *et al.* 2009; Wang *et al.* 2009) or ring opening polymerization of cyclic lactide (Kim *et al.* 1992). The synthesized polymer using these two methods is respectively called polylactic acid, with low molecular weight, and polylactide, which contains high molecular weight polymer chains (Lunt 1998). Stereo-chemically pure PLAs are categorized into *L*-lactide (PLLA) and *D*-lactide (PDLA) (Drumright *et al.* 2000). Depending on the *D*-lactide content, it can be semi-crystalline or totally amorphous (Drumright *et al.* 2000; Najafi *et al.* 2012). A synthesized PLA comprising less than 7 % *D*-lactide will be semi-crystalline, while the degree of crystallinity is enhanced with increasing *L*-lactide monomer purity (Drumright *et al.* 2000).

Polylactide is one of the most promising candidates from both economic and environmental perspectives to substitute some petroleum-based polymers such as polystyrene (PS), polyethylene terephthalate (PET), and polyurethane (PU) (Garlotta 2001). A relatively low melt strength and non-strain hardening behavior of linear PLA is known to limit its applications in foaming, blow molding, and thermoforming (Liu *et al.* 2012; Wang *et al.* 2012b; Wang *et al.* 2012a; Eslami and

Kamal 2013; Najafi *et al.* 2014). An efficient technique that has been used to improve the melt strength of linear polymers is the introduction of long chain branches into the polymer backbone (Najafi *et al.* 2012; Wang *et al.* 2012a; Eslami and Kamal 2013; Najafi *et al.* 2014).

In our earlier work (Najafi *et al.* 2012; Najafi *et al.* 2014), it was found that the incorporation of a multifunctional chain extender, Joncryl©, into PLA had a profound effect on the molecular weight and led to the formation of a long-chain branched (LCB) structure. The impact of the LCB structure on rheological properties and foaming behavior of PLA was discussed in details in our most recent study (Najafi *et al.* 2014). The aim of the present investigation is to determine the impact of the branched molecular structure and shear on the isothermal quiescent and shear-induced crystallization kinetics, and morphology of PLA. To this end, LCB-PLAs were prepared in the presence of a multifunctional chain extender using two different PLA grades and different processing strategies. Molten polymers are subjected to high shear rate for short times as they pass through dies and nozzles. An intense shear strain is accordingly imposed on the melt. Reproducing these conditions in a rotational rheometer is not possible, however if a low shear rate is applied for a long time a considerable strain is experienced by the sample. This study is also limited to the nucleation regime, and consequently shish-kebab like structures, which have a major influence on properties, were not observed in this work. First, the quiescent crystallization behavior of linear and LCB-PLAs is reported. Then, the shear-induced crystallization kinetics and morphology of PLAs of different molecular structures are examined.

5.3 Experimental

5.3.1 Materials

The commercial grades of polylactide used in this study, PLA 3001D and PLA2003D, were purchased from NatureWorks LLC Co. (USA). They are semi-crystalline linear polyesters with *L*-lactide to *D*-lactide ratio of 98.5: 1.5 (Kramschuster and Turng 2009) and 95.75: 4.25 (Mujica-Garcia *et al.* 2014), respectively. As reported by the supplier, PLA 3001D, with a melt flow rate (MFR) of 22 g/10 min under a load of 2.16 kg at 210 °C, is less viscous than PLA 2003D with a MFR of 6 g/10 min in the same conditions. Joncryl® ADR-4368F was used as the chain extender (CE). It is a modified acrylic copolymer with multiple epoxy functions, which was supplied by BASF (Germany). Details on the reaction mechanisms of Joncryl with PLA can be found in (Meng

et al. 2012) whereas the effect of Joncryl on the rheological properties of PLA can be found in (Najafi *et al.* 2012; Najafi *et al.* 2014).

5.3.2 Material processing

Melt compounding of PLA with the chain extender (CE) was performed using a counter-rotating Brabender Plasti-Corder® internal mixer. Before compounding, the PLA granules were dried at 70 °C in a vacuum oven for 24 h. The dried PLA was then blended in the molten state with 0.4 and 0.7 wt% CE in the internal mixer at a set temperature of 185 °C. The mixing was conducted under a nitrogen atmosphere at a rotation speed of 100 rpm for 10 min, after which a relatively steady-state torque was established. Neat PLAs were dried, processed, and used as references in this study. To further examine the impact of CE and molecular topology, PLAs containing 0.4 wt% of CE were prepared using two different compounding strategies. In the first strategy (S1), PLA and 0.4 wt% of CE were directly mixed in the internal mixer under the aforementioned conditions. In the second strategy (S2), PLA was first compounded with 0.8 wt% of CE in the internal mixer for 10 min at conditions stated above. The resulting blend was dried in a vacuum oven (70 °C) for 24 h. Then, in the second run, it was mixed with the neat PLA at a weight ratio of 50:50 in the same conditions. The processed materials were placed in a vacuum oven (70 ºC) for 24 h. To investigate the rheological properties, disk-shaped samples with 25 mm diameter and 1.5 mm thickness were prepared by compression molding. This process was conducted under a nitrogen atmosphere at 185 ºC and 20 MPa for 8 min, followed by a fast cooling to ambient temperature on a metal plate. The prepared samples were stored in a desiccator until used.

5.3.3 Characterization

The prepared disk-shaped samples were used to measure dynamic rheological properties. Small amplitude oscillatory shear (SAOS) experiments were conducted using a MCR-501 rotational rheometer (Anton Paar, Austria) with parallel plate flow geometry of 25 mm diameter and 1.1 mm gap size. The strain amplitude was set at 0.05, large enough to give a reliable signal while remaining in the linear viscoelastic regime prior to crystallization. The quiescent crystallization behavior was investigated at a frequency, ω, of 6.28 rad.s^{-1} and the results were then used as the reference point for the study of the shear-induced crystallization. To examine the effect of ω on the quiescent crystallization kinetics, measurements were also conducted at ω = 1 rad.s^{-1} for the neat

PLA 3001D sample and for the 0.7 wt% CE formulation. The shear-induced isothermal crystallization studies followed the experimental protocol illustrated in Figure 5.1: i) The disk-shaped sample was heated up to 190 ºC, above the polymer melting point (160 ºC), at a rate of 30 ºC/min under a nitrogen atmosphere. ii) The molten sample was held at this temperature for 10 min to remove the thermal history and obtain an isotropic melt. iii) The sample was cooled down to 180 ºC. iv) A constant shear rate ($\dot{\gamma}$) ranging from 0.1 to 1 s^{-1} was, then, applied to the melt for a time varying from 1 to 10 min prior to starting the test. v) The molten sample was cooled down to the crystallization temperature, T_c (120 or 130 ºC), at a rate of 30 ºC/min. vi) Time sweep tests were, thereafter, conducted at T_c and frequency, ω, of 6.28 rad.s^{-1} to monitor the *G'* and η*.

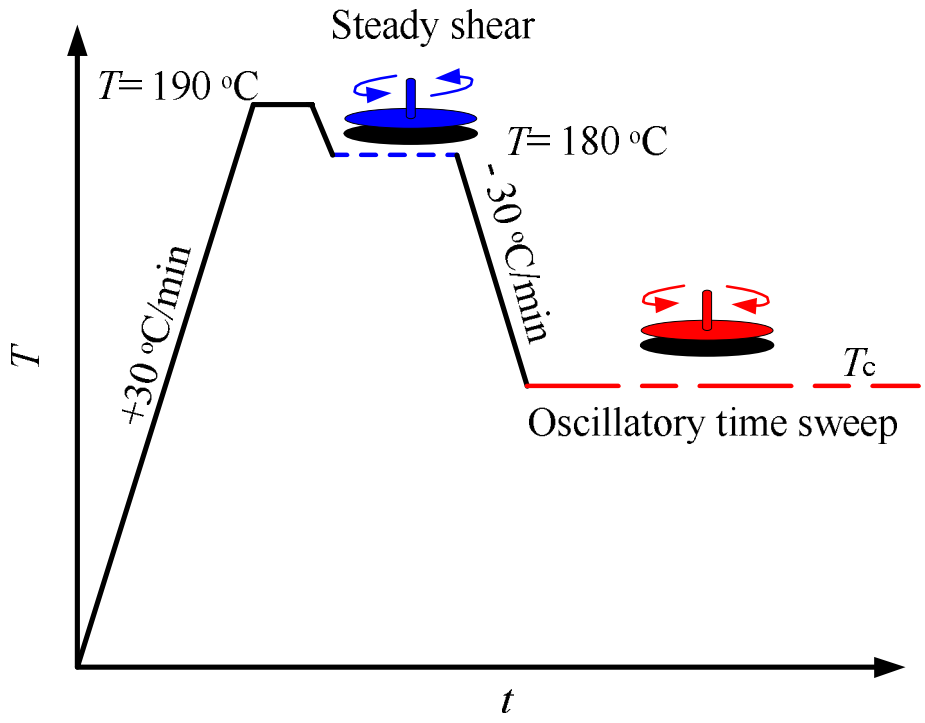

Figure 5.1: Schematic representation of the thermal and pre-shearing treatments applied to the linear and LCB-PLAs before starting the isothermal crystallization test.

In a previous study in our research group, Arias (Arias 2014) imposed a constant normal force throughout her rheological experiments to counterbalance the shrinkage of PLA during cooling and crystallization and improve the reproducibility of the tests. In the present work, the results obtained

using the normal force control were compared with those obtained without. No significant differences were observed and the measurements were therefore performed without imposing a normal force.

The isothermal melt-crystallization behavior of linear and LCB- PLAs was studied at 110 °C. All the specimens were first heated at 60 °C/min to 200 °C and held there for 5 min. The molten samples were then cooled down to crystallization temperature (T_c) at 30 °C/min. The samples were kept at T_c until the crystallization was complete.

The morphology evolution of linear and LCB-PLA was monitored using a Linkam CSS450 (Surrey, UK) shearing hot stage in quiescent and shear flow conditions. This device operates with the same principle as a rotational rheometer with a parallel plate flow geometry. The Linkam system is able to impose shear on the melt although it cannot measure the melt viscosity (torque); hence, this instrument was strictly used for visualization purposes. To this end the sample was placed in the Linkam optical cell and heated up to 200 °C at 30 °C/min and kept for 10 min to eliminate the thermal history. The molten polymer was pressed between the two plates of the Linkam cell to achieve a gap of 200 µm. The sample was then cooled down to 180 °C and subjected to an imposed shear rate of 1 s^{-1} for 5 min. After stopping the shear flow, the temperature was reduced to the T_c (130 °C). In the absence of shear flow, the sample was directly cooled at the same rate to the set temperature of 130 °C to observe crystallization. The pictures were then recorded by a CCD camera connected to a video recorder. Quantitative analysis of the digital images in terms of nucleation density and growth rate was carried out using appropriate software (ImageJ, NIH, USA).

5.4 Results and discussion

5.4.1 Crystallization in quiescent conditions

The quiescent crystallization behavior of linear and LCB-PLAs prepared using the two different strategies was investigated by rotational rheometer at T of 120 and 130 °C. The evolution of η^* with time is presented here. The initial values of $\eta^*$of the linear and LCB-PLAs at crystallization temperatures of 120 and 130 °C are presented in Table 5.1.

Table 5.1: Initial value of the complex viscosity, $\eta^*_{t=0}$, of the linear and LCB-PLAs CE, at crystallization temperatures of (a) 120 and (b) 130 °C. The frequency of the rheological test, ω, was set at 6.28 rad.s^{-1}.

Description			Sample Name	$\eta^*_{(t=0)}$ (kPa.s)	$\eta^*_{(t=0)}$ (kPa.s)
PLA grade	CE concentration (wt%)	Mixing strtategy		T =120 °C	T =130 °C
PLA2003D	0	S1	PLA2003-Neat	57 ± 1.4	34 ± 1.1
PLA 2003D	0.4	S1	PLA2003-0.4 J-S1	83 ± 2.7	60 ± 2.3
PLA 2003D	0.4	S2	PLA2003-0.4 J-S2	88 ± 2.5	69 ± 1.9
PLA 2003D	0.7	S1	PLA2003-0.7 J- S1	93 ± 4.6	74 ± 3.5
PLA3001D	0	S1	PLA 3001-Neat	43 ± 1.3	25 ± 1.3
PLA 3001D	0.4	S1	PLA3001-0.4 J-S1	60 ± 2.1	40 ± 1.9
PLA 3001D	0.4	S2	PLA3001-0.4 J-S2	66 ± 2.4	43 ± 2.1
PLA 3001D	0.7	S1	PLA 3001-0.7 J-S1	76 ± 3.5	55 ± 3.4

The major potential sources of errors in rheological measurements are related to temperature control, strain and torque measurement sensitivity of the rheometer. The $\eta^*_{(t=0)}$ of the neat PLA 2003D is larger than that of the neat PLA 3001 D due to its larger molecular weight. The incorporation of the chain extender into the neat PLAs, as shown here and discussed in our previous work (Najafi *et al*. 2014), considerably increases its rheological response, depending on the CE content.

To ensure that the samples were free of crystals when starting the isothermal test at crystallization temperature, the initial values of the measured complex viscosity at t=0 ($\eta^*_{(t=0)}$) (Table 5.1) were compared with the values predicted by the Arrhenius equation at T_c. To this end the SAOS data of two systems, the neat PLA 3001D, with low crystallization rate, and the corresponding S2-compounded sample, with the highest crystallization rate, were obtained at 200 °C and at lower temperatures down to 140 °C, following a cooling at 30 °C/min and during time periods short enough to avoid crystallization. Figures 5.2a and b present the variations of the η^* as a function of ω for these systems at various temperatures, ranging from 140 to 200 °C. We note the very large viscosity increases as the temperature is decreased from 200 to 140 °C; also, as noted in Table 5.1 the viscosity of the PLA 3001D containing 0.4 wt% CE (Figure 5.2b) is considerably larger than that of the neat PLA 3001D (Figure 5.2a). The η^* data have been shifted using the shift factors obtained from the storage modulus and the master curves are plotted in Figures 5.2c and d.

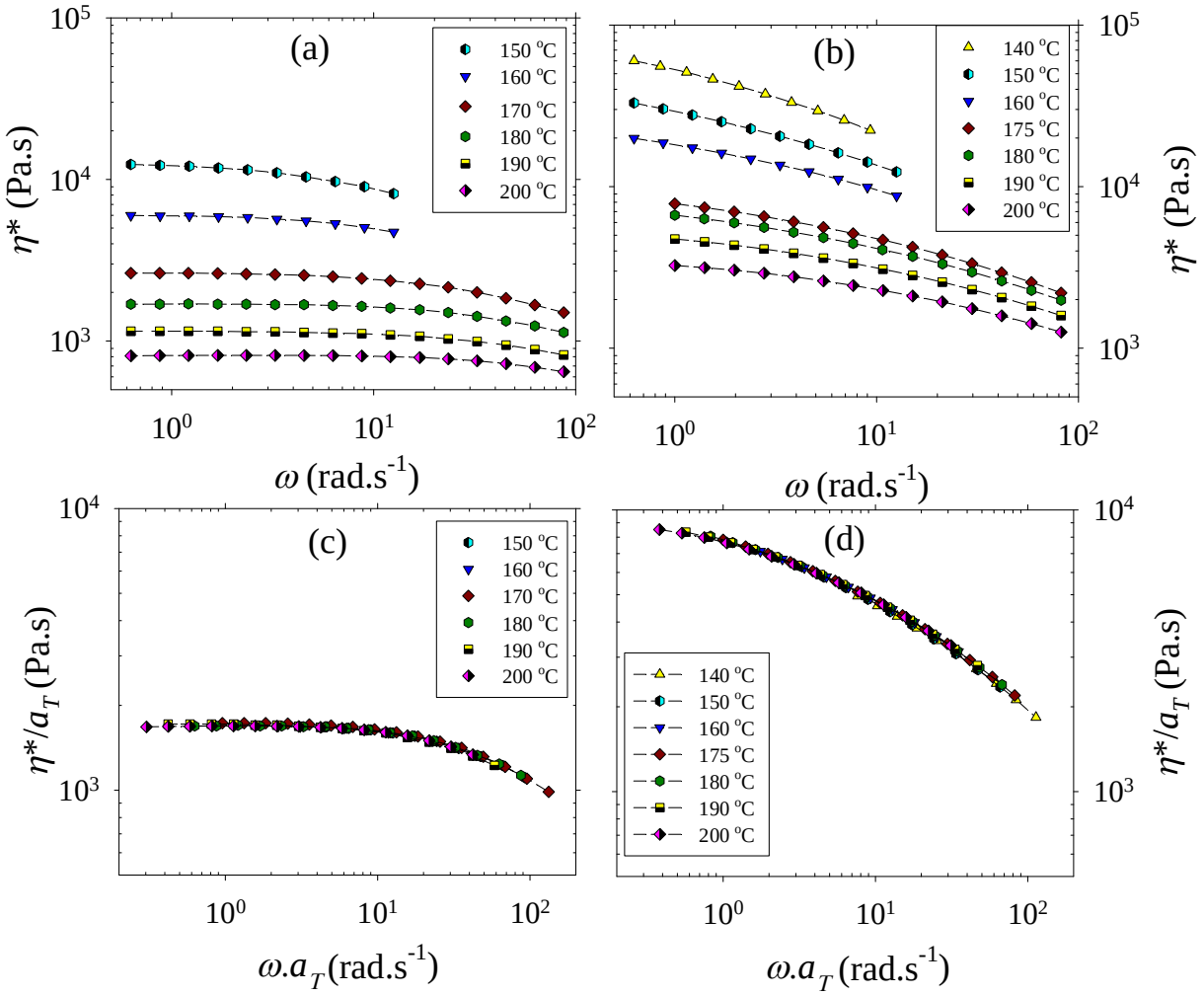

Figure 5.2: The complex viscosity of (a) neat PLA 3001D, (b) PLA 3001D containing 0.4 wt% CE prepared using strategy S2, and the complex viscosity master curves of (c) neat PLA 3001D, (d) PLA 3001D containing 0.4 wt% CE prepared using strategy S2, at temperatures ranging from 140 to 200 °C.

The calculated shift factors (a_T) over this broad range of temperatures (140-200 °C) are plotted in Figure 5.3 (filled squares) to determine the flow activation energy (E_a).

A change of slope, related to E_a, is observed for the neat PLA at T = 180 °C and the S2-compounded sample at T = 175 °C (around T_g + 100 °C), indicating that the flow activation energy is temperature dependent over this broad temperature range. Therefore, a narrower range of data (the lower temperature region) was used to extrapolate the shift factors at T_c using the Arrhenius law.

The experimental shift factors at T_c (filled triangles) were obtained by horizontally shifting the initial value of the storage modulus ($G'_{t=0}$) along the frequency axis on the G' data obtained at the reference temperatures (180 °C for neat PLA, and 175 °C for the S2 sample). A comparison of the predicted (unfilled squares) with the measured (filled triangles) shift factors in Figure 5.3a reveals that they are the same at T = 120 and 130 °C, confirming that the neat PLA contained no significant amount of crystals at the beginning of the isothermal crystallization test. Similarly, the measured shift factor of the S2-compounded sample at T = 130 °C (corresponding to η*=43 kPa.s) is quite close to the predicted one (η*=42 kPa.s). However, the measured complex viscosity at 120 °C (66 kPa.s) is higher than the predicted complex viscosity (60 kPa.s) from a_T (Figure 5.3b), indicating the presence of a significant amount of crystals at the beginning of the test at 120 °C.

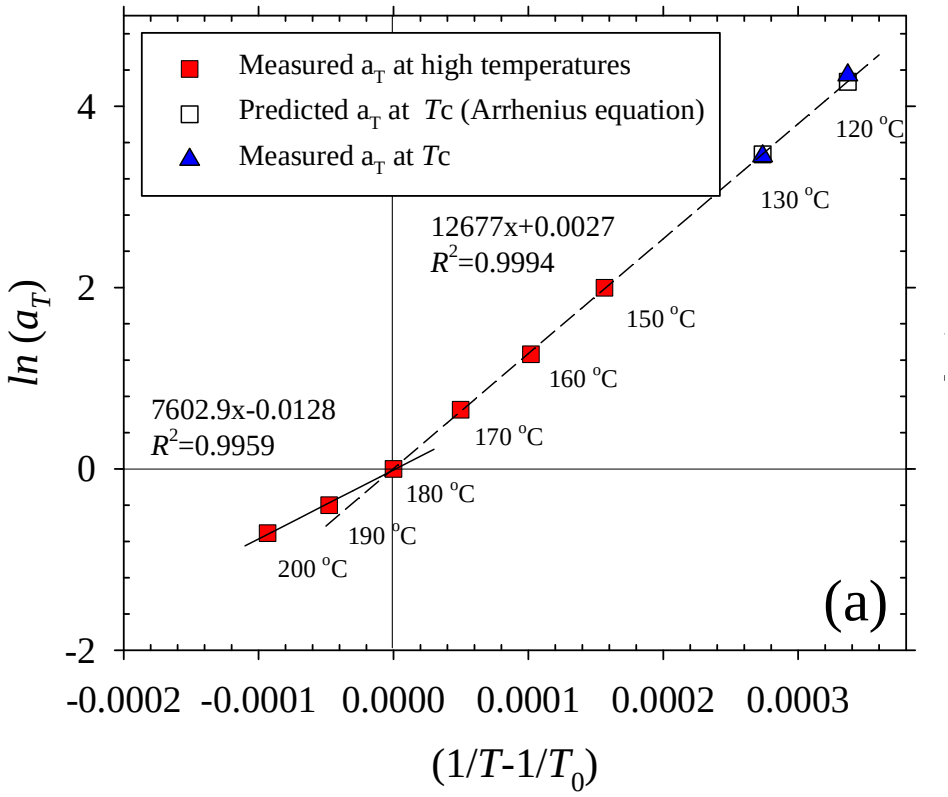

Figure 5.3: Arrhenius plots of the shift factor as a function of the reciprocal (absolute) temperature for (a) Neat PLA 3001D, (b) PLA 3001D containing 0.4 wt% CE prepared using strategy S2, at temperatures from 120 to 200 °C.

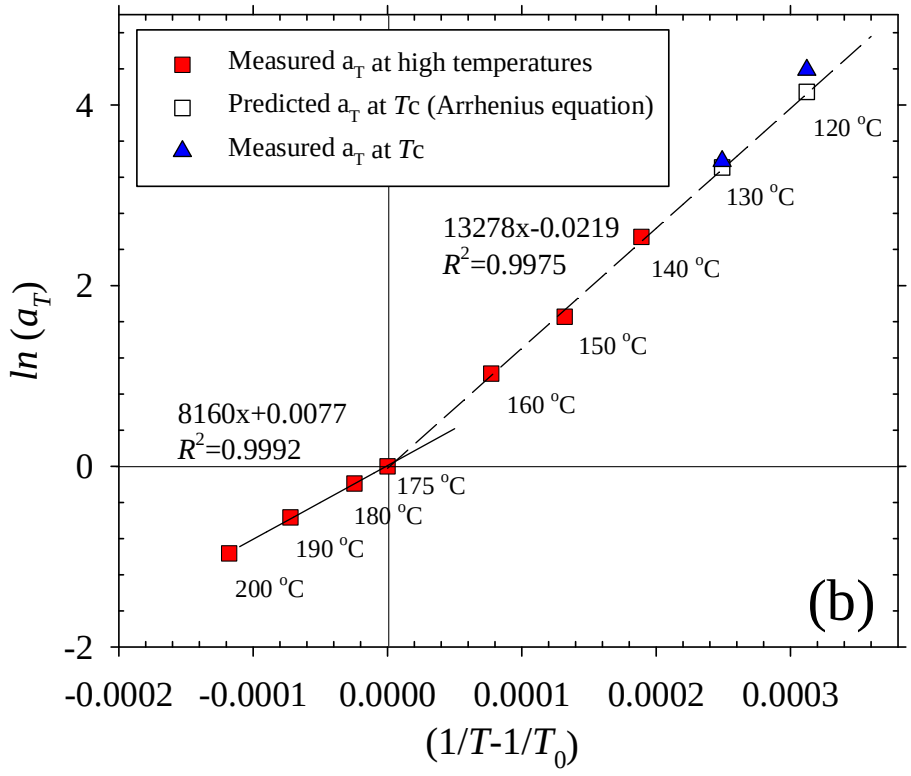

Figure 5.3 (continued): Arrhenius plots of the shift factor as a function of the reciprocal (absolute) temperature for (a) Neat PLA 3001D, (b) PLA 3001D containing 0.4 wt% CE prepared using strategy S2, at temperatures from 120 to 200 °C.

In order to verify this possibility, tests with similar temperature cycling conditions were performed in differential scanning calorimetry (DSC). DSC results (not shown here for brevity) showed that the crystallization onset (or induction) time for the neat PLA and S2-compounded sample was, respectively, 255 and 135 s at 130 °C. The onset time was reduced to 128 s in the case of the neat PLA and 65 s for the S2-compounded sample as the crystallization temperature was decreased to 120 °C. In the rheometer, once the temperature is lowered to T_c, the sample needs time to reach thermal equilibrium during which the viscoelastic properties rapidly increase and reach steady state values. Based on the rheological measurements, the minimum time to reach to steady state is estimated to be 100 s at T_c of 130 °C and 130 s at T_c of 120 °C. Considering that the time at 130 °C (100 s) is less than the onset time obtained from DSC measurements, it can be concluded that all the samples are free from crystals in these conditions. Similarly, the neat PLA is free of crystals

when starting the SAOS isothermal test at T_c of 120 °C. Consequently, the measured complex viscosity is the same as that predicted by the Arrhenius equation (Figure 5.3). However, in the case of the S2-compounded sample, the time required to reach thermal equilibrium at 120 °C (130 s) is longer than its crystallization onset time (65 s from DSC). Hence, further crystallization studies were performed only at T_c = 130 °C.

The effect of the applied frequency, ω, on the quiescent crystallization kinetics is illustrated in Figure 5.4, which presents the reduced complex viscosity, $\eta_r^* = \eta^*_{(t)} / \eta^*_{(t=0)}$, of the linear and LCB-PLAs (PLA 3001D containing 0.7 wt% CE) as a function of time at frequencies of 1 and 6.28 rad.s^{-1} and T_c of 130 °C.

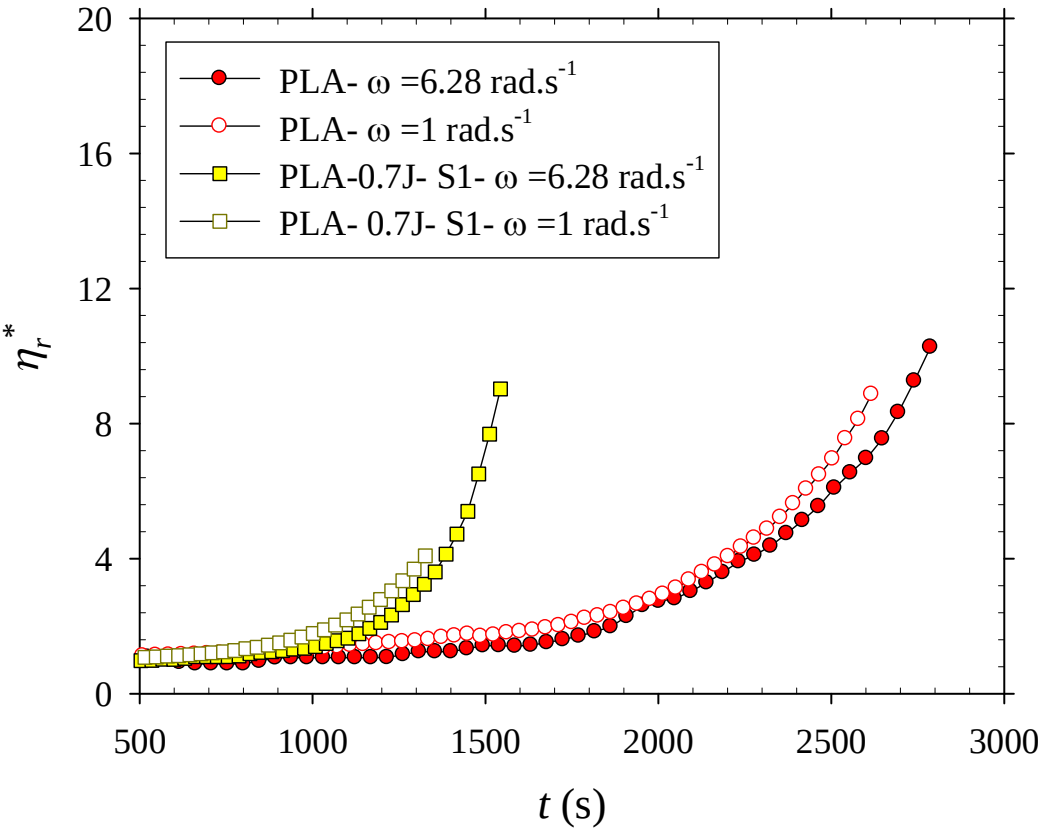

Figure 5.4: Reduced complex viscosity, η_r^*, of the linear and LCB-PLAs (3001D) as a function of time at ω of 1 and 6.28 rad.s^{-1}. The crystallization temperature was set at 130 °C.

The η_r^* value starts to slowly increase at the early stage of the test, and then increases rapidly. The substantial increase in η_r^* with time is attributed to the growth of the nucleated crystals. A continuous increase in the crystalline fraction strongly decreases the chain mobility, leading to dramatic changes in the rheological properties. Due to transducer overload near the end of the crystallization process, the later data are not reliable and not reported. The results shown in Figure 5.4 indicate that the onset of crystallization is marginally affected by frequency, although η_r^* seems to further increase with time at the lower frequency of 1 rad.s^{-1}. There are two possible explanations for this difference: (i) the impact of the formed crystals (as a solid part) are more pronounced at lower frequencies, (ii) a decreased elasticity and stiffness of the polymer chains at lower frequencies facilitates the chain-folding process (Hu 2001) and increases the crystallization kinetics. Considering that the effect of ω on crystallization is marginal, further studies were conducted at ω = 6.28 rad.s^{-1}.

The η_r^* evolution of both grades of PLA, PLA 2003D and PLA 3001D, containing various quantities of CE is presented as a function of time at ω of 6.28 rad.s^{-1} and T of 130 ^{o}C in Figures 5.5a and b, respectively.

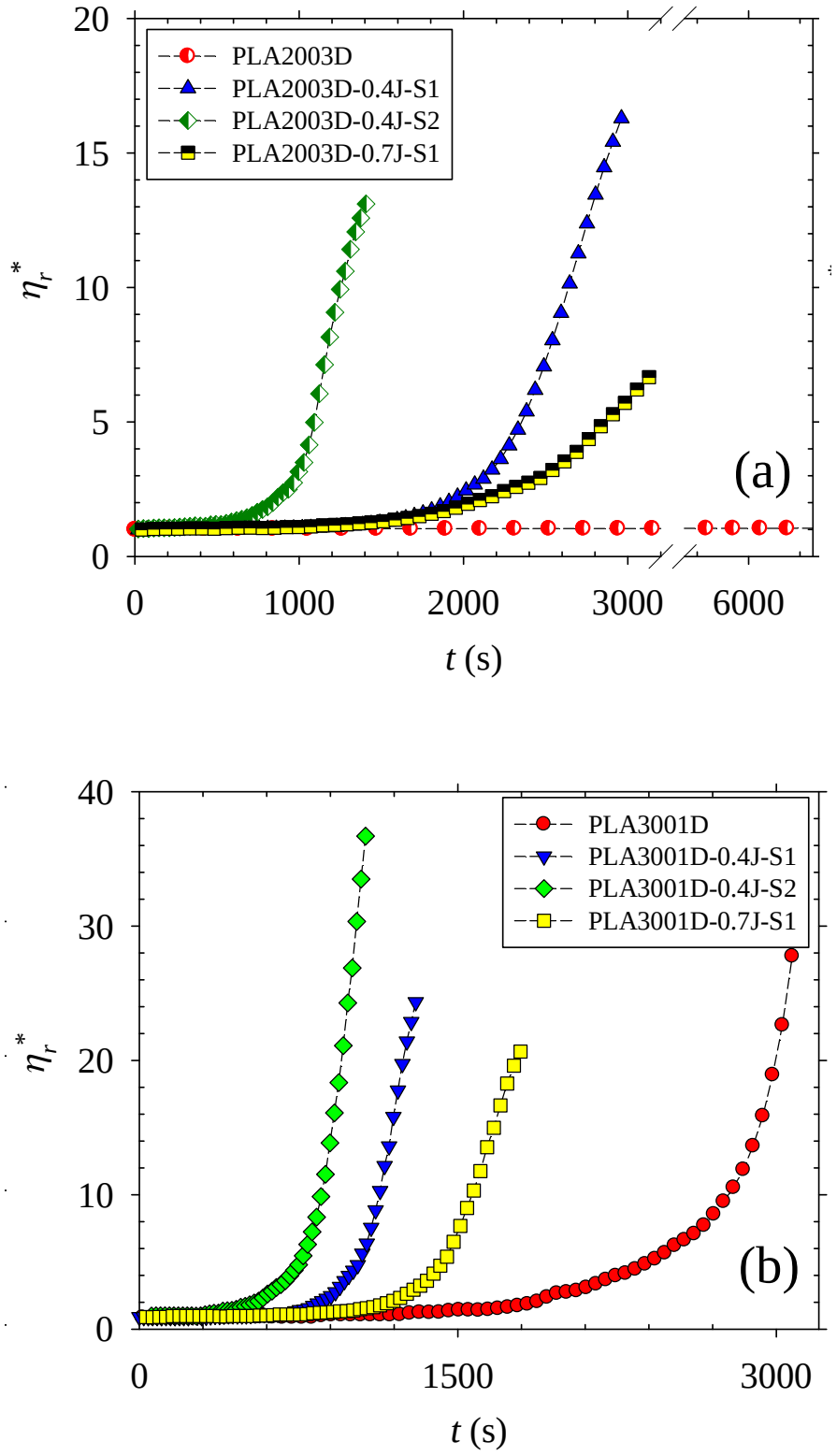

Figure 5.5: Normalized complex viscosity, η_r^*, of (a) PLA 2003D, (b) PLA 3001D with various contents of CE prepared using different strategies, as a function of time at 130 °C.

The results show the quiescent crystallization behavior of the linear and LCB PLAs at 130 °C. The neat PLAs have a linear structure with virtually no branching. The addition of 0.4 wt% CE to the neat PLA using strategy S1 results in the formation of a LCB structure. In strategy S2, increased CE content (in the first run) favored the formation of a more developed LCB structure in the compounded sample, as compared with that prepared using S1 (Najafi *et al.* 2014). Hence the incorporation of an LCB structure into linear PLA promotes the crystallization kinetics.

The induction time of crystallization, t_{in}, is an important characteristic of the kinetics of crystallization. The standardized residuals technique, r_i, (Eq. 5.1) was used to determine the induction time of PLA crystallization:

$$r_i = \frac{e_i}{\sqrt{\sigma^2}} = \frac{e_i}{\sqrt{\frac{1}{n-1}\sum_{i=1}^{n}(e_i - e)^2}} \qquad \text{Eq. 5.1}$$

where, e_i is the real residual (the difference between the measured η^* and the initial value of η^* (at t=0)) and the divider is the standard deviation of the residuals. This method has been reported to effectively define the induction time of PLA crystal formation (Yuryev and Wood-Adams 2010). In the present study, the residuals were determined as the differences between the measured complex viscosity and the initial value of the complex viscosity ($\eta^*_{t=0}$). The standardized residuals for the linear and LCB-PLAs (PLA 2003D and 3001D) at 130 °C are presented in Figures 5.6a-d. Their initial values are close to zero for some time, after which a sharp rise is observed.

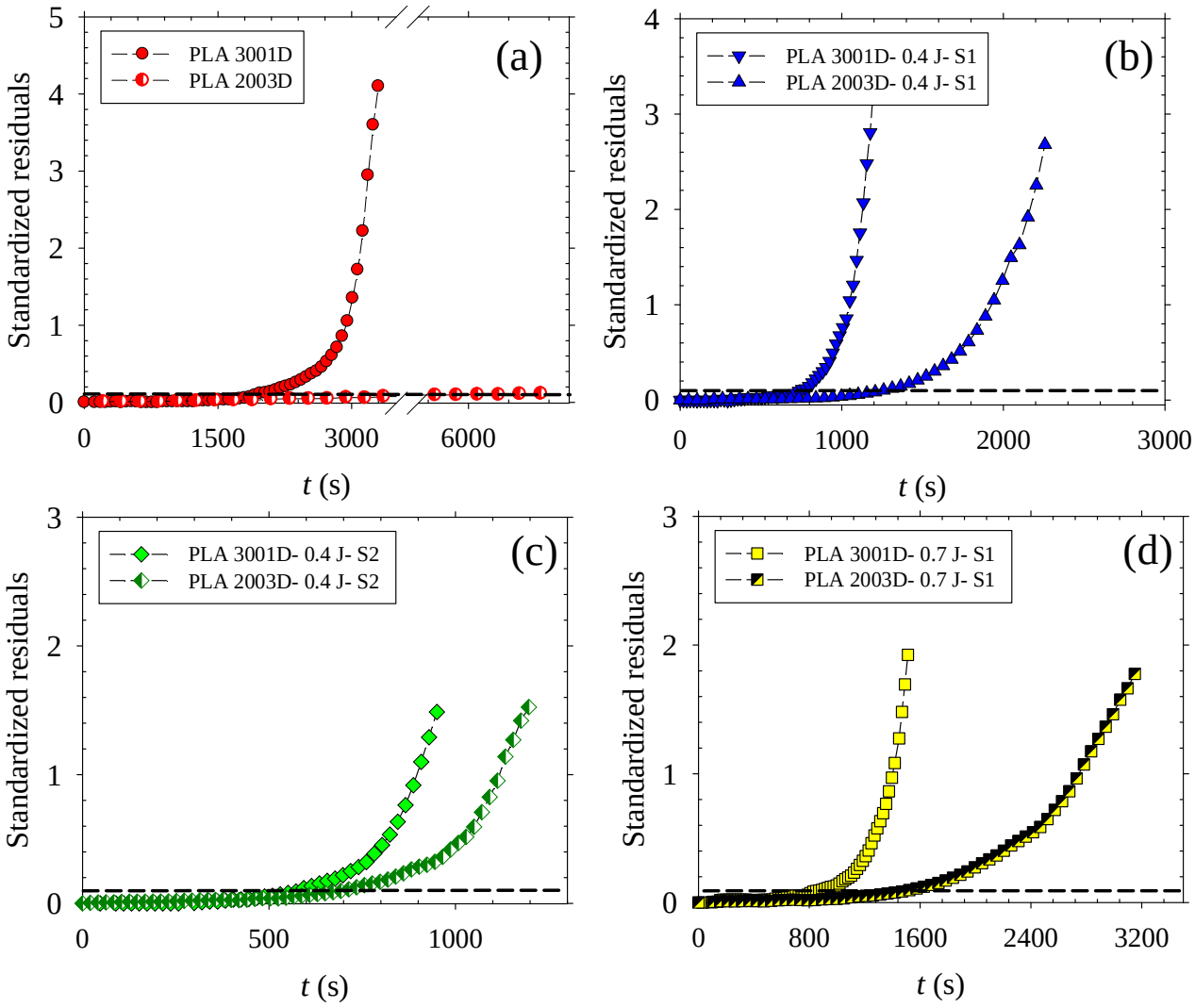

Figure 5.6: Standardized residuals of the complex viscosity, η^*, for (a) neat PLAs (2003D and 3001D), (b) PLAs containing 0.4 wt% CE prepared using strategy S1, (c) PLAs containing 0.4 wt% CE prepared using strategy S2, and (d) PLAs containing 0.7 wt% CE, as a function of time at 130 °C. The dash lines show the standardized residual value of 0.1.

To determine the induction time of crystallization, a straight horizontal line was drawn at a standardized residual value of 0.1. The time at which the curves cross this straight line is arbitrarily defined as the induction time. The induction time, $t_{in,}$ values for the linear and LCB-PLAs prepared using both grades of PLA at 130 °C are reported in Table 5.2. The experimental variability on t_{in} is less than 8 % in this work.

Table 5.2: Induction time, t_{in}, for the onset of quiescent crystallization of the linear and LCB-PLAs prepared using two different grades and strategies at 130 °C. The experimental error is less than 8%.

Sample	t_{in} at 130 °C (s)	Sample	t_{in} at 130 °C (s)
PLA2003-Neat	-	PLA 3001-Neat	1890
PLA2003-0.4 J-S1	1250	PLA3001-0.4 J-S1	730
PLA2003-0.4 J-S2	660	PLA3001-0.4 J-S2	580
PLA2003-0.7 J- S1	1570	PLA 3001-0.7 J-S1	870

For the neat PLAs, shown in Figure 5.6a and reported in Table 5.2, the onset of crystallization occurs after a long annealing time (t_{in} of PLA 2003D is not observed and that of PLA 3001D is 1890 s), suggesting that the isothermal crystallization of PLA is quite slow (Arias *et al.* 2013).

In comparison with PLA 2003D, PLA 3001D exhibits a shorter induction time due to its lower *D*-content, lower M_W, and higher crystallization ability. The chain architecture is a critical parameter affecting the crystallization kinetics (Duplay *et al.* 1999; Heeley *et al.* 2006). The newly formed branched structure resulting from the addition of 0.4 wt% CE using strategy S1 leads to a significant reduction of the induction time, from above 6500 to 1250 s and from 1890 to 730 s for PLA 2003D and 3001D, respectively, at 130 °C (Figure 5.6b). This time reduction suggests that the branched structure acts as nucleation sites for the linear chains having a higher local order, and accelerates the crystal nucleation by an heterogeneous mechanism (Yang *et al.* 2011), leading to an enhanced crystallization rate. However, the branched structure may also increase the chain folding energy barrier and hinder PLA chains from folding back into crystal lamellae (Yu *et al.* 2009). For the case examined here, i.e. 0.4 wt% CE, the negative impact of branching on the crystallization kinetics seems overridden by the nucleation ability of the branches. The onset of crystallization of PLA 2003D and PLA 3001D is further reduced to 660 and 580 s, respectively, as LCB-PLA containing 0.4 wt% CE is produced using strategy S2 (Figure 5.6c). The existence of highly branched macromolecules in comparison with sample S1 is responsible for the observed decrease of t_{in}.

The higher degree of LCB due to the addition of 0.7 wt% CE increases the induction time of PLAs as shown in Figure 5.6d and Table 5.2 (t_{in} of PLA2003D and PLA3001D increases from 660 to 1570 and from 580 to 870s, respectively). The observed increases of t_{in} may result from the detrimental impact of LCB on the chain folding energy barrier, as discussed earlier. This implies that there is a critical degree of LCB above which the effect is reversed. These finding are in good agreement with DSC results. To examine how long chain branching impacts the degree of PLA crystallinity, the isothermal crystallization behavior of linear and LCB-PLAs (PLA 3001D) has been studied at 110 °C. The neat PLA (PLA 3001D) degree of crystallinity was 13 %. As a result of heterogeneous nucleation, the extent of crystallinity increased from 13 to 27 % in LCB-PLA prepared using strategy S1. The degree of crystallinity was further enhanced (32 %) when LCB-PLA was prepared using strategy S2. The introduction of a higher content of CE (0.7 wt%) however reduced the extent of crystallization from 32 to 25 %.

5.4.2 Shear-induced crystallization

In addition to the molecular structure, thermal history, and the presence of additives, flow conditions imposed on the polymer melt during processing are key factors influencing the crystallization kinetics. To investigate the impact of shear flow on the crystallization process, a constant $\dot{\gamma}$ of 0.1 or 1 s^{-1} was applied to the different samples for 1, 5, and 10 min and, then, quenched from the initial flow temperature (180 °C) to the T_c (130 °C). To avoid repetition, focus is on PLA 3001D in this section since this sample is more prone to crystallization (lower *D*-content). The η_r^* values of the linear and LCB-PLAs prepared using different strategies are illustrated in Figure 5.7 as function of time. The corresponding induction times, t_{in}, are reported in Table 5.3. To further explore the effect of the applied shear rate on the crystallization process, the samples were pre-sheared at another constant rate, $\dot{\gamma}$, of 0.1 s^{-1} for 1, 5 and 10 min. The results are not presented here for the sake of brevity: however, the measured t_{in} are provided in Table 5.3.

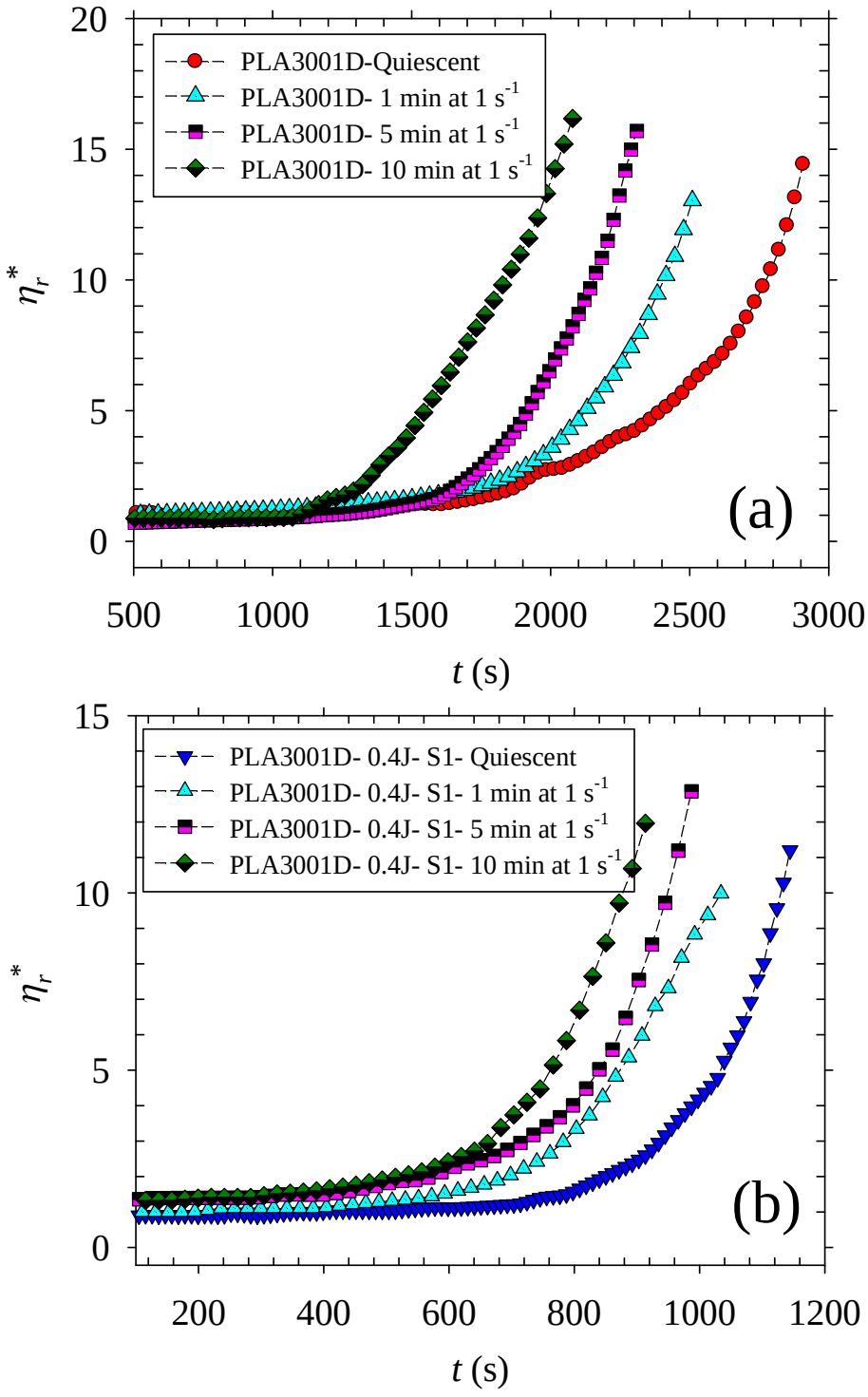

Figure 5.7: Normalized complex viscosity, η_r^*, of (a) the neat PLA3001D, PLA3001D containing 0.4 wt% CE prepared using (b) strategy S1, (c) strategy S2, and (d) PLA3001D containing 0.7 wt% CE, as a function of time after 1, 5, and 10 min preshearing at 1 s^{-1}: T_c = 130 °C.

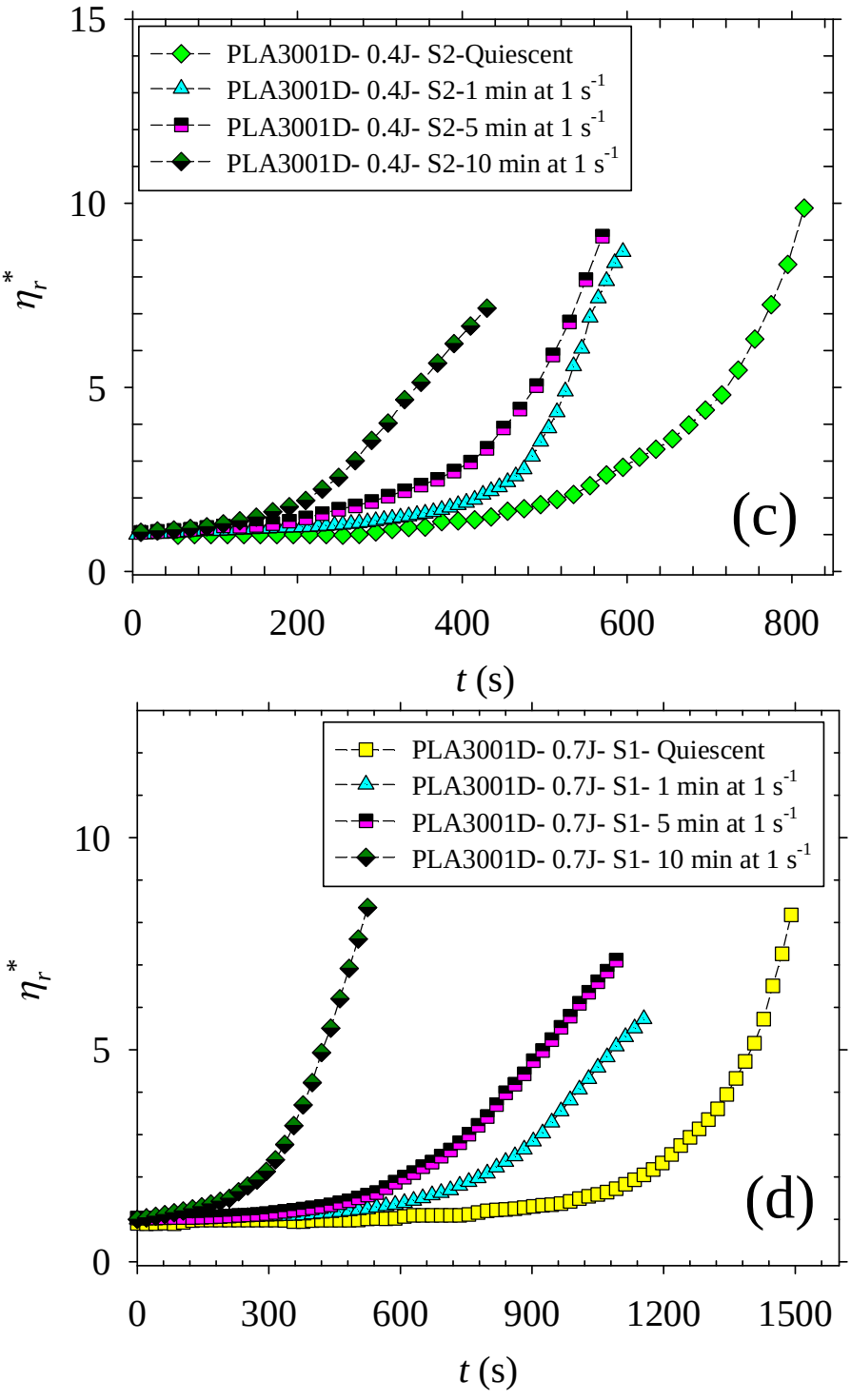

Figure 5.7 (continued): Normalized complex viscosity, η_r^*, of (a) the neat PLA3001D, PLA3001D containing 0.4 wt% CE prepared using (b) strategy S1, (c) strategy S2, and (d) PLA3001D containing 0.7 wt% CE, as a function of time after 1, 5, and 10 min preshearing at 1 s^{-1}: T_c = 130 ^oC.

Table 5.3: Induction time, t_{in} (s), for the onset of quiescent crystallization of the linear and LCB-PLAs after different periods of pre-shearing at $\dot{\gamma}$ of 0.1 and 1 s^{-1}. T_c was set at 130 °C and the experimental variability is less than 3%.

$\dot{\gamma}_{(s^{-1})}$	γ	PLA 3001D-Neat	PLA3001D-0.4 J-S1	PLA3001D-0.4 J-S2	PLA 3001D-0.7 J- S1	PLA 2003D-0.4 J-S2	PLA 2003D-0.7 J- S1
0.1	6	1840	695	545	775	-	-
0.1	30	1810	650	505	695	-	-
0.1	60	1745	590	460	645	550	1235
1	60	1725	580	445	625	-	-
1	300	1450	490	370	520	-	-
1	600	1140	375	195	220	440	750

Figure 5.7a shows the η_r^* evolution of the linear PLA 3001D after different periods of shearing at a constant $\dot{\gamma}$ of 1 s^{-1}. The induction time for the onset of crystallization is reduced from 1890 to 1725 s, as reported in Table 5.3, for the sample subjected to 1 min pre-shearing (γ= 60). It is further decreased to 1450 and 1140 s as the pre-shearing time is increased to 5 min (γ= 300) and 10 min (γ= 600), respectively.

A reduction in the onset of crystallization as a consequence of increasing shear strain was also observed by other researchers in polybutene (Baert and Van Puyvelde 2006), polypropylene (PP) (Yu *et al.* 2009), and polycaprolactone (PCL) (Lellinger *et al.* 2003; Madbouly and Ougizawa 2003) systems. It is believed that the molecular chains are oriented and extended, and form "liquid fibrils" in the sheared melts (Lellinger *et al.* 2003; Yu *et al.* 2008). The pre-ordered chains or segments serve as precursors or primary nuclei for crystal nucleation, leading to an increase in the nucleation and crystallization growth rate (Lellinger *et al.* 2003; Madbouly and Ougizawa 2003; Yu *et al.* 2008).

Once polymer melts are subjected to a longer pre-shearing time, more molecular chains are oriented and, thus, the crystal nucleation process is accelerated. A similar trend is observed in the crystallization behavior of the compounded samples S1 (Figure 5.7b) and S2 (Figure 5.7c), and for the PLA containing 0.7 wt% CE (Figure 5.7d). The results, furthermore, indicate that the impact of pre-shearing becomes more pronounced after the incorporation of CE into the PLA and the formation of LCB structure. This pattern of behavior was also observed by Yu *et al.* (2009) for a

LCB-PP system. The role of LCB and molecular weight on the shear-induced crystallization of PLA can be further clarified by defining a normalized induction time, $\theta = t_{in(s)}/t_{in(q)}$, as the ratio of the induction time at a given shear rate to the induction time under quiescent conditions.

The normalized induction time of the linear and LCB-PLAs prepared using different strategies after 1, 5 and 10 min pre-shearing is plotted as a function of shear rate, $\dot{\gamma}$, in Figure 5.8.

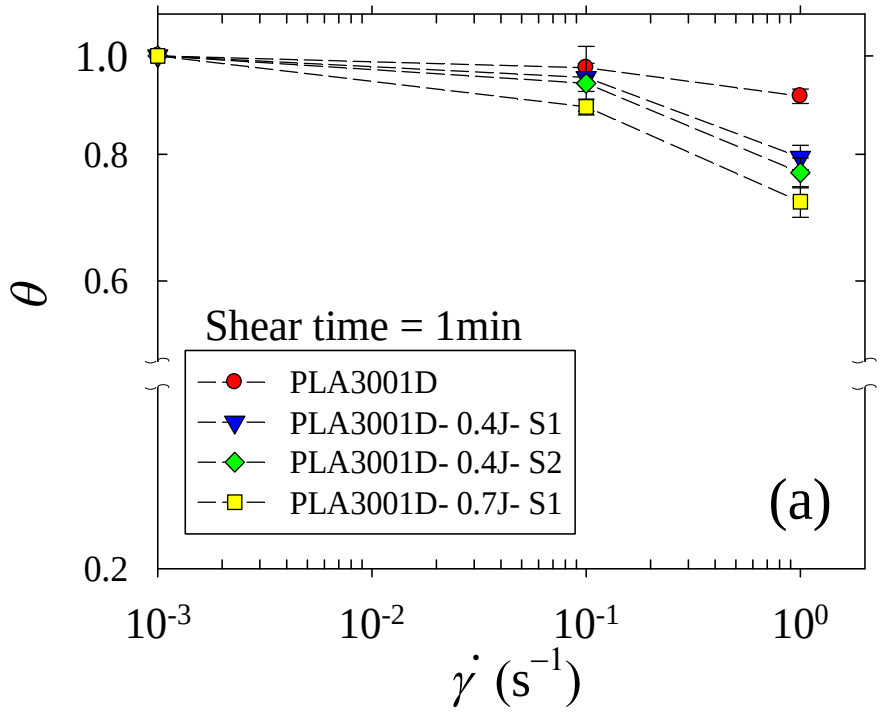

Figure 5.8: Normalized induction time, $\theta = t_{in(s)}/t_{in(q)}$, of the linear and LCB-PLAs with various contents of CE prepared using different strategies as a function of shear rate after (a) 1 min, (b) 5 min and (c) 10 min preshearing. T_c was set at 130 °C. The PLA grade is 3001D.

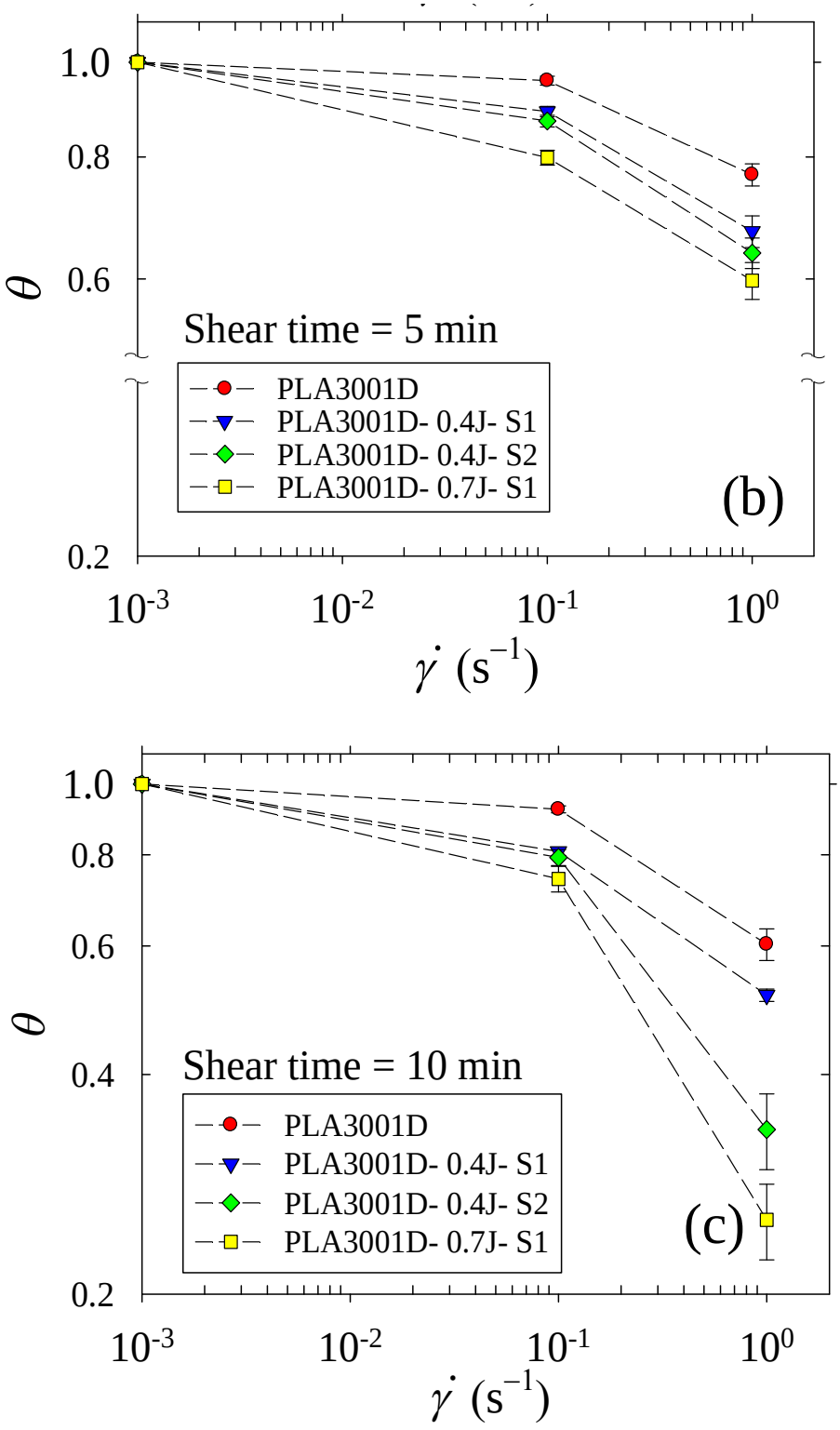

Figure 5.8 (continued): Normalized induction time, $\theta = t_{in(s)}/t_{in(q)}$, of the linear and LCB-PLAs with various contents of CE prepared using different strategies as a function of shear rate after (a) 1 min, (b) 5 min and (c) 10 min preshearing. T_c was set at 130 °C. The PLA grade is 3001D.

The corresponding t_{in} for quiescent crystallization ($\dot{\gamma}$=0) is presented at $\dot{\gamma}$ of 10^{-3} s^{-1} instead of 0 for convenience. A comparison of Figures 5.8a and b with Figure 5.8c reveals that the normalized induction time, θ, of the linear and LCB-PLAs decreases with increasing pre-shearing time and shear rate.

For instance at $\dot{\gamma}$ of 1 s^{-1}, θ of the neat PLA3001D, S1 and S2 compounded samples, and PLA3001D containing 0.7 wt% CE drops from 0.77, 0.67, 0.64, and 0.60 to 0.61, 0.51, 0.34, and 0.25, respectively, as the pre-shearing time increases from 5 to 10 min. In addition, the normalized induction time drops more rapidly, particularly at $\dot{\gamma}$ of 1 s^{-1}, after the introduction of CE and increasing LCB structure. These results confirm that the LCB macromolecules play imperative key role on shear-induced crystallization. It has been generally accepted that the introduction of a LCB structure to the linear backbone of PLA leads to an increased M_w and, subsequently, to a larger relaxation time. The time-weighted relaxation spectra of these samples were calculated using the NLREG software (non-linear regularization) and presented in our previous work (Najafi *et al.* 2014). The characteristic relaxation time, λ_c, which is the time corresponding to the peak of the time-weighted relaxation spectra for linear PLA 3001D, S1, S2 compounded samples, and the PLA containing 0.7 wt% CE was 0.01, 0.76, 1.06, and 1.08 s at 180 ^oC, respectively. As discussed earlier, oriented nuclei will be formed under a shear flow. Once the deformation is withdrawn, they will relax to the original conformation, and therefore, crystallize quiescently. An increased relaxation time, resulting from the LCB structure, retards the relaxation process, which is favorable to retain the oriented chains and generate precursors of crystallization.

To evaluate how optical impurity (*D*-lactide content) influences the shear-induced crystallization behavior of PLA, LCB-PLAs based on PLA 2003D (containing 4.25 % *D*-lactide) were also subjected to 10 min pre-shearing at 0.1 and 1 s^{-1} and, then, the results compared with those obtained for PLA3001D (containing 1.5 % *D*-lactide). The θ values, of both PLA 2003D and 3001D, treated with 0.4 and 0.7 wt% CE after 10 min pre-shearing, are compared in Figure 5.9 as a function of shear rate, $\dot{\gamma}$.

The θ values of the LCB-PLAs based on PLA 2003D are less reduced with increasing shear rate in comparison with the corresponding values of samples based on PLA 3001D. For example, θ of the PLA2003D treated with 0.4 and 0.7 wt% CE decreases to 0.79 and 0.48, respectively, after 10 min

pre-shearing at 1 s^{-1}, indicating that PLA 2003D is less sensitive than PLA 3001D to the applied shear due to its lower ability to crystallize. The optically impure *D*-lactide units are found to incorporate defects into the crystal structure, leading to a delayed crystal nucleation and decelerated growth rate (Tsuji and Ikada 1996; Baratian *et al.* 2001).

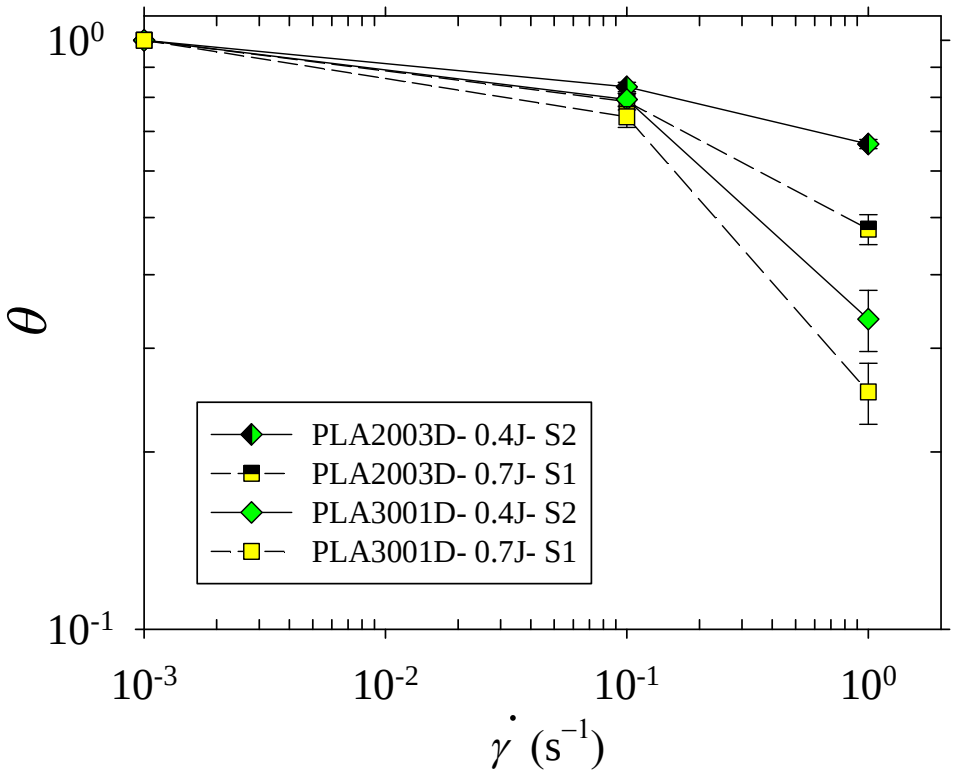

Figure 5.9: Normalized induction time, θ, of PLA containing 0.4 and 0.7 wt % CE based on PLA 2003D and PLA 3001D, as a function of shear rate after 10 min pre-shearing. T_c was set at 130 °C. The error bars show the variation of the normalized induction time.

In addition to total strain, γ, the contribution of the shear rate, $\dot{\gamma}$, to the crystallization kinetics was investigated at three different values, 0.5, 0.8, and 1 s^{-1}, for a constant γ of 300. Two different compositions were considered in this part of the study; the linear PLA3001D with the longest induction time in quiescent conditions (1890 s) and the PLA3001D treated with 0.4 wt% of CE prepared using strategy S2 with the shortest induction time (580 s). The results for the η_r^* evolution are presented in Figure 5.10.

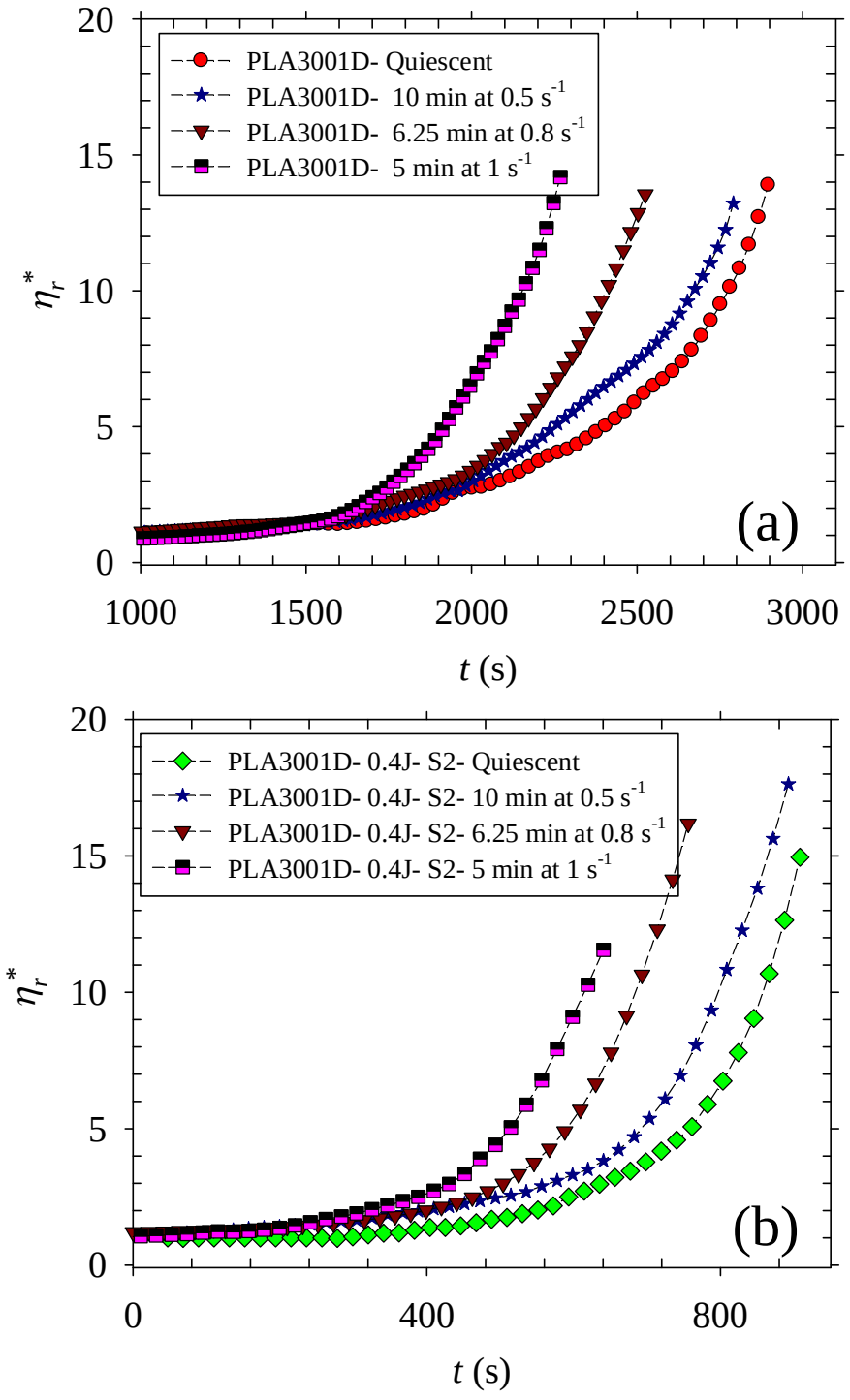

Figure 5.10: Normalized complex viscosity, η_r^*, of (a) the neat PLA 3001D, (b) PLA containing 0.4 wt% CE prepared using strategy S2 as a function of time after preshearing at shear rate, $\dot{\gamma}$, of 0.5, 0.8 and 1 s^{-1} while keeping constant the total strain (γ = 300). T_c was set at 130 °C.

The corresponding induction times were obtained with an experimental error of less than 5 %, and are reported in Table 5.4. As the shear rate is increased from 0.5 to 0.8 s^{-1}, t_{in} is reduced from 1740 to 1575 s for the linear PLA, and from 515 to 460 s for the LCB-PLA. With increasing $\dot{\gamma}$ to 1 s^{-1}, t_{in} of the linear and LCB-PLAs is further decreased to 1450 and 370 s, respectively.

Table 5.4: Induction time, t_{in} (s), for the onset of crystallization for the linear and LCB-PLA (3001D) after pre-shearing at $\dot{\gamma}$ of 0.5, 0.8, and 1 s^{-1}, while keeping the total strain, γ, equal to 300. T_c was set at 130 °C and the experimental variability was less than 5%.

Shear time (s)	$\dot{\gamma}$(s^{-1})	γ	Neat PLA 3001D	PLA3001D-0.4 J-S2
Quiescent	0	0	1890	580
600	0.5	300	1740	515
375	0.8	300	1575	460
300	1	300	1450	370

This result implies that a higher shear rate applied for a shorter time is more effective to initiate crystallization than a lower shear rate for a longer time. A similar observation was also reported in the literature (Baert and Van Puyvelde 2006; Yu *et al.* 2008) for other polymeric materials.

The observed phenomenon, indeed, results from the impact of shear rate on the degree of orientation in the molecular chains. As the shear rate is decreased, even at large shear strain, the molecular chains have more time for relaxing back to their original conformation. Consequently, less oriented chain segments are formed to promote nucleation and reduce the induction time.

It is worth to note that the sensitivity of the normalized induction time to the applied $\dot{\gamma}$, illustrated in Figure 5.11 at a constant total strain (γ = 300), is more evident after the incorporation of the LCB structure into PLA and increased M_w.

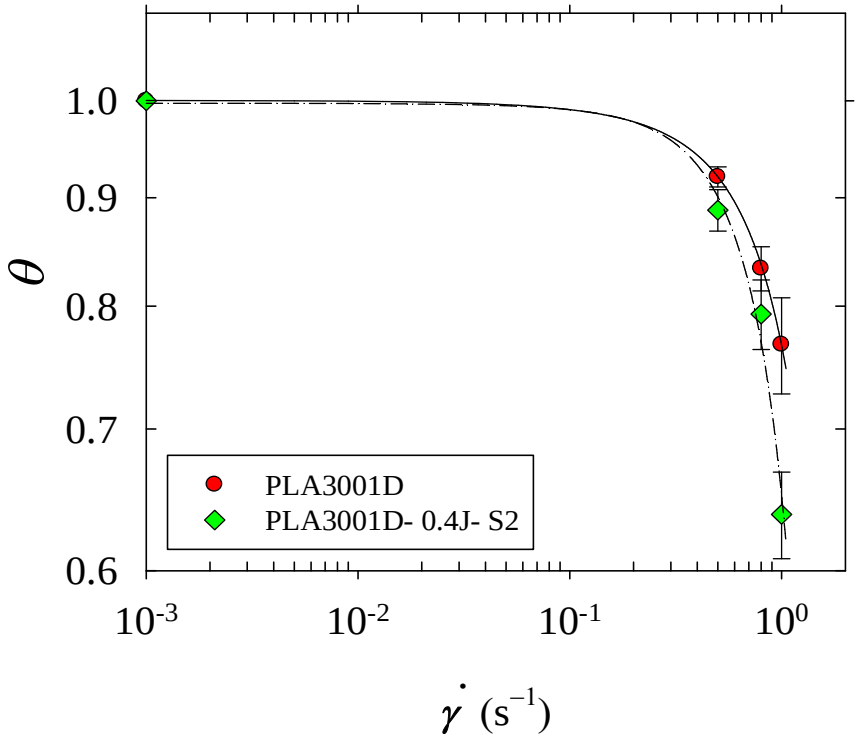

Figure 5.11: Normalized induction time, θ, of the neat PLA3001D and PLA3001D treated with 0.4 wt% CE prepared using strategy S2 after pre-shearing at $\dot{\gamma}$ of 0.5, 0.8, and 1 s^{-1} while keeping the total strain, γ, equal to 300. T_c was set at 130 °C.

5.4.3 Morphology

To assess how the LCB structure and pre-shearing influence the crystallization, the morphology of the linear PLA (PLA 3001D) and the LCB-PLA (PLA 3001D treated with 0.4 wt % CE and prepared using strategy S2) was monitored using the Linkam optical shearing system. The isothermal crystallization of the linear and LCB-PLAs was conducted at 130 °C under quiescent conditions and after 5 min pre-shearing at $\dot{\gamma}$ of 1 s^{-1}. The results for the crystal structure development of the linear and LCB-PLAs under quiescent conditions and after a step shear rate are presented in Figure 5.12. The spherulite density of these samples, evaluated from optical photomicrographs after 8 min of annealing, is given in Table 5.5.

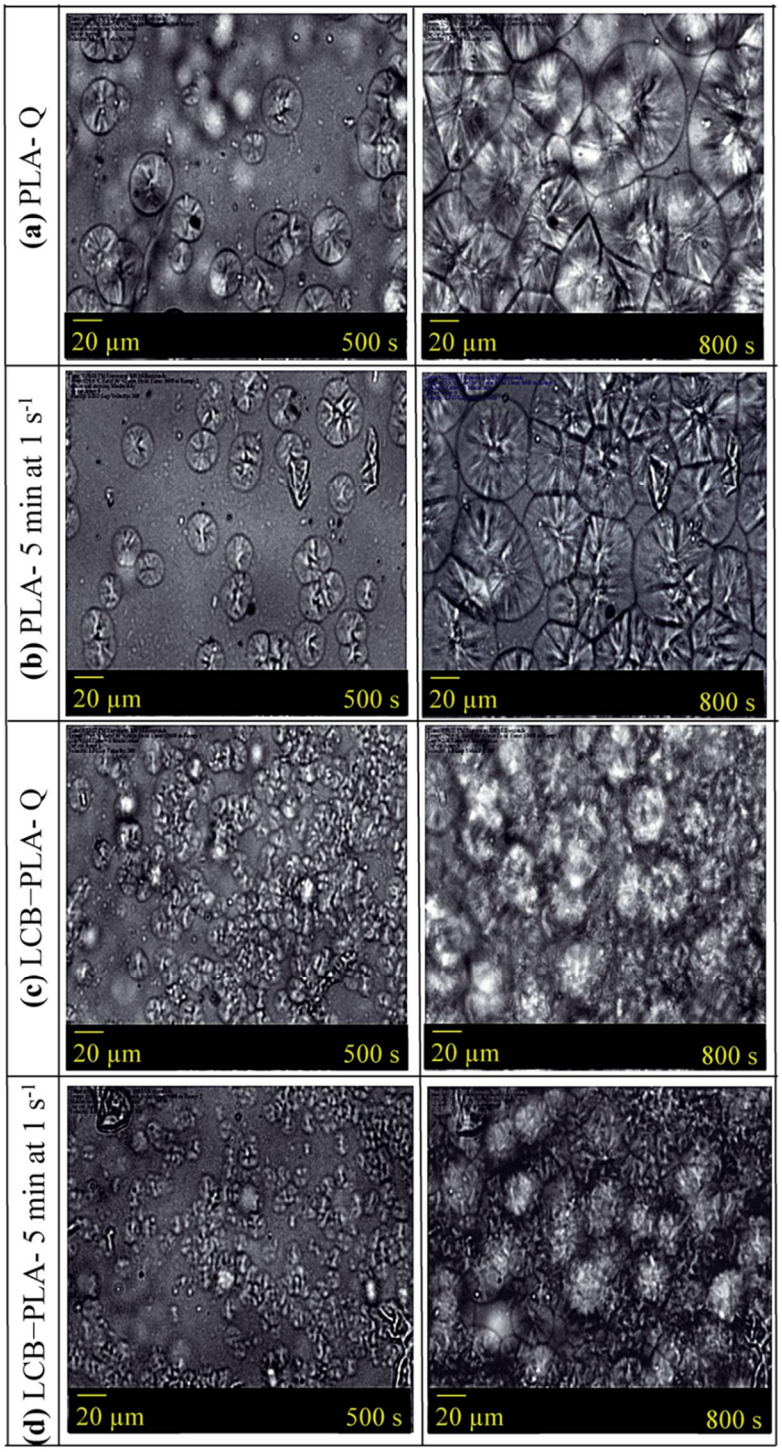

Figure 5.12: Characteristic crystal morphologies of (a) the linear PLA3001D in quiescent conditions, (b) linear PLA subjected to 5 min pre-shearing at $\dot{\gamma}$ of 1 s^{-1}, (c) LCB-PLA3001D in quiescent conditions, (d) LCB-PLA subjected to 5 min pre-shearing at $\dot{\gamma}$ of 1 s^{-1}. LCB-PLA3001D was produced by incorporating 0.4 wt% CE using strategy S2. Tests were performed at 130 ^{o}C after 500 and 800 s annealing times.

Table 5.5: The spherulite density of the linear and LCB-PLA (3001D) at quiescent and after 300 s pre-shearing at rate of 1 s^{-1}. The crystallization temperature was set at 130 °C.

Shear time (s)	$\dot{\gamma}$(s^{-1})	γ	Neat PLA 3001D	PLA3001D-0.4 J-S2
			Spherulite density, #/mm^2	Spherulite density, #/mm^2
Quiescent	0	0	1050	7000
300	1	300	1400	8050

The linear PLA (Figure 5.12a) exhibits a well-defined spherulitic structure. The crystals grow and impinge upon each other as the annealing time increases. The variation of the size of the spherulites with time is used to determine the spherulite growth rate. The average radius size of isolated unimpinged spherulites is reported in Figure 5.13, where the crystal size is found to increase linearly with time.

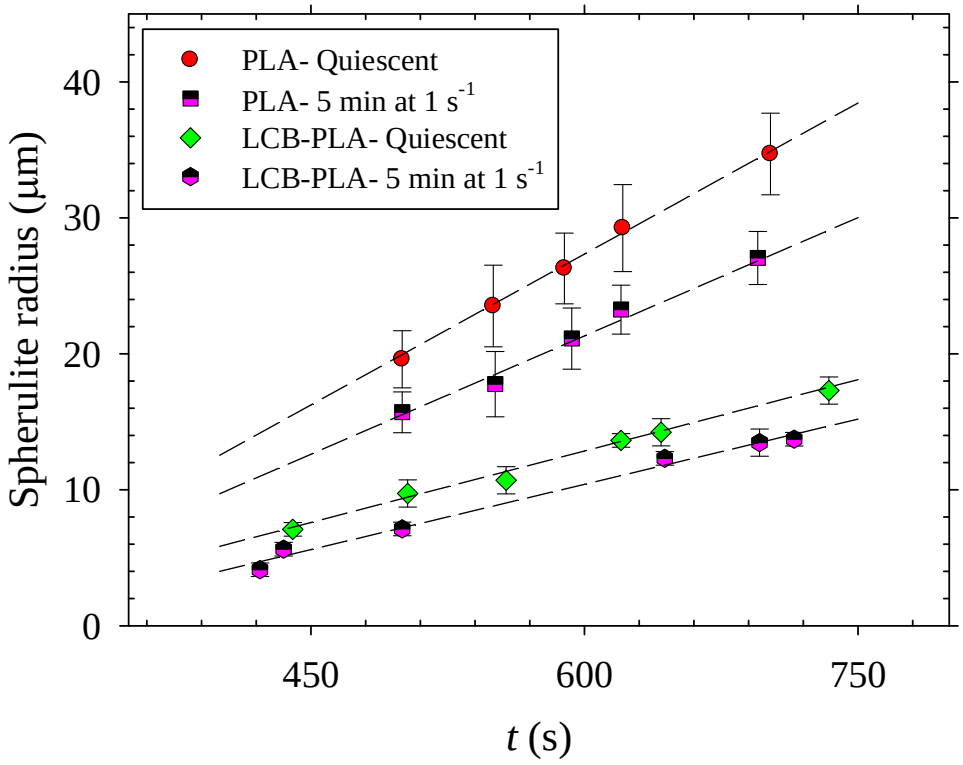

Figure 5.13: Average radius of unimpinged spherulites for the linear and LCB-PLA3001D under isothermal crystallization as a function of time. T_c was set at 130 °C.

As seen in Table 5.5, the number of spherulites after 8 min annealing is increased from 1050 crystals/mm^2 under quiescent conditions to 1400 crystals/mm^2 after imposing a shear flow (5 min at $\dot{\gamma}$ of 1 s^{-1}) on the polymer melt, while the crystal size decreases as shown in Figures 5.12b and 5.13.

These findings are in good agreement with the results reported by (Favaro *et al.* 2009) and (Baert and Van Puyvelde 2006) for different polymeric materials. Figure 5.12c displays the crystal morphology and size of LCB-PLA under quiescent conditions for two different annealing times. In comparison with the linear PLA (Figure 5.12a), the number of spherulites is impressively increased (from 1050 to 7000 crystals/mm^2) while the average crystal size also drops considerably (Figure 5.13). This evidence confirms that the LCB structure acts as nucleation sites and enhances the crystallization rate of PLA. Based on the results presented in Figure 5.13, the radial growth rate of spherulites reduces from 4.4 µm/min for the neat PLA to 2.0 µm/min after the introduction of the LCB structure in quiescent conditions. This decrease is mainly attributed to reduction of the chain mobility and the difficulty for branched structures to chain pack. Figure 5.12d shows the impact of pre-shearing on the crystal morphology of LCB-PLA. Similar to what was observed for the linear counterpart, the number of spherulites is further increased from 7000 to 8050 crystals/mm^2, and the size of crystal slightly decreases (see Figure 5.13) as a shear field is applied. The spherulite growth rate of the neat PLA and LCB structure is respectively reduced from 4.4 to 3.5 and from 2.0 to 1.8 µm/min under shear induced conditions. Regarding the effect of shear on spherulite growth rate, different results are reported. De Santis *et al.* (2014) found that the effect of shear on the spherulite growth rate is significantly affected by the moment at which it was applied and how long it was maintained for. The spherulite growth rate was nearly independent of shear rate if the step shear rate was immediately applied as soon as reaching T_c and then letting crystallization occurs without shear flow. In a second methodology, a step shear rate was applied as soon as the spherulites formed under quiescent condition and then maintained. Their results indicated that the spherulite growth rate remarkably increased in the second approach during the application of shear, and reduce back to the initial growth rate right after shear cessation. The effect of step shear rate and shearing time was extensively investigated by Zhang *et al.* (Zhang *et al.* 2008; Zhang *et al.* 2015). In this case it was found that there is a critical shearing time below which spherulite growth rate increases with shear time and further increases in shearing time leads to a reduction of the spherulite growth rate. According to the authors, applying a short-time shearing

helped to disentangle the molecular chains and decrease the activation diffusion energy, leading to an increased spherulite growth rate. However, it would take more time for stretched chains to relax and join the crystal growth front, leading to a reduced spherulite growth rate which may be the case in the present work. In addition, the fact that the shearing was applied at high temperature, and then the sample cooled down to crystallization temperature, may also explain the difference with the work of De Santis *et al.* (2014).

It is of interest to compare the structure development observed by optical microscopy with the evolution of the reduced viscosity, η_r^*, obtained in rheological measurements. Similar to the study reported for PCL (Acierno *et al.* 2006), the spherulites are found to appear and grow when η_r^* is still constant in the plateau region. In fact, the structure development can be detected by microscopy and consists of small spherulites surrounded by the amorphous matrix phase, even within the onset time determined by rheometry. Such a behavior was also observed by other authors (Bove and Nobile 2002; Hadinata *et al.* 2005; R. Iervolino 2006) for polybutene (PB). Considering that the crystallization is a local phenomenon and the rheometer measures an overall microscopic viscosity of the melt, a recently developed device, called RheoDSc (Kiewiet *et al.* 2008) is suggested for these types of experiments. This technique allows a simultaneous combination of in situ rheological measurements and thermal analysis (DSC) on the same sample.

5.5 Conclusion

The isothermal crystallization behavior of linear and long-chain branched (LCB) PLAs, based on two different grades of PLA, 3001D and 2003D, was investigated under quiescent and shear flow conditions using rheometry and optical microscopy. LCB-PLAs were prepared by a melt grafting reaction in the presence of a multi-functional chain extender (CE). The quiescent crystallization behavior of the linear and LCB structures of both PLA grades was studied at 130 °C. In comparison with the PLA 2003D, PLA 3001D exhibited a shortened crystallization induction time due to its lower *D*-lactide content. The incorporation of a LCB structure into linear PLA using 0.4 wt % CE promoted the crystallization kinetics, thus leading to shorter induction times. The impact of shear on the crystallization of PLA was also examined. The shear-induced crystallization of the linear and LCB-PLAs was influenced not only by the total shear strain but also by the shear rate. To determine the effect of shear strain, a pre-shear treatment was applied on the melt at constant shear

rates of 0.1 and 1 s^{-1} for a period of 1, 5, and 10 min. The obtained results implied that increase of total shear strain further decreased the onset time of crystallization. The shear strain impact on the crystallization kinetics was more pronounced as the degree of LCB and molecular weight increased. To assess the role of shear rate on the induced crystallization, pre-shear was applied at rates of 0.5, 0.8, and 1 s^{-1} while keeping the total strain constant (γ=300). The induction time of linear and LCB-PLAs was shortened as the shear rate increased for the same total shear strain.

The crystal morphology of the linear and LCB- PLAs under quiescent and shear flow conditions was observed using a Linkam optical shear system. The optical micrographs provided information about the spherulite density and growth rate. An increase in the spherulite density was observed in the strained melt of both linear and LCB-PLAs, as compared with those of unstrained counterparts. A comparison of the crystal structure of linear PLA with that of LCB-PLA revealed that long chain branching significantly promoted the nucleation density, although it diminished the crystal growth rate (from 4.4 to 2 µm/min for neat PLA).

5.6 Acknowledgements

Financial support from Auto 21 (Canada's automotive R&D program) and NCE (Networks of Centres of Excellence of Canada) is gratefully acknowledged.

5.7 References

Achmad F, Yamane K, Quan S, Kokugan T (2009) Synthesis of polylactic acid by direct polycondensation under vacuum without catalysts, solvents and initiators Chemical Engineering Journal 151:342-350 doi:http://dx.doi.org/10.1016/j.cej.2009.04.014

Acierno S, Di Maio E, Iannace S, Grizzuti N (2006) Structure development during crystallization of polycaprolactone Rheologica Acta 45:387-392 doi:10.1007/s00397-005-0054-2

Acierno S, Palomba B, Winter H, Grizzuti N (2003) Effect of molecular weight on the flow-induced crystallization of isotactic poly(1-butene) Rheologica Acta 42:243-250 doi:10.1007/s00397-002-0280-9

Ahn SH, Cho CB, Lee KY (2002) The Kinetics of Shear-Induced Crystallization in Poly(Ethylene Terephthalate) Journal of Reinforced Plastics and Composites 21:617-628 doi:10.1177/0731684402021007026

Arias A (2014) Development of Natural Fiber Reinforced Polylactide-Based Biocomposites. Dissertation, Ecole Polytechnique of Montreal

Arias A, Heuzey M-C, Huneault M (2013) Thermomechanical and crystallization behavior of polylactide-based flax fiber biocomposites Cellulose 20:439-452 doi:10.1007/s10570-012-9836-8

Baert J, Van Puyvelde P (2006) Effect of molecular and processing parameters on the flow-induced crystallization of poly-1-butene. Part 1: Kinetics and morphology Polymer 47:5871-5879 doi:http://dx.doi.org/10.1016/j.polymer.2006.06.009

Baratian S, Hall ES, Lin JS, Xu R, Runt J (2001) Crystallization and Solid-State Structure of Random Polylactide Copolymers: Poly(l-lactide-co-d-lactide)s Macromolecules 34:4857-4864 doi:10.1021/ma001125r

Binsbergen FL (1966) Orientation-induced Nucleation in Polymer Crystallization Nature 211:516-517

Bove L, Nobile MR (2002) Shear-induced crystallization of isotactic poly(1-butene) Macromolecular Symposia 185:135-147 doi:10.1002/1521-3900(200208)185:1<135::aid-masy135>3.0.co;2-s

Chen Q, Fan Y-R, Zheng Q (2007) Shear induced crystallization of high-density polyethylene Journal of Central South University of Technology 14:174-177 doi:10.1007/s11771-007-0239-1

De Santis F, Scermino R, Pantani R, Titomanlio G (2014) Spherulitic nucleation and growth rates in a sheared polypropylene melt AIP Conference Proceedings 1593:294-297 doi: http://dx.doi.org/10.1063/1.4873785

Drumright RE, Gruber PR, Henton DE (2000) Polylactic Acid Technology Advanced Materials 12:1841-1846 doi:10.1002/1521-4095(200012)12:23<1841

Duplay C, Monasse B, Haudin J-M, Costa J-L (1999) Shear-induced crystallization of polypropylene: influence of molecular structure Polymer International 48:320-326 doi:10.1002/(sici)1097-0126(199904)48:4<320::aid-pi164>3.0.co;2-7

Eder G, Janeschitz-Kriegl H (2006) Crystallization. In: Materials Science and Technology. Wiley-VCH Verlag GmbH & Co. KGaA. doi:10.1002/9783527603978.mst0211

Eslami H, Kamal MR (2013) Effect of a chain extender on the rheological and mechanical properties of biodegradable poly(lactic acid)/poly[(butylene succinate)-co-adipate] blends Journal of Applied Polymer Science 129:2418-2428 doi:10.1002/app.38449

Favaro MM, Rego BT, Branciforti MC, Bretas RES (2009) Study of the quiescent and shear-induced crystallization kinetics of intercalated PTT/MMT nanocomposites Journal of Polymer Science Part B: Polymer Physics 48:113-127 doi:10.1002/polb.21852

Garlotta D (2001) A literature review of poly(lactic acid) Journal of Polymers and the Environment 9:63-84 doi:Unsp 1566-2543/01/0400-0063/0

Haas TW, Maxwell B (1969) Effects of shear stress on the crystallization of linear polyethylene and polybutene-1 Polymer Engineering & Science 9:225-241 doi:10.1002/pen.760090402

Hadinata C, Gabriel C, Ruellman M, Laun HM (2005) Comparison of shear-induced crystallization behavior of PB-1 samples with different molecular weight distribution Journal of Rheology (1978-present) 49:327-349 doi:http://dx.doi.org/10.1122/1.1835342

Han L, Han C, Dong L (2013) Effect of crystallization on microstructure and mechanical properties of poly[(ethylene oxide)-block-(amide-12)]-toughened poly(lactic acid) blend Polymer International 62:295-303 doi:10.1002/pi.4300

Heeley EL, Fernyhough CM, Graham RS, Olmsted PD, Inkson NJ, Embery J, Groves DJ, McLeish TCB, Morgovan AC, Meneau F, Bras W, and Ryan AJ (2006) Shear-Induced Crystallization in Blends of Model Linear and Long-Chain Branched Hydrogenated Polybutadienes Macromolecules 39:5058-5071 doi:10.1021/ ma0606307

Hu W (2001) Chain folding in polymer melt crystallization studied by dynamic Monte Carlo simulations The Journal of Chemical Physics 115:4395-4401 doi:http://dx.doi.org/10.1063/1.1389860

Jabbarzadeh A, Tanner RI (2010) Flow-Induced Crystallization: Unravelling the Effects of Shear Rate and Strain Macromolecules 43:8136-8142 doi:10.1021/ma100985x

Kausch H-H, Chan C-M, Li L (2005) Direct Observation of the Growth of Lamellae and Spherulites by AFM. In: Intrinsic Molecular Mobility and Toughness of Polymers II, vol 188. Advances in Polymer Science. Springer Berlin Heidelberg, pp 1-41. doi:10.1007/b136971

Kiewiet S, Janssens V, Miltner HE, Van Assche G, Van Puyvelde P, Van Mele B (2008) RheoDSC: A hyphenated technique for the simultaneous measurement of calorimetric and rheological evolutions Review of Scientific Instruments 79:- doi:http://dx.doi.org/10.1063/ 1.2838585

Kim SH, Han Y-K, Kim YH, Hong SI (1992) Multifunctional initiation of lactide polymerization by stannous octoate/pentaerythritol Die Makromolekulare Chemie 193:1623-1631 doi:10.1002/macp.1992.021930706

Kramschuster A, Turng L-S (2009) An injection molding process for manufacturing highly porous and interconnected biodegradable polymer matrices for use as tissue engineering scaffolds Journal of Biomedical Materials Research Part B: Applied Biomaterials 92B:366-376 doi:10.1002/jbm.b.31523

Kumaraswamy G, Kornfield JA, Yeh F, Hsiao BS (2002) Shear-Enhanced Crystallization in Isotactic Polypropylene. 3. Evidence for a Kinetic Pathway to Nucleation Macromolecules 35:1762-1769 doi:10.1021/ma0114180

Lellinger D, Floudas G, Alig I (2003) Shear induced crystallization in poly(caprolactone): effect of shear rate Polymer 44:5759-5769 doi:http://dx.doi.org/10.1016/S0032-3861(03)00633-5

Li L, Chan C-M, Yeung KL, Li J-X, Ng K-M, Lei Y (2000) Direct Observation of Growth of Lamellae and Spherulites of a Semicrystalline Polymer by AFM Macromolecules 34:316-325 doi:10.1021/ma000273e

Liedauer S, Eder G, Janeschitz-Kriegl H, Jerschow P, Geymayer W, Ingolic E (1993) On the Kinetics of Shear Induced Crystallization in Polypropylene International Polymer Processing 8:236-244 doi:10.3139/217.930236

Liu J, Zhang S, Zhang L, Bai Y (2012) Crystallization Behavior of Long-Chain Branching Polylactide Industrial & Engineering Chemistry Research 51:13670-13679 doi:10.1021/ie301567n

Lunt J (1998) Large-scale production, properties and commercial applications of polylactic acid polymers Polymer Degradation and Stability 59:145-152 doi:http://dx.doi.org/10.1016/S0141-3910(97)00148-1

Ma Z, Balzano L, van Erp T, Portale G, Peters GWM (2013) Short-Term Flow Induced Crystallization in Isotactic Polypropylene: How Short Is Short? Macromolecules 46:9249-9258 doi:10.1021/ma401833k

Madbouly SA, Ougizawa T (2003) Rheological Investigation of Shear-Induced Crystallization of Poly(Caprolactone) Journal of Macromolecular Science, Part B 42:269-281 doi:10.1081/mb-120017118

Meng Q, Heuzey M-C, Carreau PJ (2012) Control of thermal degradation of polylactide/clay nanocomposites during melt processing by chain extension reaction Polymer Degradation and Stability 97:2010-2020 doi:http://dx.doi.org/10.1016/j.polymdegradstab.2012.01.030

Mujica-Garcia A, Navarro-Baena I, Kenny JM, Peponi L (2014) Influence of the Processing Parameters on the Electrospinning of Biopolymeric Fibers Journal of Renewable Materials doi:10.7569/jrm.2013.634130

Nagahata R, Sano D, Suzuki H, Takeuchi K (2007) Microwave-Assisted Single-Step Synthesis of Poly(lactic acid) by Direct Polycondensation of Lactic Acid Macromolecular Rapid Communications 28:437-442 doi:10.1002/marc.200600715

Najafi N, Heuzey M-C, Carreau P, Therriault D, Park C (2014) Rheological and foaming behavior of linear and branched polylactides Rheologica Acta 53:779-790 doi:10.1007/s00397-014-0801-3

Najafi N, Heuzey MC, Carreau PJ (2013) Crystallization behavior and morphology of polylactide and PLA/clay nanocomposites in the presence of chain extenders Polymer Engineering & Science 53:1053-1064 doi:10.1002/pen.23355

Najafi N, Heuzey MC, Carreau PJ, Wood-Adams PM (2012) Control of thermal degradation of polylactide (PLA)-clay nanocomposites using chain extenders Polymer Degradation and Stability 97:554-565 doi:http://dx.doi.org/10.1016/j.polymdegradstab.2012.01.016

Norton DR, Keller A (1985) The spherulitic and lamellar morphology of melt-crystallized isotactic polypropylene Polymer 26:704-716 doi:http://dx.doi.org/10.1016/0032-3861(85)90108-9

R. Iervolino (2006) Rheology and morphology of the flow induced crystallization in polymers.Chemical and Food Engineering Department, University of Salerno

Ryan A, Terrill N, Fairclough JPA (1999) A Scattering Study of Nucleation Phenomena in Homopolymer Melts. In: Scattering from Polymers, vol 739. ACS Symposium Series. American Chemical Society, pp 201-217. doi:10.1021/bk-2000-0739.ch013

Suryanegara L, Nakagaito AN, Yano H (2009) The effect of crystallization of PLA on the thermal and mechanical properties of microfibrillated cellulose-reinforced PLA composites

Composites Science and Technology 69:1187-1192 doi:http://dx.doi.org/10.1016/j.compscitech.2009.02.022

Tsuji H, Ikada Y (1996) Crystallization from the melt of poly(lactide)s with different optical purities and their blends Macromolecular Chemistry and Physics 197:3483-3499 doi:10.1002/macp.1996.021971033

Wang L, Jing X, Cheng H, Hu X, Yang L, Huang Y (2012a) Blends of Linear and Long-Chain Branched Poly(l-lactide)s with High Melt Strength and Fast Crystallization Rate Industrial & Engineering Chemistry Research 51:10088-10099 doi:10.1021/ie300526u

Wang L, Jing X, Cheng H, Hu X, Yang L, Huang Y (2012b) Rheology and Crystallization of Long-Chain Branched Poly(l-lactide)s with Controlled Branch Length Industrial & Engineering Chemistry Research 51:10731-10741 doi:10.1021/ie300524j

Wang Z-Y, Li X-W, Li J-N, Li G-M, Tao J-Q (2009) Synthesis of poly(lactic acid)-poly(phenyl phosphate) via direct polycondensation and its characterization Journal of Polymer Research 16:255-261 doi:10.1007/s10965-008-9224-0

Wereta A, Gogos CG (1971) Crystallization studies on deformed polybutene-1 melts Polymer Engineering & Science 11:19-27 doi:10.1002/pen.760110105

Wunderlich B, Mielillo L (1968) Morphology and growth of extended chain crystals of polyethylene Die Makromolekulare Chemie 118:250-264 doi:10.1002/macp.1968.021180116

Yang B, Yang M, Wang W-J, Zhu S (2011) Effect of long chain branching on nonisothermal crystallization behavior of polyethylenes synthesized with constrained geometry catalyst Polymer Engineering & Science 52:21-34 doi:10.1002/pen.22040

Yu F, Zhang H, Liao R, Zheng H, Yu W, Zhou C (2009) Flow induced crystallization of long chain branched polypropylenes under weak shear flow European Polymer Journal 45:2110-2118 doi:http://dx.doi.org/10.1016/j.eurpolymj.2009.03.011

Yu F, Zhang H, Zheng H, Yu W, Zhou C (2008) Experimental study of flow-induced crystallization in the blends of isotactic polypropylene and poly(ethylene-co-octene) European Polymer Journal 44:79-86 doi:http://dx.doi.org/10.1016/j.eurpolymj.2007.10.022

Yuryev Y, Wood-Adams P (2010) Rheological properties of crystallizing polylactide: Detection of induction time and modeling the evolving structure and properties Journal of Polymer Science Part B: Polymer Physics 48:812-822 doi:10.1002/polb.21953

Zhang Q-P, Xia X-C, He S, Feng J-M, Yang M-B, Li Y-T, Zhou Y-L (2015) Tuning Crystalline Morphology of High-Density Polyethylene by Tailoring its Molecular Weight Distribution for Coupling with a Secondary Flow Field Macromolecular Materials and Engineering: doi:10.1002/mame.201500008

Zhang R-C, Xu Y, Lu A, Cheng K, Huang Y, Li Z-M (2008) Shear-induced crystallization of poly(phenylene sulfide) Polymer 49:2604-2613 doi: http://dx.doi.org/10.1016/j.polymer.2008.03.041

CHAPTER 6
ARTICLE 3

Mechanical and morphological properties of injection molded linear and branched-polylactide (PLA) nanocomposite foams

N. Najafi[1,2], M. C. Heuzey[1] *, P. J. Carreau[1], D. Therriault[2], C. B. Park[3]

1- Research Center for High Performance Polymer and Composite Systems, CREPEC, Department of Chemical Engineering, Ecole Polytechnique, Montreal, Quebec, Canada

2- Research Center for High Performance Polymer and Composite Systems, CREPEC, Department of Mechanical Engineering, Ecole Polytechnique, Montreal, Quebec, Canada

3- Microcellular Plastics Manufacturing Laboratory, Department of Mechanical and Industrial Engineering, University of Toronto, Toronto, Ontario, Canada

Submitted to *Composite Science and Technology* (July 2015)

6.1 Abstract

Linear and long chain branched (LCB) polylactide (PLA)-clay nanocomposites were prepared via melt compounding using a twin-screw extruder. An organo-modified clay, Cloisite 30B, and a chain extender, Joncryl, were employed in this study. The resulting systems were also foamed in a conventional injection molding machine using a chemical blowing agent, namely activated azodicarbonamide. The PLA crystallinity, clay dispersion, and foam cellular morphology were characterized. Unlike the linear PLA, the addition of nanoclay markedly reduced the crystallinity of the LCB-PLA. The clay inclusion as well as the LCB structure generally decreased the cell size and foam density, while increasing the cell density. The mechanical properties of the unfoamed and foamed linear and LCB-PLA samples and their corresponding nanocomposites were also characterized by tensile and Izod impact testing. The corresponding results revealed that the LCB-PLA nanocomposite with 0.5 wt% clay loading exhibited a significantly improved cellular structure in comparison with other foamed samples, leading to increased values of the specific modulus, tensile and impact strength.

Keywords: Long-chain branching; Nanocomposites; Injection foam molding; Mechanical properties

6.2 Introduction

A significant attention has been recently paid to biodegradable biomaterials due to the environmental impact of petroleum-based polymers. Polylactic acid or polylactide (PLA) is a biodegradable thermoplastic synthesized from renewable resources such as corn and starch [1]. The remarkable properties of PLA such as high strength, high modulus, and transparency make it a very interesting material for key applications [1-5]. PLA is also currently used in biomedical applications [1, 2, 6] and in industrial and food packaging [1, 4, 5, 7, 8]. In addition to these markets, the use of biomaterials is growing in some industries in the scope of sustainability, particularly in the automotive industry [9]. Automobile fuel consumption is known to be significantly affected by the car weight, hence a weight reduction while maintaining the performance is one of the main challenges in the automotive field [10]. A potential method to fulfill this aim through the development of lightweight materials is foaming.

To develop a polymeric foam structure, the polymer is first saturated with a high pressure gas, either injected or generated *in situ*. The resulting single-phase polymer-gas solution is then subjected to a thermodynamic instability induced by either a sudden pressure release or temperature increase. Numerous cells are nucleated as a result of the rapid gas liberation from the polymer and start to grow until they stabilize [11]. Polymer foaming can be performed through a batch process [12, 13], extrusion [8, 14, 15] or injection molding [2, 5, 6, 11, 16, 17]. From an industrial point of view, however, the extrusion and injection molding processes are preferred, since their productivity is higher than batch methods and, when using chemical blowing agents, standard processing equipment can be used. PLA foaming has recently raised interest since it can reduce the weight and cost of the final products [2, 4-6, 8, 12, 13]. However, PLA was found to exhibit poor foamability because it suffers from low melt strength and elasticity, slow crystallization and narrow processing window [2, 4, 5, 13, 18]. Our previous studies [13, 19] revealed that the incorporation of a multifunctional chain extender, Joncryl, into PLA led to the formation of long chain branching (LCB), increasing the melt strength and crystallization rate of PLA.

Recently, the impact of this chain extender on the foamability of PLA in extrusion was investigated by Julien *et al.* [20]. They varied the chain extender content from 0 to 3 wt% and foamed the PLA samples in an extruder using a chemical blowing agent (CBA). Their results showed that, in the best case, the cell size decreased to 64 μm while the cell density increased to 2.7×10^6 cells/cm^3 after the addition of 2 wt% chain extender.

Although injection foaming is a promising manufacturing technique, very little work has nevertheless been published on injection foam molding of PLA. High-pressure foam injection molding (i.e., MuCell® Technology– microcellular injection molding) has been used in the majority of these studies. In this technique, gas is blended in supercritical state with the polymer melt, thereby facilitating the generation of a homogeneous single phase polymer-gas solution [21]. Furthermore, a vigorous shearing and mixing of the materials under a high melt pressure significantly accelerates the gas dissolution in the polymer. The pressure level in high pressure injection molding is approximately 10 times higher than that in conventional injection molding [21]. Pilla *et al.* [22] studied the influence of hyper-branched polyesters (HBPs) and nanoclay on controlling the cellular morphology of a microcellular PLA. They used supercritical nitrogen fluid (SCF) as a physical blowing agent (PBA) and foamed the samples in a microcellular injection molding (MIM) machine equipped with the MuCell® technology. Depending on the concentration

of HBPs and nanoclay added to PLA, the cell density increased up to 10 times (16×10^6 cells/cm^3), while the cell size and weight of the microcellular samples were reduced by 4 times and 16 %, respectively. In other studies, Pilla *et al.* [23, 24] investigated the injection foaming behavior of PLA-multi-walled carbon nanotube (MWCNT) nanocomposites [23] and PLA/flax fiber composites [24]. It was found that the addition of a high aspect ratio filler decreased the cell size, while increasing the cell density. Kramschuster *et al.* [25] studied the foaming behavior of PLA/recycled paper shopping bag fibers in a MIM equipped with the MuCell® technology. It was demonstrated that the fiber inclusion resulted in an increase of the cell density and a reduction of the average cell size.

Low pressure injection foam molding is another technique that has been used to produce foamed plastics. Few investigations have been conducted to develop foamed PLAs using a conventional injection molding machine [5, 6]. The injection foam molding of PLA using combined CBA and PBA was performed by Seo *et al.* [26]. Based on their findings, using CBA and PBA at the same time increased the cell density and reduced the cell size and microcellular weight by a factor of 2 (from 100 to 50 μm), and by 14%, respectively. Peinado *et al.* [5] recently foamed a PLA reinforced with 1 to 10 wt% needle-like sepiolite nanoclay in low pressure injection foam molding using 2 wt% CBA. They achieved a relatively uniform cellular structure with a high void fraction of 30 %. Although they did not quantitatively analyze the morphology of the produced foams, the results clearly showed that the cell density increased, particularly after the addition of 5 and 10 wt% of nano-filler.

This paper aims at examining how LCB and nanoclay incorporation impact PLA foaming in the conventional injection molding (IM) process. To this end, LCB-PLAs are prepared in the presence of a multifunctional chain extender. A commercial grade PLA and LCB-PLA reinforced with organo-clay are foamed in a conventional IM machine using a chemical blowing agent. Crystallinity, cellular structure and mechanical properties of the various nanocomposites are investigated and correlated with the polymer molecular architecture and the nanocomposite structure.

6.3 Experimental

6.3.1 Materials

The injection grade polylactide used in this study, PLA 3001D, was supplied by NatureWorks LLC Co. (USA). The melt flow rate of the selected grade is 22 g/10 min (2.16 kg, 210 °C) as reported by the manufacturer. PLA 3001D is a semi-crystalline linear polymer with an *L*-lactide to *D*-lactide ratio of 98.5:1.5 [16]. Joncryl® ADR-4368F, an epoxy-based chain extender purchased from BASF (Germany), was used as a chain extender (CE). The organo-modified nanoclay Cloisite 30B, a commercial product from Southern Clay Inc., was used as a cell nucleating agent. Activated azodicarbonamide (Celogen 754-A) was selected as the chemical blowing agent (CBA). As reported by the manufacturer, Lion Copolymer LLC (USA), it decomposes at temperatures around 160-180 °C and generates about 210–220 mL of gases (N_2: 65%, NH_3: 5%, CO: 25%, and CO_2: 5%) per g of CBA.

6.3.2 Material processing

The nanocomposites were prepared by melt blending using a small-size corotating twin-screw extruder (CICO-TSE) of Leistritz Corp. with a 18 mm diameter and *L*/*D* ratio of 40. Our previous findings [27] demonstrated that a homogeneous clay dispersion in the PLA matrix can be achieved if clay and CE are added in two steps. In accordance, linear and LCB- polylactide (PLA) nanocomposites were prepared by a masterbatch process. Before compounding, the PLA and clay were dried at 60 °C in a vacuum oven for 24 h. To prepare masterbatches, dried PLA and 0.5, 1, and 2 wt % clay were initially dry-mixed and then extruded at a rotation speed of 150 rpm. The extruder was operated using a temperature profile set at 175, 180, 185, 190, 190, 195, 195, and 195 °C (for the different zones from the hopper to the die). The resulting masterbatches were dried in a vacuum oven (60 °C) for 24 h. Linear PLA-clay nanocomposites with a nominal content of 0.25, 0.5 and 1 wt% clay were obtained by melt mixing of the various masterbatches with the commercial PLA at a weight ratio of 50:50 via the extruder, operated under the same conditions. To produce LCB-PLA nanocomposites, a highly long chain branched structure was first prepared by compounding the neat PLA with 0.8 wt% of CE in the extruder in the conditions stated above. The masterbatches and LCB-PLA were then blended at a weight ratio of 50:50 to achieve nanocomposites for a nominal content of 0.25, 0.5 and 1 wt % clay and 0.4 wt % CE. After each

processing step, the extruded materials were cooled in an ice-water bath, pelletized and, then, dried in the oven (60 ºC) for 24 h. To investigate the nanocomposite structure, disks of 25 mm diameter and 1 mm thickness were prepared by compression molding at 185 ºC and pressure of 20 MPa under a nitrogen atmosphere.

Injection foaming experiments were conducted in an all-electric injection molding machine (Sumitomo SE50S). The nanocomposites and the CBA were dry-mixed before introduction into the feed hopper. The machine used in this study is equipped with a mechanical shut-off nozzle to keep the pressure and prevent premature cell nucleation, while maintaining the shot size constant from one cycle to the other. A one-runner gate die mold was used to prepare samples for morphological and mechanical characterization. The material was injected into the mold through one sprue at the extremity of the mold. Two different geometries, rectangular bars with dimensions of about 127 × 12.7 x 3.1 mm and dog-bone specimens with 162 mm in total length, a gauge section of 12.7 mm wide and a thickness of 3.1 mm, were used. Several operating parameters such as the CBA concentration, shot size, injection speed, back pressure, cooling time, and nozzle temperature were initially varied to optimize the processing conditions. Accordingly, the CBA concentration and shot size were, respectively, set to 1.5 wt% and 70% of the cavity volume (17 mm for the rectangular bars and 19 mm for the dog-bone specimens). The temperature profile was 160, 200, 190, and 160 ºC from the hopper to the nozzle to ensure decomposition of the chemical blowing agent. Other processing parameters used in this study are as follows: screw rotation speed, 100 rpm; injection speed, 150 mm/s; back pressure, 2 MPa; mold temperature, 40 °C; and cooling time, 25 s. The linear PLA was extruded and foamed at the aforementioned conditions and used as a reference in this study.

6.3.3 Characterization

The non-isothermal melt-crystallization behavior of the linear and LCB-PLA nanocomposites was investigated using a differential scanning calorimeter, DSC-Q 2000 (TA Instruments, USA) under a N_2 atmosphere. Samples (~10 mg), encapsulated in aluminum standard pans, were first heated at a scanning rate of 10 °C/min from 30 to 205 °C and held for 5 min at this temperature. They were then cooled down to 30 °C at a rate of 5 °C/min to determine the crystallization enthalpy (ΔH_c) and degree of crystallinity (X_c).

The nanoclay gallery spacing (d_{001}) was determined by X-ray diffraction (XRD) analysis via a Philips X'Pert X-ray diffractometer using Cu-Kα radiation (λ = 0.1542 nm), operating at 50 kV and 40 mA. The data were measured over a scattering angle (2θ) range from 1 to 10°.

The density of foamed samples was measured using Archimedes's principle at ambient pressure and temperature. A known mass of foamed sample was attached to a sinker and immersed in distilled water and the volume of the sample was obtained. The relative density (ρ_r) was determined as the ratio of the density of the foamed sample (ρ_f) to that of the solid (unfoamed) one (ρ_s=1.24 g/cm^3). The cellular morphology of the rectangular foamed specimens was investigated using a JSM-840 scanning electron microscope (SEM) (JEOL, USA) operated at an accelerating voltage of 10 kV. Prior to the SEM observations, the samples were cryo-fractured in their center in liquid nitrogen and the fractured surface was sputter-coated with a thin layer of gold. A quantitative analysis of the average cell density and size of 500 cells was performed using an image analysis tool (ImageJ, NIH). The cell density, or the number of cells per unit volume (cm^3) of the unfoamed polymer, was calculated using Eq. 1[28]:

$$\text{Cell density} = \left(\frac{n}{A}\right)^{3/2} \cdot \left(\frac{\rho_s}{\rho_f}\right) \qquad \text{Eq. 6.1}$$

where n and A are the number of cells and area of the micrograph (cm^2), respectively.

The tensile properties were determined from the injection molded dog-bone specimens. The testing was performed on an Instron tensile machine (model 4400R) equipped with a 5 kN load cell according to standard ASTM D638 (Type I). All tests were carried out under ambient conditions using a cross-head speed of 5 mm/min. To accurately measure the strain and, hence, the Young modulus, an Instron extensometer was mounted on the test specimen. All the reported values were obtained by averaging over eight specimens for each composition.

The rectangular injection molded bars were used to obtain the impact strength of unfoamed, foamed linear and LCB-PLA nanocomposites. The Izod impact test was performed on unnotched samples using a CEAST impact tester, equipped with a pendulum of 2 J energy at room temperature. The values reported here are the averages of five specimens for each composition.

6.4 Results and discussion

6.4.1 Thermal analysis

The non-isothermal crystallization behavior from the melt state is of increasing technological importance since these conditions are the closest to real industrial processing situations. The non-isothermal melt crystallization behavior of the linear and LCB-PLA nanocomposites, at a cooling rate of 5 °C/min, are presented in Figure 6.1a and b, respectively. The degree of crystallinity (X_c) was calculated according to Eq. 6.2.

$$X_c(\%) = \left(\frac{\Delta H_c}{\Delta H_m^o \left(\frac{\phi_{PLA}}{100} \right)} \right) \times 100 \qquad \text{Eq. 6.2}$$

where ΔH_c and ΔH^o_m are the melt crystallization enthalpy of the component and the melting enthalpy of perfectly crystalline PLA (93.6 J/g [29]), respectively, and ϕ_{PLA} is the matrix weight percent in the samples.

Figure 6.1a shows that the neat PLA exhibits a very small exothermic peak on the cooling curve, indicating that it does not significantly crystallize during the cooling process, with a degree of crystallinity of 1 %. As expected the inclusion of nanoclay particles in the linear PLA affects the degree of crystallization (X_c). This increment can be attributed to the heterogeneous nucleation effect of nano-sized dispersed particles that facilitate the crystallization process. As a result of heterogeneous nucleation, X_c increases from 1 to 6 and 11% in the PLA containing 0.25 and 0.5 wt% clay, respectively. The X_c value, however, drops to 3 % as the clay concentration is further raised to 1 wt%. This phenomenon indicates that dispersed silicate layers play a dual role during non-isothermal melt crystallization: increase of crystal nucleation induced by the heterogeneous mechanism, leading to enhanced degree of crystallinity, in competition with the restriction of chain mobility that makes chain packing in the crystal structure more difficult [12]. Due to strong interactions between PLA polymer chains and the organic surfactant of Cloisite 30B platelets, the PLA molecules at the surface of the dispersed layers are partially immobilized [12]. The melt crystallization behavior of the LCB-PLA with different clay loadings is presented in Figure 6.1b.

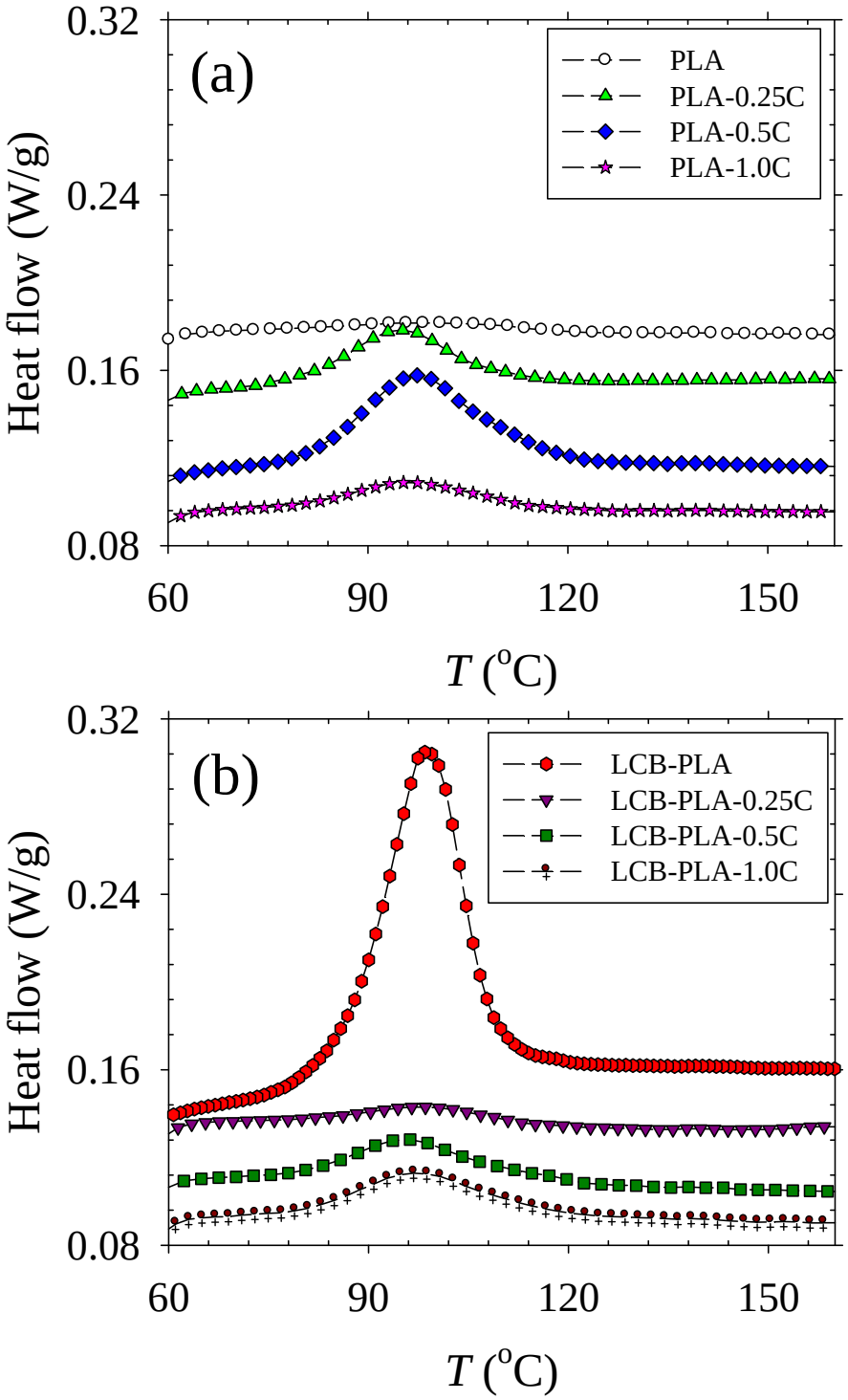

Figure 6.1: Non-isothermal melt crystallization thermograms of (a) linear and (b) LCB-PLA nanocomposites at a cooling rate of 5 °C/min. The curves are vertically shifted for clarity.

The introduction of a LCB structure into the neat PLA makes X_c increases from 1 to 30%. The formed branched structure acts as nucleation sites for the remaining linear chains having a higher local order and, hence, increases the crystallization degree [30]. Therefore, although LCB increases the chain folding energy of PLA chains and hinders them from folding back into crystal lamellas [30], this negative impact on crystallization can be offset by the nucleation ability of the branches. The inclusion of the clay nanoparticles, however, decreases the X_c values to 2, 5, and 6 % after the addition to the LCB-PLA of 0.25, 0.5 and 1 wt % of clay, respectively. Such a behavior was also observed in a LCB-PE-clay system by He *et al.*[31]. The coexistence of a LCB structure and dispersed nanoparticles strongly hinders chain mobility, resulting in a lowering of crystallinity.

6.4.2 Morphology of nanocomposites

The structure of linear and LCB-PLA nanocomposites containing various clay loadings is characterized on compression molded samples using X-ray diffraction. Figure 6.2 presents the XRD patterns of Cloisite 30B, the linear PLA and LCB-PLA nanocomposites.

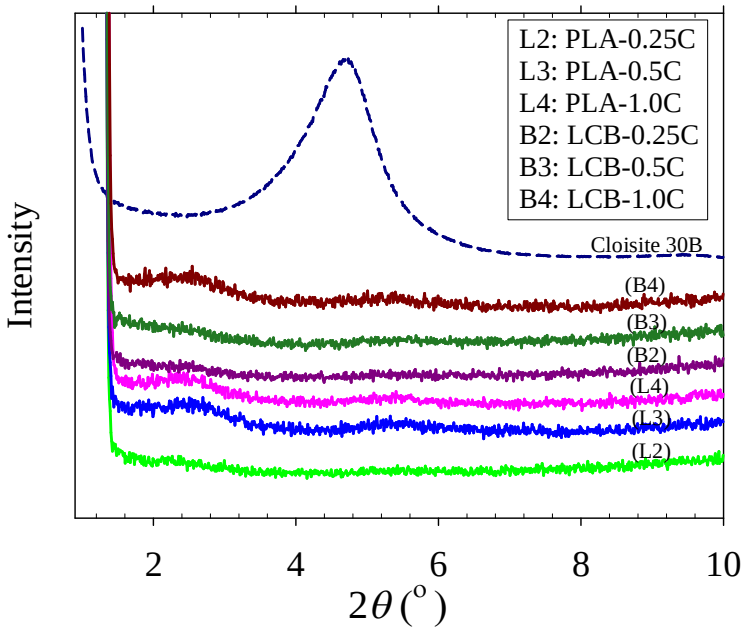

Figure 6.2: XRD patterns of the linear PLA and LCB-PLA nanocomposites containing different clay concentrations. The intensity axis has been shifted for clarity.

The diffraction pattern of Cloisite 30B exhibits a sharp reflection peak at 2θ = 4.73° that corresponds to a mean interlayer space of 1.86 nm. No peak was observed in the XRD pattern of the linear PLA nanocomposite containing 0.25 wt% clay, indicating that nanoparticles are somehow exfoliated in the PLA matrix.

The good clay dispersion is a result of the shearing during melt blending, enthalpic interactions of polymer chains with the organo-modified clay and diffusion of polymer chains through the clay galleries. An increase of the clay content to 0.5 and 1 wt% produce small peaks at 2θ of 2.5 and around 5° in the XRD pattern of linear PLA nanocomposites. The first and second peaks observed are, respectively, attributed to the basal spacing between clay layers (d_{001}) after intercalation of polymer chains into the galleries and the d_{002} reflection or possibly a peak reflecting some degradation of the organo-clay. In comparison to Cloisite 30B, the first peak intensity is significantly reduced in the nanocomposites and shifted to a lower angle.

The corresponding interlayer spacing, calculated using the Bragg equation, increases from 1.86 (original clay) to 3.53 nm. Based on the XRD results, the structure of the linear PLA nanocomposites containing 0.5 and 1 wt% clay are characterized by the coexistence of intercalated and exfoliated clay layers. Reduced exfoliation is achieved at higher clay content due to the following reasons: on the one hand, the incorporation of the organo-modified clay into PLA was found to intensify the thermal degradation, leading to a reduction of the PLA molecular weight (M_w) and, consequently, a reduced shearing force during melt mixing [7]. On the other hand, a good layered-silicate distribution in the matrix affects the polymer chain mobility and hinders the penetration of polymer into the clay gallery [32]. The XRD results of the LCB-PLA nanocomposites in Figure 6.2 reveal that the clay characteristic peak disappears in nanocomposites containing 0.25 and 0.5 wt% suggesting an exfoliated structure. The interactions occurring between the clay and LCB-PLA during melt blending and the increased shear force, provided by the higher molecular weight matrix in the following extrusion step, are responsible for the homogeneous clay dispersion. The LCB-PLA nanocomposite having 1 wt% clay, however, exhibits an intercalated-exfoliated structure due to the aforementioned factors. Morphological details of the linear and LCB-PLA nanocomposites containing 2 wt% Cloisite 30B, prepared using the same method, were examined using SEM and transmission electron microscopy (TEM) in our previous work [27] and confirm the present findings.

6.4.3 Morphology of foams

Representative SEM micrographs of the cross sections at the center of the molded foamed specimens are presented in Figure 6.3.

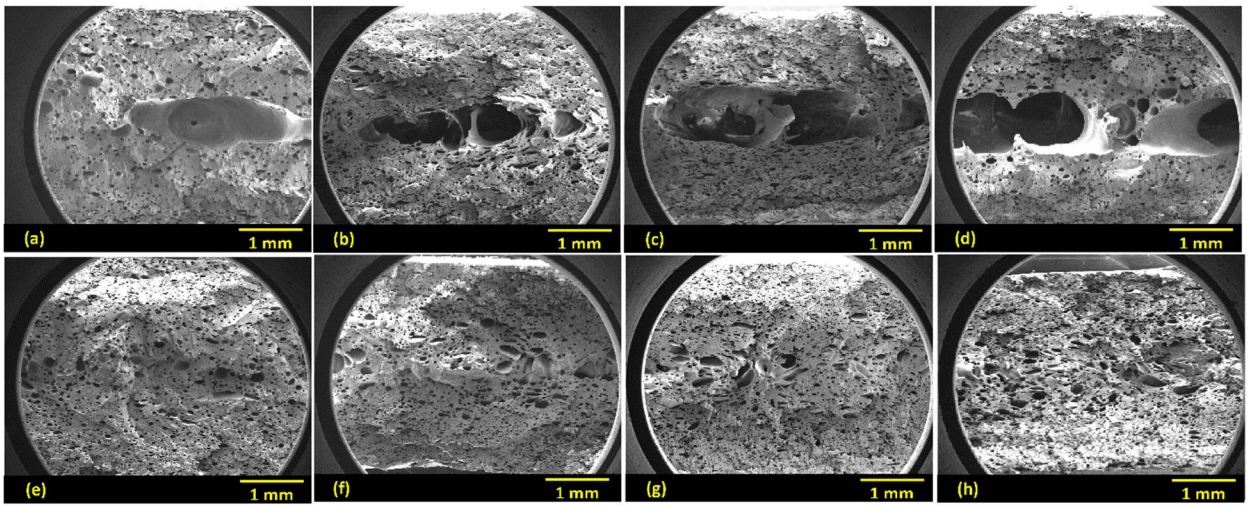

Figure 6.3: Representative SEM micrographs of cryo-fractured surfaces of (a) neat PLA, (b) PLA-0.25 wt% clay, (c) PLA-0.5 wt% clay, (d) PLA-1 wt% clay, (e) long-chain branched (LCB)-PLA, (f) LCB-PLA-0.25 wt% clay, (g) LCB-PLA-0.5 wt% clay, and (h) LCB-PLA-1 wt% clay.

The micrographs illustrate that closed cell structural foams consisting of three layers; two unfoamed (skin) layers and foamed (core) layer were obtained with a skin layer thickness of about 50-70 μm. The SEM micrographs of the linear PLA nanocomposite foams reveal that large gas pockets are formed in the core region of the cellular structure and the size of the pockets increases with nanoclay content (see Figures 6.3b-d). It seems that due to the low melt viscosity of the linear PLA, the shearing force during melt mixing is not sufficient to well disperse and distribute the gas into the matrix and generate a homogeneous polymer-gas mixture. The PLA thermal degradation and decreased melt viscosity induced by clay loading [7] may further reduce the shear force during mixing and worsen the dispersion/distribution of the gas in the polymer. The non-uniformity of the resulting cellular structure dramatically influences the mechanical properties, as discussed later.
The LCB-PLA and the corresponding nanocomposites, however, exhibit more uniform cellular structure in comparison with the linear PLA-based counterparts, as shown in Figures 6.3e-h.

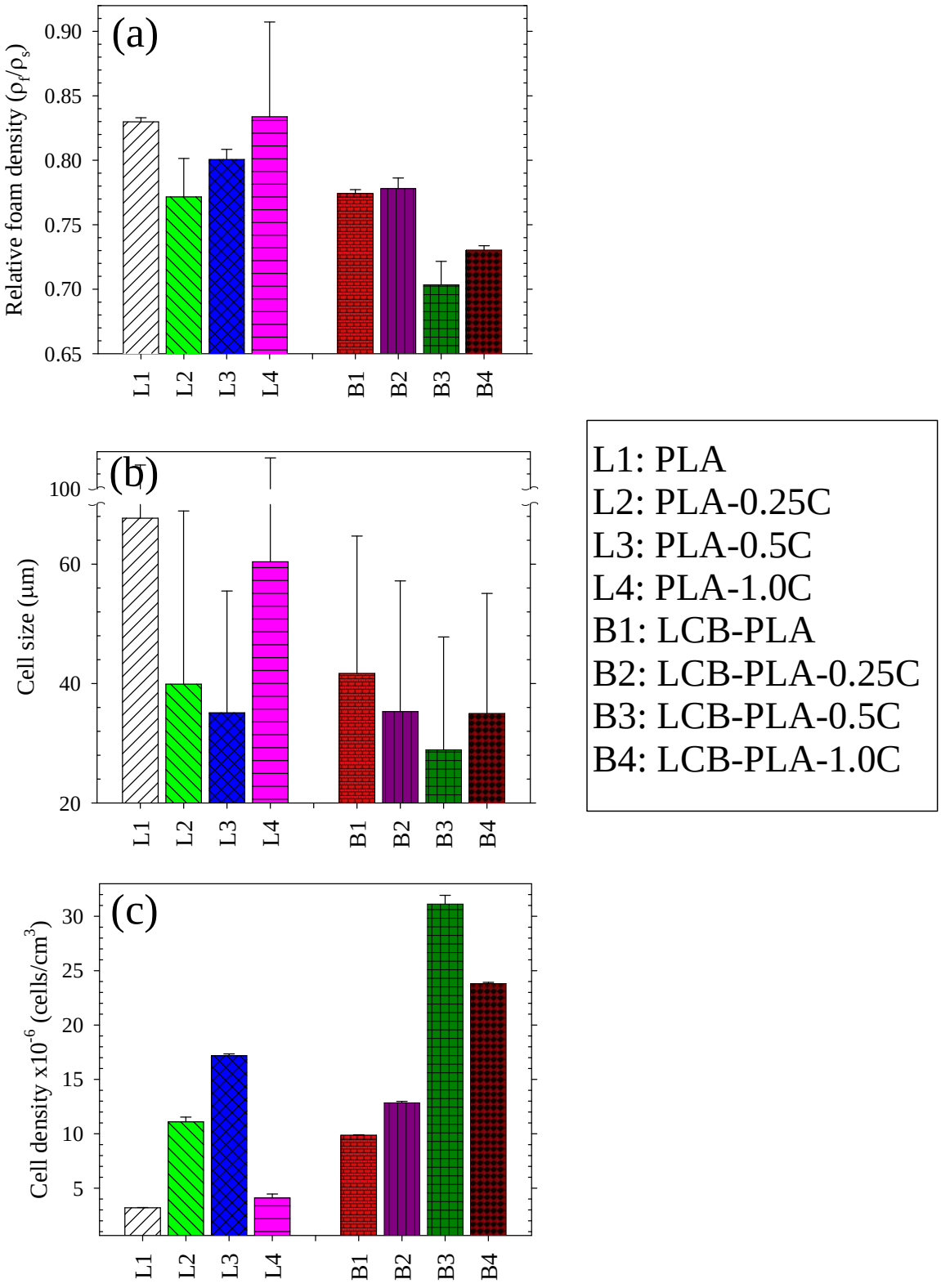

Figure 6.4: The effect of long chain branching and clay content on (a) relative foam density, (b) cell size, and (c) cell density of PLA foams.

The increased melt strength of the LCB-PLAs [13] and larger shearing force, as a result of branching, accelerates the gas diffusion rate [11]. It facilitates the generation of a uniform polymer-gas solution, thereby minimizing the chance of forming large undissolved gas pockets. The relative foam density (ρ_f/ρ_s, where ρ_s = 1.24 g/cm^3)), average cell size and cell density of the foamed PLAs and nanocomposites were determined for different clay loadings and are presented in Figures 6.4a, b and c, respectively. The foam characteristics are found to be strongly dependent on the blend composition. The neat PLA shows a non-uniform cellular structure with a relative density of 0.83. The calculated average cell size (excluding gas pockets) and cell density are 68 μm and 3.2×10^6 cells/cm^3, respectively. The addition of only 0.25 wt% clay to the neat PLA decreases the relative foam density and cell size to 0.77 and 40 μm, respectively, while increasing the cell density to 11.1×10^6 cells/cm^3. A further increase of the clay content up to 0.5 wt% results in a reduction of the cell size from 40 to 35 μm and an increase of the cell density from 11.1×10^6 to 17.2×10^6 cells/cm^3 as illustrated in Figures 6.4b and c. However, the relative density is slightly enhanced (from 0.77 to 0.80) as compared with that of the PLA containing 0.25 wt% clay.

The increased cell density in the presence of clay results from the nucleation effect of the dispersed silicate layers, thereby promoting heterogeneous cell nucleation. It was found that [33] the presence of solid filler particles tends to induce local stress fluctuations in polymer-gas solutions, leading to a significant reduction of the critical bubble radius and, thus, an increased cell nucleation density. In addition, the melt crystallization behavior of the linear PLA nanocomposites indicates that the crystallization starts earlier (a higher temperature) after the addition of nanoparticles up to 0.5 wt%. Furthermore, the plasticization effect of the dissolved gas [4] and shear force imposed during injection can further accelerate the crystallization rate [19]. The nucleated crystals can also act as nucleating agents and promote heterogeneous cell nucleation [34]. Due to an enhanced cell density in nanocomposites, less gas is available for each nucleated cell to grow [8], leading to the formation of cells of smaller size.

The fundamental mechanisms controlling the expansion ratio, and subsequently, the relative density of polymer foams were investigated by Naguib *et al.* [15]. The final expansion ratio was found to be governed either by the gas loss that occurred through diffusion out of the foam or by the crystallization and melt stiffening of the polymer matrix. A reduction of gas loss in the linear PLA nanocomposites containing 0.25 and 0.5 wt% clay is responsible for the reduced foam density

in comparison with the neat PLA. A dispersion of clay layers in the PLA matrix increases the tortuosity path and, thus, hinders the gas diffusion process [27]. As a result, the volume of gas retained in the foam is increased, leading to a greater volume expansion ratio and a reduced foam density. The PLA containing 0.5 wt% clay exhibits a slightly higher crystallization degree (11%) than the nanocomposite containing 0.25 wt% Cloisite 30B (6%). The enhanced degree of crystallinity as well as increased clay content limits the volume expansion of created cells causing an increment of foam density. The SEM image, shown in Figure 6.3d, and the results presented in Figure 6.4 illustrate that the addition of 1 wt% clay to the linear PLA impairs the morphology. The relative density and cell size (excluding gas pockets) increases to 0.84 and 60 μm, respectively. Despite the nucleation effect of dispersed clay layers, the cell density is significantly reduced (4.1×10^6 cells/cm^3), as compared with the other foamed linear PLA-based nanocomposites. The further reduction of the melt viscosity, as a result of thermal degradation, promotes the formation of large undissolved gas pockets, leading to the deterioration of the cellular morphology. Considering that gas molecules tend to diffuse into such pockets due to cell coarsening, the ability of the polymer-gas solution to generate new cells around them is vastly undermined [14]. Moreover, small nucleated cells around these large pockets collapse due to cell coarsening [35]. Therefore, smaller cells would continue to shrink while larger ones grow, leading to an enlarged average cell size.

The incorporation of the chain extender into the neat PLA and the resulting long chain branching significantly improve the cellular structure. The relative density and cell size are decreased, respectively, from 0.83 to 0.77 and from 68 to 42 μm. Meanwhile, the cell density is increased by a factor of 3 (9.9×10^6 cells/cm^3) as compared with the neat PLA (3.2×10^6 cells/cm^3). Once the gas diffusion and mass transfer become more difficult, because of an increased melt stiffness and increased crystallinity (30 %) of LCB-PLA, the amount of gas lost is reduced, causing a higher volume expansion and reduced foam density. The cell density is found to be related to the cell nucleation rate, which is controlled by the pressure drop and pressure drop rate ($-dP/dt$) [11, 36]; these are directly affected by the injection speed and the polymer gas mixture viscosity [11]. The increased melt viscosity and melt strength of the LCB-PLA result in larger pressure drop and pressure drop rate, but hinder the gas diffusion and mass transfer into nucleated bubbles. The gas contained in the polymer solution, thus, preferentially nucleate new microcells rather than diffusing into existing cells. Moreover, nucleated crystals in the LCB-PLA increases the number of

nucleation sites through heterogeneous nucleation, leading to an increase of the cell density. The reduction of the average cell size might be due to an increased melt strength and cell density. Similar to the linear PLA, the incorporation of nanoclay into the LCB-PLA significantly improves the cellular structure since more potential nucleation sites are formed. For instance, a finer (29 μm) and denser (31.1×10^6 cells/cm^3) cellular structure with a relative density of 0.7 is obtained in the foamed LCB-based nanocomposite containing 0.5 wt% clay. In comparison with the best-case results (cell size: 64 μm; cell density: 2.7×10^6 cells/cm^3) presented in Ref. [20], two times smaller cell size and 10 times larger cell density are obtained in this work, while using lower contents of chain extender and CBA. The LCB-PLA nanocomposite containing 1 wt% clay presents a reduction in cell density (23.8×10^6 cells/cm^3) and an increment in cell size (35 μm) in comparison with the LCB-based nanocomposite containing 0.5 wt% clay. The lower cell density achieved in this case can be attributed to a worse dispersion of the clay, as discussed in the XRD analysis. Such a detrimental impact of clay on the morphology implies that the clay concentration should be optimized to have finer cells and denser cell morphology.

6.4.4 Mechanical properties

The representative stress-strain curves of the unfoamed and foamed linear and LCB-PLAs containing no clay and 0.5 wt% Cloisite 30B are plotted in Figure 6.5a and the strain at break, specific modulus, and strength, are respectively, summarized in Figures 6.5b-d. The enhanced ductility of PLA nanocomposite is clearly evident on the stress-strain curve shown in Figure 6.5a. The incorporation of clay improves the deformation behavior of nanocomposites (see Figure 6.5b) since it retards the micro-void coalescence and subsequent crack formation [27], thereby increasing the toughness. The strain at break of the LCB-PLA and the corresponding nanocomposites is lower than that of the linear PLA based nanocomposites, as shown in Figure 6.5b. Long chain branching was found to increase the entanglement density of the polymer structure [37]. It, thus, further hinders the slippage [38] and orientation of the chains upon elongation, leading to a reduction of the strain at break. The specific properties are achieved by taking into account the respective density of the various samples. Unfoamed PLA is found to be very brittle with a strain at break of 3% while having a high specific modulus and tensile strength of 2680 and 48 MPa/(kg·m^{-3}), respectively.

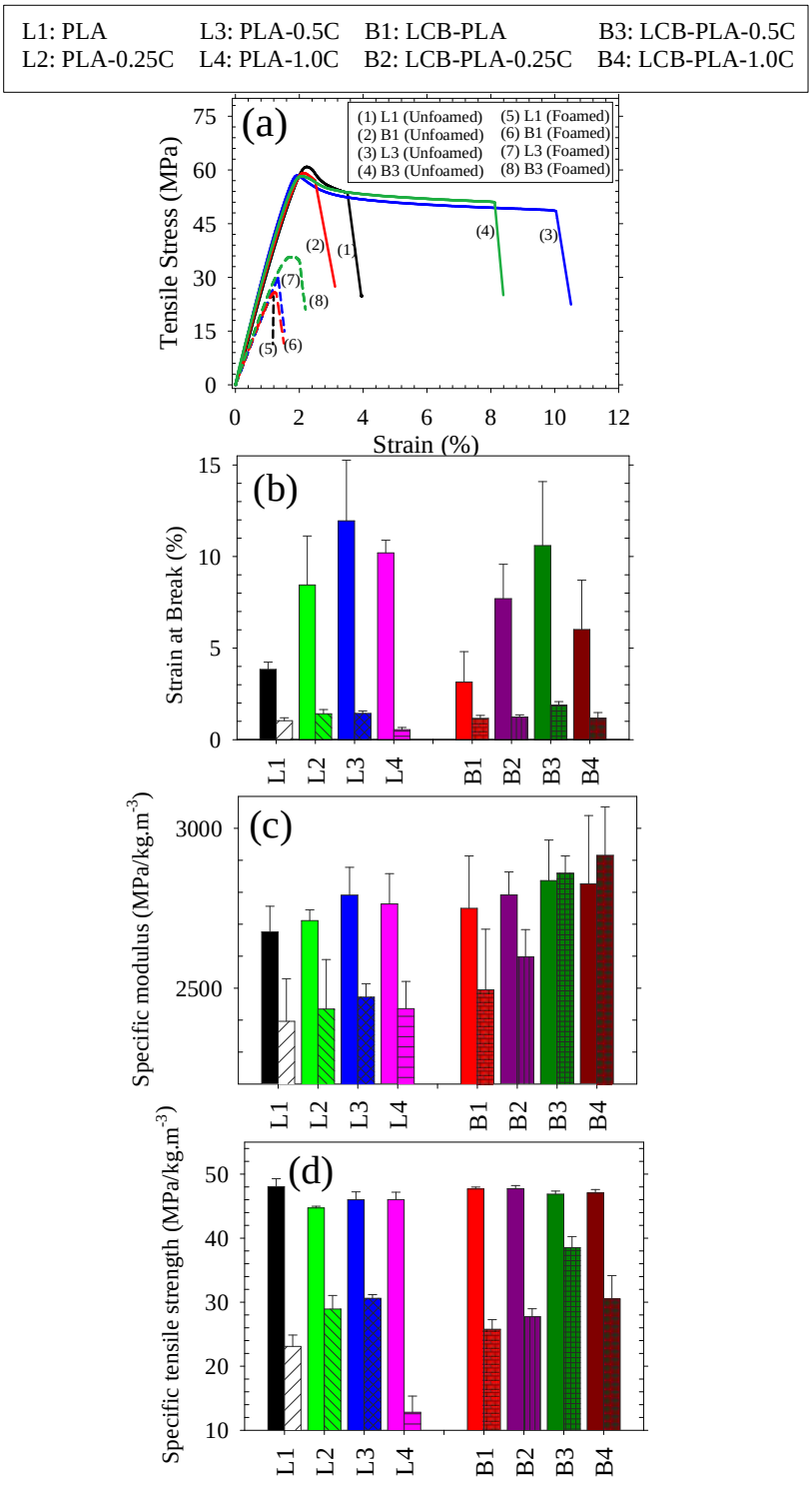

Figure 6.5: Tensile mechanical properties: (a) typical stress-strain curves, (b) strain at break, (c) specific tensile modulus, and (d) specific tensile strength of linear- and branched-based unfoamed (solid bars) and foamed nanocomposites (patterned bars).

The Young modulus of the unfoamed PLA nanocomposites is enhanced in comparison with that of the neat unfoamed PLA (Figure 6.5c). Considering that the silicate layers possess a larger modulus (6.2 GPa [39]) than the polymeric matrix, the modulus of the nanocomposites increases as expected with the clay content.

Crystallinity is another factor affecting the mechanical properties of the semi-crystalline polymer. To better analyze the mechanical properties, the degree of crystallization X_c of the solid specimens are calculated from the first DSC heating scans. The X_c values of the linear PLA containing 0, 0.25, 0.5 and 1 wt % Cloisite 30B were found to be 4, 22, 23, and 14%, respectively. Van der Wal *et al.* [40] showed that the modulus of polypropylene increased with increasing matrix crystallinity. Accordingly, the improved modulus of the nanocomposites results from an enhanced crystallinity and clay addition. In spite of increasing X_c, the tensile strength of the unfoamed linear PLA-based nanocomposites slightly drops in comparison with the neat PLA (Figure 6.5d), possibly explained by the reduction of the PLA M_w resulting from thermal degradation during processing.

The specific Young modulus of the LCB-PLA is 2750 MPa/(kg.m^{-3}), which is slightly larger than that of the linear one (2680 MPa/(kg.m^{-3})). The *X*c values of the LCB-PLA containing 0, 0.25, 0.5 and 1 wt % Cloisite 30B, calculated from the first DSC heating scans, are 18, 9, 11, and 12%, respectively. The increased crystallinity and enhanced molecular weight resulting from the long chain branching, are, thus, responsible for the increment of the modulus (Figure 6.5c). Similar to the neat PLA, the incorporation of clay into the LCB-PLA improves the Young modulus. The tensile strength of the LCB-PLA is almost unaffected by clay concentration and comparable with that of the linear PLA (Figure 6.5d). It is interesting to note that the properties of the compound with 1 wt% clay loading are slightly decreased as compared with samples containing 0.5 wt% clay, in all unfoamed systems. This is probably due to the lower quality of the clay dispersion, as discussed in the XRD analysis.

The mechanical properties of the foamed structure are significantly influenced by the cellular structure. The foamed linear-PLA based nanocomposites exhibit a premature fracture before reaching the yield point, as shown in Figure 6.5a (curves no. 5 and 7). These specimens have lower specific properties than the unfoamed ones. Based on the SEM results, large cavities are formed in the core region of these specimens. High stress concentrations are generated near these voids, causing a premature failure in tensile testing. In comparison with foams based on the linear PLA, increased strain at break, specific tensile modulus and strength are observed in the foamed LCB-

PLA systems, as evidenced in Figures 6.5b, c, and d. This is explained by the increased M_w and the formation of a more uniform, finer and denser cellular structure, as shown in the SEM micrographs of Figure 6.3. These values increase with increasing clay content up to 0.5 wt%, so that the largest mechanical properties are achieved in the foamed LCB-PLA nanocomposite with 0.5 wt % clay loading. Note that although the foamed LCB-PLA nanocomposite with 1 wt% clay possesses a higher specific modulus than the nanocomposite with 0.5 wt% clay (see Figure 6.5c), a larger error bar for this sample indicates a greater variability. These findings are consistent with the morphological observations where the LCB-PLA nanocomposite with 0.5 wt % clay exhibits smaller cell size and higher cell density than other samples.

The results for specific impact strength of the unfoamed and foamed linear and LCB-PLA systems are presented in Figure 6.6. A specific impact strength of 17.5 and 16.8 $(kJ.m^{-2})/(kg.m^{-3})$ is obtained for the unfoamed linear PLA and LCB-PLA specimens, respectively. The higher crystallinity of the unfoamed LCB-PLA (18 %) compared to the linear counterpart (4%) is responsible for a slight reduction in the impact strength of LCB-PLA. The impact strength is generally related to the polymer chain mobility and response to imposed stress [38].

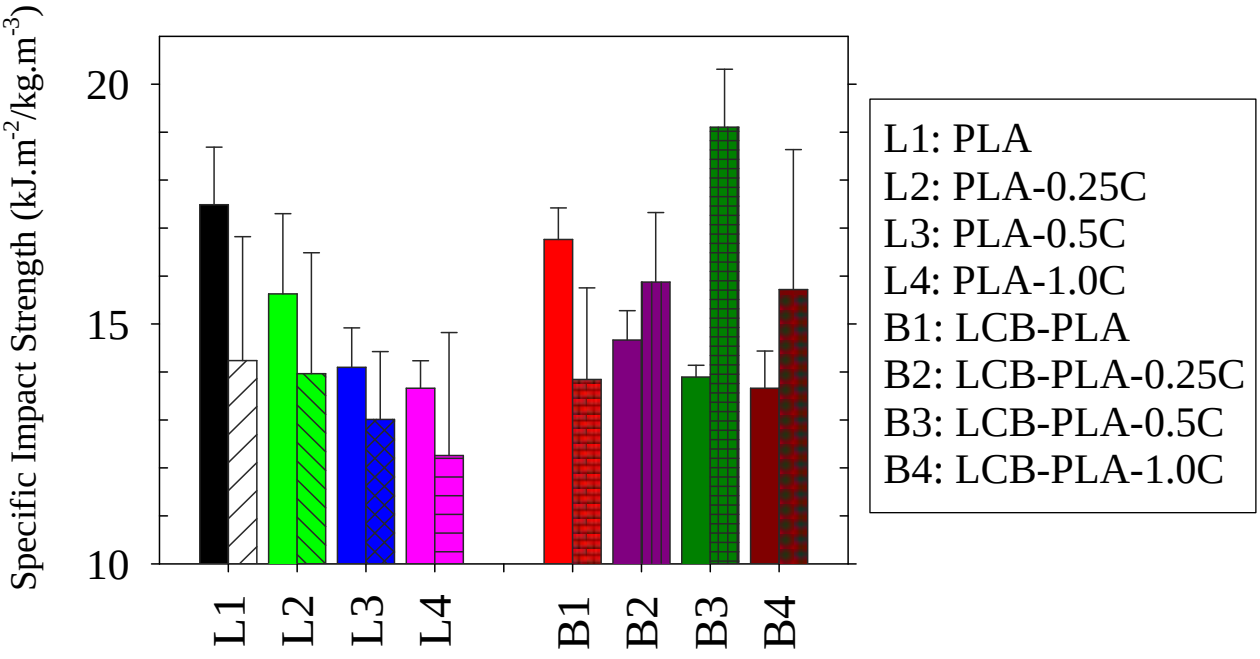

Figure 6.6: Specific impact strength of the linear- and branched-based PLA nanocomposites with unfoamed (solid bars) and foamed structures (patterned bars).

Considering that the crystal phase restricts the motion of chains, it decreases the impact strength of polymers that have a T_g well above the test temperature [38], which is the case of PLA (T_g ~ 60 °C). The incorporation of clay into the linear PLA and LCB-PLA gradually reduces the specific impact strength, most probably because the clay layers confine the chains mobility. It is worth noting that the dispersion of clay particles into the linear PLA increased the degree of crystallization. It is, therefore, another reason why the impact strength of the linear PLA decreased after adding clay. In addition, Figure 6.6 clearly reveals that the specific impact strength of the foamed samples is significantly affected by the cellular structure. The foamed linear PLA-based nanocomposites exhibit a specific impact strength lower than that of the unfoamed counterparts, while revealing a similar trend in terms of the role of clay. The large cavities observed in the core region (see Figures 6.3a-d) may act as crack initiators and, thus, significantly reduce the impact resistance. In the foamed LCB-PLA nanocomposites, however, the specific impact strength increases with clay content and is higher than that of the unfoamed counterparts. This increase is more pronounced in the case of the LCB-PLA containing 0.5 wt% Cloisite 30B, for which the specific impact resistance increases from 13.9 to 19.1 $(kJ.m^{-2})/(kg.m^{-3})$ (37%). This enhancement is most probably the result of the improved cell morphology, with a larger number of uniformly distributed smaller-sized cells that enhance the energy absorption [2].

6.5 Conclusion

The impact of clay inclusion and long chain branching (LCB) on the cellular structure of PLA were investigated. Linear PLA and LCB-PLA nanocomposites with different clay loadings were prepared via melt extrusion and, then, foamed in a conventional injection molding machine. The degree of crystallinity, clay dispersion, cellular morphology and mechanical properties were characterized. The addition of clay generally increased the crystallinity of the linear PLA while a reverse effect was observed for the LCB-PLA. The morphological observations and quantifications revealed that a more uniform, finer and denser cellular structure was achieved in the LCB-PLA reinforced by clay. In addition, 0.5 wt % clay was found to be the optimum content for achieving a uniform morphology with high cell density in the LCB-PLA, beyond which the cell density decreased. The mechanical properties of the foamed specimens were significantly influenced by

the cellular structure and a significant improvement of the mechanical properties was obtained at 0.5 wt% clay loading.

6.6 Acknowledgments

Financial support from AUTO21 (Canada's automotive R&D program) and NCE (Networks of Centres of Excellence of Canada) is gratefully acknowledged.

6.7 References

[1] Drumright RE, Gruber PR, Henton DE. Polylactic Acid Technology. Advanced Materials. 2000;12(23):1841-1846.

[2] Ameli A, Jahani D, Nofar M, Jung PU, Park CB. Development of high void fraction polylactide composite foams using injection molding: Mechanical and thermal insulation properties. Composites Science and Technology. 2014;90(0):88-95.

[3] Najafi N, Heuzey MC, Carreau PJ. Crystallization behavior and morphology of polylactide and PLA/clay nanocomposites in the presence of chain extenders. Polymer Engineering & Science. 2013;53(5):1053-1064.

[4] Nofar M, Tabatabaei A, Ameli A, Park CB. Comparison of melting and crystallization behaviors of polylactide under high-pressure CO2, N2, and He. Polymer. 2013;54(23):6471-6478.

[5] Peinado V, García L, Fernández Á, Castell P. Novel lightweight foamed poly(lactic acid) reinforced with different loadings of functionalised Sepiolite. Composites Science and Technology. 2014;101:17-23.

[6] Pantani R, Volpe V, Titomanlio G. Foam injection molding of poly(lactic acid) with environmentally friendly physical blowing agents. Journal of Materials Processing Technology. 2014;214(12):3098-3107.

[7] Najafi N, Heuzey MC, Carreau PJ, Wood-Adams PM. Control of thermal degradation of polylactide (PLA)-clay nanocomposites using chain extenders. Polymer Degradation and Stability. 2012;97(4):554-565.

[8] Pilla S, Kim SG, Auer GK, Gong S, Park CB. Microcellular extrusion foaming of poly(lactide)/poly(butylene adipate-co-terephthalate) blends. Materials Science and Engineering: C. 2010;30(2):255-262.

[9] So K. Automotive giants turn to bioplastics. Eur Plast News 2012;39:31-32.

[10] Airale A, Carello M, Scattina A. Carbon fiber monocoque for a hydrogen prototype for low consumption challenge. Material Science and Engineering :C. 2011;42(5):386-392.

[11] Xu J, Pierick D. Microcellular foam processing in reciprocating-screw injection molding machines. Journal of Injection Molding Technology. 2001;5(3):152.

[12] Di Y, Iannace S, Maio ED, Nicolais L. Poly(lactic acid)/organoclay nanocomposites: Thermal, rheological properties and foam processing. Journal of Polymer Science Part B: Polymer Physics. 2005;43(6):689-698.

[13] Najafi N, Heuzey M-C, Carreau P, Therriault D, Park C. Rheological and foaming behavior of linear and branched polylactides. Rheol Acta. 2014;53(10-11):779-790.

[14] Wong A, Park CB. Fundemental mechanisms of cell nucleation in plastic foam processing. In: Lee ST, Park CB, editors. Foam Extrusion: Principles and Practice: CRC Press; 2014.

[15] Naguib HE, Park CB, Reichelt N. Fundamental foaming mechanisms governing the volume expansion of extruded polypropylene foams. Journal of Applied Polymer Science. 2004;91(4):2661-2668.

[16] Kramschuster A, Turng L-S. An injection molding process for manufacturing highly porous and interconnected biodegradable polymer matrices for use as tissue engineering scaffolds. Journal of Biomedical Materials Research Part B: Applied Biomaterials. 2009;92B(2):366-376.

[17] Ameli A, Jahani D, Nofar M, Jung PU, Park CB. Processing and characterization of solid and foamed injection-molded polylactide with talc. Journal of Cellular Plastics. 2013.

[18] Nofar M, Park CB. Poly (lactic acid) foaming. Progress in Polymer Science. 2014;39(10):1721-1741.

[19] Najafi N, Heuzey MC, Carreau P, Therriault D. Quiescent and shear-induced crystallization of linear and branched polylactides. Rheol Acta. 2015;Accepted.

[20] Julien JM, Quantin JC, Bénézet JC, Bergeret A, Lacrampe MF, Krawczak P. Chemical foaming extrusion of poly(lactic acid) with chain-extenders: Physical and morphological characterizations. European Polymer Journal. 2015;67(0):40-49.

[21] Kharbas H, Nelson P, Yuan M, Gong S, Turng L-S, Spindler R. Effects of nano-fillers and process conditions on the microstructure and mechanical properties of microcellular injection molded polyamide nanocomposites. Polymer Composites. 2003;24(6):655-671.

[22] Pilla S, Kramschuster A, Lee J, Clemons C, Gong S, Turng L-S. Microcellular processing of polylactide–hyperbranched polyester–nanoclay composites. Journal of Materials Science. 2010;45(10):2732-2746.

[23] Pilla S, Kramschuster A, Gong S, Chandra A, Turng LS. Solid and microcellular polylactide-carbon nanotube nanocomposites. International Polymer Processing. 2007;22(5):418-428.

[24] Pilla S, Kramschuster A, Lee J, Auer GK, Gong S, Turng L-S. Microcellular and Solid Polylactide–Flax Fiber Composites. Composite Interfaces. 2009;16(7-9):869-890.

[25] Kramschuster A, Pilla S, Gong S, Chandra A, Turng LS. Injection Molded Solid and Microcellular Polylactide Compounded with Recycled Paper Shopping Bag Fibers. International Polymer Processing. 2007;22(5):436-445.

[26] Seo J-H, Han J, Lee KS, Cha SW. Combined Effects of Chemical and Microcellular Foaming on Foaming Characteristics of PLA (Poly Lactic Acid) in Injection Molding Process. Polymer-Plastics Technology and Engineering. 2012;51(5):455-460.

[27] Najafi N, Heuzey MC, Carreau PJ. Polylactide (PLA)-clay nanocomposites prepared by melt compounding in the presence of a chain extender. Composites Science and Technology. 2012;72(5):608-615.

[28] Xu X, Park CB, Xu D, Pop-Iliev R. Effects of die geometry on cell nucleation of PS foams blown with CO2. Polymer Engineering & Science. 2003;43(7):1378-1390.

[29] Fischer EW, Sterzel H, Wegner G. Investigation of the structure of solution grown crystals of lactide copolymers by means of chemical reactions. Colloid and Polymer Science. 1973;251(11):980-990.

[30] Yu F, Zhang H, Zhou C. Flow induced crystallization of long chain branched polypropylenes under weak shear flow. European Polymer Journal. 2009;45(7):2110-2118.

[31] He F-A, Zhang L-M. Study on branching structure, melting, and crystallization of polyethylene prepared by nickel a-diimine catalyst covalently intercalated inside OapPOSS-modified laponite clay gallery. Polymer Testing. 2014;35:80-86.

[32] Lew CY, Murphy WR, McNally GM. Preparation and properties of polyolefin-clay nanocomposites. Polymer Engineering & Science. 2004;44(6):1027-1035.

[33] Wang C, Leung SN, Bussmann M, Zhai WT, Park CB. Numerical Investigation of Nucleating-Agent-Enhanced Heterogeneous Nucleation. Industrial & Engineering Chemistry Research. 2010;49(24):12783-12792.

[34] Keshtkar M, Nofar M, Park CB, Carreau PJ. Extruded PLA/clay nanocomposite foams blown with supercritical CO2. Polymer. 2014;55(16):4077-4090.

[35] Zhu Z, Xu D, Park CB, Fenton RG. Finite Element Analysis of Cell Coarsening in Plastic Foaming. Journal of Cellular Plastics. 2005;41(5):475-486.

[36] Park CB, Baldwin DF, Suh NP. Effect of the pressure drop rate on cell nucleation in continuous processing of microcellular polymers. Polymer Engineering & Science. 1995;35(5):432-440.

[37] Zhao W, Huang Y, Liao X, Yang Q. The molecular structure characteristics of long chain branched polypropylene and its effects on non-isothermal crystallization mechanical properties. Polymer. 2013;54(4):1455-1462.

[38] Landel RF, Nielsen LE. Mechanical properties of polymers and composites: CRC Press; 1993.

[39] Bandyopadhyay K, Vanorio T, Mavko G, Wenk HR, Voltolini M. Elastic anisotropy of clay. SEG Technical Program Expanded Abstracts 2008. p. 1835-1839.

[40] Van der Wal A, Mulder JJ, Oderkerk J, Gaymans RJ. Polypropylene–rubber blends: 1. The effect of the matrix properties on the impact behaviour. Polymer. 1998;39(26):6781-6787.

CHAPTER 7

GENERAL DISCUSSION

The manufacturing of polylactide (PLA) foams has recently drawn increasing attention since this technique reduces the weight and cost of the final products. PLA was, however, found to exhibit poor foamability because of low melt strength and melt elasticity, slow crystallization rate and narrow processing window. Low viscosity and melt strength may cause cell coalescence and coarsening and, hence, a reduction of the cell density.

In this regard, the first part of this study was devoted at producing long chain branched PLAs with various degrees of branching and investigating how the long chain branching and the molecular structure impact the melt rheology and batch foaming behavior of PLA. LCB-PLAs were prepared by a melt grafting reaction in the presence of a multi-functional chain extender (CE), Joncryl. Two different concentrations, 0.4 and 0.7 wt%, CE were added to the neat PLA to achieve different degrees of branching. LCB-PLA containing 0.4 wt% CE were prepared using two strategies called S1 and S2. In the strategy S1, the PLA and CE was directly mixed, leading to the formation of a LCB structure. In the second approach, strategy S2, the PLA was first compounded with 0.8 wt% CE and formed a highly LCB structure. Then, it was blended with the neat PLA at a weight ratio of 50:50. In fact, a highly LCB structure was introduced and blended with the linear PLA.

To find out how the chain extender reacted with PLA, the chain end content of the PLA was quantified. PLA polymeric chains contain two functional groups: hydroxyl groups (OH) and carboxylic acid groups (COOH). Although both chain ends can react with the epoxy groups of the chain extender, carboxyl groups react preferentially than hydroxyl groups with the epoxy groups [55, 155]. Hence, the variation of COOH group content after the incorporation of the CE was quantified using a titration method presented in Appendix A. The amount of carboxyl groups of the samples prepared using different strategies is reported in Figure AA.1 (Appendix A). The amount of consumed COOH groups as a result of reaction with the epoxy groups of the chain extender is shown in Figure AA.2 (Appendix A).

Neat (unprocessed) PLA contains 60.4 μmol of COOH groups per 1 g of polymer. Due to thermal degradation and chain scission occurring during processing, the COOH group content increased to 80.5 μmol/g in the processed PLA. The COOH group content, however, was reduced to 55.9

µmol/g after the addition of 0.4 wt% of CE using strategy S1. This result indicates that 30.6% of the PLA carboxyl groups were consumed by the epoxy groups of the CE. The addition of 0.7 wt% of the CE, using strategy S1, led to a consumption of 48.7 % of PLA COOH groups. The theoretical amount of consumed COOH groups by 0.7 wt% CE was calculated using Eq. 7.1:

$$\frac{(80.5-55.9)}{0.4}\times 0.7 = 43.05 \quad \text{The amount of consumed COOH groups}$$
$$\frac{43.05}{80.5}\times 100 = 53.4\,\% \quad \text{Percentage of the consumed COOH groups} \qquad \text{Eq. 7.1}$$

Therefore, theoretically 53.4 % of the carboxyl groups should be consumed after the addition of 0.7 wt% CE. The discrepancy between the theoretical value and that obtained using the titration method confirmed that a part of the CE epoxy groups reacted with PLA hydroxyl groups. As both chain ends of PLA (-OH and -COOH) react with the epoxy groups of CE, a highly LCB structure is formed, as sketched in Figure 7.1. In the case of the S2 compounded sample, the amount of consumed COOH groups obtained using the titration method (15.8 %) was much lower than the theoretical value (30.6 %). It suggests that a considerable amount of the epoxy groups reacted with hydroxyl groups of PLA, leading to the formation of a more developed LCB structure.

According to this finding, the molecular architecture of the different compounds is speculated and schematically illustrated in Figure 7.1. The neat PLA has a linear structure without branching (see Figure 7.1a). The addition of 0.4 wt% CE to the neat PLA using strategy S1 leads to the formation of a LCB structure, while linear polymer chains still co-exist (Figure 7.1b). In the strategy S2, 0.8 wt% of the CE was first compounded with the neat PLA, leading to the formation of a LCB structure (black lines in Figure 7.1c) and some highly LCB structure as shown with blue lines in Figure 7.1c. Red lines represents those PLA chains whose both chain ends (-OH and -COOH) reacted with the CE epoxy groups.

The resulting compound is then blended with the neat PLA in the internal mixer. Therefore, the CE-modified PLA prepared using strategy S2 contains a highly LCB structure co-existing with more linear segments, in comparison with that prepared using strategy S1. In the case of the PLA containing 0.7 wt% CE, the incorporation of a higher content of CE into the neat PLA, as depicted in Figure 7.1d, leads to an increase in the degree of long chain branching on the backbone chains (black lines), while some highly LCB macromolecules are formed (blue lines).

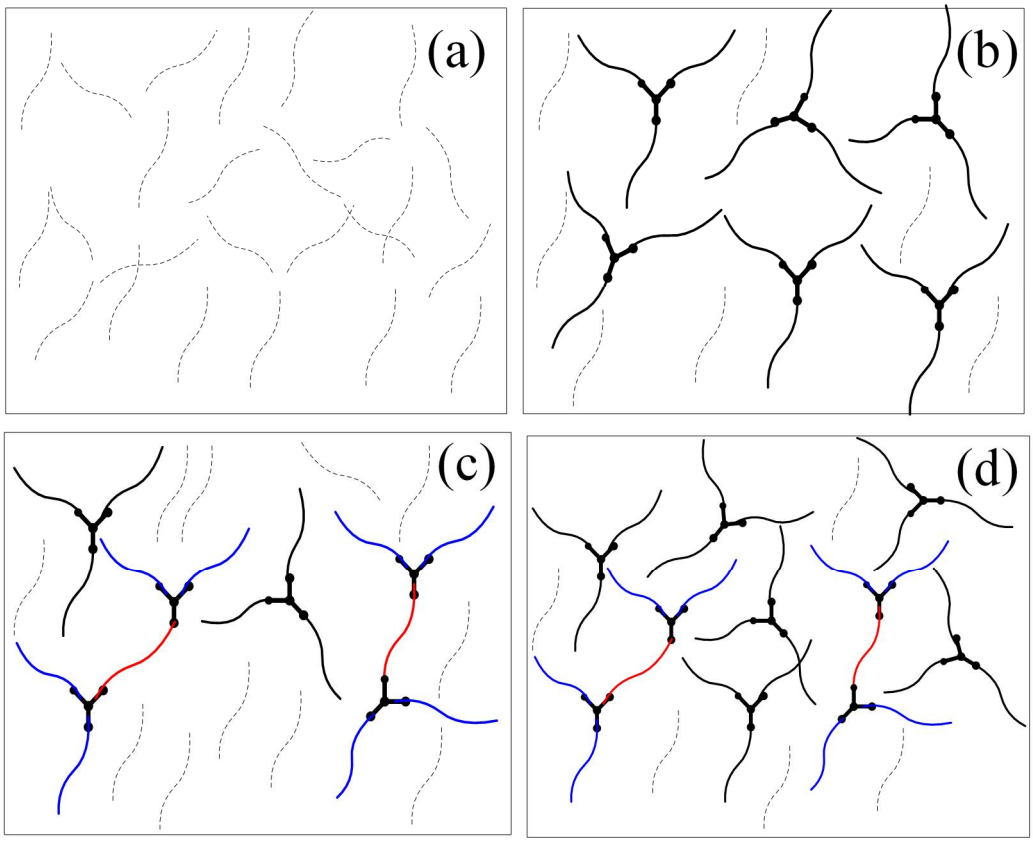

Figure 7.1: Schematic of molecular structure of (a) neat PLA, (b) PLA containing 0.4 wt% CE prepared using strategy S1, (c) PLA containing 0.4 wt% CE prepared using strategy S2 and (d) PLA containing 0.7 wt% CE.

The neat PLA is characterized by a low complex viscosity and shear viscosity. It is less sensitive to the applied shear rate and exhibits a broad Newtonian plateau (poor shear sensitivity). The incorporation of CE into the neat PLA and the formation of the LCB structure changes its rheological response, considerably. The magnitude of the complex and steady shear viscosity increased by two orders of magnitude at low frequencies or shear rates, depending on the CE content. The presence of a microstructure with a long relaxation time resulted in shifting the transition from a Newtonian plateau to the so-called shear-thinning regime to a lower frequency or shear rate. The formation of such highly branched macromolecules in the S2 compounded sample was responsible for further broadening of the MWD, increasing viscosity, and elasticity at low frequencies as compared to that of the S1 compounded sample.

In foaming processes, the deformation takes place over a limited period of time, during which the flow does not have enough time to get fully developed [3]. Therefore, the transient flow properties are more relevant than steady-state properties in foaming processes. The transient flow properties, the normalized shear stress growth coefficient and the transient uniaxial elongational viscosity, were investigated, since they significantly affect the foamability of the polymer. In addition to these properties, the transient biaxial elongational viscosity of these samples was also studied in collaboration with Rebecca Mick and Prof. David Venerus from the Illinois Institute of Technology (IIT) and are presented in Figure AB.1 (Appendix B). Our results as well as these results demonstrate that the elongational viscosity of the LCB-PLAs significantly deviated from the linear viscoelasticity at all strain rates, and showed a strain-hardening behavior at longer times. The enhanced entanglement density in LCB-macromolecules, in fact, hindered the chain contraction during extension, leading to a pronounced strain-hardening behavior in both the transient uniaxial and biaxial elongational viscosity.

To examine the role of material composition and molecular structure on the PLA foamability, the batch foaming of the linear and LCB-PLAs was conducted at three different foaming temperatures of 130, 140, and 155 ^{o}C. In contrast with the linear PLA, the LCB-PLAs did not foam, well, at the foaming temperature of 130 ^{o}C due to the too high stiffness and strength of the molten polymers. However, at higher foaming temperatures of 140 and 155 ^{o}C, the LCB-PLAs exhibited more uniform cells with smaller size and larger cell density as compared with the linear PLA. The void fraction was found to strongly depend on the LCB content and processing conditions. The void fraction of the foamed neat PLA was reduced with increasing foaming temperature, while a reverse behavior was observed for the LCB-PLAs. The cell density of the neat PLA continuously decreased with increasing foaming temperature. It was attributed to severe cell coalescence and cell rupture, resulting from a reduction of the polymer melt strength. As a result, most of the nucleated cells were broken during expansion and the cell density of the foam was markedly reduced. The incorporation of the chain extender into neat PLA promoted cell density by two orders of magnitude. A higher melt strength and strain hardening behavior, resulting from long chain branching, stabilized the nucleated cells by minimizing the cell coalescence during expansion and, thereby, increased the cell density

Crystallinity is another factor profoundly affecting cell nucleation and growth phenomena in PLA foaming processes. The crystal phase may induce heterogeneous cell nucleation, resulting in an

increased cell density and a reduced cell size. This is a reason why a low concentration of chain extender was used in this study. PLA suffers from low degree and low rate of crystallization. The introduction of a LCB structure into PLA, resulting from the addition of 0.4 wt% of CE using strategy S1, significantly increased the crystallization rate and degree. This finding indicated that the newly formed branched structure acted as nucleation sites for the linear chains having a higher local order, and hence, accelerated the crystallization kinetics.

The introduction of a higher content of CE (0.7 wt%), however, reduced the rate and degree of crystallization. This suggested that LCB might play a dual role during crystallization: first, increase of the crystal nucleation induced by the heterogeneous mechanism, leading to enhanced degree and rate of crystallization and second, increase the chain folding energy barrier and hinder PLA chains from folding back into crystal lamellae. This implied that there is a critical degree of LCB above which the effect is reversed. Therefore, a low concentration of CE (0.4 wt%) was chosen to be added to the PLA, but using another strategy, called strategy S2. The presence of some highly LCB structure and more linear segments in S2-compounded sample promoted crystal nucleation and crystal growth, respectively. The preparation of LCB structure using strategy S2, not only improved the melt strength of PLA, but also enhanced the rate and degree of crystallization.

The quiescent and shear-induced isothermal crystallization behavior of linear and LCB- PLAs was investigated by rotational rheometry at a temperature of 130 ^{o}C in the second part of this study. In a previous study in our research group, Arias *et al.* [156] imposed a constant normal force throughout her rheological experiments to counterbalance the shrinkage of PLA during cooling and crystallization. Arias *et al.* [156] applied a shear rate at the crystallization temperature (110-130 ^{o}C) , leading to accelerated flow induced crystal nucleation. As a consequence of that, the sample significantly shrunk (30%) throughout the experiment and its contact with the upper plate of the rheometer was lost. In the present work, the results obtained using the normal force control were compared with those obtained without. No significant differences were observed since the shear rate was applied at a much higher temperature (180°C, hence in the molten state). Therefore, the measurements were performed without imposing a normal force in this work.

The evolution of the reduced viscosity ($\eta_r^* = \eta_t^* / \eta_{t=0}^*$) with time was used to study the crystallization kinetics. To ensure that the samples were free of crystals when starting the

isothermal test at crystallization temperature, the initial values of the measured complex viscosity at $t = 0$ ($\eta^*_{(t=0)}$) were compared with the values predicted by time-temperature superposition. The Arrhenius equation (Eq. 7.2) [157] and Williams–Landel–Ferry (WLF) equation (Eq. 7.3) [157] were used to obtain the shift factors:

$$a_T = \exp\left(\frac{-E_a}{R}\left(\frac{1}{T} - \frac{1}{T_{ref}}\right)\right) \quad \text{Eq. 7.2}$$

$$\log a_T = \exp\left(\frac{-c_1(T - T_{ref})}{c_2 + (T - T_{ref})}\right) \quad \text{Eq. 7.3}$$

where a_T, E_a, R, T and T_{ref}, respectively, are shift factor, activation energy, gas constant, measurement temperature(K) and reference temperature (K), while c_1 and c_2 are temperature dependent constants. In this work, even though the WLF equation should have been preferentially used because of the temperature range considered (less than 100 °C above *T*g), this equation could not fit the experimental data; however, the Arrhenius equation well predicted the rheological properties at low temperatures. The predicted viscosities of these samples using the Arrhenius equation at the crystallization temperature of 130 °C were comparable with the measured viscosities, confirming that they contained no significant amount of crystals at the beginning of the isothermal crystallization test.

A reduction in the onset of crystallization as a consequence of increasing shear strain was observed in both linear PLA and LCB-PLAs. This reduction resulted from the formation of oriented amorphous chains in the sheared melts that served as primary nuclei for crystal nucleation. Once the molten polymers were subjected to a longer pre-shearing time, more liquid fibrils were formed and, thus, accelerated the crystal nucleation process. The induction time dropped more rapidly after the introduction of CE and increasing LCB structure, due to an increase of the relaxation time. The oriented chains, formed under shear flow, with low relaxation time would relax to the original conformation once the deformation was withdrawn, and, therefore, crystallized quiescently. An increased relaxation time, resulting from the LCB structure, retarded the relaxation process, which was favorable to retain the oriented chains and generate precursors of crystallization. In addition to total strain, the contribution of shear rate to the crystallization kinetics of linear and LCB- PLAs was also investigated at three different values, 0.5, 0.8, and 1 $s^{-1,}$ for a constant strain of 300. The

results indicated that applying a higher shear rate for a shorter time was more effective to initiate crystallization at constant strain. An increase in the number of oriented chain segments were responsible for the reduced induction time.

To assess how the LCB structure and pre-shearing influenced the crystal morphology, the spherulite structure of linear and LCB- PLAs was monitored using a Linkam optical shearing system. The linear PLA showed a well-defined spherulitic structure. The introduction of LCB-structure to the PLA led to a significant increase of the spherulite density, confirming the nucleation effect of the branched structure. Meanwhile, the cell size and growth rate decreased in the LCB-PLAs due to a reduction of the chain mobility. The spherulite density was found to increase after imposing shear flow, while the growth rate decreased. The stretching of macromolecular chains in long-term shearing was responsible for the reduced growth rate. The stretched chains, in fact, needed a longer time to relax and join the crystal growth front. As a result, the spherulite growth rate was reduced in the sheared melts.

In the last part of this study, the impact of LCB and nanoclay incorporation on the injection foaming behavior of PLA were examined. Cloisite 30B was used because it is an organo-modified montmorillonite having two hydroxyl groups. The reaction occurring between its hydroxyl groups and the carboxyl groups of PLA promotes the delamination of clay platelets in the matrix [17]. The addition of clay increased the linear PLA crystallinity due to the heterogeneous nucleation effect of nano-sized dispersed particles. Although the LCB structure increased the crystallization degree of the neat PLA, the inclusion of LCB chains and clay nanoparticles, at the same time, decreased the degree of crystallinity. The coexistence of a LCB structure and dispersed nanoparticles strongly hindered chain mobility, thereby lowering the crystallinity.

The morphological observations and quantifications revealed that large gas pockets were formed in the core region of the cellular structure of the linear PLA nanocomposites. Due to the low melt viscosity of the linear PLA, the mechanical shearing force during melt mixing was not sufficient to well disperse and distribute the gas into the matrix and generated a homogeneous polymer-gas mixture. The presence of such large voids dramatically impaired the mechanical properties. However, a more uniform, finer, and denser cellular structure was achieved in the LCB-PLA and corresponding nanocomposites due to generation of a uniform polymer-gas solution and an increased pressure drop rate. The clay concentration of 0.5 wt % was found to be the optimum

content for achieving a uniform cellular structure in the LCB-PLA with a high cell density and a relative foam density of 0.7.

The mechanical properties of the foamed specimens were significantly affected by the cellular structure. A premature fracture, before reaching the yield point, was observed in the foamed linear-PLA based nanocomposites owing to a presence of large cavities in the core region of these specimens. High stress concentrations were generated near these voids led to a premature failure in tensile testing. In comparison with foams based on the linear PLA, a general increase in the strain at break, specific tensile modulus, tensile and impact strength was achieved in the foamed LCB-PLA systems. They results from the increased *M*w and formation of more uniform, finer and denser cellular structure. A significant improvement of the mechanical properties was observed in the LCB-PLA containing 0.5 wt % Cloisite 30B due to the increased cell density, reduced cell size, and uniformity of the cellular structure.

Finally, it is worth to note that by manipulating the molecular structure of polymer chains by the addition of just 0.4 wt% CE, the introduction of 0.5 wt% nanoclay as well as optimizing the processing conditions the weight of PLA nanocomposites was reduced by 30 %; also a uniform fine cellular structure with acceptable mechanical properties was developed, as planned in the main objective of this thesis. This system allowed us to produce PLA foams with two times smaller cell size and 10 times higher cell density than what are currently reported in the literature [108].

CHAPTER 8

CONCLUSIONS AND RECOMMENDATIONS

8.1 Conclusions

In this dissertation, the foaming behavior of polylactide (PLA) and its dependency on the molecular structure and rheological properties were investigated. As a critical factor affecting the foamability, the melt strength and strain hardening behavior was improved by the formation of long chain branched (LCB) structure. LCB-PLAs were prepared by a melt grafting reaction in the presence of a multi-functional chain extender (CE). CE at two different concentrations, 0.4 and 0.7 wt%, was added to the neat PLA to achieve different degrees of branching. LCB-PLAs containing 0.4 wt% CE were prepared using two strategies called S1 and S2. The steady and transient rheological properties of the linear and LCB-PLAs revealed that the introduction of the CE profoundly affected the melt viscosity and elasticity. The LCB-PLAs exhibited an increased viscosity, shear sensitivity, and longer relaxation time in comparison with the linear PLA. The incorporation of CE into PLA and the resulting LCB, moreover, caused a strong strain-hardening behavior in uniaxial and biaxial elongational flows whereas no strain hardening was observed for the linear PLA. Batch foaming of the linear PLA and LCB-PLAs was conducted using CO_2 at different foaming temperatures ranging from 130 to 155 ^oC in a high pressure vessel hosted in a rheometer. The impacts of molecular structure, crystallinity, and foaming temperature on the cell morphology, void fraction, cell density and cell size were examined. It was found that increasing the melt strength, elasticity, and crystallinity, resulting from branching, strongly increased the cell uniformity, cell density and void fraction. In general, the cell growth was accelerated with increasing foaming temperature. The cell density of LCB-PLAs was enhanced as the foaming temperature increased up to 140 ^oC, beyond which the cell density decreased. Among the investigated compositions, the PLA containing 0.4 wt% CE prepared by strategy S2 provided smaller cell size and higher cell density than the others.

The isothermal crystallization behavior of linear PLA and LCB-PLAs was investigated under quiescent and shear flow conditions using rheometry and optical microscopy. The quiescent crystallization behavior was studied at 130 ^oC and used as the reference point for the study of the shear-induced crystallization. The incorporation of an LCB structure into the linear PLA promoted

the crystallization kinetics. Among the investigated compositions, PLA containing 0.4 wt% CE prepared by strategy S2 exhibited the highest degree of crystallinity and fastest rate of crystallization. The shear-induced crystallization was affected by both the total shear strain and the shear rate. To determine the effect of shear strain, a pre-shear treatment was applied on the melt at constant shear rates of 0.1 and 1 s^{-1} for a period of 1, 5, and 10 min. The total shear strain further increased the crystallization rate. The shear strain impact on reducing the onset time of crystallization was more pronounced as the degree of LCB and molecular weight increased. To investigate the role of shear rate on the induced crystallization, a pre-shear was applied at rates of 0.5, 0.8, and 1 s^{-1} while keeping the total strain constant (γ=300). The induction time of the linear PLA and LCB-PLAs was reduced with increasing shear rate, even though the total shear strain was kept constant. The crystal morphology of the linear PLA and LCB-PLAs under quiescent and shear flow conditions was observed using a Linkam optical shear system. The spherulite density was found to increase in the strained melts as compared with those of unstrained counterparts. The optical micrographs also revealed that the nucleation density was significantly promoted in LCB-PLA, although the crystal growth rate was diminished.

The injection foam molding of the linear PLA and LCB-PLAs with different formulations was performed using a chemical blowing agent (CBA) in a conventional injection molding machine. In this step, CBA content, degree of LCB and injection molding processing parameters such as shot size, injection speed, back pressure, cooling time, nozzle and mold temperatures were varied to optimize the formulation and processing conditions. The optimized formulation and processing conditions were then used for the preparation of foamed Linear PLA and LCB-PLA nanocomposites for various contents of organoclay, Cloisite 30B. Then, they were, successfully, foamed using a chemical blowing agent (CBA) in a conventional injection molding machine. The intercalation, morphological, thermal, and mechanical properties were examined. The intensity of the XRD peaks was reduced for the LCB-PLA nanocomposites, indicating a higher level of delamination. The addition of clay increased the crystallinity of the linear PLA. However, the degree of crystallization was decreased in LCB-PLAs after clay inclusion. The incorporation of clay nano-platelets into the LCB-PLAs led to the formation of a more uniform, finer and denser cellular structure. Finally, it should be noted that the addition of just 0.4 wt% CE and 0.5 wt% nanoclay led to the formation of a uniform cellular structure with a relative density of 0.7, a cell density increased by 10 times and an improved mechanical properties.

8.2 Original contributions

In the first part of this study the role of molecular features and degree of long chain branching on the viscoelastic properties, crystallization behavior and foamability of PLA were well demonstrated. Furthermore, a strategy was developed through which a high melt strength and crystallized PLA appropriate for foaming was produced. A fundamental study was performed, in the second part of this thesis, to investigate the shear induced crystallization behavior of the linear and LCB-PLAs. The impact of LCB-structure, shear strain and shear rate on the crystallization rate, spherulite density and spherulite growth rate was clarified using rheological and microscopic techniques. It was shown that the shear-induced crystallization of the linear and LCB-PLAs was influenced not only by the total shear strain but also by the shear rate. The linear and LCB-PLAs reinforced with small amount of nanoclay were foamed using a conventional injection molding machine in the last part of this research. It was revealed that the morphological and mechanical properties significantly improved if just 0.4 wt% CE and 0.5 wt% nanoclay were judiciously added to the PLA.

8.3 Recommendations

1- Although the impact of shear stress on the crystal nucleation of the linear and LCB- PLAs was visualized using an optical device in this study, the cell nucleation process of these systems under shear stress was not observed yet. The in-situ visualization of the cell nucleation phenomenon of linear and LCB-PLAs under various shear stresses is recommended.

2- The transient rheological properties of linear and LCB-PLA at ambient pressure were investigated. To study further the effect of dissolved gas on these properties, it is recommended to perform at or above supercritical pressure the testing of the elongational behavior of the PLA-gas system.

3- The materials are subjected to complex shear and elongational deformation at the die and nozzle in continuous and semi-continuous process, respectively. The impact of shear flow on the shear-induced crystallization behavior of the linear and branched PLA were examined. It is recommended to elucidate the effect of elongational flow on the crystallization behavior of

linear and LCB-PLA. To this end, the impact of stretching on degree and rate of crystallization in linear and LCB-PLA should be analyzed.

4- The cell size, cell distribution, and consequently, mechanical properties of the foamed samples are affected by the gas dissolution and dispersion into the molten polymer. The screw configuration is one of the key factors affecting the uniformity of gas distribution. Although we used a standard screw typical for injection molding, the effect of screw configuration with different kneading blocks and mixing sections on cell size and distribution should be examined.

5- It was found that both the magnitude and the rate of pressure drop play a strong role in foaming process. The pressure phenomenon influences the thermodynamic instability and the competition between cell nucleation and growth. The sprue length and gate diameter affect the pressure drop and pressure drop rate. Optimization of the sprue length and gate diameter in order to achieve small cell size and uniform cell size distribution should be considered.

6- Hybrid composites are materials made by combining two or more different types of filler in a polymeric matrix. The resulting composites, generally, offer some advantages in terms of mechanical properties that are not achievable with using a single type of filler. The long chain branched PLA-fiber-nanoclay hybrid composites are strongly recommended to be prepared by twin screw extruder and then foamed using a chemical blowing agent (CBA) in a conventional injection molding machine.

BIBLIOGRAPHY

[1] Szeteiova K. Automotive materials: Plastic in automotive markets today. , Slovak University of Technology Bratislava: Institute of Production Technologies, Machine Technologies and Materials, Faculty of Material Science and Technology in Trnava; 2014.

[2] Srivastava V, Srivastava R. Advances in automotive polymer applications and recycling. International Journal of Innovative Research in Science, Engineering and Technology. 2013;2(3).

[3] Contributing to the use of Ecological Plastic for approximately 60% of an automobile interior surface area.

[4] Toyota north american environmental report: green innovation. 2012.

[5] Lim LT, Auras R, Rubino M. Processing technologies for poly(lactic acid). Progress in Polymer Science. 2008;33(8):820-852.

[6] Harris AM, Lee EC. Improving mechanical performance of injection molded PLA by controlling crystallinity. Journal of Applied Polymer Science. 2008;107(4):2246-2255.

[7] Harris AM, Lee EC. Injection molded polylactide (PLA) composites for automotive applications. Proceedings of the society of polymer engineers' automotive composites conference, 2006. p. 1-9.

[8] Fukushima K, Tabuani D, Camino G. Nanocomposites of PLA and PCL based on montmorillonite and sepiolite. Materials Science and Engineering: C. 2009;29(4):1433-1441.

[9] Sargent FT. Trailer hitch carriage. Google Patents; 1981.

[10] Lee LJ, Zeng C, Cao X, Han X, Shen J, Xu G. Polymer nanocomposite foams. Composites Science and Technology. 2005;65(15–16):2344-2363.

[11] Wong A. In Situ observation of plastic foaming under static condition, extensional flow and shear flow. University of Toronto, Mechanical and Industrial Engineering, 2012.

[12] Di Maio E, Mensitieri G, Iannace S, Nicolais L, Li W, Flumerfelt RW. Structure optimization of polycaprolactone foams by using mixtures of CO2 and N2 as blowing agents. Polymer Engineering & Science. 2005;45(3):432-441.

[13] Faruk O, Bledzki AK, Matuana LM. Microcellular Foamed Wood-Plastic Composites by Different Processes: a Review. Macromolecular Materials and Engineering. 2007;292(2):113-127.

[14] Gendron R. Thermoplastic foam processing, principles and development: CRC Press; 2005.

[15] Najafi N, Heuzey MC, Carreau PJ, Wood-Adams PM. Control of thermal degradation of polylactide (PLA)-clay nanocomposites using chain extenders. Polymer Degradation and Stability. 2012;97(4):554-565.

[16] Sinha Ray S, Yamada K, Okamoto M, Ueda K. New polylactide-layered silicate nanocomposites. 2. Concurrent improvements of material properties, biodegradability and melt rheology. Polymer. 2003;44(3):857-866.

[17] Krikorian V, Pochan DJ. Poly (l-Lactic Acid)/Layered Silicate Nanocomposite: Fabrication, Characterization, and Properties. Chemistry of Materials. 2003;15(22):4317-4324.

[18] Perego G, Cella GD, Bastioli C. Effect of molecular weight and crystallinity on poly(lactic acid) mechanical properties. Journal of Applied Polymer Science. 1996;59(1):37-43.

[19] Saeidlou S, Huneault MA, Li H, Park CB. Poly(lactic acid) crystallization. Progress in Polymer Science. 2012;37(12):1657-1677.

[20] Barzegari MR, Rodrigue D. The effect of injection molding conditions on the morphology of polymer structural foams. Polymer Engineering & Science. 2009;49(5):949-959.

[21] Saiz-Arroyo C, Rodríguez-Pérez MA, Tirado J, López-Gil A, de Saja JA. Structure–property relationships of medium-density polypropylene foams. Polymer International. 2013;62(9):1324-1333.

[22] Klink G, Rouilloux G, Znojek B. Plastics: The future for automakers and chemical companies. Available online:https://www.atkearney.com/paper/-/asset_publisher/dVxv4Hz2h8bS/ content/ plastics-the-future-for-automakers-and-chemical-companies/10192, 2012.

[23] Rudnik E. Outlines & highlights for compostable polymer materials 2011.

[24] Sinha Ray S, Bousmina M. Biodegradable polymers and their layered silicate nanocomposites: In greening the 21st century materials world. Progress in Materials Science. 2005;50(8):962-1079.

[25] Theinsathid P, Chandrachai A, Keeratipibul S. Managing Bioplastics Business Innovation in Start Up Phase. Journal of Technology Management & Innovation. 2009;4(1):82.

[26] Soppimath KS, Aminabhavi TM, Kulkarni AR, Rudzinski WE. Biodegradable polymeric nanoparticles as drug delivery devices. Journal of Controlled Release. 2001;70(1–2):1-20.

[27] Biopolymers in automotive interiors : a step towards sustainability. www.Plastemart.com, 2003.

[28] Che Wen Tseng S. Using bio-based materials in the automotive industry. University of Windsor, Mechanical Engineering, 2012.

[29] Garlotta D. A Literature Review of Poly(Lactic Acid). Journal of Polymers and the Environment. 2001;9(2):63-84.

[30] Bajpai PK, Singh I, Madaan J. Development and characterization of PLA-based green composites: A review. Journal of Thermoplastic Composite Materials. 2014;27(1):52-81.

[31] Bledzki AK, Jaszkiewicz A. Mechanical performance of biocomposites based on PLA and PHBV reinforced with natural fibres – A comparative study to PP. Composites Science and Technology. 2010;70(12):1687-1696.

[32] Crank M, Marscheider-Weidemann F, Schleich J, Husing B, Angerer G. Techno-economic Feasibility of Large-scale Production of Bio-based Polymers in Europe. In: Wolf O, editor., Spain: European Commission; 2005. p. 256.

[33] Saygin D, Gielen D, Draeck M, Worrell E, Patel MK. Assessment of the technical and economic potentials of biomass use for the production of steam, chemicals and polymers. Renewable and Sustainable Energy Reviews. 2014;40:1153-1167.

[34] Mohanty AK, Misra M, Lawrence TD. Natural fibers, biopolymers, and biocomposite. Michigan: Taylor & Francis; 2005.

[35] Mihai M, Huneault MA, Favis BD, Li H. Extrusion Foaming of Semi-Crystalline PLA and PLA/Thermoplastic Starch Blends. Macromolecular Bioscience. 2007;7(7):907-920.

[36] Achmad F, Yamane K, Quan S, Kokugan T. Synthesis of polylactic acid by direct polycondensation under vacuum without catalysts, solvents and initiators. Chemical Engineering Journal. 2009;151(1–3):342-350.

[37] Nagahata R, Sano D, Suzuki H, Takeuchi K. Microwave-Assisted Single-Step Synthesis of Poly(lactic acid) by Direct Polycondensation of Lactic Acid. Macromolecular Rapid Communications. 2007;28(4):437-442.

[38] Wang Z-Y, Li X-W, Li J-N, Li G-M, Tao J-Q. Synthesis of poly(lactic acid)-poly(phenyl phosphate) via direct polycondensation and its characterization. Journal of Polymer Research 2009;16(3):255-261.

[39] Hrkach JS, Ou J, Lotan N, Langer R. Synthesis of Poly(L-lactic acid-co-L-lysine) Graft Copolymers. Macromolecules. 1995;28(13):4736-4739.

[40] Kim SH, Han Y-K, Kim YH, Hong SI. Multifunctional initiation of lactide polymerization by stannous octoate/pentaerythritol. Die Makromolekulare Chemie. 1992;193(7):1623-1631.

[41] Lunt J. Large-scale production, properties and commercial applications of polylactic acid polymers. Polymer Degradation and Stability. 1998;59(1–3):145-152.

[42] Dos SGBCM, Simoes MDA, Mendes GMH. Process for preparing high molecular weight poly(lactic acid) by melt polycondensation. WO2013184014 A1: Google Patents; 2013.

[43] Drumright RE, Gruber PR, Henton DE. Polylactic Acid Technology. Advanced Materials. 2000;12(23):1841-1846.

[44] Ray SS. Recent Trends and Future Outlooks in the Field of Clay-Containing Polymer Nanocomposites. Macromolecular Chemistry and Physics. 2014;215(12):1162-1179.

[45] Wang Y, Chen F-B, Wu K-C. Twin-screw extrusion compounding of polypropylene/organoclay nanocomposites modified by maleated polypropylenes. Journal of Applied Polymer Science. 2004;93(1):100-112.

[46] Alexandre M, Dubois P. Polymer-layered silicate nanocomposites: preparation, properties and uses of a new class of materials. Materials Science and Engineering: R: Reports. 2000;28(1–2):1-63.

[47] Ahmadi SJ, Huang YD, Li W. Synthetic routes, properties and future applications of polymer-layered silicate nanocomposites. Journal of Materials Science. 2004;39(6):1919-1925.

[48] Matuana L, Faruk O. Hybrid HDPE/woodflour/montmorillonite nanocomposites. 9th international conferences on wood and biofiber plastics compoaites, Forest Products Society Madison, USA 2007. p. 107-112.

[49] Chen G-X, Yoon J-S. Clay Functionalization and Organization for Delamination of the Silicate Tactoids in Poly(L-lactide) Matrix. Macromolecular Rapid Communications. 2005;26(11):899-904.

[50] Paul M-A, Alexandre M, Degée P, Calberg C, Jérôme R, Dubois P. Exfoliated Polylactide/Clay Nanocomposites by In-Situ Coordination–Insertion Polymerization. Macromolecular Rapid Communications. 2003;24(9):561-566.

[51] Urbanczyk L, Ngoundjo F, Alexandre M, Jérôme C, Detrembleur C, Calberg C. Synthesis of polylactide/clay nanocomposites by in situ intercalative polymerization in supercritical carbon dioxide. European Polymer Journal. 2009;45(3):643-648.

[52] Ogata N, Jimenez G, Kawai H, Ogihara T. Structure and thermal/mechanical properties of poly(l-lactide)-clay blend. Journal of Polymer Science Part B: Polymer Physics. 1997;35(2):389-396.

[53] Li Y, Ren P-G, Zhang Q, Shen T-T, Ci J-H, Fang C-Q. Properties of Poly(Lactic Acid)/ Organo-Montmorillonite Nanocomposites Prepared by Solution Intercalation. Journal of Macromolecular Science, Part B. 2013;52(8):1041-1055.

[54] Chen G-X, Kim H-S, Shim J-H, Yoon J-S. Role of Epoxy Groups on Clay Surface in the Improvement of Morphology of Poly(l-lactide)/Clay Composites. Macromolecules. 2005;38(9):3738-3744.

[55] Najafi N, Heuzey MC, Carreau PJ. Polylactide (PLA)-clay nanocomposites prepared by melt compounding in the presence of a chain extender. Composites Science and Technology. 2012;72(5):608-615.

[56] Shen J, Zeng C, Lee LJ. Synthesis of polystyrene–carbon nanofibers nanocomposite foams. Polymer. 2005;46(14):5218-5224.

[57] Zhai W, Yu J, Wu L, Ma W, He J. Heterogeneous nucleation uniformizing cell size distribution in microcellular nanocomposites foams. Polymer. 2006;47(21):7580-7589.

[58] Pilla S, Kim SG, Auer GK, Gong S, Park CB. Microcellular extrusion foaming of poly(lactide)/poly(butylene adipate-co-terephthalate) blends. Materials Science and Engineering: C. 2010;30(2):255-262.

[59] Lee JWS, Wang J, Park CB, Tao G. Use of injection speed profile to achieve a uniform void fraction distribution in injection molded structural foams. Annual Technical Conference - ANTEC, vol. 2 2007. p. 742-746.

[60] Bledzki AK, Faruk O. Effects of the chemical foaming agents, injection parameters, and melt-flow index on the microstructure and mechanical properties of microcellular injection-molded wood-fiber/polypropylene composites. Journal of Applied Polymer Science. 2005;97(3):1090-1096.

[61] Naguib HE, Park CB, Panzer U, Reichelt N. Strategies for achieving ultra low-density polypropylene foams. Polymer Engineering & Science. 2002;42(7):1481-1492.

[62] Lee JWS, Wang J, Yoon JD, Park CB. Strategies to Achieve a Uniform Cell Structure with a High Void Fraction in Advanced Structural Foam Molding. Industrial & Engineering Chemistry Research. 2008;47(23):9457-9464.

[63] Lee S-T, Ramesh NS. Polymeric foam: mechanisms and materials: CRC Press; 2004.

[64] Lee S-T, Scholz D. Polymeric foams; technology and developments in regulation, process, and products: CRC Press 2009.

[65] Molina MJ, Rowland FS. Stratospheric sink for chlorofluoromethanes: chlorine atomc-atalysed destruction of ozone. Nature. 1974;249(5460):810-812.

[66] The Montreal protocol on substrances that deplete the ozone layer In: Programme UNE, editor.: United Nation; 2000. p. 1-47.

[67] Park CB, Baldwin DF, Suh NP. Effect of the pressure drop rate on cell nucleation in continuous processing of microcellular polymers. Polymer Engineering & Science. 1995;35(5):432-440.

[68] Xu J, Pierick D. Microcellular foam processing in reciprocating-screw injection molding machines. Journal of Injection Molding Technology. 2001;5(3):152.

[69] Zhu W, Zhou N, Wu H. Multiplex shear stress-induced nucleation in dynamic microcellular foaming process. Polymer Engineering & Science. 2006;46(12):1728-1738.

[70] Gibbs JW. The Scientific Papers of J. Willard Gibbs, Vol. 1: Thermodynamics New York 1961.

[71] Leung SN, Wong A, Guo Q, Park CB, Zong JH. Change in the critical nucleation radius and its impact on cell stability during polymeric foaming processes. Chemical Engineering Science. 2009;64(23):4899-4907.

[72] Tucker AS, Ward CA. Critical state of bubbles in liquid-gas solutions. Journal of Applied Physics. 1975;46(11):4801-4808.

[73] Kim SG, Leung SN, Park CB, Sain M. The effect of dispersed elastomer particle size on heterogeneous nucleation of TPO with N2 foaming. Chemical Engineering Science. 2011;66(16):3675-3686.

[74] Pilla S, Kramschuster A, Lee J, Clemons C, Gong S, Turng L-S. Microcellular processing of polylactide–hyperbranched polyester–nanoclay composites. Journal of Materials Science. 2010;45(10):2732-2746.

[75] Taki K, Kitano D, Ohshima M. Effect of Growing Crystalline Phase on Bubble Nucleation in Poly(L-Lactide)/CO2 Batch Foaming. Industrial & Engineering Chemistry Research. 2011;50(6):3247-3252.

[76] Chen L, Wang X, Straff R, Blizard K. Shear stress nucleation in microcellular foaming process. Polymer Engineering & Science. 2002;42(6):1151-1158.

[77] Baldwin DF, Park CB, Suh NP. A microcellular processing study of poly(ethylene terephthalate) in the amorphous and semicrystalline states. Part I: Microcell nucleation. Polymer Engineering & Science. 1996;36(11):1437-1445.

[78] Wong A, Guo Y, Park CB. Fundamental mechanisms of cell nucleation in polypropylene foaming with supercritical carbon dioxide—Effects of extensional stresses and crystals. The Journal of Supercritical Fluids. 2013;79(0):142-151.

[79] Naguib HE, Park CB, Reichelt N. Fundamental foaming mechanisms governing the volume expansion of extruded polypropylene foams. Journal of Applied Polymer Science. 2004;91(4):2661-2668.

[80] Leung SNS. Mechanisms of cell nucleation, growth, and coarsening in plastic foaming: theory, simulation, and experiment University of Toronto, Mechanical and Industrial Engineering, 2009.

[81] Park CB, Cheung LK. A study of cell nucleation in the extrusion of polypropylene foams. Polymer Engineering & Science. 1997;37(1):1-10.

[82] Yao K, Tan H, Lin Y, Zhang G, Gong J, Jiang Z. Effect of polystyrene long branch chains on melt behavior and foaming performance of poly(vinyl chloride)/graphene nanocomposites. RSC Advances. 2014;4(109):64053-64060.

[83] Chaudhary AK, Jayaraman K. Extrusion of linear polypropylene–clay nanocomposite foams. Polymer Engineering & Science. 2011;51(9):1749-1756.

[84] Okamoto M, Nam PH, Maiti P, Kotaka T, Hasegawa N, Okamoto H. Biaxial Flow-Induced Alignment of Silicate Layers in Polypropylene/Clay Nanocomposite Foam. Nano Letters. 2001;1(9):503-505.

[85] Wong A, Wijnands SL, Kuboki T, Park C. Mechanisms of nanoclay-enhanced plastic foaming processes: effects of nanoclay intercalation and exfoliation. Journal of Nanoparticle Research. 2013;15(8):1-15.

[86] Lee E-K, Choi S-Y. Preparation and characterization of natural rubber foams: Effects of foaming temperature and carbon black content. Korean Journal of Chemical Engineering. 2007;24(6):1070-1075.

[87] Ding J, Ma W, Song F, Zhong Q. Effect of nano-Calcium Carbonate on microcellular foaming of polypropylene. Journal of Materials Science. 2013;48(6):2504-2511.

[88] Forest C, Chaumont P, Cassagnau P, Swoboda B, Sonntag P. Polymer nano-foams for insulating applications prepared from CO2 foaming. Progress in Polymer Science. 2015;41:122-145.

[89] Kaewmesri W, Rachtanapun P, Pumchusak J. Effect of solvent plasticization on polypropylene microcellular foaming process and foam characteristics. Journal of Applied Polymer Science. 2008;107(1):63-70.

[90] Sorrentino L, Aurilia M, Iannace S. Polymeric foams from high-performance thermoplastics. Advances in Polymer Technology. 2011;30(3):234-243.

[91] Di Y, Iannace S, Di Maio E, Nicolais L. Reactively Modified Poly(lactic acid): Properties and Foam Processing. Macromolecular Materials and Engineering. 2005;290(11):1083-1090.

[92] Lin H, Freeman BD. Gas Permeation and Diffusion in Cross-Linked Poly(ethylene glycol diacrylate). Macromolecules. 2006;39(10):3568-3580.

[93] Reignier J, Tatibouët J, Gendron R. Batch foaming of poly(ε-caprolactone) using carbon dioxide: Impact of crystallization on cell nucleation as probed by ultrasonic measurements. Polymer. 2006;47(14):5012-5024.

[94] Zhang W, Chen B, Zhao H, Wen J, Peng X. Processing and characterization of supercritical CO2 batch foamed poly(lactic acid)/poly(ethylene glycol) scaffold for tissue engineering application. Journal of Applied Polymer Science. 2013;130(5):3066-3073.

[95] Velasco JI, Antunes M, Realinho V, Ardanuy M. Characterization of rigid polypropylene-based microcellular foams produced by batch foaming processes. Polymer Engineering & Science. 2011;51(11):2120-2128.

[96] Bing L, Wu Q, Nanqiao Z, Baoshan S. Batch Foam Processing of Polypropylene/Polydimethylsiloxane Blends. International Journal of Polymeric Materials and Polymeric Biomaterials. 2010;60(1):51-61.

[97] Spitael P, Macosko CW. Strain hardening in polypropylenes and its role in extrusion foaming. Polymer Engineering & Science. 2004;44(11):2090-2100.

[98] Zhai W, Park CB, Kontopoulou M. Nanosilica Addition Dramatically Improves the Cell Morphology and Expansion Ratio of Polypropylene Heterophasic Copolymer Foams Blown in Continuous Extrusion. Industrial & Engineering Chemistry Research. 2011;50(12):7282-7289.

[99] Li Q, Matuana LM. Foam extrusion of high density polyethylene/wood-flour composites using chemical foaming agents. Journal of Applied Polymer Science. 2003;88(14):3139-3150.

[100] Kuboki T, Lee YH, Park CB, Sain M. Mechanical properties and foaming behavior of cellulose fiber reinforced high-density polyethylene composites. Polymer Engineering & Science. 2009;49(11):2179-2188.

[101] Zhang C, Zhu B, Lee LJ. Extrusion foaming of polystyrene/carbon particles using carbon dioxide and water as co-blowing agents. Polymer. 2011;52(8):1847-1855.

[102] Han X, Zeng C, Lee LJ, Koelling KW, Tomasko DL. Extrusion of polystyrene nanocomposite foams with supercritical CO2. Polymer Engineering & Science. 2003;43(6):1261-1275.

[103] Lee JWS, Wang K, Park CB. Challenge to Extrusion of Low-Density Microcellular Polycarbonate Foams Using Supercritical Carbon Dioxide. Industrial & Engineering Chemistry Research. 2005;44(1):92-99.

[104] Huang Q, Seibig B, Paul D. Melt Extruded Open-Cell Microcellular Foams for Membrane Separation: Processing and Cell Morphology Relationship. Journal of Cellular Plastics. 2000;36(2):112-125.

[105] Matuana LM, Faruk O, Diaz CA. Cell morphology of extrusion foamed poly(lactic acid) using endothermic chemical foaming agent. Bioresource Technology. 2009;100(23):5947-5954.

[106] Zhang J-F, Sun X. Biodegradable foams of poly(lactic acid)/starch. I. Extrusion condition and cellular size distribution. Journal of Applied Polymer Science. 2007;106(2):857-862.

[107] Mihai M, Huneault MA, Favis BD. Rheology and extrusion foaming of chain-branched poly(lactic acid). Polymer Engineering & Science. 2010;50(3):629-642.

[108] Julien JM, Quantin JC, Bénézet JC, Bergeret A, Lacrampe MF, Krawczak P. Chemical foaming extrusion of poly(lactic acid) with chain-extenders: Physical and morphological characterizations. European Polymer Journal. 2015;67:40-49.

[109] Guo M-C, Heuzey M-C, Carreau PJ. Cell structure and dynamic properties of injection molded polypropylene foams. Polymer Engineering & Science. 2007;47(7):1070-1081.

[110] Ameli A, Jahani D, Nofar M, Jung PU, Park CB. Development of high void fraction polylactide composite foams using injection molding: Mechanical and thermal insulation properties. Composites Science and Technology. 2014;90:88-95.

[111] Tovar-Cisneros C, González-Núñez R, Rodrigue D. The Effect of Mold Temperature on Morphology and Mechanical Properties of Injection Molded HDPE Structural Foams. Annual Technical Conference, ANTEC, 2007. p. 2108-2112.

[112] Tovar-Cisneros C, González-Núñez R, Rodrigue D. Effect of Mold Temperature on Morphology and Mechanical Properties of Injection Molded HDPE Structural Foams. Journal of Cellular Plastics. 2008;44(3):223-237.

[113] Chen S-C, Liao W-H, Chien R-D. Structure and mechanical properties of polystyrene foams made through microcellular injection molding via control mechanisms of gas counter pressure and mold temperature. International Communications in Heat and Mass Transfer. 2012;39(8):1125-1131.

[114] Peinado V, García L, Fernández Á, Castell P. Novel lightweight foamed poly(lactic acid) reinforced with different loadings of functionalised Sepiolite. Composites Science and Technology. 2014;101:17-23.

[115] Li G, Li H, Turng LS, Gong S, Zhang C. Measurement of gas solubility and diffusivity in polylactide. Fluid Phase Equilibria. 2006;246(1–2):158-166.

[116] Sato Y, Fujiwara K, Takikawa T, Sumarno, Takishima S, Masuoka H. Solubilities and diffusion coefficients of carbon dioxide and nitrogen in polypropylene, high-density polyethylene, and polystyrene under high pressures and temperatures. Fluid Phase Equilibria. 1999;162(1–2):261-276.

[117] Stange J, Münstedt H. Rheological properties and foaming behavior of polypropylenes with different molecular structures. Journal of Rheology. 2006;50(6):907-923.

[118] Nam GJ, Yoo JH, Lee JW. Effect of long-chain branches of polypropylene on rheological properties and foam-extrusion performances. Journal of Applied Polymer Science. 2005;96(5):1793-1800.

[119] Yamaguchi M, Suzuki K-I. Rheological properties and foam processability for blends of linear and crosslinked polyethylenes. Journal of Polymer Science Part B: Polymer Physics. 2001;39(18):2159-2167.

[120] Li S, Xiao M, Zheng S, Xiao H, Guan Y, Zheng A. The characterization of rheological properties of melt grafting polypropylene for foaming. Polymer Bulletin. 2009;63(1):111-123.

[121] Laguna-Gutierrez E, Van Hooghten R, Moldenaers P, Rodriguez-Perez MA. Understanding the foamability and mechanical properties of foamed polypropylene blends by using extensional rheology. Journal of Applied Polymer Science. 2015;132(33).

[122] Bhattacharya S, Gupta RK, Jollands M, Bhattacharya SN. Foaming behavior of high-melt strength polypropylene/clay nanocomposites. Polymer Engineering & Science. 2009;49(10):2070-2084.

[123] Liao X, Nawaby AV, Whitfield PS. Carbon dioxide-induced crystallization in poly(L-lactic acid) and its effect on foam morphologies. Polymer International. 2010;59(12):1709-1718.

[124] Marrazzo C, Di Maio E, Iannace S. Conventional and nanometric nucleating agents in poly(ϵ-caprolactone) foaming: Crystals vs. bubbles nucleation. Polymer Engineering & Science. 2008;48(2):336-344.

[125] Wang C, Leung SN, Bussmann M, Zhai WT, Park CB. Numerical Investigation of Nucleating-Agent-Enhanced Heterogeneous Nucleation. Industrial & Engineering Chemistry Research. 2010;49(24):12783-12792.

[126] Liao R, Yu W, Zhou C. Rheological control in foaming polymeric materials: II. Semi-crystalline polymers. Polymer. 2010;51(26):6334-6345.

[127] Keshtkar M, Nofar MR, Majithiya K, Park CB, Carreau PJ. Foaming behavior of PLA/nanocolay nanocomposites in continious extrusion. BioFoams, Italy 2011.

[128] Jabbarzadeh A, Tanner RI. Flow-Induced Crystallization: Unravelling the Effects of Shear Rate and Strain. Macromolecules. 2010;43(19):8136-8142.

[129] Li H, Huneault MA. Effect of nucleation and plasticization on the crystallization of poly(lactic acid). Polymer. 2007;48(23):6855-6866.

[130] Yu F, Zhang H, Liao R, Zheng H, Yu W, Zhou C. Flow induced crystallization of long chain branched polypropylenes under weak shear flow. European Polymer Journal. 2009;45(7):2110-2118.

[131] Sherwood CH, Price FP, Stein RS. Effect of shear on the crystallization kinetics of poly(ethylene oxide) and poly(e-caprolactone) melts. Journal of Polymer Science: Polymer Symposia. 1978;63(1):77-94.

[132] Fang H, Zhang Y, Bai J, Wang Z. Shear-Induced Nucleation and Morphological Evolution for Bimodal Long Chain Branched Polylactide. Macromolecules. 2013;46(16):6555-6565.

[133] Yuryev Y, Wood-Adams P. Rheological properties of crystallizing polylactide: Detection of induction time and modeling the evolving structure and properties. Journal of Polymer Science Part B: Polymer Physics. 2010;48(7):812-822.

[134] Xu J. Effect of injection molding process parameters on the morphology and quality of microcellular foam. Annual Technical Conference, ANTEC, North Carolina, USA 2006. p. 2770-2774.

[135] Xu J. Microcellular injection molding: John Wiley & Sons; 2010.

[136] Chandra A, Gong S, Turng L-S, Gramann P. Cell Development in Microcellular Injection Molded Polyamide-6 Nanocomposite and Neat Resin. Journal of Cellular Plastics. 2004;40(5):371-382.

[137] Wong S, Lee JWS, Naguib HE, Park CB. Effect of Processing Parameters on the Mechanical Properties of Injection Molded Thermoplastic Polyolefin (TPO) Cellular Foams. Macromolecular Materials and Engineering. 2008;293(7):605-613.

[138] Fujimoto Y, Ray SS, Okamoto M, Ogami A, Yamada K, Ueda K. Well-Controlled Biodegradable Nanocomposite Foams: From Microcellular to Nanocellular. Macromolecular Rapid Communications. 2003;24(7):457-461.

[139] Lee ST, Kareko L, Jun J. Study of Thermoplastic PLA Foam Extrusion. Journal of Cellular Plastics. 2008;44(4):293-305.

[140] Reignier J, Gendron R, Champagne MF. Extrusion foaming of poly(lactic acid) blown with CO_2 : Toward 100% green material. Cellular polymers. 2007;26(2):83-115.

[141] Wang J, Zhu W, Park CB, Randall J. Impact of molecular branching on microcellular foaming of polylactic acid in extrusion. Annual Technical Conference-ANTEC, Illinois, USA 2009. p. 36-40.

[142] Nofar M, Barzegari MR, Tabatabaei A, Keshtkar M, Park CB. Effect of various additives (talc, nanoclay, and nanosilica) on extrusion foaming of pla through crystallization. Annual Technical Conference -ANTEC, Florida, USA 2012. p. 2384-2388.

[143] Wang J, Zhu W, Zhang H, Park CB. Continuous processing of low-density, microcellular poly(lactic acid) foams with controlled cell morphology and crystallinity. Chemical Engineering Science. 2012;75:390-399.

[144] Yuan H, Liu Z, Ren J. Preparation, characterization, and foaming behavior of poly(lactic acid)/poly(butylene adipate-co-butylene terephthalate) blend. Polymer Engineering & Science. 2009;49(5):1004-1012.

[145] Grimes E, Keeley S. Foaming of PLA - the use of melt strength enhancers to achieve lower density foams produced by chemical blowing agents. Society of Plastics Engineers; 2010. p. 1-6.

[146] Liu B, Jiang L, Zhang J. Extrusion Foaming of Poly (lactic acid)/Soy Protein Concentrate Blends. Macromolecular Materials and Engineering. 2011;296(9):835-842.

[147] Pilla S, Kramschuster A, Gong S, Chandra A, Turng LS. Solid and microcellular polylactide-carbon nanotube nanocomposites. International Polymer Processing. 2007;22(5):418-428.

[148] Pilla S, Kramschuster A, Lee J, Auer GK, Gong S, Turng L-S. Microcellular and Solid Polylactide–Flax Fiber Composites. Composite Interfaces. 2009;16(7-9):869-890.

[149] Kramschuster A, Pilla S, Gong S, Chandra A, Turng LS. Injection Molded Solid and Microcellular Polylactide Compounded with Recycled Paper Shopping Bag Fibers. International Polymer Processing. 2007;22(5):436-445.

[150] Li K, Cui Z, Sun X, Turng L-S, Huang H. Effects of Nanoclay on the Morphology and Physical Properties of Solid and Microcellular Injection Molded Polyactide/Poly(butylenes

adipate-co-terephthalate) (PLA/PBAT) Nanocomposites and Blends. Journal of Biobased Materials and Bioenergy. 2011;5(4):442-451.

[151] Seo J-H, Han J, Lee KS, Cha SW. Combined Effects of Chemical and Microcellular Foaming on Foaming Characteristics of PLA (Poly Lactic Acid) in Injection Molding Process. Polymer-Plastics Technology and Engineering. 2012;51(5):455-460.

[152] Guo Q. Visualization of polymer foaming using a batchfoaming simulation system with a high pressure-drop rate. University of Toronto, Mechanical and Industrial Engineering, 2007.

[153] Kharbas H, Nelson P, Yuan M, Gong S, Turng L-S, Spindler R. Effects of nano-fillers and process conditions on the microstructure and mechanical properties of microcellular injection molded polyamide nanocomposites. Polymer Composites. 2003;24(6):655-671.

[154] Spörrer ANJ, Altstädt V. Controlling Morphology of Injection Molded Structural Foams by Mold Design and Processing Parameters. Journal of Cellular Plastics. 2007;43(4-5):313-330.

[155] Bikiaris DN, Karayannidis GP. Chain extension of polyesters PET and PBT with two new diimidodiepoxides. II. Journal of Polymer Science Part A: Polymer Chemistry. 1996;34(7):1337-1342.

[156] Arias A. Development of Natural Fiber Reinforced Polylactide-Based Biocomposites. Ecole Polytechnique of Montreal, Chemical Engineering Department, 2014.

[157] Carreau PJ, Kee DD, Chhabra RP. Rheology of polymeric systems principles and applications. Hanser Publishers; 1997.

APPENDICES

APPENDIX A

TITRATION OF THE LINEAR AND LCB-POLYLACTIDES

To determine the difference between the molecular structure of the linear PLA and PLA containing chain extender, the amount of chain end content was measured using titration. Considering that the epoxy based CE used in this study prefer to react with the COOH groups [1], the amount of carboxyl groups is quantified.

To quantify the amount of carboxyl groups 0.2 g of the samples were dissolved in 40 mL THF at 55 ^{o}C for 60 min. The solutions were then titrated by 0.1 mol/L NaOH ethanol solution using phenolphthalein as indicator. The amount of carboxyl groups will be calculated using Eq. AA.1.

$$\mathrm{COOH\,[mol/g]} = \frac{(V_1 - V_0)10^{-3}C}{m} \qquad \text{Eq. AA.1}$$

where V_0 is the amount of NaOH consumed by using THF as reference [mL], V_1 is the amount of NaOH consumed by sample [mL], C is the mole concentration of titration solution [mol/L] and m is the weight of the sample.

Figures AA.1 presents the amount of carboxyl groups of the samples prepared using different strategies. The amount of consumed COOH groups as a result of reaction with the epoxy groups of the chain extender is calculated from Eq. AA.2 and shown in Figure AA.2.

$$\frac{\left([COOH]_{processed\ \ PLA} - [COOH]_{CE-modified\ PLA}\right)}{[COOH]_{processed\ \ PLA}} \times 100 \qquad \text{Eq. AA.2}$$

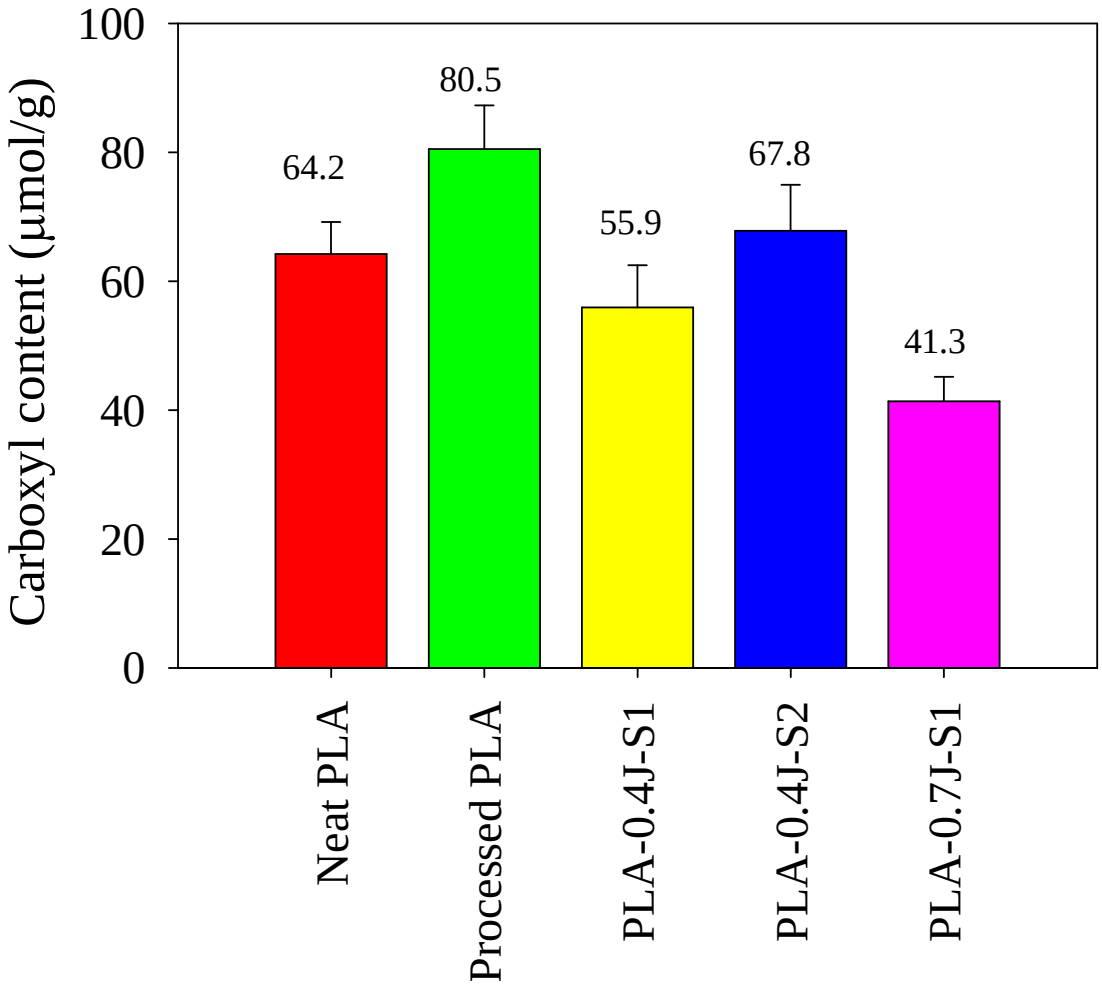

Figure AA.1: The amount of carboxyl group content of the linear and LCB-PLAs obtained using the titration method.

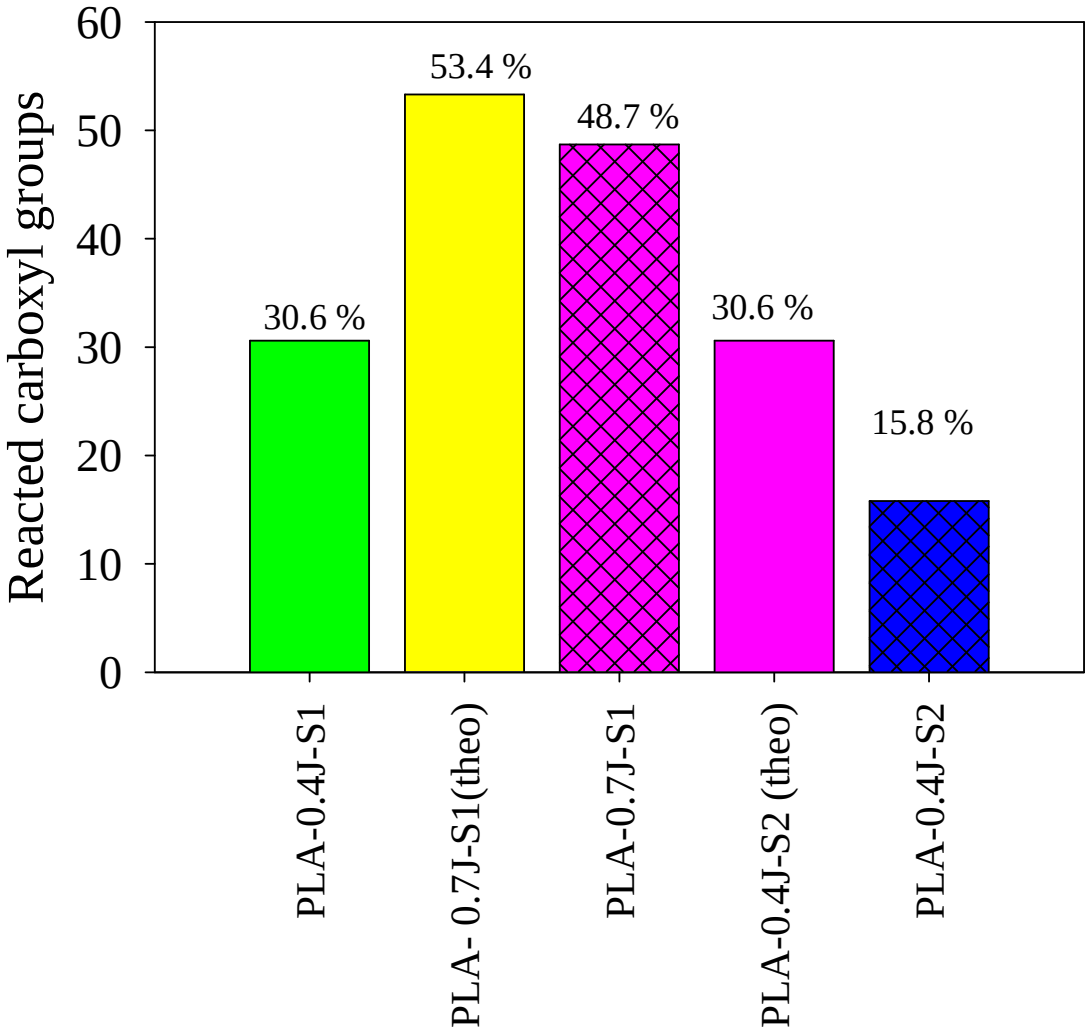

Figure AA.2: Amount of carboxyl group content reacted with the chain extender in the linear and LCB-PLAs obtained using two different strategies.

APPENDIX B

TRANSIENT BIAXIAL ELONGATIONAL VISCOSITY OF LINEAR AND LCB-POLYLACTIDES

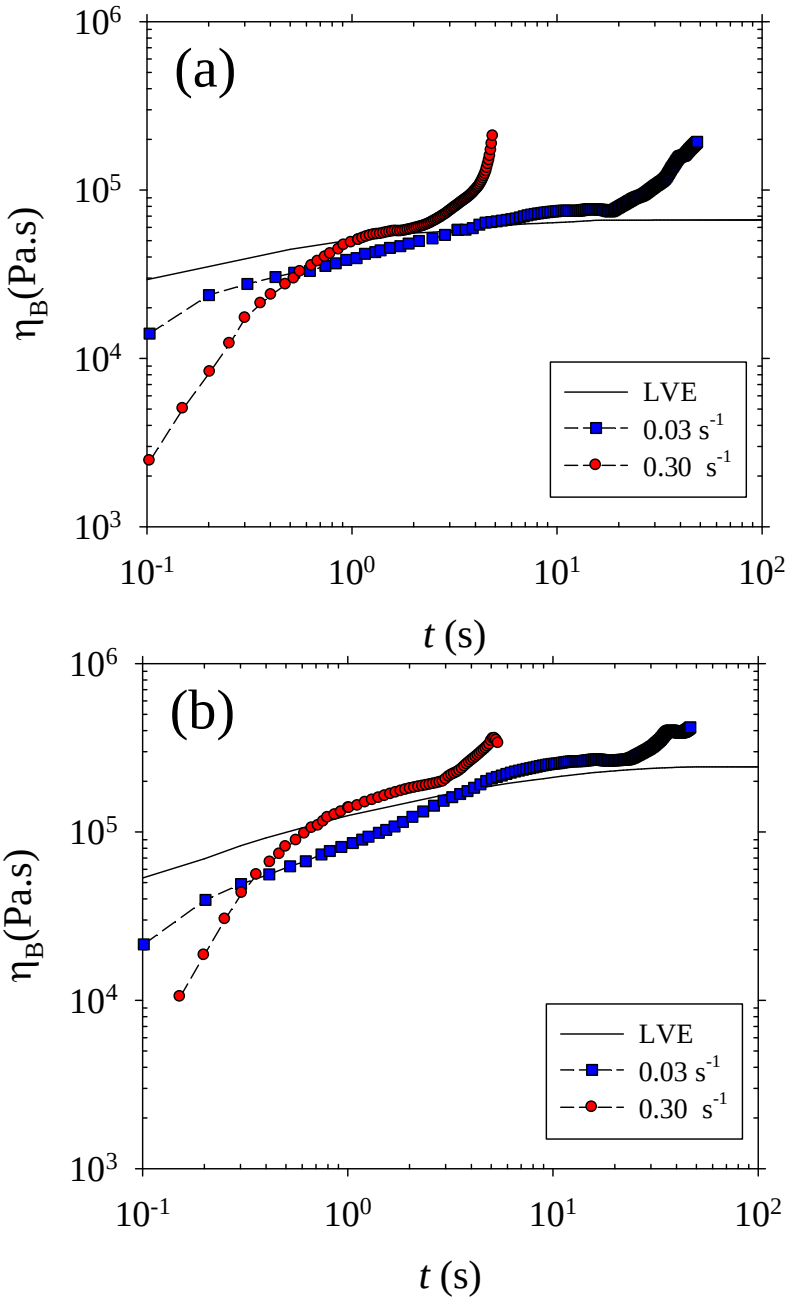

Figure AB.1: Transient biaxial elongational viscosity as a function of time for different Hencky strain rates for (a) PLA-0.4 wt% CE prepared using strategy S1 and (b)) PLA-0.7 wt% CE prepared using strategy S1 at 180 °C (the experiments were conducted in the laboratory of Prof. David Venerus at the Illinois Institute of Technology (IIT) in Chicago).

APPENDIX C

CRYSTALLIZATION BEHAVIOR OF LINEAR AND LCB-POLYLACTIDES

The isothermal melt-crystallization behavior of PLA containing different contents of CE and prepared using different compounding strategies was studied at 110 °C. All the specimens were first heated at 60 °C/min to 205 °C and held there for 5 min. The molten samples were then cooled down to crystallization temperature (T_c) at 60 °C/min. The samples were kept at T_c until the crystallization was complete.

To examine the impact of the molecular architecture on kinetics of melt crystallization, the isothermal crystallization behavior of linear and LCB-PLAs is also studied using DSC at 110 °C. The isothermal crystallization thermograms and development of relative crystallinity are respectively reported in Figures AC.1a and b as a function of time. The degree of crystallinity was calculated using Eq. AC.1 and reported in Table AC.1.

$$X_c = (\Delta H_c / \Delta H_m) \times 100 \qquad \text{Eq. AC.1}$$

where ΔH_c is the crystallization enthalpy of the component, and ΔH_m is the melting enthalpy of perfectly crystalline PLA which is 93.6 J/g.

The DSC curve of the linear PLA exhibits a broad exothermic peak with a crystallization half-time ($t_{1/2}$) of 18.9 min, suggesting that the isothermal crystallization of PLA is very slow. Considering that crystallization highly depends on the chain architecture, the introduction of a LCB structure into PLA is expected to significantly affect the crystallization kinetics. As shown in Figures AC.1 and reported in Table AC.1, the onset of crystallization and $t_{1/2}$ are reduced after adding 0.4 wt% CE (t_{on} and $t_{1/2}$ decreases from 6 to 3.7 min and 18.9 to 11 min, respectively) using the S1 strategy.

This finding indicates that the newly formed branched structure acts as nucleation sites for the linear chains having a higher local order, and hence, accelerates the crystallization kinetics. The onset of crystallization and crystallization half-time is further reduced to 1 and 5.7 min, respectively, as LCB-PLA containing 0.4 wt% CE produced using the strategy S2. The existence of highly LCB-macromolecules and more linear segments, in comparison with the S1 sample, are

responsible for the observed increase in crystallization kinetics. The addition of 0.7 wt% of CE and further increasing degree of LCB decelerates the crystallization rate of PLA ($t_{1/2}$ increases from 5.7 to 9.8 min).

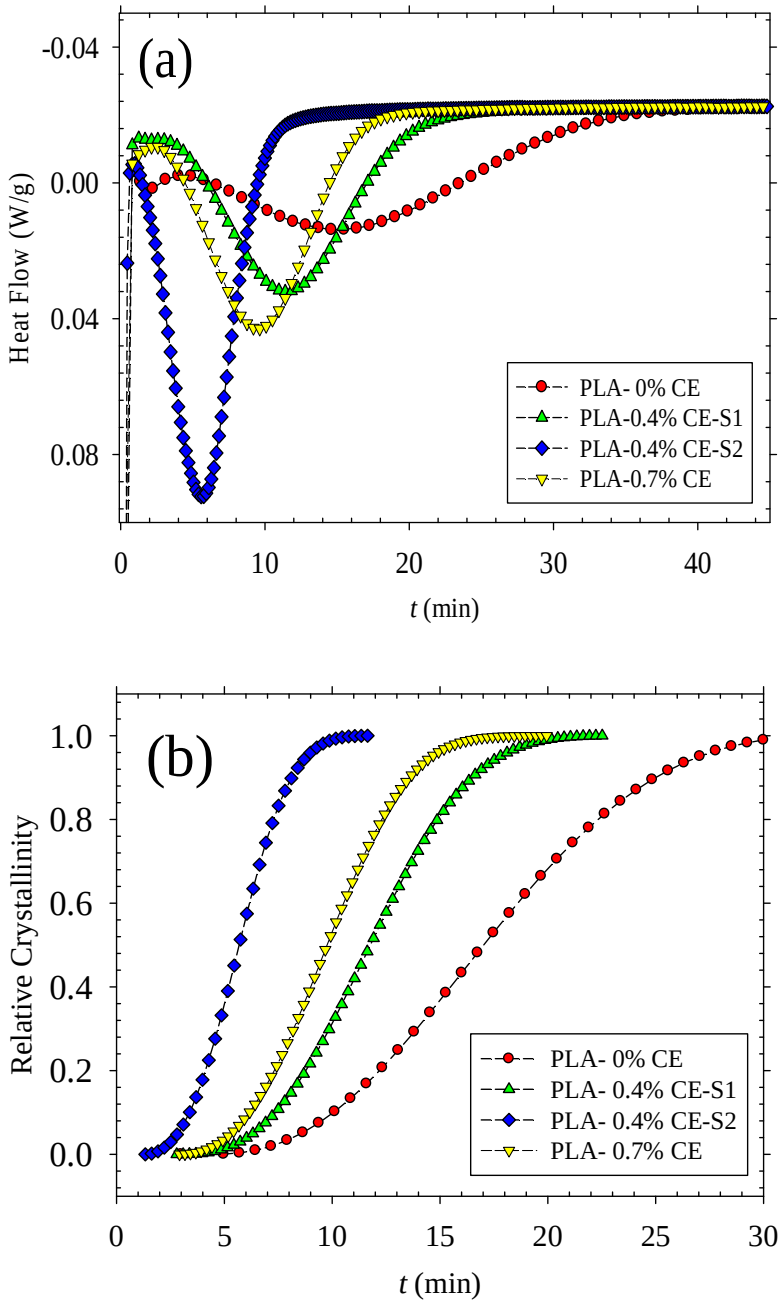

Figure AC.1: DSC results (a) isothermal melt crystallization thermograms and (b) relative crystallinity development of linear and LCB-PLAs as a function of time at 110 °C.

Although the LCB structure performs the heterogeneous nucleation to facilitate the crystallization, it, on the other hand, restrains the chain mobility and reptation ability of polymer backbones, leading eventually to a reduction of the crystallization rate. Such a detrimental impact of long chain branching on the crystallization rate implies that the degree of LCB should be optimized to maximize the crystallization rate.

Table AC.1: Isothermal degree of crystallization, onset time and crystallization half-time of linear and LCB-PLAs at 110 °C.

Composition	t_{on} (min)	$t_{1/2}$ (min)	*Xc (%)*
PLA-0 wt% CE	6.0	18.9	13
PLA-0.4 wt% CE-S1	3.7	11.0	27
PLA-0.4 wt% CE-S2	1	5.7	32
PLA-0.7 wt% CE	2.7	9.8	25

APPENDIX D

APPROPRIATE VISCOELASTICITY FOR FOAMING

MELT VISCOSITY-MELT ELASTICITY

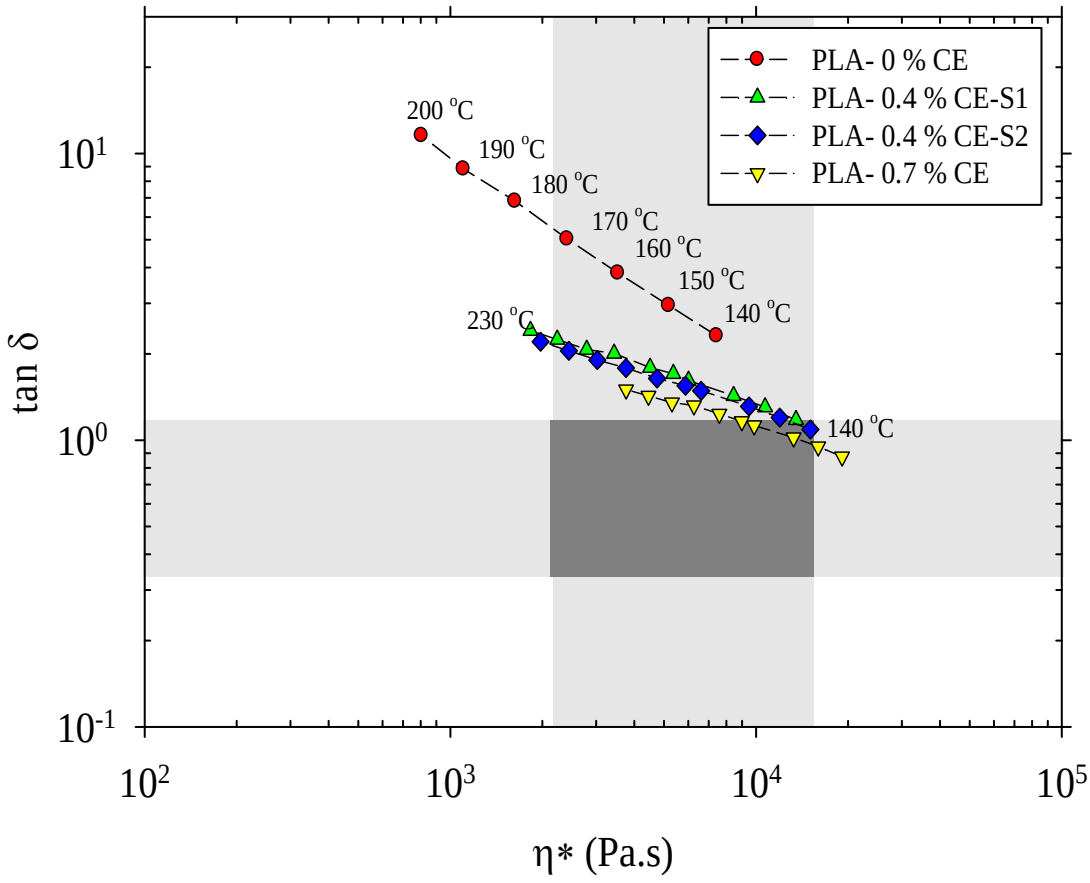

Figure AD.1: Use of two rheological parameters, *tan* δ and complex viscosity, to define the optimal processing window.

APPENDIX E

THE IMPACT OF PROCESSING CONDITIONS AND MOLECULAR STRUCTURE ON THE INJECTION FOAMING BEHAVIOR OF LINEAR AND BRANCHED POLYLACTIDES

In this investigation, the effect of several factors including CBA content, the degree of long chain branching (LCB), and injection molding processing parameters such as shot size, injection speed, back pressure, cooling time and nozzle temperature on the morphology of PLA foam are examined. The LCB-PLAs are prepared using different strategies which are shown in Table AE.1.

Table AE.1: Characteristics of the compounding strategies considered in this study.

Sample Name	Composition	Procedure
Neat PLA	PLA	PLA was extruded and then foamed in a convectional injection molding
LCB-PLA-1	PLA-0.4 wt% chain extender	PLA and 0.4 wt% were extruded simultaneously in a twin-screw extruder and then foamed in a convectional injection molding
LCB-PLA-2	PLA-0.4 wt% chain extender	PLA and 0.8 wt% were blended in the first extrusion pass. It mixed with the linear PLA at a weight ratio of 50:50 in the second pass. Then, it was foamed in a convectional injection molding
LCB-PLA-3	PLA-0.7 wt% chain extender	PLA and 0.7 wt% were dry-mixed and then foamed in a convectional injection molding
LCB-PLA-4	PLA-0.7 wt% chain extender	PLA and 0.7 wt% were extruded simultaneously in a twin-screw extruder and then foamed in a convectional injection molding

Figure AE.1 shows the effect of injection speed on the cellular structure of the linear and LCB-PLAs with different molecular structure. The injection speed was changed from 100 to 200 mm/s. The temperature profile was set at 160, 200, 190, 160 ^{o}C from hopper to nozzle. Other processing parameters used in this study are as follows: CBA concentration, 1.5 wt%; screw rotation speed, 100 rpm; shot size, 17 mm; back pressure, 2 MPa; mold temperature, 40 °C; and cooling time, 25 s. The morphology at the center of the samples are observed using scanning electron microscopy (SEM).

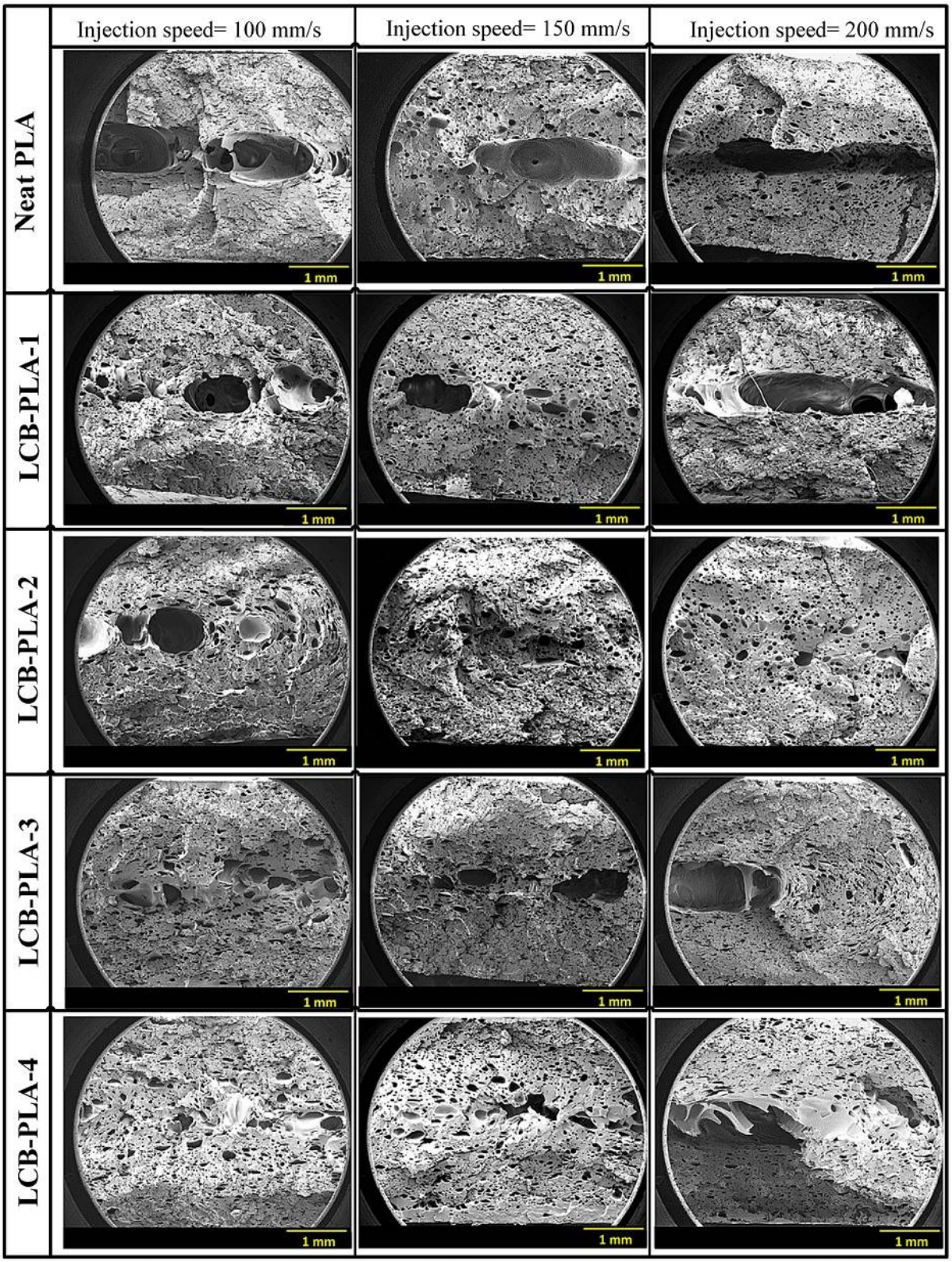

Figure AE.1: The effect of injection speed on the cellular structure of the linear and LCB-PLAs.

Figure AE.2 reveals the cellular structure uniformity of the linear and LCB-PLAs with different molecular structure along the length of the mold cavity. The structure at three points of the samples (near the gate, at the center, far from the gate) are observed using scanning electron microscopy (SEM). The temperature profile was set at 160, 200, 190, 160 ºC from hopper to nozzle. Other processing parameters used in this study are as follows: CBA concentration, 1.5 wt%; screw rotation speed, 100 rpm; injection speed, 150 mm/s; shot size, 17 mm; back pressure, 2 MPa; mold temperature, 40 °C; and cooling time, 25 s.

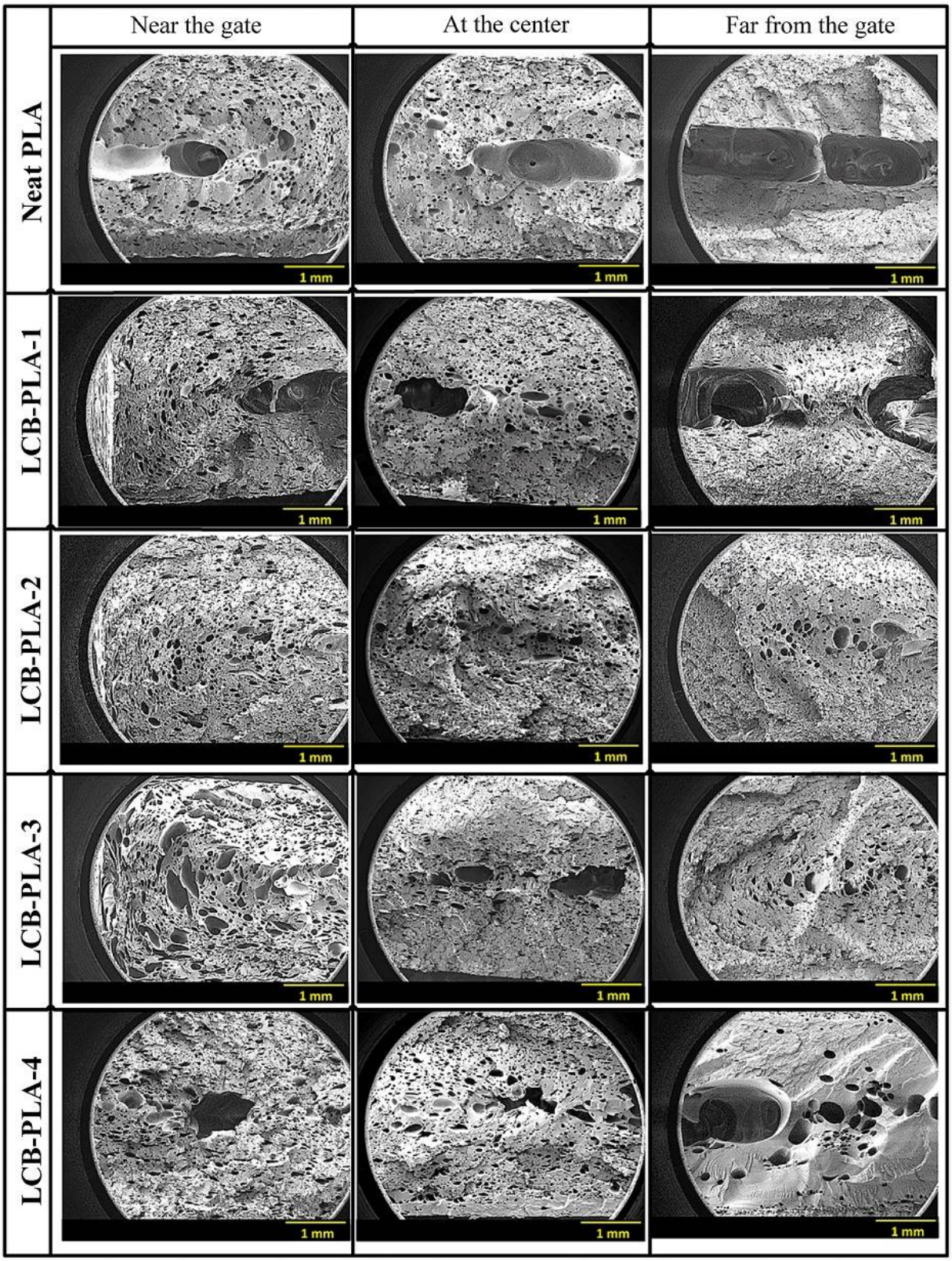

Figure AE.2: Distribution of cell size along the length of the mold cavity in the foamed linear and LCB-PLAs.

Figure AE.3 indicates the effect of CBA concentration on the morphology of the linear PLA and PLA containing 0.4 wt% CE prepared using strategy S2. The CBA content was varied from 0.4 to 1.5 wt%. The temperature profile was set at 160, 200, 190, 160 ^{o}C from hopper to nozzle. Other processing parameters used in this study are as follows: screw rotation speed, 100 rpm; injection speed, 150 mm/s; shot size, 17 mm; back pressure, 2 MPa; mold temperature, 40 °C; and cooling time, 25 s. The morphology at the center of the samples are observed using scanning electron microscopy (SEM).

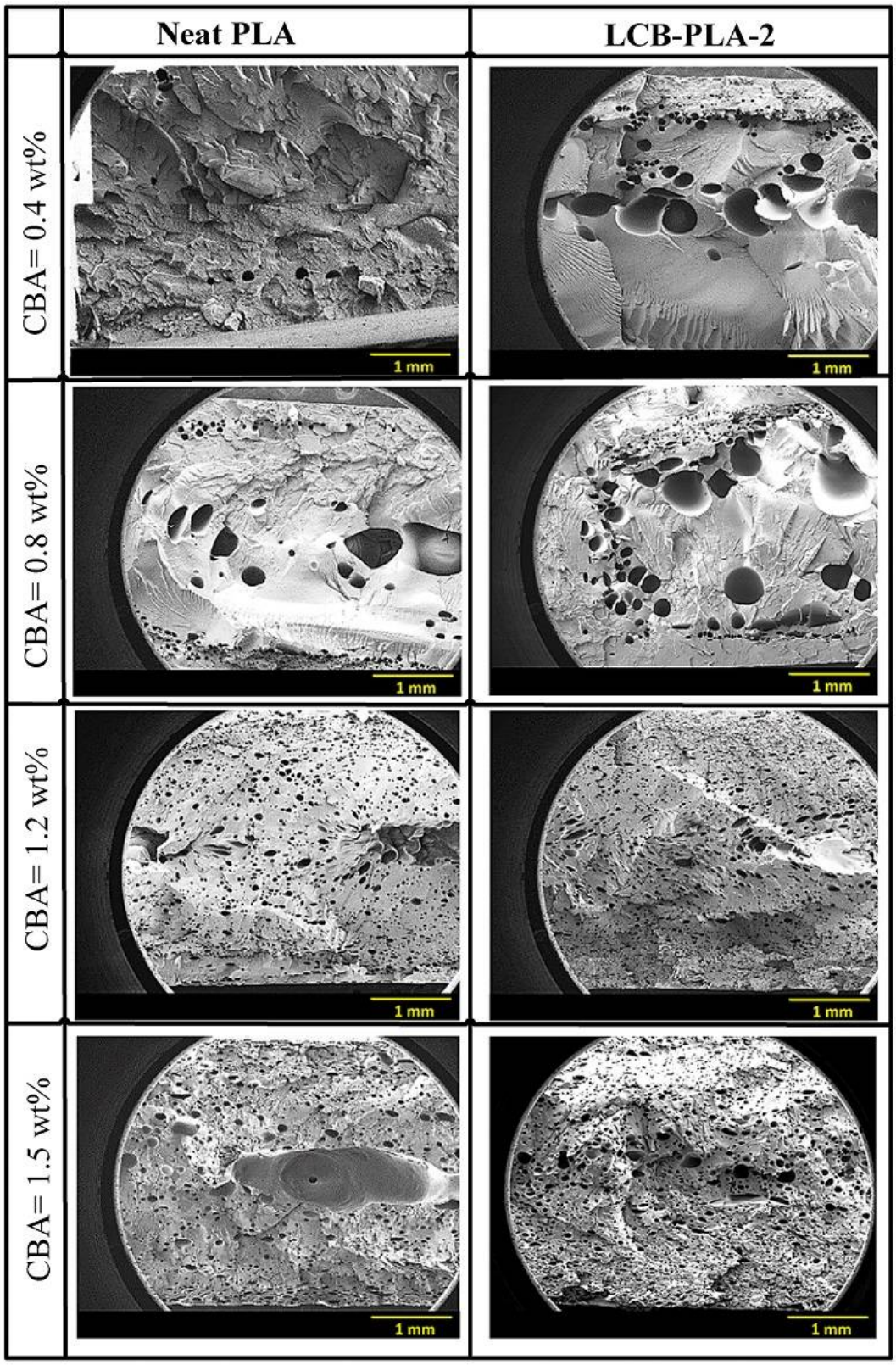

Figure AE.3: The effect of CBA concentration on the morphology of the foamed linear and LCB-PLAs.

Figure AE.4 demonstrates the effect of nozzle temperature on the cellular structure of the linear PLA and LCB-PLA containing 0.4 wt% CE prepared using strategy S2. The nozzle temperature (NT) was changed from 160 to 180 ^{o}C. The temperature profile was set at 160, 200, 190^{o}C, NT, from hopper to nozzle. Other processing parameters used in this study are as follows: CBA concentration, 1.5 wt%; screw rotation speed, 100 rpm; injection speed, 150 mm/s; shot size, 17 mm; back pressure, 2 MPa; mold temperature, 40 °C; and cooling time, 25 s. The morphology at the center of the samples are observed using scanning electron microscopy (SEM).

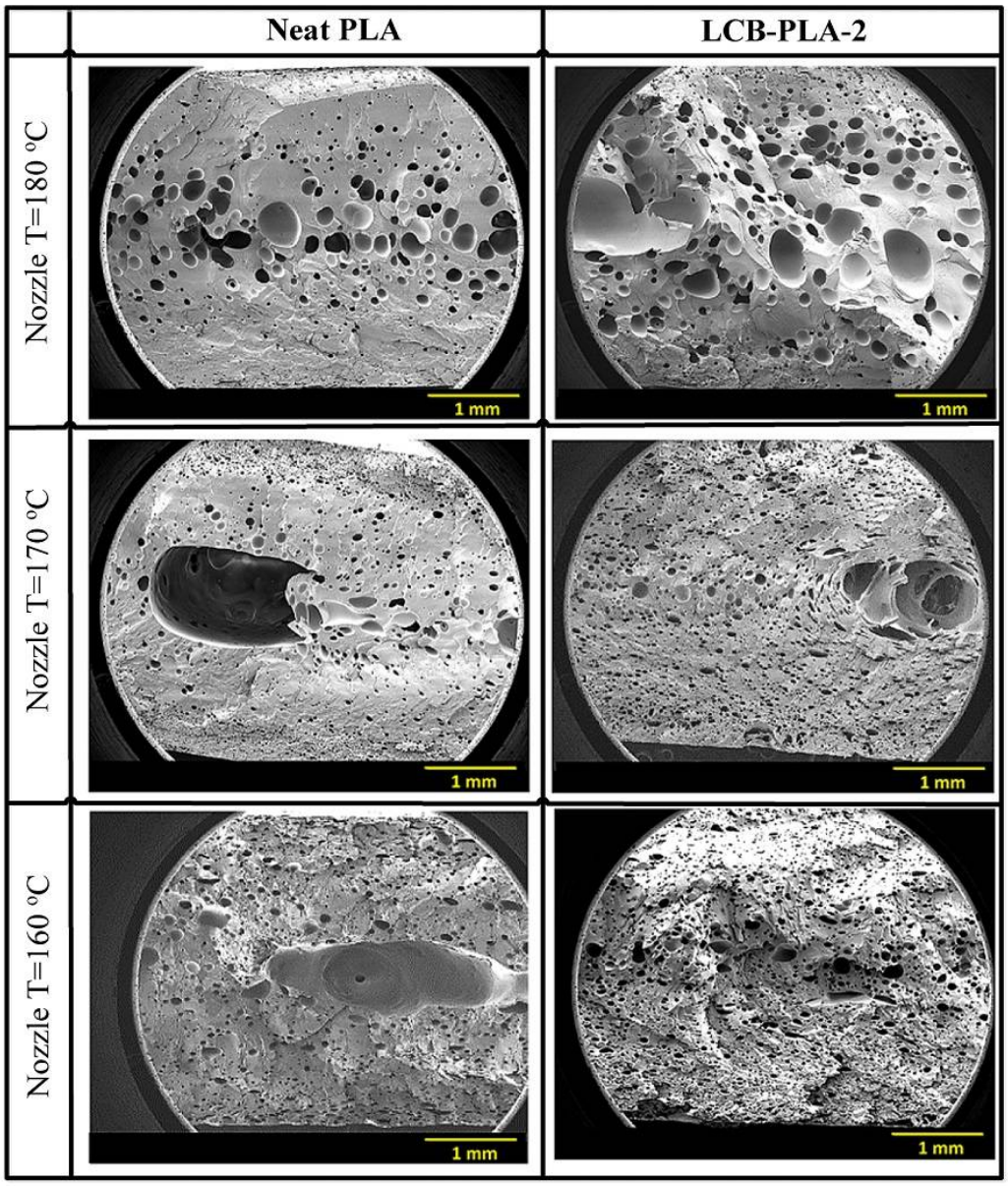

Figure AE.4: The effect of nozzle temperature on the cellular structure of the linear and LCB-PLAs.

Figure AE.5 reveals the effect of back pressure on the morphology of the linear PLA and LCB-PLA prepared using strategy S2. Two different back pressures, 2 and 10 MPa, were examined. The morphology at the center of the samples are observed using scanning electron microscopy (SEM). The temperature profile was set at 160, 200, 190, 160 ^{o}C from hopper to nozzle. Other processing parameters used in this study are as follows: CBA concentration, 1.5 wt%; screw rotation speed, 100 rpm; injection speed, 150 mm/s; shot size, 17 mm; mold temperature, 40 °C; and cooling time, 25 s.

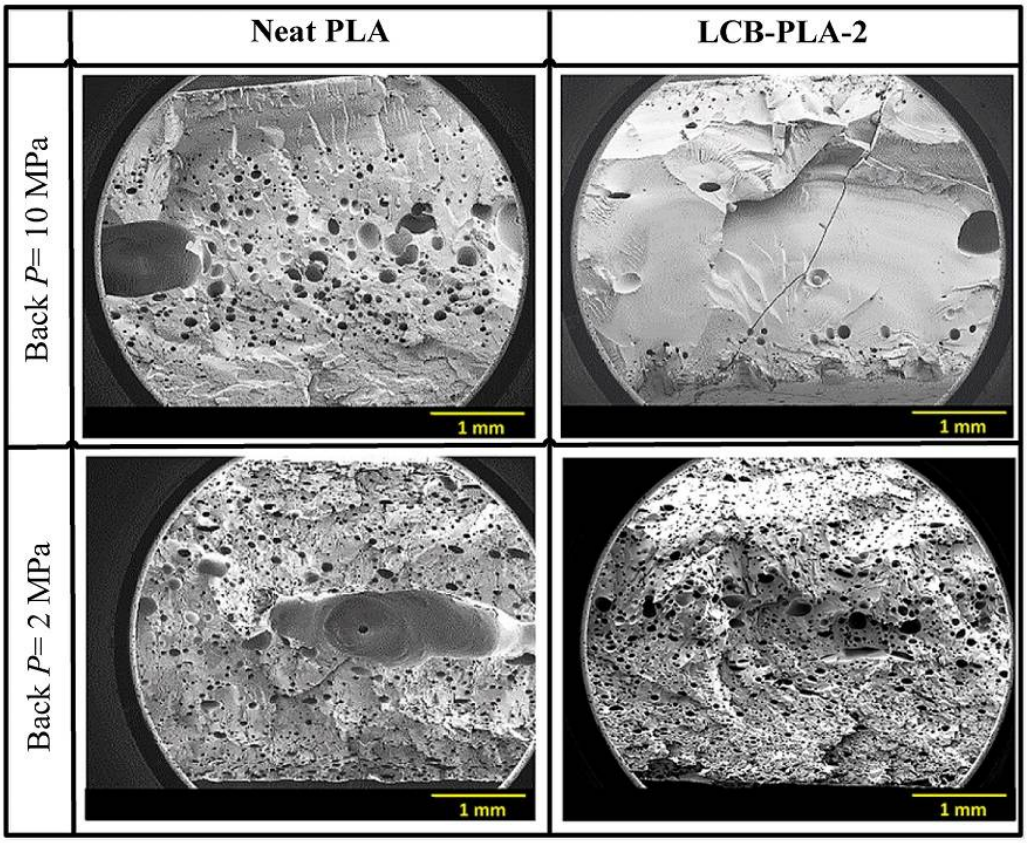

Figure AE.5: The effect of back pressure on the morphology of the linear and LCB-PLAs.

Figure AE.6 shows the effect of cooling time on the morphology of the linear PLA and LCB-PLA prepared using strategy S2. Three different cooling times, 10, 18 and 25 s, were examined. The temperature profile was set at 160, 200, 190, 160 ^{o}C from hopper to nozzle. Other processing parameters used in this study are as follows: CBA concentration, 1.5 wt%; screw rotation speed, 100 rpm; injection speed, 150 mm/s; shot size, 17 mm; mold temperature, 40 °C; and back pressure, 2 MPa. The morphology at the center of the samples are observed using scanning electron microscopy (SEM).

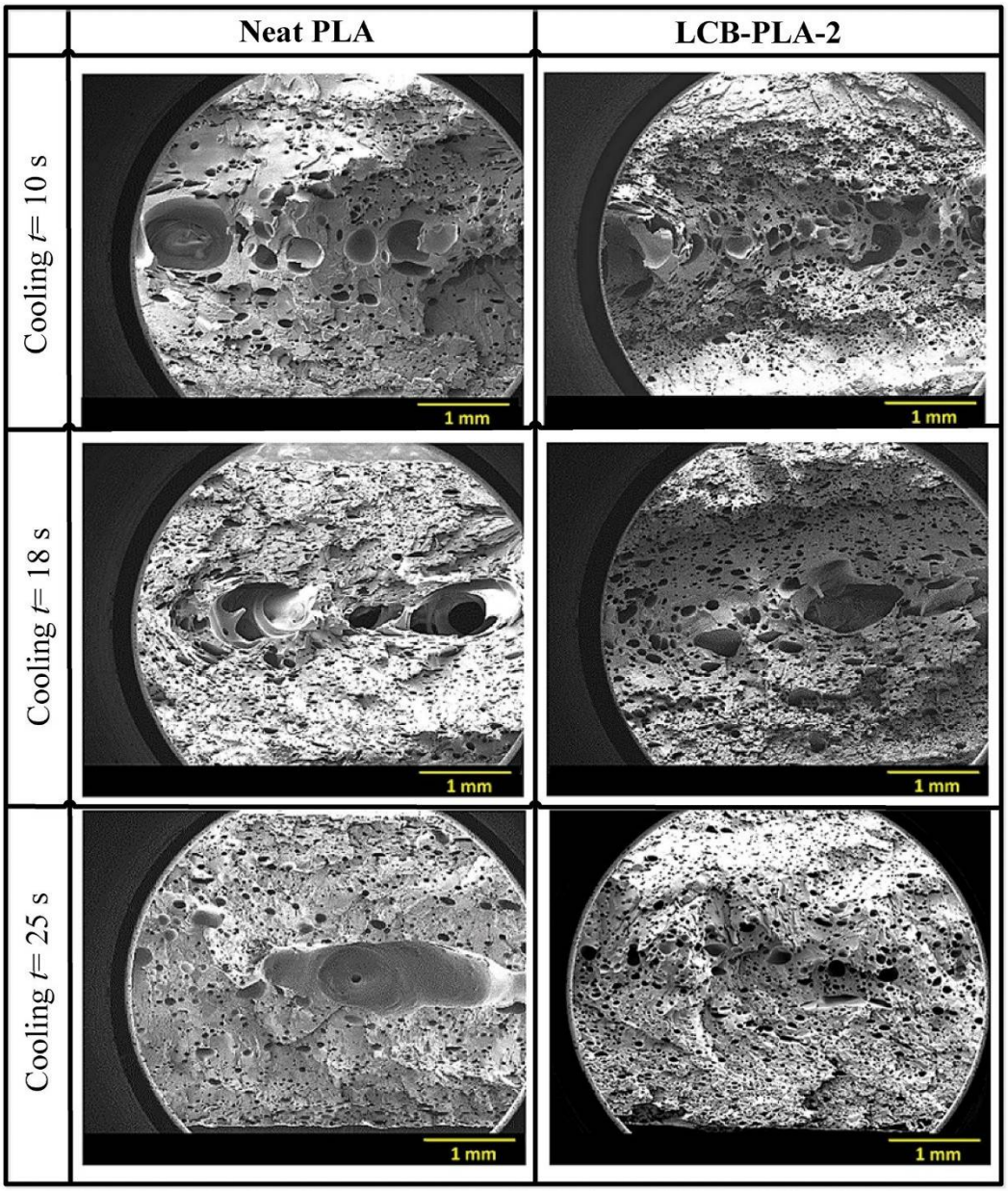

Figure AE.6: The effect of cooling time on the morphology of the linear and LCB-PLAs.

Figure AE.7 reveals the effect of shot size on the morphology of the linear PLA and LCB-PLA prepared using strategy S2. Four different shot sizes, 17, 18, 19 and 20 mm, were examined. The temperature profile was set at 160, 200, 190, 160 ºC from hopper to nozzle. Other processing parameters used in this study are as follows: CBA concentration, 1.5 wt%; screw rotation speed, 100 rpm; injection speed, 150 mm/s; shot size, 17 mm; mold temperature, 40 °C; back pressure, 2 MPa; cooling time, 25 s. The morphology at the center of the samples are observed using scanning electron microscopy (SEM).

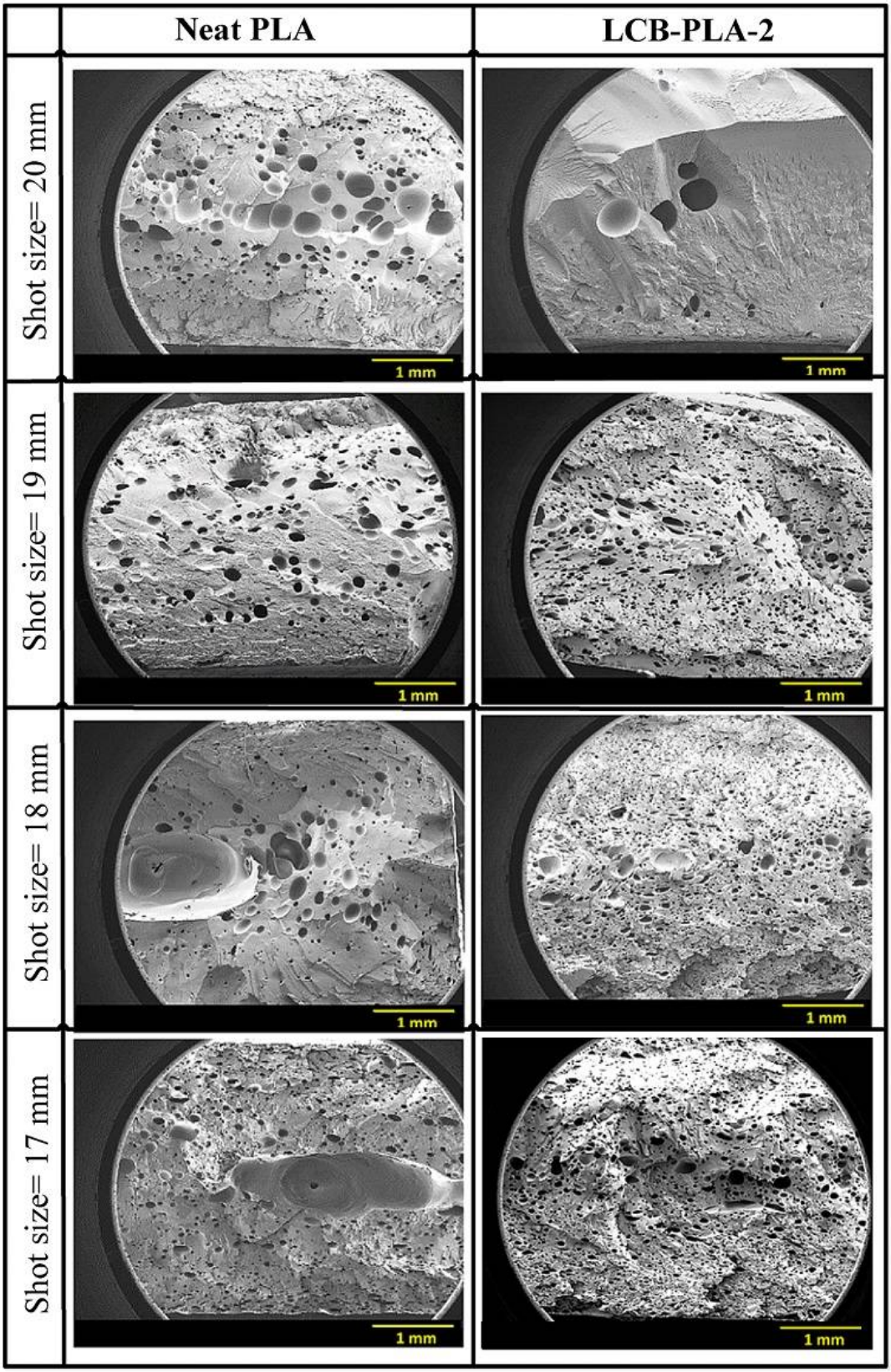

Figure AE.7: The effect of shot size on the morphology of the linear and LCB-PLAs.

APPENDIX F

TENSILE STRESS-STRAIN CURVES OF UNFOAMED AND FOAMED LINEAR AND BRANCHED PLA NANOCOMPOSITES

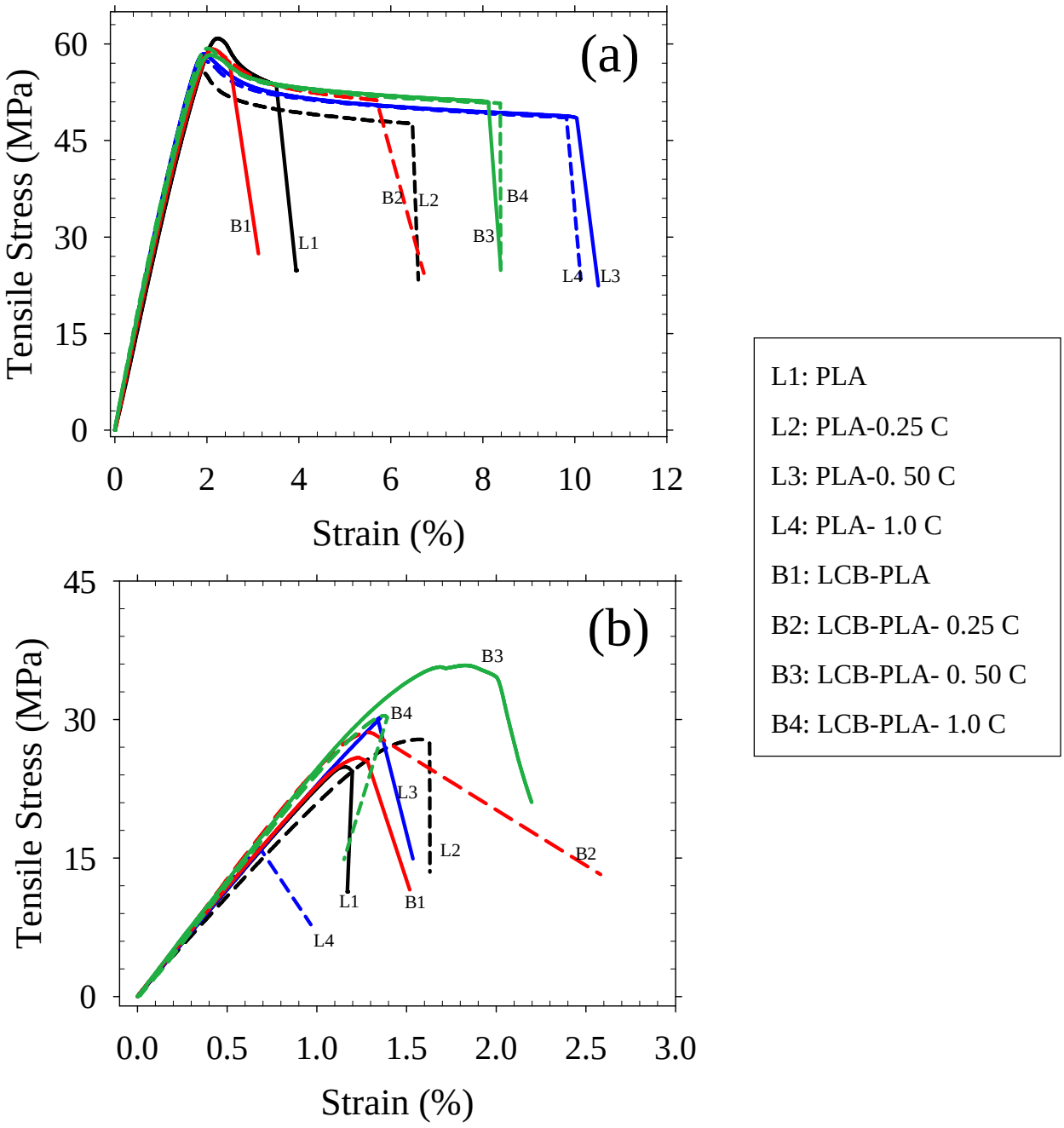

Figure AF.1: Tensile stress –strain curves of (a) unfoamed and (b) foamed linear and LCB-PLA nanocomposites